Simulation Study
of
A Low-Low Satellite-to-Satellite Tracking Mission

by

Jeongrae Kim, B.S., M.S.

Dissertation

Presented to the Faculty of the Graduate School of

The University of Texas at Austin

in Partial Fulfillment

of the Requirements

for the Degree of

Doctor of Philosophy

The University of Texas at Austin

May 2000

Simulation Study
of
A Low-Low Satellite-to-Satellite Tracking Mission

Publication No._____

Jeongrae Kim, Ph.D.

The University of Texas at Austin, 2000

Supervisor: Byron D. Tapley

The Gravity Recovery and Climate Experiment (GRACE) is a dedicated spaceborne mission to map the Earth's gravity field with unprecedented accuracy. The GRACE mission is planned to launch in 2001, for a lifetime of approximately 5 years. It consists of two satellites, co-orbiting in nearly polar orbit, at approximately 300-500 km altitude, separated by 100-500 km along track. Primary measurements are the range change between the two satellites, which represents the gravity perturbation differences between the two locations. These range changes are measured by a high accuracy microwave raging system. To detect the non-gravitational perturbations, which also affect the range change, three axis accelerometers are used.

In this study, full numerical simulations were performed to evaluate the gravity recovery accuracy, and to determine sensitivity of gravity estimation to mission and design parameters. The measurement and dynamic model equations were derived and presented along with the description of the simulation procedure. The error models on two major instruments, the inter-satellite ranging system and accelerometer, were described and their effect on the estimation accuracy were discussed. Series of extensive simulations were performed to analyze the impact of the various simulation parameters, which included the orbit parameters, measurement types, and so on. Comprehensive error models made it possible to perform realistic analyses.

To the extent that the error sources assumed in the simulations represent those actually encountered during the mission, the simulation results will predict the performance of the GRACE mission. The GRACE mission is expected to improve the current knowledge of the Earth gravity field by order of magnitude. The geoid error level is expected to be less than 1cm to spherical harmonic degree 70.

Table of Contents

Abbreviations

AMA	Analytic Mechanics Associates
APL	Applied Physics Laboratory
CHAMP	Challenging Micro-Satellite Payload
CM	Center of Mass
CNES	Centre National d'Etudes Spatiales
CPR	Cycle-Per-Revolution
DDV	Degree Difference Variance
DEV	Degree Error Variance
DLR	Deutsches Zentrum für Luft und Raumfahrt
DSS	Dornier Satellite System
DTM	Drag Temperature Model
ESSP	Earth System Science Pathfinders
GFZ	GeoForchungs Zentrum Potsdam
GPS	Global Positioning System
GRACE	Gravity Recovery and Climate Experiment
GSFC	Goddard Space Flight Center
JPL	Jet Propulsion Laboratory
LaRC	Langley Research Center
LLISS	Large Linear System Solver
LOS	Line-of-Sight
MSODP	Multi-Satellite Orbit Determination Program

NASA	National Aeronautics and Space Administration
ONERA	Office National d'Etudes et de Recherches Aerospatials
POD	Precision Orbit Determination
PSD	Power Spectral Density
RMS	Root Mean Square
SMRD	Science and Mission Requirements Document
SNR	Signal-to-Noise Ratio
SS/L	Space System Loral
SST	(Low-Low) Satellite-to-Satellite Tracking
USO	Ultra Stable Oscillator
UT/CSR	University of Texas at Austin / Center for Space Research
UTOPIA	University of Texas Orbit Determination Program

1 INTRODUCTION

1.1 BACKGROUND

The accurate determination of the Earth gravity field is essential for a variety of geophysical applications, including oceanography, hydrology, glaciology, geodesy, and the solid Earth science. Among many methods to measure the Earth's gravity field, the use of satellite data has become critically important. This satellite method is based on the fact that the orbit of any satellite in a near Earth orbit is dependent on the globally integrated effect of the mass distributions and movements in the Earth system. By observing the motion of such satellites, the Earth gravity field can be estimated. One of the objectives to improve the gravity field is to improve satellite orbit estimations since large portion of the orbit accuracy is limited by the gravity model accuracy.

Since the launch of Sputnik 1 in 1957, the tracking data of the orbits have been used to develop Earth gravity field models [77]. Those tracking data include optical observation, laser tracking, Doppler tracking data, and so on. These satellite tracking data have achieved a significant improvement on the knowledge of the Earth gravity field. With the operation of the Global Positioning System (GPS), a high-low satellite-to-satellite tracking method, tracking between the GPS satellite and a low earth satellite, began to be used for the satellite tracking and the gravity field improvement in 1990's. However, due to the attenuation of the gravity signal with height, these conventional methods do not provide enough information on the short wavelength gravity signals and the improvement is

limited to the long and medium wavelength signals. Those satellites were not intended for the gravity estimation and even the long wavelength accuracy is limited. To obtain a significant improvement on the short wavelength accuracy as well as the long wavelength accuracy, dedicated satellite gravity missions have been considered since 1960's [69]. Those proposed missions can be classified into two broad categories, low-low satellite-to-satellite tracking (SST) and satellite gravity gradiometry (SGG).

The low-low satellite-to-satellite tracking utilizes differential tracking of two low altitude satellites and thereby measures orbit perturbations. This range change can be measured by an accurate microwave or laser raging system. Accelerometers are required to measure the surface force effect, e.g. atmospheric drag and radiation pressure, on the satellite orbit. The gravity gradiometry mission determines the local gravity gradient by measuring the differences in acceleration of two masses within a single spacecraft. Comparison studies between these two missions were performed by many investigators. The Committee on Earth Gravity from Space of the National Research Council examined the advantage of each mission by simulation studies [11,49]. While the low-low SST would provide accurate long and mid wavelength model, the gravity gradiometry would provide accurate short wavelength model, but its long wavelength accuracy is lower than the low-low SST. Two missions are thus complementary to each other.

In the early 1980's the National Aeronautics and Space Administration (NASA) proposed a Geopotential Research Mission (GRM) to globally determine high precision gravitational and magnetic fields of the Earth. It consisted of two

nearly identical satellites in a low altitude of 160 km [35], and the orbit was to be a near circular polar orbit. The relative range-rate between the two satellites was to be measured by microwave ranging system [35,44,52]. The orbit effects due to non-gravitational forces such as atmospheric drag and solar radiation pressure were to be controlled by means of a Disturbance Compensation System (DISCOS) that appropriately fires thrusters to offset the drag effects [1]. Due to its low altitude and large fuel consumption of the DISCOS, the proposed mission lifetime was six months. In 1990's, two low-low SST missions were proposed. The Gravity And Magnetic Earth Surveyor (GAMES) mission [77] consisted of a primary satellite with a laser for tracking a passive second satellite and a GPS receiver for orbit determination of the primary satellite. The primary satellite would carry an accelerometer for measuring non-gravitational forces. The Gravity Recovery and Climate Experiment (GRACE) mission [69] utilized a microwave tracking system for measuring the relative range between two identical satellites. Each satellite carries a GPS receiver and an accelerometer.

Since 1980's, several satellite missions have been proposed for the gravity gradiometry. The European Space Agency (ESA) proposed the ARISTOTELES mission [4], which was to carry four accelerometers in a non drag-compensated spacecraft. The NASA Super-conducting Gravity Gradiometer (SGG) mission [50] was based on more sensitive cryogenic instrument, to be flown in a drag-compensated spacecraft. It was to carry a six-axis high precision gradiometry. The GOCE (Gravity field and steady-state Ocean Circulation Explorer) mission [75] has been recently proposed by the ESA. This concept is a combination of a three-

axis satellite gravity gradiometry and high-low satellite-to-satellite tracking. This is one of four candidate Earth Explorer Missions defined by ESA that are awaiting selection and, if selected, it will fly in 2004.

1.2 GRACE MISSION OVERVIEW

In March 1998, the NASA announced plans to fly the Gravity Recovery and Climate Experiment (GRACE) mission, a low-low satellite-to-satellite tracking (SST) mission. It was selected as the second Earth System Science Pathfinder (ESSP) mission and is planned to be launched in June 2001 with a five-year lifetime. It is a joint project between the NASA and the Deutsches Zentrum für Luft und Raumfart (DLR) [19]. The NASA Jet Propulsion Laboratory (JPL) leads the development of the science instrument and satellite system in partnership with Space System/Loral (SS/L) and Dornier Satellitensysteme (DSS). The German Space Operation Center (GSOC) will take a responsibility of operation of the GRACE satellites with its ground tracking facilities. The observation data collected by GSOC will be processed in a cooperative approach by JPL, University of Texas / Center for Space Research (UT/CSR), and GeoForschungsZentrum (GFZ) in Germany.

The GRACE mission concept is illustrated in Figure 1.1. The orbit of any satellite in a near Earth orbit is dependent on the globally integrated effect of the mass distributions and movements in the Earth system. The orbits of the two satellites, sensing these effects at slightly different phases, will be perturbed differentially [19]. This difference in perturbations is manifested in the inter-

satellite range changes. The GRACE microwave ranging instrument will provide very accurate measurements of the range changes. By making these differential measurements, the higher frequency content of the gravitational signals will be amplified; thus enabling significant improvement in the estimates of the higher resolution features of the Earth gravity field. Since the two satellites are separated in orbit by 220±50 km along-track, the errors due to media effects are minimized as compared to space-based or ground-based tracking. This also ensures the homogeneity of data quality. The orbit inclination will be between 87° and 90° to maximize global coverage. The altitude will be no more than 500 km and the altitude will decrease to 300 km at the end of the five-year mission lifetime. This relatively low altitude makes it possible to detect high frequency gravity signals.

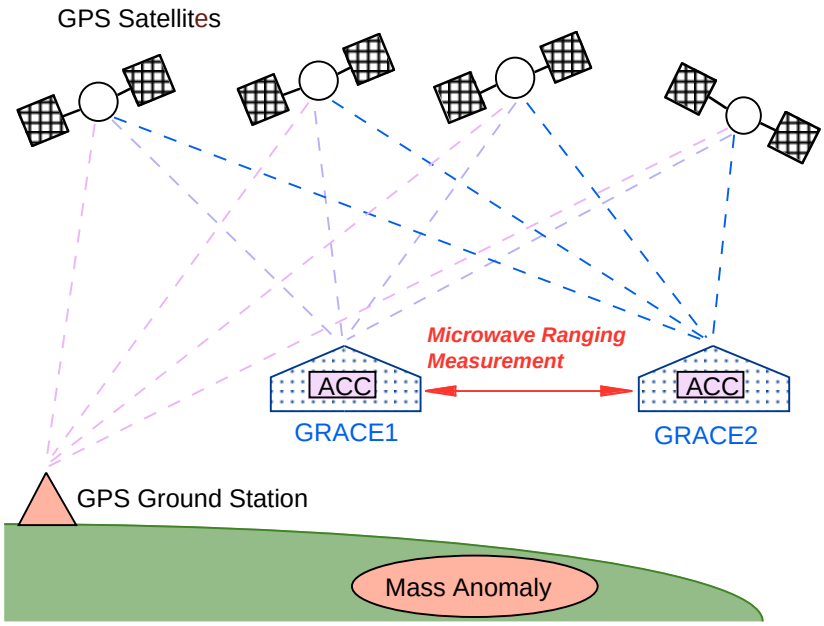

Figure 1.1 GRACE mission concept

In order to measure the inter-satellite range change precisely, the GRACE satellites will use a dual-one way ranging system. With identical transmission and reception subsystems, each satellite transmits the carrier signals to another satellite. The received signals from the two satellites are sent to ground stations and then combined. The frequency fluctuations due to oscillator instability have nearly equal and opposite effects on each satellite's measurement. Therefore, in the proposed approach combining those measurements cancels the oscillator errors effectively. The cancellation would be perfect if it were not for the separation between two satellites and the effectiveness of this cancellation decreases as the separation distance increases. With 1 ms time-of-flight, which corresponds to a 300 km separation distance, this dual one-way ranging system would remove the oscillator noise at frequency lower than 1 KHz. Another error source is the signal delay due to ionosphere, and two frequency signals, K and Ka bands, will be used to correct for this delay. The accuracy of the inter-satellite range-rate is expected to be better than 1 μm/s.

The satellite orbit is affected not only by the gravitational accelerations but also by non-gravitational accelerations, e.g. atmospheric drag and radiation pressure, and its effect must be accurately measured and corrected to utilize the gravitational information in the range change measurements. For this purpose, the GRACE satellites carry high precision three axis accelerometers, which are located at the mass center of each satellite to detect the non-gravitational accelerations only. The SuperSTAR accelerometer developed by the French space

agency ONERA will be used and the design accuracy is about 0.1 nm/s^2 for 10 Hz samples.

Each satellite also carries a geodetic quality GPS receiver to ensure that the orbits for the satellites can be continuously and accurately determined and that the gravity field estimates can be correctly registered in a terrestrial reference frame. Since the individual trajectories are non-observable by the SST measurements only, the GPS measurements are necessary to eliminate that singularity. Comparing with the GRM mission described in the previous section, use of the GPS measurement solves two critical issues unresolved in 1980's, accurate time tagging and geo-locating the observables [69]. This can be solved by collecting GPS data concurrently with the inter-satellite range data. The accurate orbits and clock synchronization can eliminate the unsolved issues.

A dedicated Laser Retro Reflector (LRR) on each satellite allows an external calibration of the onboard GPS system for orbit determination [19]. Laser ranging from the ground can also be used in conjunction with the GPS to support precise orbit determination and gravity field recovery.

Two GRACE satellites have an identical configuration, and Figure 1.2 shows the GRACE satellite configuration and its instrument accommodation. The length and mass are 2.8 m and 420 kg, respectively, but these values are subject to change.

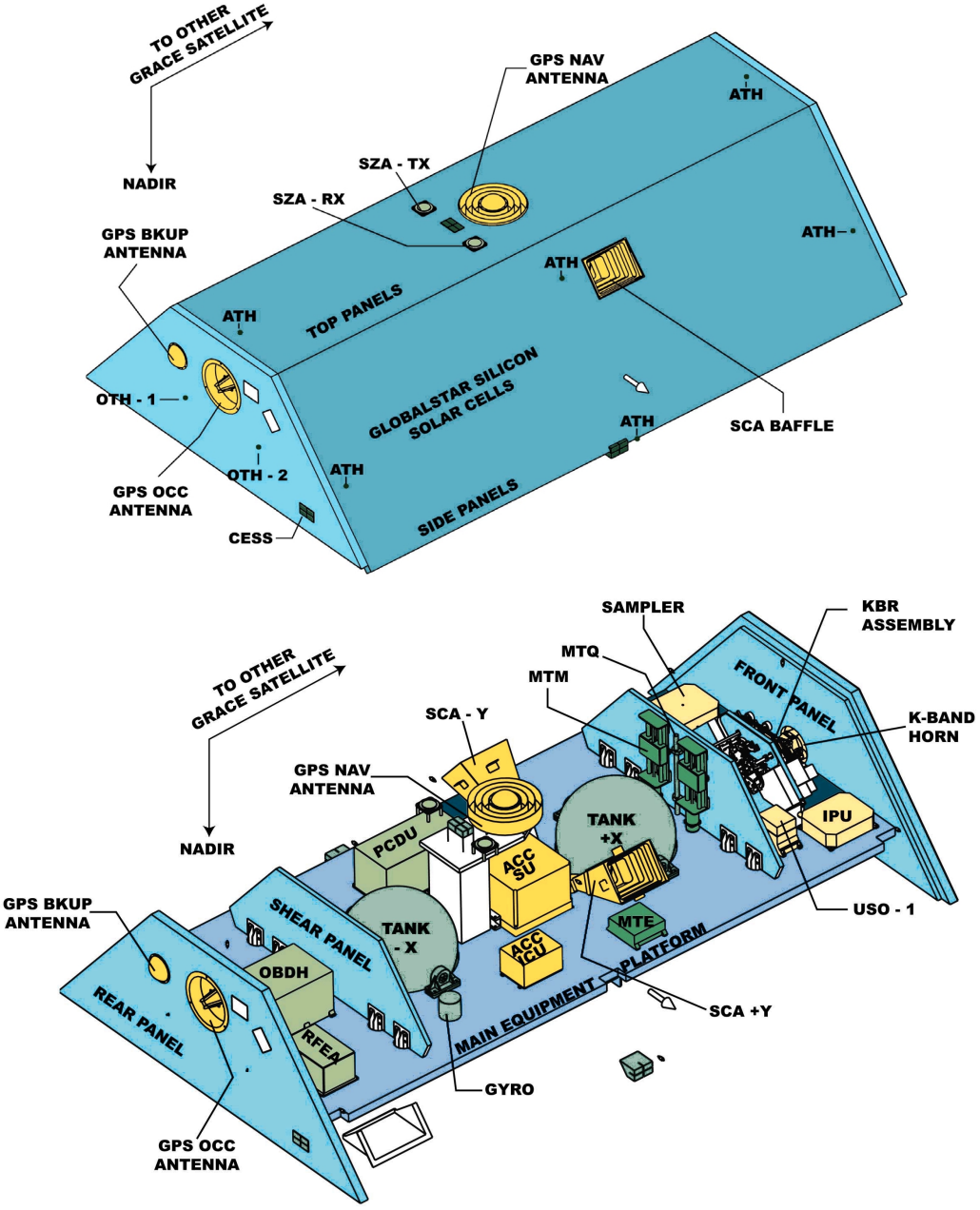

Figure 1.2 GRACE satellite configuration

1.3 PREVIOUS STUDIES

Since the concept of the low-low satellite-to-satellite tracking was first proposed by Wolf [82], there have been many studies showing that a significant improvement can be achieved by using the low-low SST. Several studies based on analytic theory have been performed to evaluate the performance of the SST mission. These studies derived a SST range-rate as a linear function of geopotential coefficients. Kaula [34] and Wagner [79] used Lagrangian perturbation theory to show the feasibility of estimating gravity coefficients from simulated range-rate observations. Colombo [9] and Mackenzie [45,46] derived the range-rate equation using Hill's equation, which describes a near circular satellite motion due to perturbation.

Some of studies focused on the instruments of the GRM mission. Studies by Pisacane [52], MacArthur [44], and Yionoulis [84] described the inter-satellite range-rate system and the drag compensation system (DISCOS). Schutz [63,64] studied the range and range-rate signal characteristics using realistic simulation models. Many of studies, e.g. Antreasian [1], were directed on the DISCOS design and analysis. A report by Keating [35] summarized the overall aspect of the GRM mission.

Until the 1990's, the estimation of a large number of gravity coefficients had been a challenge, and many algorithms were studied to reduce the computational requirements. One method was to utilize a sparse structure of the estimation matrix when the satellite orbit meets a special condition, a repeat orbit. In order to meet this requirement, a large amount of thrust fuel is required,

especially at the low altitude, below 400km, and this requirements derives a short mission lifetime, e.g. 6 months. Advent of powerful super computer has enabled the estimation of the large gravity coefficients with a standard dense estimation matrix. Sharma [65] studied more realistic cases by using full numerical simulations without the orbit repeat restriction. His study was a part of demonstration study on the GRACE mission.

Most of the previous studies focused on the estimation of the gravity coefficients rather than noise modeling. Usually, a simple white noise was applied for the instrument noise. Use of the full numerical simulations, instead of analytic method, enables to implement more comprehensive error models. This study focused more on the instrument modeling than the previous studies did, and the comprehensive modeling makes it possible to obtain more realistic results.

1.4 DISSERTATION OBJECTIVES

The principal objective of this study was to provide the information for the satellite design and orbit selections through comprehensive numerical simulations. For this purpose, the following studies were performed. The first part includes development and explanation of the mathematical concepts for the GRACE observations, and development of methods for extracting gravity field solution from these data. The second part includes the development of simulation models of major instrument errors and the analysis of their effects on the

observations. Third part includes certain trade studies on the effects of orbit selection and the measurement processing methodology.

The equations for the observables and mathematical tools for explaining the observations and their sensitivities are derived. Correction algorithms for processing actual phase measurements are presented. Most of the significant error models and their implementations on the simulation are described. A modified version of the MSODP (Multi Satellite Orbit Determination Program), a precision orbit determination program developed at the UT/CSR [57], was used to estimate satellite trajectories and gravity field coefficients in the simulation. Extensive numerical simulations were performed to quantify the effect of various error sources on the gravity estimation. Sensitivity studies were performed as well by changing orbit parameters. To discuss the simulation results, degree error variances, geoid error plots, and PSD (Power Spectral Density) plots from these simulations are presented. The results of the study will enable assessment of the estimation accuracy for the gravity model coefficients.

1.5 DISSERTATION OUTLINE

Chapter 2 describes the mathematical formulation for processing the GPS and SST data. The general formulations of the satellite-to-satellite tracking (SST) observables, which may be applied to the high-low tracking as well as the low-low tracking, are described. The GPS measurement models include phase measurement processing, double difference measurements, and measurement partial derivatives. The SST measurement models describe how the oscillator

instability is reduced by the dual-one way ranging. The measurement partials implemented in the MSODP [57] are presented as well. The batch estimation algorithm is presented with the specification of estimation parameters.

Chapter 3 describes the models and procedures implemented for the numerical simulations. Force models, which include gravity, atmospheric drag, and other thrust and surface force models, are presented. Empirical parameters used to treat unmodeled force and measurement effects are described. The simulation procedure to generate and to process simulated measurements is presented with the list of simulation parameters applied. In addition to the full numerical simulations, a semi-analytic method was used to overcome computing time limitations. This method utilizes an analytic mapping function derived by Jekeli [29], but it was modified by Bettadpur [5,8] to apply simulated measurements. This formulation is summarized along with the prediction procedure.

Chapter 4 describes the dual one-way ranging, or SST measurement, error models. Several important error sources identified by the JPL GRACE team [71] are included. The procedure to derive the oscillator noise from the Allan variance of the oscillator is discussed. Another important error source, the system noise, is discussed as well. The multipath effect on the SST measurement is described with the formulations and the simulated attitude error time series, which governs the multipath error level. This chapter also describes the correction algorithm to convert a phase-derived range to an instantaneous range. The effect of time tag error is analyzed.

Chapter 5 describes the accelerometer error models, which is one of the important error sources in the GRACE mission. The description of generating simulated accelerometer measurements with various error sources is followed by the description of processing those measurements with estimates of the accelerometer scale factors and biases. Numerical simulations were performed to identify the effect of individual error sources on the gravity solutions. Some design issues related to the accelerometer are discussed as well.

Chapter 6 discusses parameter studies, e.g. orbit selection and measurement type, in consideration of their effect on the gravity accuracy. The orbit selection study includes orbit inclination, altitude, and separation distance. The effect of altitude on the ground track repeat and ultimate observability are studied as well. The variations of the instrument noise level due to the altitude and separation variations were considered. The range measurement is compared to the range-rate measurement by spectrum analyses and some numerical simulations. The expected gravity recovery accuracy is presented with typical simulation results.

Chapter 7 summaries this study and presents conclusions and recommendations for further studies. Appendix A describes an analytic form of the low-low SST equations by using Hill's equations, and it provides insight on the behavior of the SST observation and on the empirical parameterizations. Appendix B describes the details on the simulation procedure. Appendix C summarized the definitions of the power spectral density and degree variances used in this study.

2 SATELLITE-TO-SATELLITE TRACKING MODELS

2.1 INTRODUCTION

The mathematical formulations for processing the SST and GPS data are described in this chapter. The mathematical formulations of the satellite-to-satellite tracking (SST) measurements are described, including both high-low and low-low measurements. The former represents the measurements between the GPS and GRACE satellites and the latter represents the direct measurements between the two GRACE satellites. However, the abbreviation SST represents the low-low satellite-to-satellite tracking in all other parts of this study.

The GRACE mission uses the dual one-way K-band ranging system for precise inter-satellite phase measurements. This system combines the phase measurements from each of the two satellites to remove the effect of oscillator instability. This procedure yields the low-low range and range-rate observables, which are the primary observations of the GRACE mission. The SST and GPS measurement models are described and the partial derivatives are derived. The partial derivatives map the measurements to epoch for the estimation of the parameters. The implementation of these measurements is described along with the measurement partials.

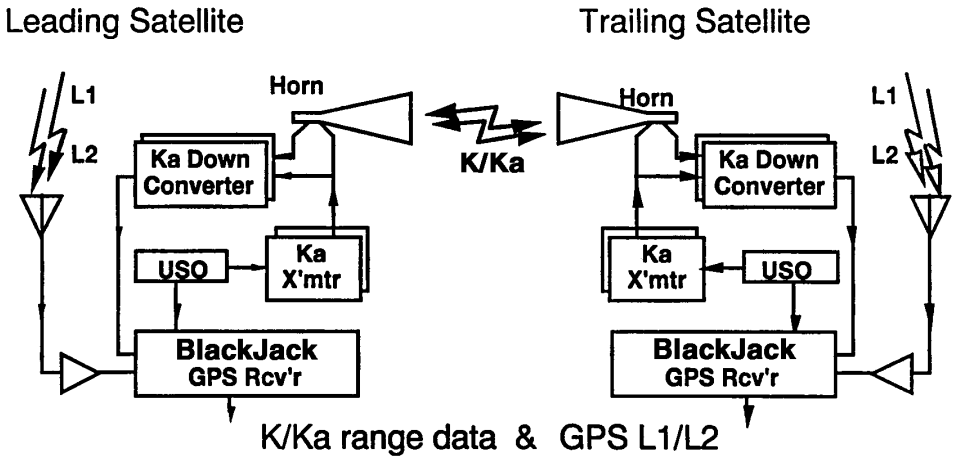

Figure 2.1 Schematic block diagram for the microwave ranging system and the GPS receivers [20]

A block diagram of the microwave ranging system and the GPS receivers are presented in Figure 2.1 [20]. The two GRACE satellites differ only in the radio frequencies for communication with the ground and in the microwave frequencies for the inter-satellite link. The ultra stable oscillator (USO) drives both the microwave ranging (SST) and the GPS receivers. Two microwave frequencies, K (24GHz) and Ka (32GHz), are used to correct the ionosphere effect.

The batch estimation algorithm, as implemented in the MSODP (Multi Satellite Orbit Determination Program) [57], was used to estimate satellite trajectories and gravity field coefficients from the measurements. The overview of the estimation algorithm is described with the classification of estimation parameters.

2.2 SATELLITE-TO-SATELLITE MEASUREMENT PROCESSING

2.2.1 Dual One-Way Ranging Overview

To minimize the effect of oscillator frequency instability on the SST measurement, the GRACE satellites use the dual one-way microwave ranging system to measure the low-low satellite-to-satellite range. Each GRACE satellite transmits K/Ka band microwave signals to the other satellite and receives that satellite's signals. Combination of the received signal and the reference signal that is equivalent to the transmit signal, generates a phase measurement. A phase-locked loop algorithm is used to detect the phase shift due to the relative position changes [71]. The phase measurements received by each satellite are transmitted to the ground station and then combined in ground processing. Since both satellites' phase measurements contain nearly identical oscillator drift noises, combining the two phase measurements effectively eliminates the oscillator instability effect on the range measurement. Figure 2.2 illustrates the oscillator noise cancellation by the dual one-way ranging system. The oscillator noise of one satellite is contained in the measurements of both satellites, and their sampling times are only different by the time-of-flight, less than 1ms. Differencing of these two phases cancels the long and medium period parts of the oscillator noise. Only the high frequency noise, whose period is shorter than 1ms, remains after the dual one-way ranging measurement. This combined phase measurement is converted to the biased range between the two satellites and treated as the fundamental measurement of the GRACE mission.

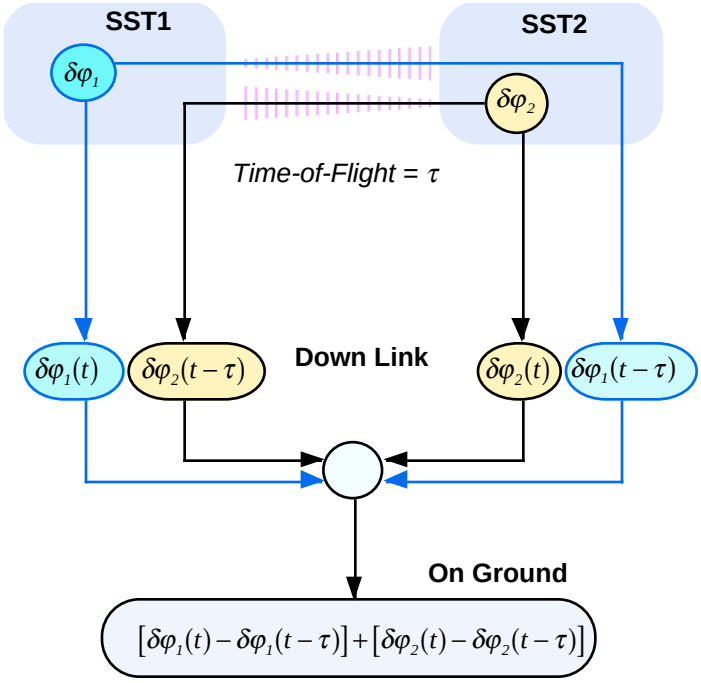

Figure 2.2 Illustration of oscillator noise reduction by the dual one-way ranging system.

The actual dual one-way phase measurements will be pre-processed before the gravity estimation process. The pre-processing includes measurement time tag corrections and biased-range conversion. Figure 2.3 shows the pre-processing procedure of the dual one-way range measurements. The pre-processing algorithm is under development and its full aspect is not covered in this study. Two issues concerning the pre-processing are covered in this study: time-tag correction and instantaneous range correction. The following is the overview of the pre-processing and these two issues.

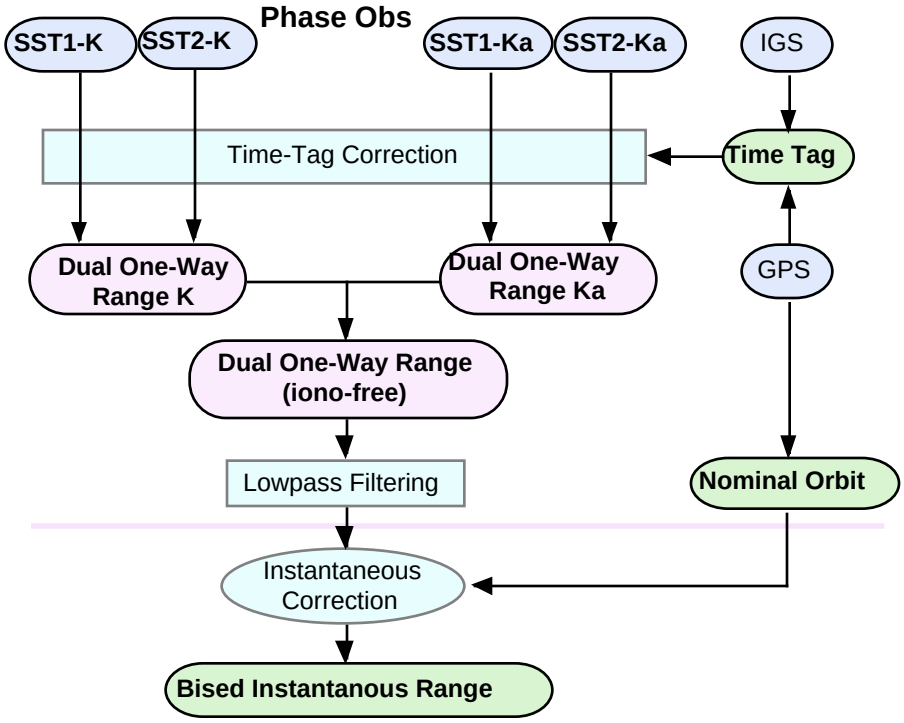

Figure 2.3 Pre-processing procedure of the dual one-way range measurements

The phase measurement of each satellite will be sampled at a specified time, assumed to be close to a common nominal time. Due to the GRACE clock (oscillator) error in each satellite, the actual measurement time is different from the nominal time. With the GPS measurements, the clock error can be corrected to a certain level. This is called time-tag correction. Then, each measurement will be interpolated to its value at the nominal time. These two time-tag corrected phase measurements will be combined into a dual one-way phase measurement of the nominal time and converted to the biased-range. In the IGS network, the time-tag difference is stable, and is estimated accurately to better than 70 pico second over

a day after a linear term is removed [71]. Since the time-tag correction algorithm is under development, its full aspect is not covered in this study.

This biased-range conversion assumes an identical time-of-flight for the two phase measurements. The two phase measurements represent the phases received at the same nominal time but their transmit times are different. These different transmit times imply different time-of-flights. The actual range measurement derived from the dual one-way phase range measurements contains both of these different time-of-flights. Since the two satellites are always moving nearly in the same direction, the time-of-flight of the phase signal from the leading satellite to the trailing satellite is shorter than the time-of-flight of the opposite signal. By using the GPS data to determine the two satellites' states, the actual phase-derived range can be accurately converted into the instantaneous range. The error analysis in Section 4.5 shows that the range error during this instantaneous range conversion can be much lower than the required SST measurement noise level 10 μm [19].

The pre-processed measurement will be assumed to be time-tag corrected and to represent an instantaneous range at a nominal measurement time in the simulation. This instantaneous range model is used to estimate the satellite orbits and gravity coefficients in the simulations. The SST noise models, described in Chapter 4, represent the impact of several error sources on the instantaneous range. The error level due to the time-tag correction inaccuracy is discussed in Section 4.4. The algorithm of the instantaneous correction and its error level are discussed in Section 4.5.

2.2.2 Dual One-Way Ranging Formulations

The single frequency carrier phase measurement between the two GRACE satellites at a specified nominal time *t* can be modeled as follows

$$\varphi_1^2(t+\Delta t_1) = \varphi_1(t+\Delta t_1) - \varphi^2(t+\Delta t_1) + N_1^2 + I_1^2 + d_1^2 + \varepsilon_1^2 \qquad (2.1)$$

$$\varphi_2^1(t+\Delta t_2) = \varphi_2(t+\Delta t_2) - \varphi^1(t+\Delta t_2) + N_2^1 + I_2^1 + d_2^1 + \varepsilon_2^1 \qquad (2.2)$$

where

$\varphi_1^2(t+\Delta t_1)$ = *differential phase measurement at SST1*

$\varphi_2^1(t+\Delta t_2)$ = *differential phase measurement at SST2*

t = *nominal reception time*

$\Delta t_1, \Delta t_2$ = *time tag error of SST1 and SST2*

$\varphi_1(t+\Delta t_1)$ = *SST1 receiver's reference phase*

$\varphi^2(t+\Delta t_1)$ = *received phase transmitted by SST2*

$\varphi_2(t+\Delta t_2)$ = *SST2 receiver's reference phase*

$\varphi^1(t+\Delta t_2)$ = *received phase transmitted by SST1*

N_1^2, N_2^1 = *integer ambiguities*

$I_1^2,\ I_2^1$ = *phase shift due to ionosphere*

$d_1^2,\ d_2^1$ = *phase shift due to neutral atmosphere, instrument, offset, multipath, etc.*

$\varepsilon_1^2,\ \varepsilon_2^1$ = *random measurement noise*

where SST1 and SST2 represent the leading and trailing satellites, respectively. The time tag errors Δt_1 and Δt_2 represent the time difference between the nominal time and the actual reception time. The carrier frequency band is either K (26GHz) or Ka (32GHz) band. The unit of the phase measurement is cycle. Figure 2.4 shows the relationship between the two differential phase observables.

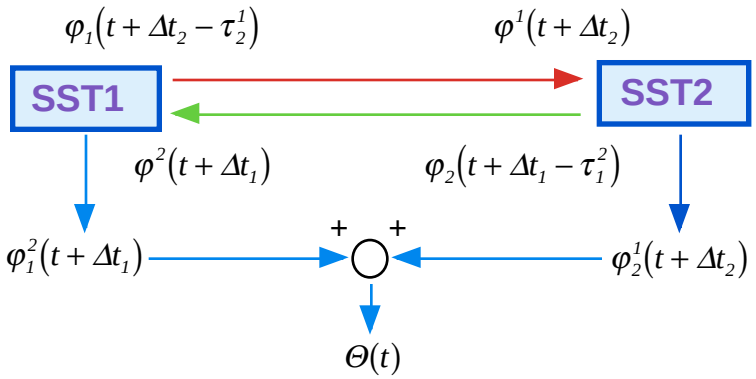

Figure 2.4 Phase observables of the dual one-way ranging system

Each phase consists of the reference phase $\overline{\varphi}_i$, which corresponds to the constant reference frequency, and the phase error $\delta\varphi_i$ due to oscillator drift or frequency instability as

$$\varphi_1(t) = \overline{\varphi}_1(t) + \delta\varphi_1(t) \tag{2.3}$$

$$\varphi_2(t) = \overline{\varphi}_2(t) + \delta\varphi_2(t) \tag{2.4}$$

Also the received phase φ^i can be represented with the transmit phase φ_i at the transmit time as follows

$$\varphi^i(t) = \varphi_i\left(t - \tau_j^i\right) \tag{2.5}$$

where τ_j^i is the time-of-flight from the *i-th* satellite to the *j-th* satellite. The time-of-flight of the two phase signals are different from each other since two satellites are moving. Substitution of (2.3), (2.4), and (2.5) into (2.1) and (2.2) yields

$$\begin{aligned}\varphi_1^2\left(t+\Delta t_1\right) &= \overline{\varphi}_1\left(t+\Delta t_1\right) + \delta\varphi_1\left(t+\Delta t_1\right) - \overline{\varphi}_2\left(t+\Delta t_1-\tau_1^2\right) - \delta\varphi_2\left(t+\Delta t_1-\tau_1^2\right) \\ &\quad + N_1^2 + I_1^2 + d_1^2 + \varepsilon_1^2 \end{aligned} \tag{2.6}$$

$$\begin{aligned}\varphi_2^1\left(t+\Delta t_2\right) &= \overline{\varphi}_2\left(t+\Delta t_2\right) + \delta\varphi_2\left(t+\Delta t_2\right) - \overline{\varphi}_1\left(t+\Delta t_2-\tau_2^1\right) - \delta\varphi_1\left(t+\Delta t_2-\tau_2^1\right) \\ &\quad + N_2^1 + I_2^1 + d_2^1 + \varepsilon_2^1 \end{aligned} \tag{2.7}$$

Adding these two phase measurements makes a dual one-way ranging phase measurement $\Theta(t)$:

$$\begin{aligned}\Theta(t) &\equiv \varphi_1^2\left(t+\Delta t_1\right) + \varphi_2^1\left(t+\Delta t_2\right) \\ &= \overline{\varphi}_1\left(t+\Delta t_1\right) - \overline{\varphi}_2\left(t+\Delta t_1-\tau_1^2\right) + \overline{\varphi}_2\left(t+\Delta t_2\right) - \overline{\varphi}_1\left(t+\Delta t_2-\tau_2^1\right) \\ &\quad + \delta\varphi_1\left(t+\Delta t_1\right) - \delta\varphi_2\left(t+\Delta t_1-\tau_1^2\right) + \delta\varphi_2\left(t+\Delta t_2\right) - \delta\varphi_1\left(t+\Delta t_2-\tau_2^1\right) \\ &\quad + \left(N_1^2 + N_2^1\right) + \left(I_1^2 + I_2^1\right) + \left(d_1^2 + d_2^1\right) + \left(\varepsilon_1^2 + \varepsilon_2^1\right) \end{aligned} \tag{2.8}$$

The phase at $t + \Delta t_i$ can be linearized around the phase at the nominal time *t* as

$$\overline{\varphi}_i\left(t+\Delta t_i\right) \approx \overline{\varphi}_i(t) + \dot{\overline{\varphi}}_i(t)\Delta t_i \tag{2.9}$$

The phase at the transmit time $t + \Delta t_i - \tau_j^i$ can be linearized around the phase at the reception time *t* as

$$\overline{\varphi}_i\left(t + \Delta t_j - \tau_j^i\right) \approx \overline{\varphi}_i(t) + \dot{\overline{\varphi}}_i(t)\Delta t_j - \dot{\overline{\varphi}}_i(t)\tau_j^i \tag{2.10}$$

By the same way, the phase error can be linearized as

$$\begin{aligned} \delta\varphi_i\left(t + \Delta t_i\right) &\approx \delta\varphi_i(t) + \delta\dot{\varphi}_i(t)\Delta t_i \\ \delta\varphi_i\left(t + \Delta t_j - \tau_j^i\right) &\approx \delta\varphi_i(t) + \delta\dot{\varphi}_i(t)\Delta t_j - \delta\dot{\varphi}_i(t)\tau_j^i \end{aligned} \tag{2.11}$$

The rate of phase change, $\dot{\overline{\varphi}}_i(t)$, is equivalent to the constant nominal frequency f_i. The rate of phase error change, $\delta\dot{\overline{\varphi}}_i(t)$, is equivalent to the frequency error, $\delta f_i(t)$. With these substitutions, the phases and phase errors can be linearized as follows

$$\begin{aligned} \overline{\varphi}_i\left(t + \Delta t_i\right) &\approx \overline{\varphi}_i(t) + f_i\Delta t_i \\ \overline{\varphi}_i\left(t + \Delta t_j - \tau_j^i\right) &\approx \overline{\varphi}_i(t) + f_i\Delta t_j - f_i\tau_j^i \end{aligned} \tag{2.12}$$

$$\begin{aligned} \delta\varphi_i\left(t + \Delta t_i\right) &\approx \delta\varphi_i(t) + \delta f_i(t)\Delta t_i \\ \delta\varphi_i\left(t + \Delta t_j - \tau_j^i\right) &\approx \delta\varphi_i(t) + \delta f_i(t)\Delta t_j - \delta f_i(t)\tau_j^i \end{aligned} \tag{2.13}$$

Replacing the phases in (2.8) with (2.12) and (2.13) cancels the phases $\overline{\varphi}_i(t)$ and the phase errors $\delta\overline{\varphi}_i(t)$. Since the same phase errors are in the both satellites' differential phase signals φ_1^2 and φ_2^1 with different signs, they are canceled after combining the two phase signals. However, the phase errors are not perfectly

canceled due to the transmit and reception time difference, i.e. the time-of-flight τ. This is shown in the second line of (2.8). The dual one-way ranging phase measurement becomes a function of the time-of-flight and other error terms as

$$\begin{aligned}\Theta(t) &= \left(f_1\tau_2^1 + f_2\tau_1^2\right) + \left(\delta f_1\tau_2^1 + \delta f_2\tau_1^2\right) \\ &+ \left(f_1 - f_2\right)\left(\Delta t_1 - \Delta t_2\right) + \left(\delta f_1 - \delta f_2\right)\left(\Delta t_1 - \Delta t_2\right) \\ &+ \left(N_1^2 + N_2^1\right) + \left(I_1^2 + I_2^1\right) + \left(d_1^2 + d_2^1\right) + \left(\varepsilon_1^2 + \varepsilon_2^1\right)\end{aligned} \tag{2.14}$$

The first term represents the true phase measurement and the second term does the errors due to the phase errors. The third term is due to the time tag errors and the fourth term is the coupling between the phase error and the time tag error. As mentioned earlier, the time-of-flights, τ_2^1 and τ_1^2, are slightly different. This difference is about 0.05 μs and much smaller than the time-of-flight τ_j^i itself, 1 ms. An algorithm was developed to compute a time-of-flight τ corresponding to the instantaneous inter-satellite range at nominal time *t* from these two time-of-flights as follows

$$\left(f_1\tau_2^1 + f_2\tau_1^2\right) \approx \left(f_1 + f_2\right)\tau - \Delta\Theta_{TOF}(t) \tag{2.15}$$

The details of the instantaneous range correction term $\Delta\Theta_{TOF}(t)$ are covered in Section 4.5. Using the GPS measurements, the time-tag errors can be minimized. After pre-processing for the time-tag correction, the time tag errors become much smaller than the other terms and ignored in this section to evaluate an overall

performance of the dual one-way ranging system. The details of the range error due to the time tag errors are described in Section 4.4.

The inter-satellite biased range is computed from the dual one-way phase of (2.14) by multiplying the speed of light c and then by dividing the sum of the two carrier frequencies, $(f_1 + f_2)$:

$$\begin{aligned} R(t) &= \frac{c\Theta(t)}{f_1 + f_2} \\ &= \rho(t) - \Delta\rho_{TOF}(t) + c\frac{\delta f_1 + \delta f_2}{f_1 + f_2}\tau \\ &+ c\frac{N_1^2 + N_2^1}{f_1 + f_2} + c\frac{I_1^2 + I_2^1}{f_1 + f_2} + c\frac{d_1^2 + d_2^1}{f_1 + f_2} + c\frac{\varepsilon_1^2 + \varepsilon_2^1}{f_1 + f_2} \end{aligned} \tag{2.16}$$

The first term represents the instantaneous range at the time t. The second term is the instantaneous range correction. The third term is the range error due to the oscillator noise. This term is approximated from the phase drift over the time-of-flight τ in (2.13), and only the short period noise, whose period is less than the time-of-flight, is contained. With 1ms time-of-flight τ, this term contains only the high frequency noise, greater than 1kHz. The dual one-way ranging system can remove long and medium wavelength oscillator noise effectively.

2.2.3 Dual Band Ionosphere Correction

To correct the ionosphere effect on the inter-satellite range measurement, the GRACE satellites use dual-band signals, K (24GHz) and Ka (32GHz). For

each band, the carrier frequency of one GRACE signal is offset from the other signal and the two frequencies are defined as f_1 and f_2. This frequency difference makes it necessary to define an effective frequency for the dual one-way phase measurement.

The ionosphere phase shift I_i^j can be approximated to be inversely proportional to the carrier frequency f_j [42,71]:

$$I_i^j = \frac{C_I}{f_j} \tag{2.17}$$

where C_I is a constant proportional to electron content along the signal path. Based on the fifth term of (2.16), the dual one-way range error due to the ionosphere becomes

$$\delta\rho(t) = c\frac{\frac{C_I}{f_1} + \frac{C_I}{f_2}}{f_1 + f_2} = c\frac{C_I}{f_1 f_2} \tag{2.18}$$

This equation can be expressed with an effective frequency $\bar{f}$ [71]:

$$\delta\rho(t) = c\frac{C_I}{\bar{f}^2} \qquad \text{where} \qquad \bar{f} = \sqrt{f_1 f_2} \tag{2.19}$$

The effective frequency for the ionosphere range error is the geometric mean of the two frequencies.

Once the biased-ranges, R_K and R_{Ka}, have been obtained for K and Ka bands, the standard dual-band combination algorithm is applied to obtain the ionosphere-free corrected range:

$$R = \frac{\bar{f}_K^2 R_K - \bar{f}_{Ka}^2 R_{Ka}}{\bar{f}_K^2 - \bar{f}_{Ka}^2} \tag{2.20}$$

where $\bar{f}_K$ and $\bar{f}_{Ka}$ are the effective frequencies for the K and Ka bands. Since both K and Ka band signals derived from the same oscillator, the effect of the oscillator noise on the biased range is equivalent for the both bands except the scaling to the carrier frequencies. The oscillator noise passes through the dual-band combination of (2.20), and its magnitude is not changed.

2.2.4 Satellite-to-Satellite Tracking Observables

The dual one-way phase measurement is converted to a biased range between the two GRACE satellites as (2.16). This biased-range is the primary observable of the GRACE mission, and range-rate and range-acceleration measurements can be generated by numerical differentiation of the range measurement. These three types of observation equations are derived in the following discussion and implemented in the MSODP to generate simulated true low-low measurements without noise. The partial derivatives of the same equations are used to process the simulated measurements.

As mentioned in Section 2.2.1, the actual phase-derived range, which accounts for the two different signal transmission times, is converted into the instantaneous range during the pre-processing. Then, this instantaneous range is processed inside the MSODP to estimate the satellite states and gravity coefficients. Since the instantaneous correction can be separated from the MSODP estimation process, this section describes the instantaneous range and its derivatives. The correction algorithm is discussed in Section 4.5.

The position vectors of satellite 1 and 2 at a nominal time *t* are defined as $\boldsymbol{r}_1$ and $\boldsymbol{r}_2$, respectively, and then the inter-satellite range becomes

$$\rho = \sqrt{(\boldsymbol{r}_1 - \boldsymbol{r}_2)^T (\boldsymbol{r}_1 - \boldsymbol{r}_2)} \tag{2.21}$$

where $\boldsymbol{r}_1$ and $\boldsymbol{r}_2$ are expressed in the inertial coordinates. This range represents an instantaneous range at the nominal time. The inter-satellite range vector $\boldsymbol{r}_{12}$ is defined by

$$\boldsymbol{r}_{12} = \boldsymbol{r}_1 - \boldsymbol{r}_2 \tag{2.22}$$

or

$$\boldsymbol{r}_{12} = \rho \hat{\boldsymbol{e}}_{12} \tag{2.23}$$

$\hat{\boldsymbol{e}}_{12}$ is the line-of-sight(LOS) unit vector defined by

$$\hat{\boldsymbol{e}}_{12} = \frac{\boldsymbol{r}_{12}}{\rho} \tag{2.24}$$

The range-rate is simply obtained by differentiation of the range observable,

$$\dot{\rho} = \dot{\boldsymbol{r}}_{12} \cdot \hat{\boldsymbol{e}}_{12}, \tag{2.25}$$

which represents a projection of the velocity difference vector along the line-of-sight vector. It is noted that this quantity is not the magnitude of the velocity difference vector.

The range-acceleration observable can be obtained by differentiation of the range-rate observable to give

$$\ddot{\rho} = \ddot{\boldsymbol{r}}_{12} \cdot \hat{\boldsymbol{e}}_{12} + \dot{\boldsymbol{r}}_{12} \cdot \dot{\hat{\boldsymbol{e}}}_{12} \tag{2.26}$$

The first term is the projection of the acceleration difference vector along the LOS vector, and the second term is the scalar product of the velocity difference vector and the rate of the LOS vector change. The rate of the LOS vector change can be represented by

$$\dot{\hat{\boldsymbol{e}}}_{12} = \frac{\boldsymbol{c}_{12}}{\rho} \tag{2.27}$$

where

$$\boldsymbol{c}_{12} = \dot{\boldsymbol{r}}_{12} - \dot{\rho}\, \hat{\boldsymbol{e}}_{12} \tag{2.28}$$

denotes the relative velocity component that is perpendicular to the LOS vector. The final form of the range-acceleration becomes

$$\ddot{\rho} = \ddot{\boldsymbol{r}}_{12} \cdot \hat{\boldsymbol{e}}_{12} + \frac{1}{\rho}\left(\left|\dot{\boldsymbol{r}}_{12}\right|^2 - \dot{\rho}^2\right) \tag{2.29}$$

2.2.5 SST Measurement Partials

Processing the SST measurements requires the partial derivatives of the SST measurement with respect to the satellite state vectors. Three types of the SST measurement, range, range-rate, and range-acceleration, will be available for the GRACE mission and the partial derivatives of these measurements with respect to the satellite position and velocity vectors are derived in this section [80]. As mentioned in the previous section, the phase-derived range is converted into the instantaneous range during the pre-processing. The estimation algorithm utilizes the instantaneous range and its derivatives.

Since the range is a function of positions only, the partial derivatives of the range have simple forms as

$$\frac{\partial \rho}{\partial \boldsymbol{r}_1} = \left(\frac{\boldsymbol{r}_1 - \boldsymbol{r}_2}{\rho}\right)^T \qquad \frac{\partial \rho}{\partial \boldsymbol{r}_2} = -\frac{\partial \rho}{\partial \boldsymbol{r}_1} \tag{2.30}$$

$$\frac{\partial \rho}{\partial \boldsymbol{v}_1} = \boldsymbol{0} \qquad \frac{\partial \rho}{\partial \boldsymbol{v}_2} = \boldsymbol{0} \tag{2.31}$$

The partial with respect to the SST2's position is the negative value of the partials with respect to the SST1's. This kind of symmetry is common for other SST measurement partial derivatives. It mainly results from the lack of geometry of the inter-satellite observables, which can not be used to determine absolute

satellite states. Only the relative position and velocity can be obtained by the inter-satellite observables. That is the reason why GPS observables are needed to augment SST observables. It should be noted that the following derivations have no assumption on the location of two satellites. That is, two satellites do not have to be in low-low mode. The formation may be either low-low or high-low.

The partial derivatives of the range-rate, which is the function of both position and velocity, become

$$\frac{\partial\dot{\rho}}{\partial\boldsymbol{r}_1}=\frac{1}{\rho}\left(\dot{\boldsymbol{r}}_{12}-\frac{\boldsymbol{r}_{12}}{\rho}\dot{\rho}\right)^T \qquad \frac{\partial\dot{\rho}}{\partial\boldsymbol{r}_2}=-\frac{\partial\dot{\rho}}{\partial\boldsymbol{r}_1} \tag{2.32}$$

$$\frac{\partial\dot{\rho}}{\partial\boldsymbol{v}_1}=\left(\frac{\boldsymbol{r}_{12}}{\rho}\right)^T \qquad \frac{\partial\dot{\rho}}{\partial\boldsymbol{v}_2}=-\frac{\partial\dot{\rho}}{\partial\boldsymbol{v}_1} \tag{2.33}$$

The partial derivatives of the range-acceleration have more complicated forms,

$$\frac{\partial\ddot{\rho}}{\partial\boldsymbol{r}_1}=\left(\frac{\partial\ddot{\boldsymbol{r}}_{12}}{\partial\boldsymbol{r}_1}\hat{\boldsymbol{e}}_{12}\right)^T+\frac{1}{\rho}\left(\boldsymbol{h}-\frac{2\dot{\rho}}{\rho}\boldsymbol{c}_{12}-\frac{1}{\rho}\left|\boldsymbol{c}_{12}\right|^2\hat{\boldsymbol{e}}_{12}\right)^T$$

$$\frac{\partial\ddot{\rho}}{\partial\boldsymbol{r}_2}=\left(\frac{\partial\ddot{\boldsymbol{r}}_{12}}{\partial\boldsymbol{r}_2}\hat{\boldsymbol{e}}_{12}\right)^T-\frac{1}{\rho}\left(\boldsymbol{h}-\frac{2\dot{\rho}}{\rho}\boldsymbol{c}_{12}-\frac{1}{\rho}\left|\boldsymbol{c}_{12}\right|^2\hat{\boldsymbol{e}}_{12}\right)^T \tag{2.34}$$

$$\frac{\partial\ddot{\rho}}{\partial\boldsymbol{v}_1}=\left(\frac{\partial\ddot{\boldsymbol{r}}_{12}}{\partial\boldsymbol{v}_1}\hat{\boldsymbol{e}}_{12}\right)^T+\frac{2}{\rho}\boldsymbol{c}_{12}^T$$

$$\frac{\partial\ddot{\rho}}{\partial\boldsymbol{v}_2}=\left(\frac{\partial\ddot{\boldsymbol{r}}_{12}}{\partial\boldsymbol{v}_2}\hat{\boldsymbol{e}}_{12}\right)^T-\frac{2}{\rho}\boldsymbol{c}_{12}^T \tag{2.35}$$

where

$$\boldsymbol{c}_{12} = \dot{\boldsymbol{r}}_{12} - \dot{\rho}\,\hat{\boldsymbol{e}}_{12} \tag{2.36}$$

$$\boldsymbol{h} = \ddot{\boldsymbol{r}}_{12} - \left(\ddot{\boldsymbol{r}}_{12} \cdot \hat{\boldsymbol{e}}_{12}\right)\hat{\boldsymbol{e}}_{12} \tag{2.37}$$

The first term in (2.34) needs information other than the satellite states since it contains the acceleration term that consists of the gravity acceleration and other accelerations that are functions of either satellite position or velocity. This makes the partial derivatives very complicated, especially when higher degree and order gravity terms are used.

2.3 GPS MEASUREMENT PROCESSING

2.3.1 GPS Measurement Model

The precision orbit determination program MSODP, which has been developed and used at the University of Texas Center for Space Research (UTCSR), is based on double differenced phase measurements as the primary observations of GPS data processing [57]. The basic equations for the phase measurements and the double differenced GPS phase measurements are described in several references [27,42,57].

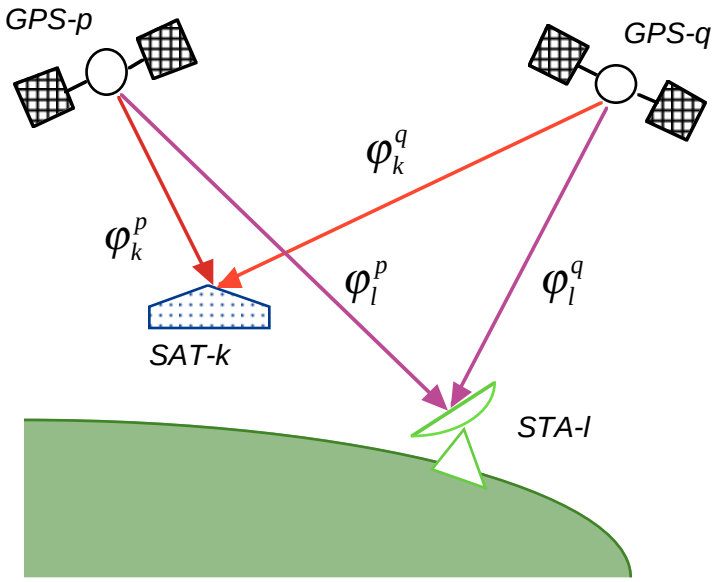

Figure 2.5 GPS carrier phase observables for the double differenced measurement

Figure 2.5 represents four carrier phase measurements, which form one double differenced measurement. The derivation of the double differenced measurement equation begins with one phase measurement. A single frequency GPS phase measurement, L_1 or L_2, is described.

The carrier phase measurement between a GPS satellite and a receiver that may be a low satellite or a ground station can be represented by the following equation [42,57]:

$$\varphi_k^p\left(t+\Delta t_k\right)=\varphi_k\left(t+\Delta t_k\right)-\varphi^p\left(t+\Delta t_k\right)+N_k^p+d_k^p+\varepsilon_k^p \tag{2.38}$$

where

$\varphi_k^p\left(t+\Delta t_k\right)$ = *phase difference between the oscillator of the receiver k and the GPS satellite p*

$\varphi_k(t+\Delta t_k)$ = *reference phase, generated by the receiver k*

$\varphi^p(t+\Delta t_k)$ = *received phase, transmitted by the GPS satellite p*

t = *nominal reception time*

Δt_k = *time tag error of the receiver k*

N_k^p = *integer ambiguity*

d_k^p = *cycle delay or advance due to ionosphere, troposphere, hardware delay, multipath, and so on*

ε_k^p = *random measurement noise*

The nominal time t is a specified time for forming a double-differenced measurement and orbit integration. The time tag error Δt_k represents the time difference between the nominal time t and the actual measurement time $t+\Delta t_k$. The difference $\varphi_k(t+\Delta t_k)-\varphi^p(t+\Delta t_k)$ is developed for a vacuum, and the corrections for the propagation media, instrument biases, and delays must be added separately. Neglecting the effect of the ionosphere and atmosphere, the received carrier phase $\varphi^p(t)$ is equivalent to the emitted phase at the GPS satellite, exactly τ_k^p earlier:

$$\varphi^p(t+\Delta t_k)=\varphi_p(t+\Delta t_k-\tau_k^p) \tag{2.39}$$

τ_k^p is the time-of-flight from the GPS satellite p to the receiver k. φ_p represents the phase emitted by the GPS satellite p. The phases at the measurement time can be related to the phase at the nominal time by the following linearization:

$$\varphi_k(t+\Delta t_k) = \varphi_k(t) + \dot{\varphi}_k(t)\Delta t_k \tag{2.40}$$

$$\varphi_p(t+\Delta t_k - \tau_k^p) = \varphi_p(t) + \dot{\varphi}_p(t)(\Delta t_k - \tau_k^p) \tag{2.41}$$

The rate of phase changes can be approximated as

$$\dot{\varphi}_k(t) = f_0 + \delta f_k \tag{2.42}$$

$$\dot{\varphi}_p(t) = f_0 + \delta f_p \tag{2.43}$$

where f_0 is the nominal frequency of the GPS phase signal and the δf_k and δf_p represent the frequency errors from f_0 due to oscillator instability. Using these approximations, the equations (2.40) and (2.41) become

$$\varphi_k(t+\Delta t_k) = \varphi_k(t) + (f_0 + \delta f_k)\Delta t_k \tag{2.44}$$

$$\varphi_p(t+\Delta t_k - \tau_k^p) = \varphi_p(t) + (f_0 + \delta f_p)(\Delta t_k - \tau_k^p) \tag{2.45}$$

The time-of-flight τ_k^p is consistent with the geometric range from the GPS satellite *p* to the receiver *k*. However, it is not the range at the nominal time *t* but the range at the measurement time $t + \Delta t_k$, and may be approximated using the range $\rho_k^p(t)$ and range-rate $\dot{\rho}_k^p(t)$ at time *t* as follows

$$\tau_k^p = \frac{1}{c}\left[\rho_k^p(t) + \dot{\rho}_k^p(t) \cdot \Delta t_k\right] \tag{2.46}$$

Substitution of (2.45) and (2.46) into (2.39) yields the received phase

$$\varphi^p(t+\Delta t_k) = \varphi_p(t) + (f_0 + \delta f_p)\left[\Delta t_k - \frac{1}{c}\rho_k^p(t) - \frac{1}{c}\dot{\rho}_k^p(t) \cdot \Delta t_k\right] \tag{2.47}$$

Substitution of (2.44) and (2.47) into (2.38) separates the phase measurement at $t + \Delta t_k$ into the phases at the nominal time *t* and other terms:

$$\begin{aligned}\varphi_k^p(t+\Delta t_k) &= \varphi_k(t) - \varphi_p(t) \\ &+\left(\delta f_k - \delta f_p\right)\Delta t_k + \frac{1}{c}\left(f_0 + \delta f_p\right)\left[\rho_k^p(t) + \dot{\rho}_k^p(t)\cdot\Delta t_k\right] \\ &+N_k^p + d_k^p + \varepsilon_k^p \end{aligned} \tag{2.48}$$

This is the carrier phase measurement equation between the receiver *k* and the GPS satellite *p*. It contains a time tag error Δt_k and two frequency errors δf_k and δf_p.

If two receivers *k* and *l*, one is a ground receiver and the other one is a low satellite, observe the same GPS satellite *p* at the same nominal time *t*, then one can write two equations of the form of (2.48). The single difference phase observable may be defined by the difference of the two received phase measurements transmitted from the same GPS satellite:

$$\begin{aligned}\varphi_{kl}^p(t) &\equiv \varphi_k^p(t+\Delta t_k) - \varphi_l^p(t+\Delta t_p) \\ &= \varphi_k(t) - \varphi_l(t) \\ &+\left(\delta f_k - \delta f_p\right)\Delta t_k - \left(\delta f_l - \delta f_p\right)\Delta t_l \\ &+\frac{1}{c}\left(f_0 + \delta f_p\right)\left[\rho_k^p(t) + \dot{\rho}_k^p(t)\cdot\Delta t_k - \rho_l^p(t) - \dot{\rho}_l^p(t)\cdot\Delta t_l\right] \\ &+N_{kl}^p + d_{kl}^p + \varepsilon_{kl}^p \end{aligned} \tag{2.49}$$

N_{kl}^{p}, d_{kl}^{p}, and ε_{kl}^{p} denotes combined ambiguity, cycle delay, and random noise, respectively. Ideally, two phases should be measured at the same nominal time *t*, but there exist time tag errors Δt_k and Δt_l.

If two receivers *k* and *l* observe two GPS satellite *p* and *q* at the same nominal time, the double difference phase observable is defined by

$$\begin{aligned}
\varphi_{kl}^{pq}(t) &\equiv \varphi_{kl}^{p}(t) - \varphi_{kl}^{q}(t) \\
&= \frac{f_0}{c}\left[\rho_k^p(t) - \rho_l^p(t) - \rho_k^q(t) + \rho_l^q(t)\right] \\
&+ \frac{f_0}{c}\left[\left(\dot{\rho}_k^p(t) - \dot{\rho}_k^q(t)\right)\Delta t_k - \left(\dot{\rho}_l^p(t) - \dot{\rho}_l^q(t)\right)\Delta t_l\right] \\
&+ \frac{\delta f_p}{c}\left(\rho_k^p(t) - \rho_l^p(t)\right) - \frac{\delta f_q}{c}\left(\rho_k^q(t) - \rho_l^q(t)\right) \\
&+ \frac{\delta f_p}{c}\left(\dot{\rho}_k^p(t)\Delta t_k - \dot{\rho}_l^p(t)\Delta t_l\right) - \frac{\delta f_q}{c}\left(\dot{\rho}_k^q(t)\Delta t_k - \dot{\rho}_l^q(t)\Delta t_l\right) \\
&-\left(\delta f_p - \delta f_q\right)\left(\Delta t_k - \Delta t_l\right) \\
&+ N_{kl}^{pq} + d_{kl}^{pq} + \varepsilon_{kl}^{pq}
\end{aligned} \tag{2.50}$$

This phase measurement can be scaled to a biased-range by multiplying the wavelength $\lambda = c / f_0$, where is f_0 is the reference frequency of the GPS signal, either 1.57542 GHz (L_1) or 1.2276 GHz (L_2):

$$\begin{aligned}
\Phi_{kl}^{pq}(t) &= \left[\rho_k^p(t) - \rho_l^p(t) - \rho_k^q(t) + \rho_l^q(t)\right] \\
&+\left[\left(\dot{\rho}_k^p(t) - \dot{\rho}_k^q(t)\right)\Delta t_k - \left(\dot{\rho}_l^p(t) - \dot{\rho}_l^q(t)\right)\Delta t_l\right]
\end{aligned}$$

$$+\left[\frac{\delta f_p}{f_0}\left(\rho_k^p(t)-\rho_l^p(t)\right)-\frac{\delta f_q}{f_0}\left(\rho_k^q(t)-\rho_l^q(t)\right)\right]$$

$$+\left[\frac{\delta f_p}{f_0}\left(\dot{\rho}_k^p(t)\Delta t_k-\dot{\rho}_l^p(t)\Delta t_l\right)-\frac{\delta f_q}{f_0}\left(\dot{\rho}_k^q(t)\Delta t_k-\dot{\rho}_l^q(t)\Delta t_l\right)\right]$$

$$-c\left(\frac{\delta f_p}{f_0}-\frac{\delta f_q}{f_0}\right)\left(\Delta t_k-\Delta t_l\right)$$

$$+C_{k\,l}^{p\,q}+\delta_{k\,l}^{p\,q}+\xi_{k\,l}^{p\,q} \tag{2.51}$$

where

$$C_{k\,l}^{p\,q}=\lambda\left[N_k^p-N_l^p-N_k^q+N_l^q\right] \tag{2.52}$$

$$\delta_{k\,l}^{p\,q}=\lambda\left[d_k^p-d_l^p-d_k^q+d_l^q\right] \tag{2.53}$$

$$\xi_{k\,l}^{p\,q}=\lambda\left[\varepsilon_k^p-\varepsilon_l^p-\varepsilon_k^q+\varepsilon_l^q\right] \tag{2.54}$$

The first line represents the double differenced geometric range and the second line represents the effect of timing error due to receiver clock errors, Δt_k and Δt_l. The third line represents the coupling between the GPS frequency errors and the range differences. The GPS satellites have very accurate onboard clocks and the frequency instability $\delta f / f_0$ is 10^{-12} [27,42]. With a range difference of 1000 km, this magnitude becomes an order of 10^{-6} m level, and this term can be neglected. The fourth line represents the coupling between the frequency errors and the range changes and its magnitude is even much smaller than that of the third line. The fifth line is the coupling the frequency error difference and the time tag error difference and can be maintained less than an order of sub-*mm* level even with

one second time tag difference. The last line represents the ambiguity, time delay, and measurement random noise. The MSODP uses this equation for processing GPS double difference observations, which are formed by the data pre-processor. The receiver clock error may be modeled as a linear function as follows

$$\Delta t_k = a_k + b_k\left(t - t_{k0}\right) \tag{2.55}$$

$$\Delta t_l = a_l + b_l\left(t - t_{l0}\right) \tag{2.56}$$

where a_i and b_i are the clock bias and drift, respectively. These time tag errors may be supplied from other sources and used during pre-processing. In that case, the single phases $\varphi_i^j\left(t + \Delta t_i\right)$ are interpolated to $\varphi_i^j(t)$ and the second term of (2.51) can be ignored.

2.3.2 GPS Measurement Partials

For mapping the GPS observations into the satellite state and other parameters, the partial derivatives of the GPS double difference measurement with respect to the satellite state and the measurement parameters need to be computed. The partial derivatives are formed with respect to low satellite positions, ground receiver positions, GPS satellite positions, combined ambiguity, clock parameters, zenith path delay, and so on.

The partial derivatives of (2.51) with respect to the ground station position becomes

$$\left[\frac{\partial \Phi_{k\,l}^{p\,q}}{\partial \boldsymbol{r}_k}\right]^T = \frac{\boldsymbol{r}_k - \boldsymbol{r}^p}{\rho_k^p} - \frac{\boldsymbol{r}_k - \boldsymbol{r}^q}{\rho_k^q} \tag{2.57}$$

where

$\boldsymbol{r}_k$ = *position of ground station k,* $\left(x_k, y_k, z_k\right)^T$

$\boldsymbol{r}^p, \boldsymbol{r}^q$ = *position of GPS satellites p and q*

$\rho_k^p = \sqrt{\left(\boldsymbol{r}_k - \boldsymbol{r}^p\right)^T \left(\boldsymbol{r}_k - \boldsymbol{r}^p\right)}$

= *geometric range between ground station k and GPS satellite p*

$\rho_k^q = \sqrt{\left(\boldsymbol{r}_k - \boldsymbol{r}^q\right)^T \left(\boldsymbol{r}_k - \boldsymbol{r}^q\right)}$

= *geometric range between ground station k and GPS satellite q*

The first and second terms represent the line-of-sight unit vectors to GPS satellites *p* and *q* respectively. The partial derivative with respect to the receiver position implies the difference between two line-of-sight unit vectors.

The partial derivatives with respect to the low satellite position are represented in a similar way:

$$\left[\frac{\partial \Phi_{k\,l}^{p\,q}}{\partial \boldsymbol{r}_l}\right]^T = -\frac{\boldsymbol{r}_l - \boldsymbol{r}^p}{\rho_l^p} + \frac{\boldsymbol{r}_l - \boldsymbol{r}^q}{\rho_l^q} \tag{2.58}$$

The partial derivatives with respect to GPS satellite position vectors, $\boldsymbol{r}^p$ and $\boldsymbol{r}^q$, are represented by

$$\left[\frac{\partial \boldsymbol{\Phi}_{kl}^{pq}}{\partial \boldsymbol{r}^p}\right]^T = -\frac{\boldsymbol{r}_k - \boldsymbol{r}^p}{\rho_k^p} + \frac{\boldsymbol{r}_l - \boldsymbol{r}^p}{\rho_l^p} \tag{2.59}$$

$$\left[\frac{\partial \boldsymbol{\Phi}_{kl}^{pq}}{\partial \boldsymbol{r}^q}\right]^T = \frac{\boldsymbol{r}_k - \boldsymbol{r}^q}{\rho_k^q} - \frac{\boldsymbol{r}_l - \boldsymbol{r}^q}{\rho_l^q} \tag{2.60}$$

The kinematic parameters in the GPS measurement include the receiver clock parameters and the combined ambiguity. The partial derivatives with respect to the receiver clock parameters (a_k, b_k) or (a_l, b_l) are represented by

$$\frac{\partial \boldsymbol{\Phi}_{kl}^{pq}}{\partial a_k} = \left(\dot{\rho}_k^p - \dot{\rho}_k^q\right) \tag{2.61}$$

$$\frac{\partial \boldsymbol{\Phi}_{kl}^{pq}}{\partial b_k} = \left(\dot{\rho}_k^p - \dot{\rho}_k^q\right)\left(t - t_{k0}\right) \tag{2.62}$$

or

$$\frac{\partial \boldsymbol{\Phi}_{kl}^{pq}}{\partial a_l} = -\left(\dot{\rho}_l^p - \dot{\rho}_l^q\right) \tag{2.63}$$

$$\frac{\partial \boldsymbol{\Phi}_{kl}^{pq}}{\partial b_l} = -\left(\dot{\rho}_l^p - \dot{\rho}_l^q\right)\left(t - t_{l0}\right) \tag{2.64}$$

The partial derivative with respect to the combined ambiguity C_{kl}^{pq} becomes a constant unit number, which is usual for the measurement parameters. The equation is given by

$$\frac{\partial \Phi_{k\,l}^{p\,q}}{\partial C_{k\,l}^{p\,q}} = 1 \tag{2.65}$$

There are two types of orbit determination method using GPS observations. One is the kinematic method, which estimates the receiver satellite states only by the GPS measurements without equations of motion or description of the dynamic force models. The other one is the dynamical method, which is based on the dynamic models in the equations of motion. While the kinematic method is limited by measurement noise level, the dynamic method is mainly limited by the accuracy of the reference dynamic modeling. This dependency on the dynamic models makes it possible for the dynamic method to improve the dynamic model. MSODP uses the dynamic orbit determination so that better dynamic model, especially gravity model, gives more accurate orbit estimates.

2.4 ESTIMATION THEORY

2.4.1 Linear Estimation Theory

This section describes a conventional estimation method, least squares estimate. This method was used for the estimation of orbit and gravity solution using the simulated GRACE measurements.

The state vector is composed of all dependent variables or constant parameters, which are required to define the time rate of change of the state of the

dynamical system [67]. With this definition, the *n*-dimensional state vector, $\boldsymbol{X}$, can be represented as

$$\boldsymbol{X} = [\boldsymbol{r} \quad \boldsymbol{v} \quad \boldsymbol{\alpha}]^T \tag{2.66}$$

where $\boldsymbol{r}$ and $\boldsymbol{v}$ represent the position and velocity vectors, respectively, and $\boldsymbol{\alpha}$ represents the constant model parameters. The state equations, which are derived from an application of Newton's second law for each satellite, can be expressed as first-order ordinary differential equations as

$$\dot{\boldsymbol{X}} = \boldsymbol{F}(\boldsymbol{X}, t) \qquad \boldsymbol{X}(t_0) = \boldsymbol{X}_0 \tag{2.67}$$

The observation-state vector relationship can be expressed as

$$\boldsymbol{Y}_i = \boldsymbol{G}(\boldsymbol{X}_i, t_i) + \boldsymbol{\varepsilon}_i \tag{2.68}$$

$\boldsymbol{Y}_i$ represents an observation at time t_i and it is assumed to be a nonlinear function of the true observation $\boldsymbol{G}(\boldsymbol{X}_i, t_i)$ and the random measurement noise $\boldsymbol{\varepsilon}_i$. These nonlinear state and observation equations can be linearized in the following way.

Define the difference between true and reference values as

$$\boldsymbol{x}(t) = \boldsymbol{X}(t) - \boldsymbol{X}^*(t) \qquad \boldsymbol{y}(t) = \boldsymbol{Y}(t) - \boldsymbol{Y}^*(t) \tag{2.69}$$

$\boldsymbol{X}^*(t)$ and $\boldsymbol{Y}^*(t)$ represent a reference state vector and an associated reference observation vector, respectively. When the reference values are within the linear region of the true value, a first-order Taylor series approximation yields the following linearized equations:

$$\dot{\boldsymbol{x}}(t) = A(t)\boldsymbol{x}(t) \tag{2.70}$$

$$\boldsymbol{y}_i = \tilde{H}_i \boldsymbol{x}_i + \boldsymbol{\varepsilon}_i \tag{2.71}$$

where

$$A(t) = \frac{\partial \boldsymbol{F}}{\partial \boldsymbol{X}}\left(\boldsymbol{X}^*, t\right) \qquad \tilde{H}_i = \frac{\partial \boldsymbol{G}}{\partial \boldsymbol{X}}\left(\boldsymbol{X}_i^*, t\right) \tag{2.72}$$

The linearized state equations of (2.70) have the general solution as

$$\boldsymbol{x}(t) = \boldsymbol{\Phi}\left(t, t_0\right)\boldsymbol{x}_0 \tag{2.73}$$

The matrix $\boldsymbol{\Phi}\left(t, t_0\right)$ is called the state transition matrix and $\boldsymbol{x}_0$ is the state at a general epoch t_0. The state transition matrix can be shown to satisfy the following differential equation:

$$\dot{\boldsymbol{\Phi}}\left(t, t_0\right) = A(t)\boldsymbol{\Phi}\left(t, t_0\right) \qquad \boldsymbol{\Phi}\left(t_0, t_0\right) = I \tag{2.74}$$

where numerical integration yields the state transition matrix at any time *t*. Using (2.73), $\boldsymbol{x}_i$ in (2.71) can be replaced with $\boldsymbol{x}_0$ as follows:

$$\boldsymbol{y} = H\boldsymbol{x} + \boldsymbol{\varepsilon} \tag{2.75}$$

where

$$\boldsymbol{y} = \begin{bmatrix} \boldsymbol{y}_1 \\ \boldsymbol{y}_2 \\ \vdots \\ \boldsymbol{y}_m \end{bmatrix} \qquad H = \begin{bmatrix} \tilde{H}_1 \boldsymbol{\Phi}(t_1, t_0) \\ \tilde{H}_2 \boldsymbol{\Phi}(t_2, t_0) \\ \vdots \\ \tilde{H}_m \boldsymbol{\Phi}(t_m, t_0) \end{bmatrix} \qquad \boldsymbol{\varepsilon} = \begin{bmatrix} \boldsymbol{\varepsilon}_1 \\ \boldsymbol{\varepsilon}_2 \\ \vdots \\ \boldsymbol{\varepsilon}_m \end{bmatrix} \tag{2.76}$$

The subscript of $\boldsymbol{x}_0$ is dropped for convenience. When each measurement has different weightings, the weighted least square solution of the equation (2.75) becomes [67]

$$\hat{\boldsymbol{x}} = \left(H^T W H\right)^{-1} H^T W \boldsymbol{y} \tag{2.77}$$

If the estimate is unbiased and a linear combination of the observations, the minimum variance solution can be obtained in the similar form as

$$\boldsymbol{x} = \left(H^T R^{-1} H\right)^{-1} H^T R^{-1} \boldsymbol{y} \tag{2.78}$$

R is the covariance of the observation error $\boldsymbol{\varepsilon}$, which is assumed to have a zero mean. This minimum variance estimate requires only the first and second moments of the probability density function of the observation errors instead of complete statistical description. The matrix $\left(H^T R^{-1} H\right)^{-1}$ is called the covariance matrix and its inverse $H^T R^{-1} H$ is called the information matrix. This solution will agree with the weighted least square solution of (2.77) when the weighting matrix W is equal to the noise covariance matrix inverse R^{-1}. In addition, if the observation errors have a normal distribution, the minimum variance estimate will agree with the maximum likelihood estimate.

2.4.2 Definition of the Estimation Parameters

The constant parameter vector $\boldsymbol{\alpha}$ in (2.66) can be classified into dynamic and kinematic parameters [57]. The dynamic parameters are the set of parameters, which appear explicitly in the differential equations describing the dynamic model. These include the gravity coefficients, drag coefficient, radiation coefficient, empirical force parameters, and so on. Since not all the dynamic parameters are present in the measurement equation explicitly, they need to be mapped to the epoch state by using the state transition matrix that is usually computed by numerical integration. In this study, the accelerometer scale factors and biases are treated as dynamic parameters. The kinematic parameters generally appear in the measurement model only. They include measurement biases, ground station coordinates, the Earth rotation parameters, and so on.

The estimation vector in (2.66) can be rewritten with the dynamic parameter vector $\boldsymbol{d}$ and the kinematic parameter vector $\boldsymbol{k}$ in place of the constant parameter vector $\boldsymbol{\alpha}$:

$$\boldsymbol{X} = \begin{bmatrix} \boldsymbol{r} & \boldsymbol{v} \vdots \boldsymbol{d} & \boldsymbol{k} \end{bmatrix}^T \tag{2.79}$$

Then the matrix $A(t)$ in (2.72) becomes

$$A(t) = \frac{\partial \boldsymbol{F}}{\partial \boldsymbol{X}} = \begin{bmatrix} 0 & I & 0 & 0 \\ \partial \boldsymbol{f} / \partial \boldsymbol{r} & \partial \boldsymbol{f} / \partial \boldsymbol{v} & \partial \boldsymbol{f} / \partial \boldsymbol{d} & 0 \\ 0 & 0 & 0 & 0 \\ 0 & 0 & 0 & 0 \end{bmatrix} \tag{2.80}$$

The dynamic parameters are mapped to other time epochs by the state-transition matrix in (2.73). Their corresponding elements in $\tilde{H}$ have zero values, but those ones in H have non-zero values. On the other hand, the partials with respect to the kinematic parameters have zero values in $A(t)$, then the corresponding elements of the state-transition matrix have zero values.

3 SIMULATION MODELS AND PROCEDURE

3.1 INTRODUCTION

This chapter describes the models and procedures used for the numerical simulations of gravity recovery using the SST and GPS data. The simulation procedure consists of two major parts, generating simulated measurements and processing them to estimate the gravity field. These two procedures use different models, one is the truth model for generating measurements, and the other one is the nominal model for processing measurements. The difference between the two models represents the current uncertainty level on the models. It also enables determination of sensitivity of results to model errors.

The simulation models consist of the force models and the measurement models. The force models include gravity field, atmospheric drag, radiation pressure, and accelerometer noise models. The measurement models include the SST and GPS noise models. The SST and accelerometer models are described in the following chapters. The method of computing the optimal weighting of two information equations, one from SST measurements and the other from GPS measurements, are described.

To treat residual or unmodeled measurement error, a set of empirical parameters is used. These include 1 cycle-per-revolution (cpr) and tangential acceleration parameters to adjust the orbit trajectories. Low-low empirical parameters were also used to adjust the low-low SST measurements. Another set

of empirical parameters, accelerometer scale factor and bias, are described in Chapter 5.

Due to available computer limitations, this study limits the size of the gravity field estimation to degree 70 to 120 with the conventional least squares estimation method. This gravity size is not enough for some sensitivity studies where the accuracy of higher degree gravity field is important. To overcome this limit, a semi-analytic method, which is based on an analytic method approach, was used for predicting the geoid error spectrum for higher degree fields. These analytic results were verified to the numerical results in the low degrees. The mathematical formulations are described along with the procedure.

3.2 FORCE MODELS

The differential equations describing the motion of an Earth orbiting satellite may be expressed by

$$\ddot{\boldsymbol{r}} = -\frac{\mu}{r^3}\boldsymbol{r} + \boldsymbol{a}_c + \boldsymbol{a}_{nc} + \boldsymbol{a}_\varepsilon \tag{3.1}$$

where μ is the Earth gravitational parameter and $\boldsymbol{r}$ is the geocentric position vector of the satellite[67].

In Equation (3.1) $\boldsymbol{a}_c$ represents the force per unit mass produced by gravity, also called the conservative force, which depends on the satellite position only. Such a force can be expressed as the gradient of a potential function U that

consists of the contribution due to the gravitational geopotential, the solid Earth tides, ocean tides, N-body potential, atmospheric tides, rotational deformation, general relativity, and so on.

The term $\boldsymbol{a}_{nc}$ represents the force per unit mass due to the non-gravitational or non-conservative forces and it may consist of the following components

$$\boldsymbol{a}_{nc} = \boldsymbol{a}_a + \boldsymbol{a}_{sr} + \boldsymbol{a}_{er} + \boldsymbol{a}_{thrust} + \boldsymbol{a}_{other} \tag{3.2}$$

It includes atmospheric drag $\boldsymbol{a}_a$, solar radiation pressure $\boldsymbol{a}_{sr}$, Earth radiation pressure $\boldsymbol{a}_{er}$, thrust $\boldsymbol{a}_{thrust}$, and others $\boldsymbol{a}_{other}$. The accelerometer on the center of mass of each GRACE satellite detects only the total non-gravitational force. This accelerometer measurement can be used to identify the non-gravitational force acting on the satellite trajectory and to remove its effect on the satellite trajectory estimation. The term $\boldsymbol{a}_{\varepsilon}$ represents any unmodeled errors.

3.2.1 Gravity Field Models

The primary gravitational force used in this study was the non-spherical geopotential, which is expressed in terms of a spherical harmonic expansion in the Earth fixed reference frame as [33]

$$U_{ns}(r,\phi,\lambda,t) = \frac{\mu}{r}\sum_{n=2}^{\infty}\sum_{m=0}^{n}\left(\frac{R_e}{r}\right)^n \overline{P}_{nm}(\sin\phi)\left(\overline{C}_{nm}(t)\cos m\lambda + \overline{S}_{nm}(t)\sin m\lambda\right) \tag{3.3}$$

where R_e is the mean equatorial radius of the Earth, and $\overline{P}_{nm}$ is the normalized associated Legendre function of degree *n* and order *m*. (r, ϕ, λ) are radial distance, latitude and longitude of the satellite in the geocentric body-fixed coordinate system. The center of mass of the Earth is assumed to be coincident to the coordinate origin so that the degree $n = 1$ terms may be neglected. The coefficients $\overline{C}_{nm}(t)$ and $\overline{S}_{nm}(t)$ are the normalized spherical harmonic coefficients, which consist of the mean and time-variable parts:

$$\overline{C}_{nm}(t) = \overline{C}^{0}_{nm} + \Delta\overline{C}_{nm}(t)$$
$$\overline{S}_{nm}(t) = \overline{S}^{0}_{nm} + \Delta\overline{S}_{nm}(t) \qquad (3.4)$$

In this study, only the mean parts were considered. By the degree and order relationship, the gravity coefficients are classified into three sets, zonal ($m = 0$), sectorial ($n = m$), and tesseral ($n \neq m \neq 0$) terms.

For most numerical simulations in this study, EGM96 reference was used as the truth gravity field for the mean gravity to generate simulated measurements. EGM96 is a model complete to degree and order 360 and the result of collaboration between NASA Goddard Space Flight Center (GSFC) and the Defense Mapping Agency (DMA)[43]. EGM96 is a blended solution, which consists of a (70x70) combination solution based on direct satellite altimetry, surface gravity, and satellite tracking data. The portion of the field from degree 71 to 359 is derived from a block diagonal solution, and the solution at degree 360 comes from the corresponding quadrature solution. Because of the block diagonal solution over degree 70, it has only a (70x70) solution covariance matrix.

A clone of EGM96 was used as the nominal gravity field. The difference between the clone and truth gravity coefficients represent the uncertainty level (1 σ) of the truth model. The clone gravity coefficients up to degree 70 were made from the EGM96 covariance and the higher terms were from the uncertainty of the gravity coefficients [8,10].

The time series and amplitude spectrum of the gravity accelerations $\boldsymbol{a}_c$ on the satellite at 450km altitude are shown in Figure 3.1. The inclination is 87° and the eccentricity is 0.001. The orbit of one satellite was numerically integrated with the gravity force and the acceleration was stored for each time step. The radial component has the largest magnitude of 8.5 m/s^2 and the transverse component has a magnitude of 0.01 m/s^2. The transverse component has a strong 2-cpr (Cycle-Per-Revolution) signal, which is mainly due to the earth oblateness (J_2) but the normal component has a strong 1-cpr signal. On the other hand, the radial component has both 1 and 2-cpr signals and the former is mainly due to the orbit eccentricity.

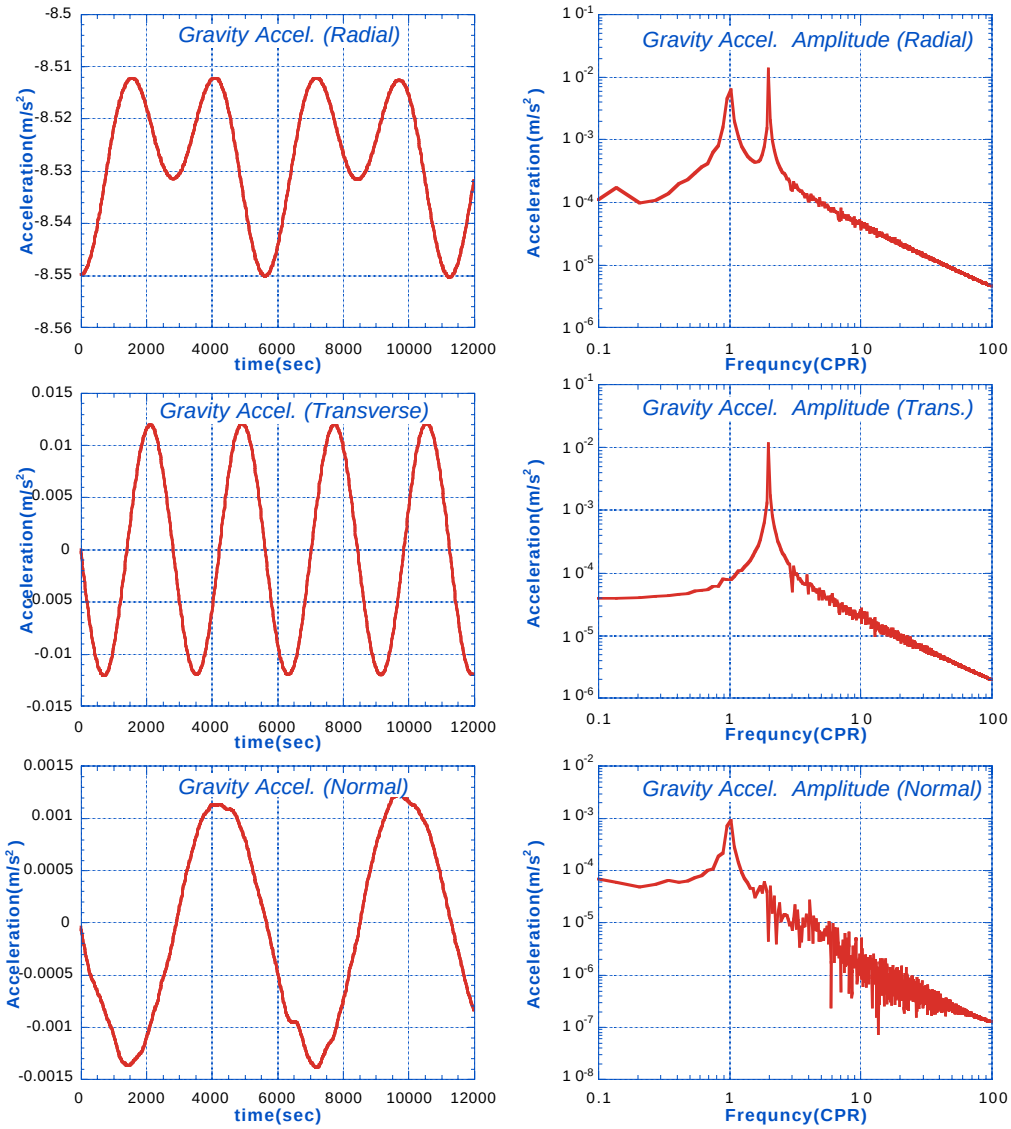

Figure 3.1 Time series and amplitude of the gravity accelerations at 450km altitude (*i* = 87°, *e* = 0.001)

3.2.2 Atmospheric Drag

A simple atmospheric model, which assumes a constant area in the direction of the relative wind, was used in this study. The force per unit mass acting on the satellite may be given by

$$\boldsymbol{a}_a = -\frac{1}{2}\rho\frac{C_d A}{m}|\boldsymbol{v}_r|\boldsymbol{v}_r \tag{3.5}$$

where

ρ = *atmospheric density*

$\boldsymbol{v}_r$ = *satellite velocity vector relative to the atmosphere*

C_d = *drag coefficient*

A = *cross sectional area of the satellite perpendicular to* $\boldsymbol{v}_r$

m = *satellite mass*

The relative velocity $\boldsymbol{v}_r$ may be related to the rotation of the atmosphere over the Earth and the horizontal winds as follows

$$\boldsymbol{v}_r = \boldsymbol{v} - \boldsymbol{\omega}_e \times \boldsymbol{r} - \boldsymbol{v}_w \tag{3.6}$$

where

$\boldsymbol{v}$ = *inertial velocity vector of the satellite*

$\boldsymbol{r}$ = *position vector of the satellite from the Earth center*

$\boldsymbol{\omega}_e$ = *rotation rate of the Earth*

$\boldsymbol{v}_w$ = *velocity vector of the horizontal winds in the Earth fixed coordinates*

Among several density models implemented in MSODP, the DTM (Density Temperature Model) [2,47] was used for simulating the truth atmospheric drag. A cannon-ball model was used and the ballistic coefficient $C_d A/m$ was taken as 1/240 [24]. The solar activity is predicted to reach near maximum in 2001, which is the planned launch year of the GRACE satellites, and to decrease during the mission lifetime. To represent this relatively high solar activity, most of the simulation epochs were set to January 1989 due to its relatively high solar activity. Usual value of the solar flux $F_{10.7}$ and the geomagnetic index K_p were 150 and 2.0, respectively.

Previous orbit determination simulations [10,57,65] used two atmospheric density models for truth and nominal drag accelerations. However, this study does not require a nominal density model since the simulated accelerometer measurements replace the nominal non-gravitational accelerations including the atmospheric drag.

3.2.3 Solar Radiation Pressure

Since the atmospheric drag is dominant in the GRACE satellite altitude (<500 km), the solar radiation pressure will have less effect on the satellite trajectory than the atmospheric drag. While the force direction of the atmospheric

drag is always the transverse direction, the direction of the solar radiation pressure is changing according to the relative position of the Sun and the satellite.

The induced acceleration from the direct solar radiation pressure $\boldsymbol{a}_{sr}$ from the Sun on a satellite can be modeled as [68]

$$\boldsymbol{a}_{sr} = -p\frac{\nu A}{m}(1+\eta)\hat{\boldsymbol{u}} \tag{3.7}$$

where

p = *momentum flux due to the Sun*

ν = *eclipse factor*

m = *mass of the satellite*

A = *cross-sectional area of the satellite perpendicular to the satellite-Sun vector*

η = *reflectivity coefficient*

$\hat{\boldsymbol{u}}$ = *unit vector from the satellite to the Sun*

The mass m was 420kg and the same value was applied for the Earth radiation pressure models. The reflectivity η of *0.5* was used but its time variability was not considered. For the variable area model, the following values were used for different sections:

$A_{roll} = 1.07\ m^2$ $\quad A_{pitch} = 1.90\ m^2$ $\quad A_{yaw} = 4.40\ m^2$

3.2.4 Earth Radiation Pressure

The energy flux of the Earth causes the Earth radiation pressure, which is similar to the solar radiation pressure. This study used the following Earth radiation model, which gives the force per unit mass as [38]

$$\boldsymbol{a}_{er} = (1+\eta)A' \frac{A_c}{m\,c} \sum_{j=1}^{N} \left[\left(\tau_j \, a_j E_s \cos\theta_s + e_j M_B \right) \hat{\boldsymbol{r}}_j \right] \tag{3.8}$$

where

η = *satellite surface reflectivity*

A' = *projected, attenuated area of a surface element of the Earth*

A_c = *nadir projected cross-sectional area of the satellite*

m = *mass of the satellite*

c = *speed of light*

τ_j = *1 if the center of the j-th element is in day-light*

0 if the center of the j-th element is in darkness

a_j, e_j = *albedo and emissivity of the j-th element*

E_s = *solar momentum flux density at 1 AU*

θ_s = *solar zenith angle*

M_B = *exitance of the Earth (= $E_s / 4$ for an ideal black body)*

$\hat{\boldsymbol{r}}_j$ = *unit vector from the center of the j-th element*

to the satellite

N = *number of earth elements*

The albedo and emmisivity may be expressed in second degree harmonics to account for latitudinal variation in Earth radiation and for seasonally dependent latitudinal asymmetry:

$$a = a_0 + a_1 P_{10}(\sin\phi) + a_2 P_{20}(\sin\phi)$$
$$e = e_0 + e_1 P_{10}(\sin\phi) + e_2 P_{20}(\sin\phi) \tag{3.9}$$

where P_{i0} is the i-*th* degree Legendre polynomials and ϕ is the latitude of the center of the element on the Earth. The degree one terms may have be periodic as

$$a_1 = \bar{a}_1 + a_{1c}\cos\omega_E(t - t_0) + a_{1s}\sin\omega_E(t - t_0)$$
$$e_1 = \bar{e}_1 + e_{1c}\cos\omega_E(t - t_0) + e_{1s}\sin\omega_E(t - t_0) \tag{3.10}$$

where ω_E is the frequency of 1/365.25 days. In this study, the following parameters were used [57]:

$a_0 = 0.34$

$\bar{a}_1 = 0.0$ $\quad a_{1c} = 0.10$ $\quad a_{1s} = 0.0$

$a_2 = 0.29$

$e_1 = 0.68$

$\bar{e}_1 = 0.0$ $\quad e_{1c} = -0.07$ $\quad e_{1s} = 0.0$

$e_2 = -0.18$

The period of degree one terms was one year. The same reflectivity coefficient as the radiation pressure $\eta = 0.5$ was used and the cross-sectional area was $4.4\ m^2$.

3.2.5 Comparison of Non-Gravitational Forces

The time series of the atmospheric drag, solar radiation pressure, and Earth radiation pressure accelerations are shown in Figure 3.2. The orbit altitude was 450 km with the inclination of 87°. The same simulation parameters described in Sections 3.2.2, 3.2.3, and 3.2.4 were used for generating the non-gravitational accelerations. The trajectory of one satellite was numerically integrated with the gravity and the individual non-gravity forces. The non-gravitational acceleration was stored for each time step along the trajectory. The β' angle, which is the angle between the orbit plane and the geocentric direction to the Sun [15], was set to 0° to maximize the radial solar radiation pressure. Since the normal component is not coupled with the in-plane motion in the linear region, the low-low SST observation hardly depends on the normal component if the two satellites are in the same orbit plane. For this reason, only the radial and transverse components are presented. The transverse component of the atmospheric drag has the strongest signal with the mean value of 300 nm/s^2. The transverse components of the other accelerations are at least an order of magnitude smaller. On the other hand, the radial component of the atmospheric drag is much smaller than that of the radiation pressure. The discontinuity of the solar radiation pressure is due to the satellite entrance into shadow region.

The amplitude spectrums of the non-gravitational accelerations are shown in Figure 3.3. All of these non-gravitational accelerations have strong tone signals, e.g. 1-cpr, 2-cpr, etc. Since this characteristic is similar to the acceleration caused by the resonant gravity coefficients, some of the accelerometer errors, which are proportional to the non-gravitational accelerations, mainly degrade those resonant coefficients. Details are described in Chapter 5. Also, the thermal variations of instruments have this tone signal and may degrade the accuracy of the resonant coefficients.

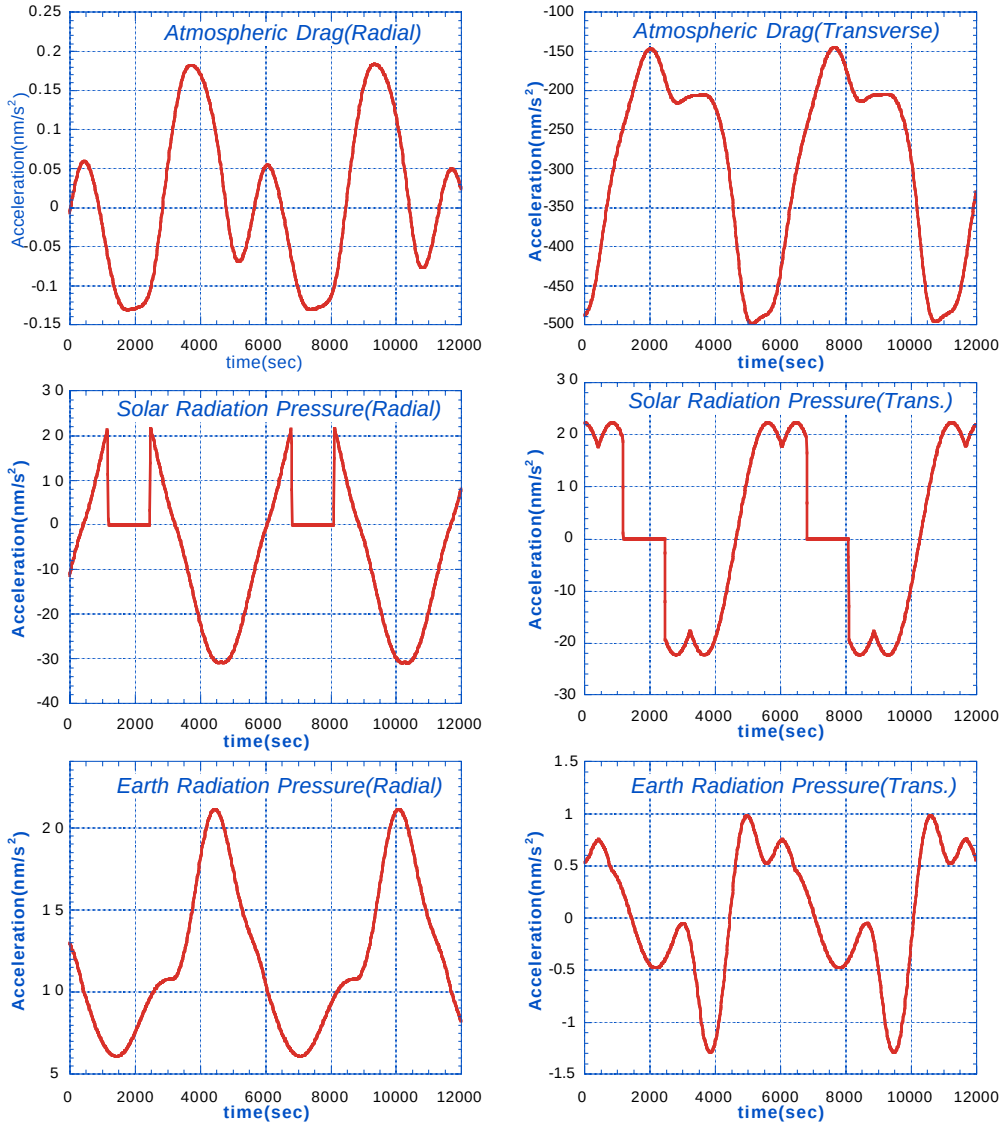

Figure 3.2 Time series of the non-gravitational accelerations
(*h* = 450km)

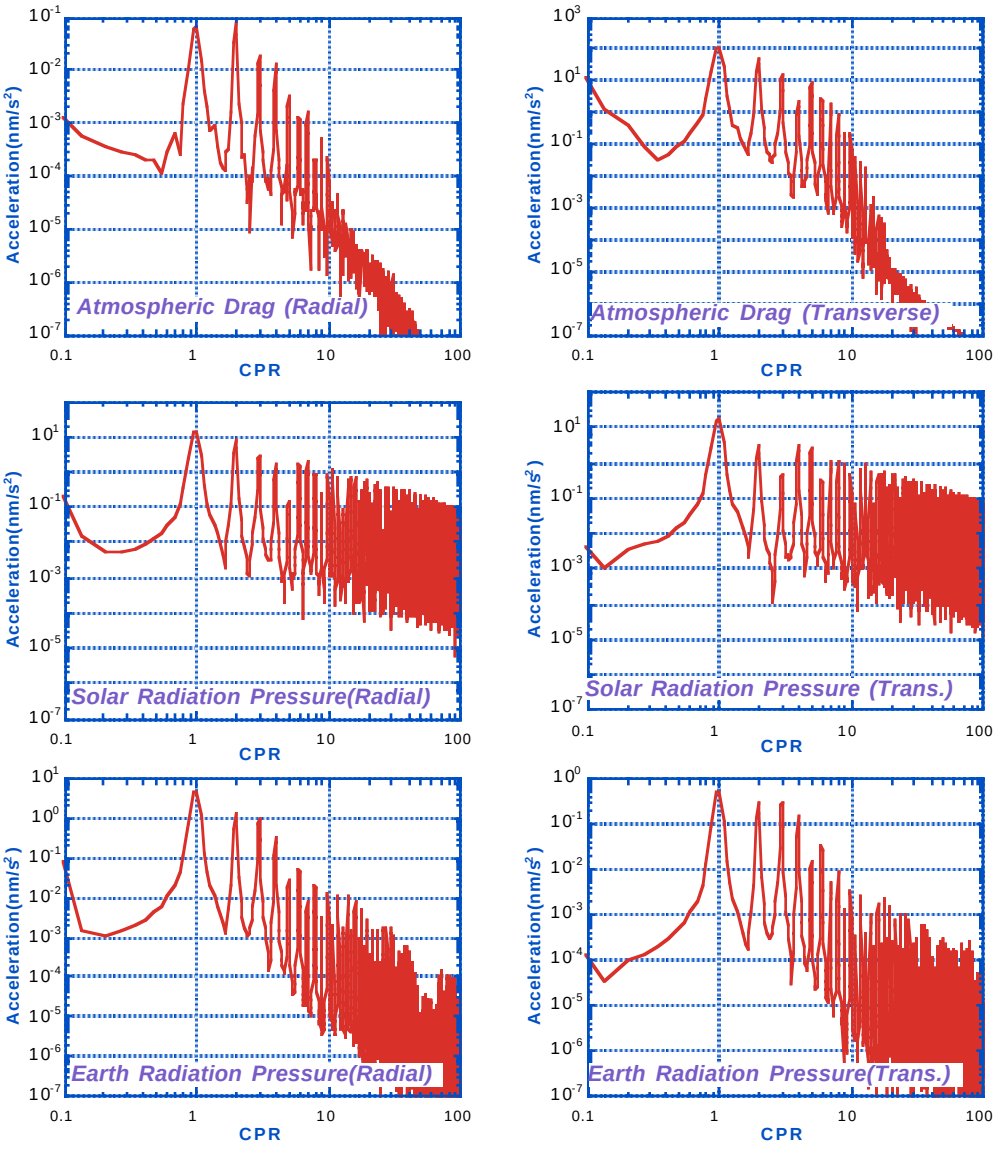

Figure 3.3 Amplitude spectrum of the non-gravitational accelerations (*h* = 450km)

3.3 EMPIRICAL PARAMETERS

One of the ways for treating mismodeled or unmodeled forces acting on a satellite is to estimate empirical force parameters. Two types of empirical parameters, dynamic and kinematic empiricals were used in this study. The dynamic parameters were used for adjusting the satellite orbits, and the kinematic parameters were for adjusting the low-low SST measurements. Strictly speaking, the dynamic empirical parameters are classified into the force models in the previous section.

3.3.1 Dynamic Empirical Parameters

One-cpr (cycle-per-revolution or once-per-rev) and constant tangential parameters were used as the dynamic parameters. The 1-cpr empirical parameters are given by [10,57]

$$F_R = C_R \cos u + S_R \sin u \tag{3.11}$$

$$F_T = C_T \cos u + S_T \sin u \tag{3.12}$$

$$F_N = C_N \cos u + S_N \sin u \tag{3.13}$$

where

F_R = *1-cpr radial empirical perturbation*

F_T = *1-cpr transverse empirical perturbation*

F_N = *1-cpr normal empirical perturbation*

u = *argument of latitude of satellite* ($u = nt$)

C_R, S_R = *1-cpr radial empirical parameter*

C_T, S_T = *1-cpr transverse empirical parameter*

C_N, S_N = *1-cpr normal empirical parameter*

The constant tangential empirical parameter is defined as

$$\boldsymbol{F}_t = C_t \hat{\boldsymbol{u}}_t \tag{3.14}$$

where

C_t = *tangential empirical parameter*

$\hat{\boldsymbol{u}}_t$ = *unit velocity vector*

They remove the long period effect of mismodeled forces and improve orbit determination accuracy. They have piecewise constant values over 3 ~ 24 hours. Since these are not explicitly present in the measurement equation, they are implemented into the estimation process via propagation of the state transition matrix as explained in Chapter 2. When pre-calibrated scale factors and biases are applied to the accelerometer measurements, the scale factors and biases should be estimated. These parameters are also classified into the dynamic parameters but will be described in Chapter 5.

3.3.2 Kinematic Empirical Parameters

The kinematic empirical parameters used in this study include low-low satellite-to-satellite tracking bias parameters. They are used to remove the error in the inter-satellite ranging measurements and explicitly shown in the low-low measurement equation. For better understanding of the use of these parameters, the power spectral density of a typical range-rate measurement residual is presented in Figure 3.4.

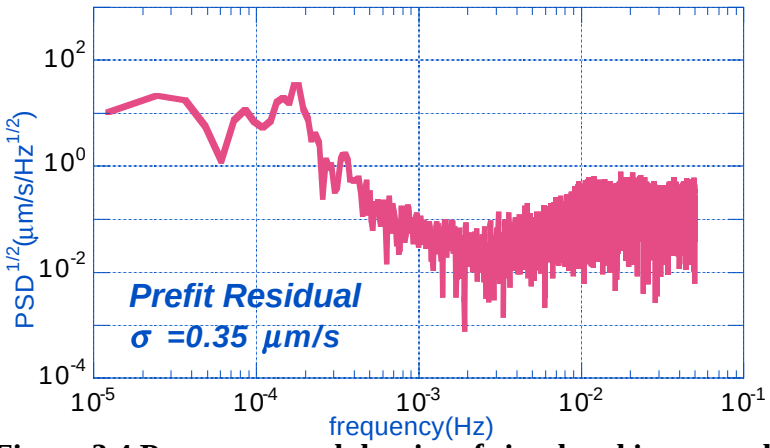

Figure 3.4 Power spectral density of simulated inter-satellite range-rate noise

Applied measurement error sources were the SST oscillator, system, and multipath noise described in Chapter 4. The accelerometer errors described in Chapter 5, random, misalignment, and attitude errors, were included as the force model errors. It is the range-rate signal difference between the simulated signal by the truth model and the signal by the nominal model. However, the gravity error is not included, so that both the truth and nominal models contain the same gravity

model. This figure reflects the measurement and force model errors due to the SST accelerometer measurement noise except the gravity field error. It shows strong low frequency power especially below 1 cpr that is equivalent to 0.00018 Hz.

Those strong constant and 1-cpr residuals can be explained by the analytic expressions of (A.20) in Appendix A, which are derived from Hill's equations. They provide expressions for the resulting SST perturbation due to a disturbing acceleration with an arbitrary frequency ω. The disturbing acceleration produces a SST perturbation at three frequencies, zero (constant), 1 cpr, and ω itself. In other words, perturbation of any frequency results in the SST perturbations of constant and 1 cpr. The disturbing acceleration may be either gravity acceleration or unmodeled acceleration. The perturbation due to the unmodeled acceleration should be removed from the observations by applying empirical parameters but the perturbation due to the gravity should be retained. The best way is to adjust the empirical parameters in all frequency ranges but it is not practical to estimate all those parameters. In most cases, the 1-cpr and constant empiricals are estimated since they are common for all acceleration-derived perturbations and have a relatively large magnitude.

By differentiation of the range perturbation equations of (A.20), range-rate partial equations can be obtained as follows:

$$\dot{\rho}_{err} = A + Bt + (E + Ft)\cos nt + (G + Ht)\sin nt$$
$$+\sum_{i=1}^{N}\left[(E_i + F_i t)\cos\omega_i t + (G_i + H_i t)\sin\omega_i t\right] \qquad (3.15)$$

where n is the mean motion of the orbit and N is the number of distinctive frequencies of the forces. Any force components at a certain frequency ω_i are grouped into one *i-th* force. This equation implies that the range-rate error is the sum of linear and harmonic terms. The purpose of the low-low empirical parameters is to remove the error contribution from the observation. This is done by estimating the linear and 1-cpr terms, A, B, E, F, G, and H. Due to the huge number of N, it is not realistic to estimate all the ω_i frequency terms, E_i, F_i, G_i, and H_i for $i = 1, 2, \ldots, N$. From this analytic basis, the following low-low empirical formulations are used for processing the range-rate measurements:

$$\dot{\rho}_{obs} - \dot{\rho}_{nom} = A + Bt + (E + Ft)\cos u + (G + Ht)\sin u \qquad (3.16)$$

where

$\dot{\rho}_{obs}$ = *observed low-low range-rate*

$\dot{\rho}_{nom}$ = *nominal low-low range-rate*

A = *low-low bias*

B = *low-low bias-rate*

E, F = *low-low periodic bias*

G, H = *low-low periodic bias-rate*

u = *argument of latitude of the midpoint of two satellites* ($u = nt$)

Another concern is the determination of arc lengths for each empirical parameter. The low-low bias and bias-rate were estimated every 45 minutes, equivalent to

half of the orbit period. Shorter arc length may harm the gravity signals since the empirical force resembles the gravity force, especially 2-cpr signal by J2 term. Low-low 1-cpr parameters are for removing time varying 1-cpr measurement errors and are estimated every 90 minutes or one orbit revolution. With this bias adjustment process, the total RMS reduced to less than 0.1 μm/s from the pre-fit value of 0.35 μm/s as shown in Figure 3.5.

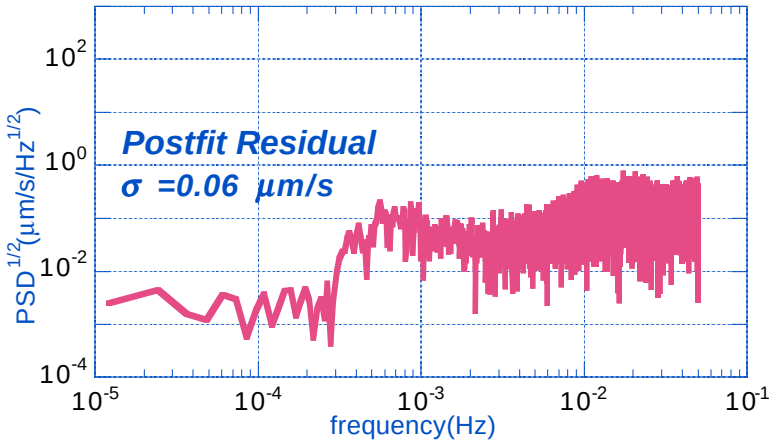

Figure 3.5 Power spectral density of simulated inter-satellite range-rate noise after adjusting empirical parameters

These empiricals are the kinematic parameters and the partial derivative of the range-rate measurement with respect to these parameters are given by

$$\frac{\partial \dot{\rho}}{\partial A} = 1 \qquad \frac{\partial \dot{\rho}}{\partial B} = t$$

$$\frac{\partial \dot{\rho}}{\partial E} = \cos u \qquad \frac{\partial \dot{\rho}}{\partial F} = t\cos u$$

$$\frac{\partial \dot{\rho}}{\partial G} = \sin u \qquad \frac{\partial \dot{\rho}}{\partial H} = t\sin u \tag{3.17}$$

3.4 GPS MEASUREMENT MODEL

The GPS tracking of each GRACE satellite provides the information on the GRACE satellite orbit and measurement time-tags. The real-time GPS solutions are used for the onboard controller for the orbit control and measurement time-tags. More refined measurements are obtained through ground processing, e.g. time-tag and ionosphere corrections, for the science purpose (gravity estimation). In this simulation study, only the ground-processed measurements were considered for the orbit information. The double difference observations formed by two GPS satellites, one GRACE satellite, and one ground receiver were used.

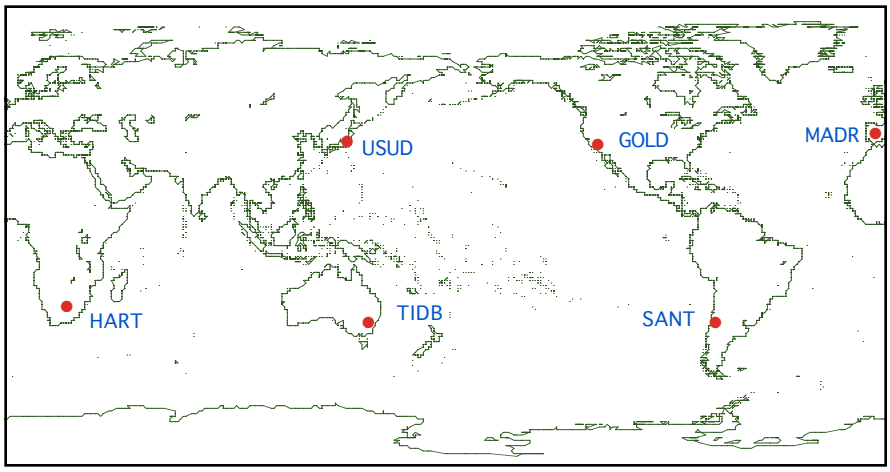

Figure 3.6 Simulation GPS tracking network

The GPS tracking scenario assumed a constellation of 24 GPS satellites and 6 GPS ground stations, as well as the GPS receivers onboard the two GRACE satellites. The GPS satellite initial conditions and ground station coordinates described in Sharma's study [65] were applied. Figure 3.6 shows the location of the ground stations, which are globally distributed for minimizing geographically correlated errors. In order to analyze the effect of the number of stations, some experiments were performed by changing the number of stations, from 6 to 24. The number of the double differenced observations is proportional to the number of ground stations. Therefore, the computational processing time is proportional to the number of stations. In spite of the computational time increase, the gravity solution improvement was not significant. For this reason, the number of ground stations was limited to six.

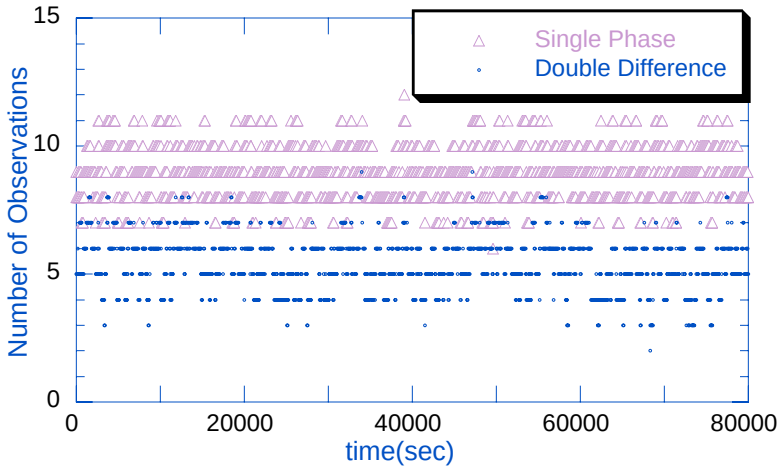

Figure 3.7 Number of GPS observations for one GRACE satellite (Single phase and double differenced phase observations)

The GPS receivers were assumed to track all the visible satellites. The elevation cut-off angles for the ground and flight receivers were 15° and 0°, respectively. Figure 3.7 shows the number of the GPS observations for one GRACE satellite. The observation time interval is 10 seconds. The average numbers of observations are 9 for the single phase observations and 5.5 for the double differenced phase observations (with six ground stations).

Gaussian random (white) noise with 5mm standard deviation was applied for the single phase-derived range measurements. One double differenced measurement consists of four phase measurements, and its corresponding noise level becomes 1cm ($=\sqrt{4}\times 5mm$). The measurements were assumed as ionosphere corrected values. The dynamic error model error for the GPS satellites was limited to the gravity model error, i.e. truth and nominal gravity model difference. The GPS orbit is less sensitive to the higher degree and order gravity

field due to its high altitude, so that a smaller size of gravity field (8×8) was applied for the GPS orbit integration.

3.5 SIMULATION PROCEDURE

3.5.1 Simulation Procedure

The primary purpose of the numerical simulations of this study was to analyze how the error sources affect the performance of the GRACE mission, which is the accuracy of the estimated gravity field. The error models were obtained through differences in two models. One was used for generating the measurements and the other one was used for processing the measurements. The former model is called the truth model and the later one is called the nominal model. The error models include gravity field, other dynamic forces, and measurement noises. Figure 3.8 shows a simplified flow chart of the simulation procedure and each step is described as follows.

(A) The simulation procedure started with generating simulated observations using the truth dynamic models. Both SST and GPS double difference measurements were computed and then noise was added. Accelerometer and attitude measurements were also generated with noise.

(B) Next step was to adjust the orbit trajectory. Due to different dynamic models and noises, the nominal orbit generated by the nominal models, was too different from the truth orbit. It is difficult to apply the linear estimation method,

which assumes that the true and nominal values are in the linear region. The nominal orbits were adjusted by using the simulated GPS measurements with the nominal gravity field. The gravity field was not estimated in this process.

(C) The SST measurement is a biased measurement of the relative distance between the two satellites and it does not provide enough information to estimate the absolute position of each satellite. Due to the singularity of the SST information, the high-low GPS information was also needed to estimate the satellite trajectories and the long wavelength component of the gravity. The partial derivatives of the SST and GPS measurements with respect to the gravity field coefficients, the initial conditions, and other parameters, were computed along the nominal trajectory computed in the previous process.

(D) The last step was to combine the SST and GPS partials and to solve them in order to estimate the satellite states, the empirical parameters, and the gravity field coefficients. This procedure was performed by LLISS (The Large Linear System Solver [85,86]), which combines the information matrices and solves for all the desired parameters. Details are described in Appendix B.1.

(E) The difference between the estimated and the truth gravity coefficients reflects the error level of the estimated gravity field. To the extent that the error sources assumed in the simulations represent those actually encountered during the mission, the results will predict the performance of the GRACE mission.

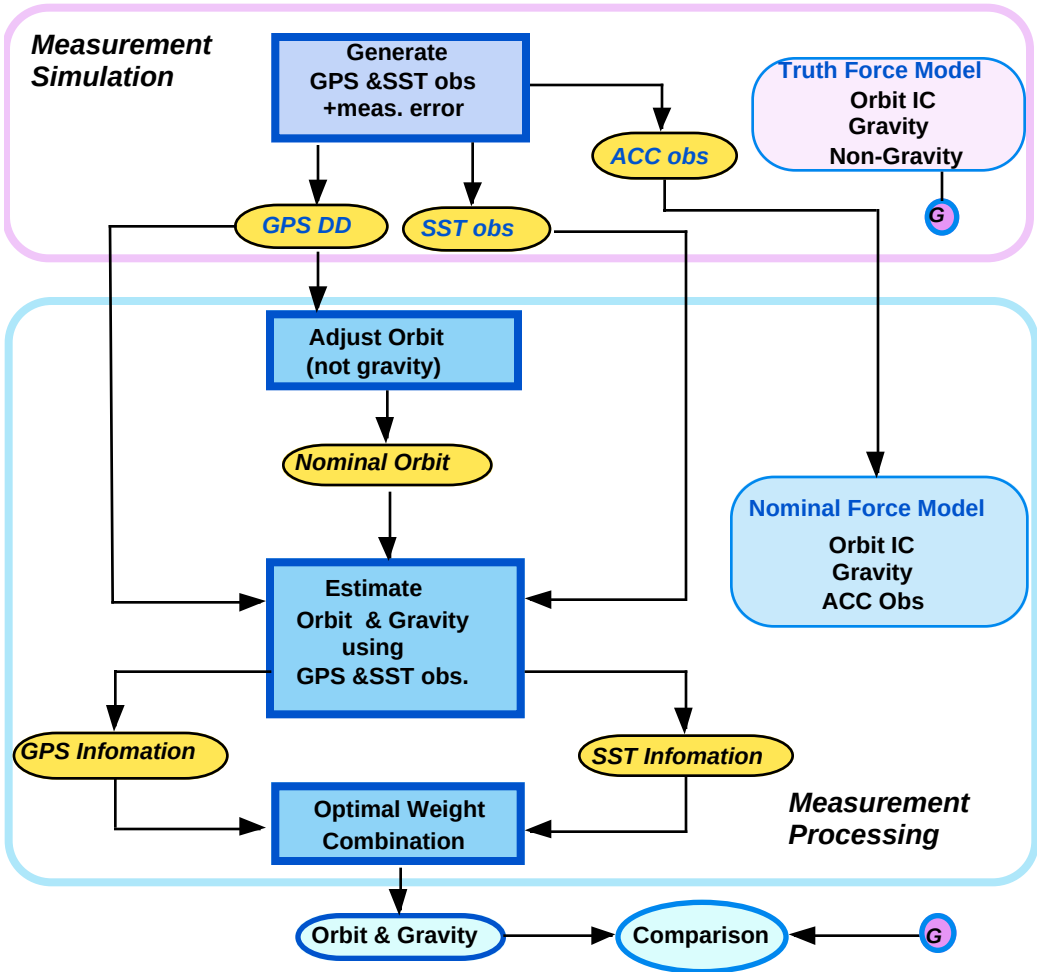

Figure 3.8 Numerical simulation procedure

3.5.2 Simulation Parameters

The simulated SST range-rate observations were used for most of the simulations. The true range-rate observation was obtained from the analytic equation of (2.25), but the range-rate noise was obtained from the range noise through the numerical differentiation. The simulated observation is a sum of these analytic and numerical quantities. This fact is somewhat different from the real mission, where the range-rate observation is entirely obtained from the range observation.

The nominal separation angle between the two GRACE satellites was 2°. For a 450km altitude, this 2° separation angle is equivalent to 238km. The altitude ranged from 300 km to 500 km. With these altitudes, the GRACE satellites have 15 or 16 orbits over the earth each day. This means that the satellite crosses the equator that many times considering either ascending or descending orbits only. That number of tracks limits the estimation of the sectorial terms, which vary in the longitude direction. The repeat period was chosen such that the resulting equatorial ground track spacing was less than one half the wavelength of the smallest geopotential features, which was the minimum requirement for proper spatial sampling. For example, to estimating up to degree N sectorial terms requires $2N$ orbits. However, this requirement is valid only if the ground track is not repeated during that period.

One orbit period of the GRACE satellite is about 90 minutes and the number of observation during one orbit period becomes $5400/\Delta t$, where Δt is

the observation interval in seconds. The Nyquist frequency of these observations becomes $2700/\Delta t$ cpr. With the averaging time of a 10 seconds, the maximum estimation degree can be 270. In this study, 10-second interval was used for the SST measurements. Since the GRACE gravity solution is less dependent on the GPS measurements, longer intervals, 30s or 60s, were used for GPS measurements.

The geopotential coefficients are estimated as global parameters over a full data span, from 7 to 30 days. The satellite initial conditions are estimated every day, and this data span is called an arc. Since the linear estimation theory, which requires the nominal value to be close to the true value, is used for the estimation procedure, the nominal orbit should be close enough to the truth orbit. In general, short arc length produces better orbit agreement with the true orbit, but it also degrades the accuracy of the gravity estimation. In this study, a one-day arc length was chosen. Table 3.1 describes the simulation parameters adopted for this study.

Table 3.1 List of simulation parameters

Gravitational Forces		
Category	***Truth***	***Nominal***
Spherical Harmonics	EGM96	EGM96 Clone

Non-Gravitational Forces (Accelerometer)		
Category	***Truth***	***Nominal***
Atmospheric Drag	- Cannon Ball Model *Density: DTM, MSIS* *Winds: HWM93*	Accelerometer measurements (including noise)
Solar Radiation Pressure	- Box Model *Flux/Reflectivity*	
Earth Radiation Pressure	- Box Model *Albedo/Emissivity*	

Inter-Satellite Measurement Model		
Category	***Truth***	***Nominal***
System Noise	1μm/Hz$^{1/2}$@ 230km	Low-Low Empirical Bias & Bias-Rate
Oscillator Noise	≈1/f^{2} in Range-Rate	
Multipath Error	3μm per mrad attitude var.	

Accelerometer Measurement Model		
Category	***Truth***	***Nominal***
Bias	10^{-6}	Bias Estimation
Scale Factor	2%	Scale Factor Estimation
Random Noise	$(1+0.005/f)x10^{-20}$ $m^2/s^4/Hz$	none
Alignment	0.3 mrad	
Attitude Error	0.05 mrad white noise	
CM Offset	0.1 mm (w/ CM Trim)	

Adjustment Procedure		
Category	***Type***	***Remark***
Orbit	- Altitude - Inclination - Eccentricity	300 ~ 480km 87 ~ 90 0.001
Data Span		7 ~ 30 days
Arc length	- Initial Conditions - Gravity Coefficients (50×50 ~ 120×120)	1 day each once per data span
Empiricals	- Ct, 1-cpr T & N (exclusive from accelerometer)	3 hr ~ 1 day
Accelerometer	- Scale, Bias (exclusive from empiricals)	once per data span
Range-Rate	- Bias & Rate - Periodic Bias & Rate	45 min 90 min

3.6 OPTIMAL WEIGHTING OF THE INFORMATION EQUATIONS

As discussed in Chapter 2, the minimum variance estimate of (2.78) is obtained from the information matrix $H^T R^{-1} H$ and the observation residual $\boldsymbol{y}$. Let us consider the minimum variance estimate with different types of observations. The best estimate can be obtained only if the observation error covariance is correct since it assumes the statistics of the observation error and a priori error are known. However, for various reasons, the true error covariance may differ significantly from the assumed or given statistics, and a systematic method is necessary to improve the quality of the estimate [85].

If only one type of observation is processed, then the same error levels can be assigned for all observations and these error levels affect the solution covariance matrix, $P = \left(H^T R^{-1} H\right)^{-1}$, not the solution itself. Unless the covariance is concerned, the error level is not of interest for single type observations. However, it becomes a problem when combining different types of observations. The relative error level between different types of observations affects not only the solution error covariance, but also the solution itself.

This is a typical problem for the GRACE mission, which needs to combine two information matrices, $\left(H^T R^{-1} H\right)_{GPS}$ and $\left(H^T R^{-1} H\right)_{SST}$. The former is generated from the GPS observations and the latter is from the SST observations. The SST observation has much higher precision than the GPS observation, so the specified error level for the SST observations should be much lower than the GPS observations. An improper relative error level may degrade the combined solution

significantly, and a systematic way to compute the proper noise level is necessary. Two methods of computing optimal scaling factor, which calibrates the given error covariance, will be summarized in the following. One is by numerical iterations and the other one is by a simple simulation. The later spends less computational time but is only possible for simulations.

3.6.1 Determination of the Optimal Scaling Factor by Iterations

The optimal scaling factor can be derived by the maximum likelihood estimate [85]. The observation state equation is given by

$$\boldsymbol{y} = H\boldsymbol{x} + \boldsymbol{\varepsilon} \tag{3.18}$$

Let us consider a k set of observations, where each set has a different covariance as

$$\boldsymbol{\varepsilon} = \begin{bmatrix} \boldsymbol{\varepsilon}_1 \\ \boldsymbol{\varepsilon}_2 \\ \vdots \\ \boldsymbol{\varepsilon}_k \end{bmatrix} \qquad R = \begin{bmatrix} R_1 & 0 & \dots & 0 \\ 0 & R_2 & \dots & 0 \\ \vdots & \vdots & \ddots & \vdots \\ 0 & 0 & \cdots & R_k \end{bmatrix} \tag{3.19}$$

No correlations between different observation sets are assumed. The number of the total observations is m and each set has m_i observations. The observation error is assumed to have a normal distribution with zero mean value, and its covariance matrix R is specified as

$$E\left[\boldsymbol{\varepsilon}_i\right] = \boldsymbol{0} \qquad E\left[\boldsymbol{\varepsilon}_i \boldsymbol{\varepsilon}_i^T\right] = R_i \qquad i = 1,2,\dots,k \tag{3.20}$$

The error covariance, R_i, should be the true value to get the best estimate. The objective is to find the proper scaling factor to calibrate a nominal error covariance to a true error covariance. The scaling factor f_i for each observation set is defined by

$$\overline{R}_i = f_i \, R_i \tag{3.21}$$

$\overline{R}_i$ is a nominal observation error covariance and R_i is a true error covariance. f_i is a scalar value.

The joint probability density function of the set of observation errors R is given by

$$\begin{aligned} F &= \frac{1}{\sqrt{(2\pi)^m \, det(R)}} exp\left[-\frac{1}{2} \boldsymbol{\varepsilon}^T R^{-1} \boldsymbol{\varepsilon} \right] \\ &= \frac{1}{\sqrt{(2\pi)^m \prod_{i=1}^{k} det(R_i)}} exp\left[-\frac{1}{2} \sum_{i=1}^{k} \boldsymbol{\varepsilon}_i^T R_i^{-1} \boldsymbol{\varepsilon}_i \right] \end{aligned} \tag{3.22}$$

A priori information is not considered. Let us choose this scalar function as a likelihood function. Maximizing this likelihood function gives the maximum likelihood estimate. Substituting (3.21) into (3.22) and taking a negative logarithm yields

$$\begin{aligned} L &= -ln \; F \\ &= \frac{1}{2}\left[m \, ln(2\pi) + \sum_{i=1}^{k} \left(-m_i \, ln \; f_i + ln \, det\left(\overline{R}_i\right) \right) + \sum_{i=1}^{k} f_i \; \boldsymbol{\varepsilon}_i^T \overline{R}_i^{-1} \; \boldsymbol{\varepsilon}_i \right] \end{aligned} \tag{3.23}$$

Minimizing this performance index L is equivalent to maximizing the likelihood function F. The true observation error $\boldsymbol{\varepsilon}_i$ may be approximated as the predicted value $\hat{\boldsymbol{\varepsilon}}_i$ by using the best estimate $\hat{\boldsymbol{x}}$ as follows

$$\hat{\boldsymbol{\varepsilon}}_i = \boldsymbol{y}_i - H_i\hat{\boldsymbol{x}} \tag{3.24}$$

Taking a partial derivative of L with respect to the scaling factor f_i and the estimation vector $\hat{\boldsymbol{x}}$ yields the optimal conditions as

$$\frac{\partial L}{\partial f_i} = -\frac{m_i}{f_i} + \left(\boldsymbol{y}_i - H_i\hat{\boldsymbol{x}}\right)^T \overline{R}_i^{-1} \left(\boldsymbol{y}_i - H_i\hat{\boldsymbol{x}}\right) = 0 \tag{3.25}$$

$$\left[\frac{\partial L}{\partial \hat{\boldsymbol{x}}}\right]^T = \left[\sum_{i=1}^{k} f_i H_i^T \overline{R}_i^{-1} \boldsymbol{y}_i\right] - \left[\sum_{i=1}^{k} f_i H_i^T \overline{R}_i^{-1} H_i\right]\hat{\boldsymbol{x}} = 0 \tag{3.26}$$

then

$$f_i = \frac{m_i}{\left(\boldsymbol{y}_i - H\,\hat{\boldsymbol{x}}_i\right)^T \overline{R}_i^{-1}\left(\boldsymbol{y}_i - H\,\hat{\boldsymbol{x}}_i\right)} \tag{3.27}$$

$$\hat{\boldsymbol{x}} = \left[\sum_{i=1}^{k} f_i H_i^T \overline{R}_i^{-1} H_i\right]^{-1}\left[\sum_{i=1}^{k} f_i H_i^T \overline{R}_i^{-1} \boldsymbol{y}_i\right] \tag{3.28}$$

This is the procedure used in the Large Linear System Solver (LLISS), which was developed by Yuan [85,86], to determine the optimal scaling factor f_i through an iterative solution.

This formulation requires the linear predicted (or post-fit) root mean square (LPRMS) that is the denominator of (3.27), which contains the estimate, $\hat{\boldsymbol{x}}_i$ in (3.28). This LPRMS is a measurement residual level and its accuracy depends on the accuracy of the estimate $\hat{\boldsymbol{x}}_i$. As the estimate is closer to the true value, the

LPRMS becomes more accurate. If the initial guess of the scaling factors is not close to true value, several iterations are required to update the estimate $\hat{\boldsymbol{x}}_i$ and the scaling factor f_i.

3.6.2 Determination of the Optimal Scaling Factor by Simulations

The GRACE simulation requires extensive computation time, and it is impractical to iterate a large information matrix combination and solver process for updating the residual $\left(\boldsymbol{y}_i - H\hat{\boldsymbol{x}}_i\right)$ and the optimal scaling factor f_i in (3.27). Therefore, an efficient way to get the optimal scaling factor was developed by Bettadpur [8]. This method gives nearly true scaling factors f_i of GPS and SST observation errors without iterations. Using these scaling factors, the LLISS combines GPS and SST information matrices without iterations. The main idea of this method is to use the truth gravity fields, which are used to generate simulated observations, when computing the linear predicted RMS (LPRMS). Since major portion of the unknowns $\hat{\boldsymbol{x}}_i$ is the gravity coefficients, the computed LPRMS with the true gravity coefficients becomes very close to its true value. This nearly true LPRMS yields a nearly true scaling factor. Of course, this technique is only available for simulations, where a true gravity model is available.

Figure 3.9 shows the optimal weighting determination procedure. This is similar to the standard estimation procedure described in the previous section. The procedure can be divided into the following steps.

(A) The way of generating simulated observations was identical with the standard simulation procedure described as Step (A) in Section 3.5.1.

(B) The second part of adjusting the initial conditions using GPS double difference observations was identical to Step (B) in Section 3.5.1, but the true gravity field was used instead of the nominal gravity field. During this process, the MSODP computes the LPRMS, and it yields the optimal scaling factor for the GPS observation error. The scaling factor is the ratio of the true error level and the nominal error level that is specified in the MSODP input deck and recorded on the GPS information matrix. The nominal value was usually 1 cm for the double difference observations.

(C) Third step involved generating SST observations using the adjusted initial conditions from the second step. It uses exactly the same force modeling as the second step to reproduce the same orbit trajectories. Subtracting these SST observations from the true SST observations from the first step yields the SST observation residual. It represents the SST observation error due to noise and modeling errors except the gravity modeling error.

(D) Fourth step involved removing the bias and bias rate from the SST observation residual obtained in the third step. This process was same as the MSODP implementation of empirical parameterizations. This residual value corresponds to the LPRMS of $\left(\boldsymbol{y}_i - H\,\hat{\boldsymbol{x}}_i\right)$. In other words, this simulation method replaces the iteration method for computing the LPRMS. However, the same equation of (3.27) is used for determining the scaling factor. Detailed procedure is described in Appendix B.2.

In most cases, this simulation method was used for computing the scaling factor, but sometimes the iteration method was used with the initial LPRMS from

the simulation method to ensure optimal weighting. Usual residual levels were 1 cm for the GPS and 0.05 μm/s for the SST after adjusting the scaling factor.

It should be noted that this method is possible only for simulations where the true gravity model is available. Real data processing, where the true model is not available, needs the iteration method described before. However, this simulation method can be very useful to guess initial scaling factors of iterations in the real data processing.

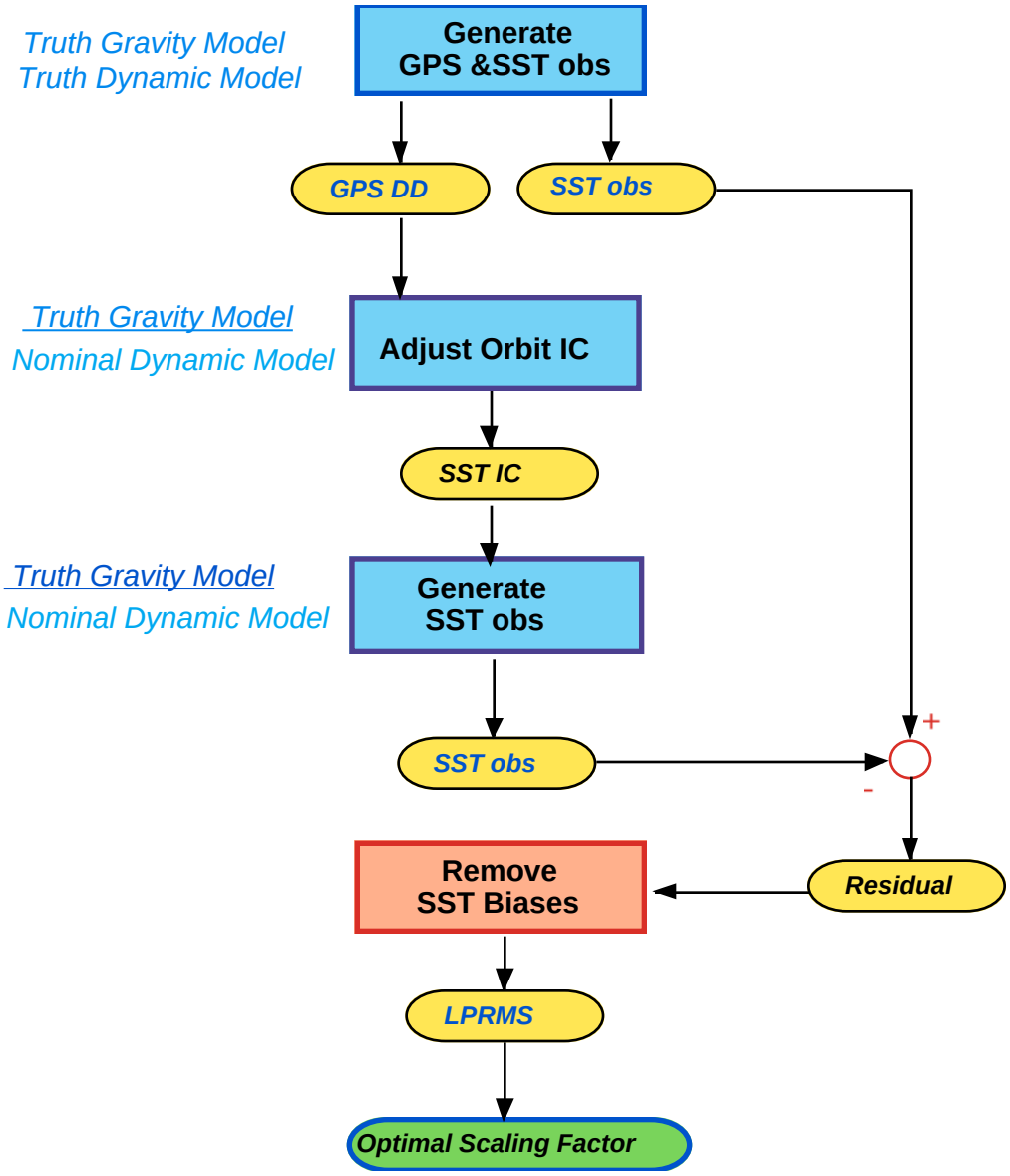

Figure 3.9 Flow chart of the optimal weighting determination procedure

3.7 SEMI-ANALYTIC METHOD FOR DEGREE ERROR PREDICTION

As an efficient way to analyze the effect of various error sources on the recovery of the high degree gravity field, a semi-analytic method has been developed by Bettadpur [8]. Unlike the full numerical simulations, which estimate the individual gravity coefficients, this method provides the gravity error level per degree. An analytic transfer function was utilized to map the instrument noise spectrum to the gravity error spectrum. Simulated measurement time series was decomposed into spherical harmonics to get a measurement noise degree spectrum. Then, this noise spectrum was mapped into geoid error spectrum by the analytic equations.

3.7.1 Formulations

If any non-conservative forces, e.g. atmospheric drag, radiation pressure, and time-dependent potential, are ignored, then the total energy, e.g. the potential energy plus kinetic energy, will be conserved. Thus, when a satellite passes into a region where the potential energy of gravity is decreasing due to a perturbing anomaly, then the loss must be made up by an increase of the kinetic energy, that is, change of velocity [29,82].

Let us consider the following energy equation

$$\frac{1}{2}v^2 - U = E \tag{3.29}$$

where E is the total energy and U is the total gravitational potential energy. v is the satellite velocity. U and v can be decomposed into a reference component and a disturbance component as

$$U = U_0 + T'$$
$$v = v_0 + \Delta v \tag{3.30}$$

U_0 is the nominal gravity potential representing the gravity at the reference ellipsoid, which consists of even zonal harmonics [72]. T' is the disturbing potential representing the difference between the actual gravity and the reference gravity. Δv denotes the velocity variation due to disturbing gravity potentials. The reference velocity v_0 is related to the reference gravity potential U_0 as following energy equation:

$$\frac{1}{2}v_0^{\,2} - U_0 = E \tag{3.31}$$

Substituting (3.30) into (3.29) and ignoring higher order term of the velocity variation yields

$$\frac{1}{2}v_0^{\,2} + v_0\Delta v - U_0 - T' = E \tag{3.32}$$

Comparing (3.31) and (3.32) yields the relationship between the velocity variation and the disturbing potential at the satellite altitude:

$$\Delta v = \frac{1}{v_0}T' \tag{3.33}$$

This equation is for one satellite, but it also implies that the velocity difference for each of the two satellites is directly proportional to the geopotential difference at their respective locations:

$$\Delta v_2 - \Delta v_1 = \frac{T_2^{'}}{v_{20}} - \frac{T_1^{'}}{v_{10}} \tag{3.34}$$

If the velocity variation is perfectly measured, then the disturbing potential can be obtained perfectly. However, there exists always measurement noise and it prevents the accurate recovery of the disturbing geopotential.

The objective of this section is to figure out how the measurement noise propagates to the geopotential estimate. The determination of the actual disturbing potential is not of interest. For this kind of works, it is better to manipulate in spectral domain rather than in space domain, and the relationship between the space domain and the spectral domain needs to be derived. The velocity variation can be expressed in the spectral domain using the spherical harmonics as

$$\Delta v(\phi,\lambda) = \sum_{n=0}^{\infty}\sum_{m=0}^{n} \overline{P}_{nm}(\sin\phi)\left(\Delta\overline{v}_{nm}^{c}\cos m\lambda + \Delta\overline{v}_{nm}^{s}\sin m\lambda\right) \tag{3.35}$$

where (ϕ,λ) are spherical coordinates: geodetic latitude and longitude. The subscripts *n* and *m* denote degree and order, respectively. $\overline{P}_{nm}$ are the normalized Legendre associated functions, and $\Delta\overline{v}_{nm}^{c}$ and $\Delta\overline{v}_{nm}^{s}$ are the harmonic coefficients. The disturbing potential at the satellite altitude can be expressed in the similar way:

$$T' = T(r,\phi,\lambda) = \frac{GM}{R_e}\sum_{n=2}^{\infty}\sum_{m=0}^{n}\left(\frac{R_e}{r}\right)^{n+1}\bar{P}_{nm}(sin\phi)\left(\bar{C}'_{nm}\,cos\,m\lambda + \bar{S}_{nm}\,sin\,m\lambda\right) \quad (3.36)$$

This expression does not include two terms, $n = 0$ for the two body term and $n = 1$ for the Earth center offset from the coordinate origin. Since the velocity equation of (3.35) has these two terms, the velocity errors in these terms are not mapped into the gravity potential error. For convenience, let us define T as the disturbing potential on Earth's surface, $r = R_e$, and T' as the disturbing gravity potential at the satellite altitude, $r = r$. The coefficients $\bar{C}'_{nm}$ are obtained by subtracting the even zonal coefficients of the normal gravity field from the full spherical harmonic coefficients [72]. The error variance of T may be defined as an average of the expectation of the squared error over the unit sphere. Due to the orthogonality, the variance of T' has a simple relationship with the degree error variance of T as follows

$$\sigma^2(\delta T') = \sum_{n=2}^{\infty}\left(\frac{R_e}{r}\right)^{2n+2}\sigma_n^2(\delta T) \quad (3.37)$$

where the *n-th* degree error variance of T is given by

$$\sigma_n^2(\delta T) = \sum_{m=0}^{n}\left(\delta\bar{C}_{nm}^2 + \delta\bar{S}_{nm}^2\right) \quad (3.38)$$

The error variance of the velocity variation is obtained in the same way. After substituting (3.35) and (3.36) into (3.33) and taking error variances, the relationship between the degree error variances of velocity and gravity is given by

$$\sigma_n^2(\Delta v) = \frac{GM}{R_e}\left(\frac{R_e}{r}\right)^{2n+1}\sigma_n^2(T) \tag{3.39}$$

The circular velocity, $v_0 = \sqrt{GM/r}$ replaces the reference velocity v_0. This is an equation not for the error in the range-rate measurement assuming only the velocity variation of one satellite. The equation for the range-rate will be depicted as follows.

For the low-low satellite-to-satellite mission, the range-rate observable is the velocity difference component along the line-of-sight. For small fixed separation angle θ and circular reference orbit, this observable can be approximated as the velocity difference between two satellites:

$$\begin{aligned}\dot{\rho} &= (\boldsymbol{v}_1 - \boldsymbol{v}_2)\cdot\hat{\boldsymbol{e}}_{12} \;\; = (|\boldsymbol{v}_1| - |\boldsymbol{v}_2|)\cos\frac{\theta}{2} \\ &\approx \Delta v_1 - \Delta v_2 \qquad\qquad \textit{for small } \theta\end{aligned} \tag{3.40}$$

In the case of GRACE mission, the reference separation angle is 2° so that it is appropriate to use the small angle approximation. Since two satellites have the same reference velocity, the velocity difference of two satellites is equivalent to the difference of velocity variations from the reference velocity. The subscript 1 and 2 represent the location of the two satellites traveling at the same altitude and on the same orbit plane.

The range-rate is not only a function of the separation distance but also a function of direction. However, it is difficult to retain the directional property

through spectral mapping, so an average value is used instead. The root-mean-square (RMS) of the range-rate over all possible directions is defined by [29]

$$\bar{\dot{\rho}} = \sqrt{\frac{1}{4\pi}\int_0^{2\pi} \left(\Delta v_1 - \Delta v_2\right)^2 d\alpha} \tag{3.41}$$

The variance of this RMS value over the unit sphere σ is given by

$$\begin{aligned} \sigma^2\left(\bar{\dot{\rho}}\right) &= \frac{1}{4\pi}\int_\sigma \left(\bar{\dot{\rho}}\right)^2 d\sigma \\ &= \sigma^2(\Delta v) - cov\left(\Delta v_1, \Delta v_2\right) \end{aligned} \tag{3.42}$$

Let us assume the velocity variation Δv is isotropic and homogeneous on the sphere. The covariance function can be expanded as

$$cov\left(\Delta v_1, \Delta v_2\right) = \sum_{n=2}^{\infty} \sigma_n^2(\delta v) P_n(\cos\theta) \tag{3.43}$$

P_n is the Legendre function and θ is the separation angle between two satellites. The degree variance of the range-rate is then related to that of the velocity variation as

$$\sigma_n^2(\delta\dot{\rho}) = \sigma_n^2(\delta v)\left[1 - P_n(\cos\theta)\right] \tag{3.44}$$

Since the factor, $\left[1 - P_n(\cos\theta)\right]$, is less than 1 in most degree, the range-rate error is lower than the velocity error. This is one of the advantages of using the inter-satellite range-rate measurements instead of the velocity measurements.

Substitution of (3.44) into (3.39) yields the spectral relationship between the range-rate error and the gravity potential error as

$$\sigma_n^2(\delta T) = \frac{1}{1 - P_n(\cos\theta)} \frac{R_e}{GM} \left(\frac{r}{R_e} \right)^{2n+1} \sigma_n^2(\delta \dot{\rho}) \tag{3.45}$$

If the degree error variance of range-rate is available, that of the gravity can be obtained from the above equation. That degree variance is comparable to the degree error variance or the degree difference variance obtained by numerical simulations.

3.7.2 Prediction Procedure

The semi-analytic error prediction method used in this study is different from the conventional analytic error prediction methods in obtaining the measurement error variance [8]. For example, Jekeli's method [29] assumes the measurement noise as a white noise, which has uniform power spectral density over all frequency range and does not have correlation over time and. It can not accommodate the complicated measurement error characteristics that come from various error sources. In the case of the GRACE mission, the measurement error comes from not only the range-rate noise but also includes the effect of the accelerometer noise and other error sources. Moreover, these errors are better approximated as colored noises that have correlations over time and frequency dependent power spectrum. To overcome this complicated noise-modeling

problem, the semi-analytic method used numerical simulations to compute the degree error variance of the measurement noise instead of the analytic white noise assumption. However, the use of an analytic mapping function from the noise spectrum to the geoid error is the same as the conventional methods. A summary of the prediction procedure will be described as follows.

(A) First step is to realize the range-rate measurement noise due to various error sources. This step is identical to the determination of the optimal weighting procedure described in Section 3.6.2. The same type of the SST measurement residual (noise) is obtained.

(B) The second step is to map the measurement error in the space domain into the degree variance in the spectral domain. The range-rate residuals over each specific area, which is called a bin, are averaged, and then each bin is assigned one residual value. All bins have the same latitude and longitude lengths and cover the entire sphere. To guarantee all the bins have enough measurements to average, global coverage is required. That is, a polar orbit with a long repeat period, usually 30 days, should be used. The binned data is converted to spherical harmonics and then the degree variances of the measurement error are obtained.

4 INTER-SATELLITE MEASUREMENT ERRORS

4.1 INTRODUCTION

The GRACE satellites will use the dual one-way microwave ranging systems to measure the range change between two satellites. Each satellite has identical transmission and reception subsystems and transmits the carrier phase signals to the other satellites. The received signals at each of the two satellites are combined on the ground to reduce the noise due to oscillator instability. This process removes most of the oscillator drift effect, whose frequency range is lower than 1 KHz. The oscillator noise, which remains after the combination process, depends on the oscillator characteristics and the dual-one way filter. The later may be a function of frequency offset, carrier frequency, and separation distance.

The other types of SST noise include the system noise, which comes from the receiver subsystem, and the time-tag error due to the different clock error for the two satellites. The multipath noise is important as well, and it is due to the indirect microwave signals that are reflected around antenna horn. This noise level depends on the reflectivity of front surface of the satellite and the satellite attitude.

This chapter describes the error sources that affect the SST measurements. The procedures to generate major error sources, which include oscillator, system, and multipath noises, are described with the simulation results. These error sources were realized as the range measurement noise, and then converted into the

range-rate noise by the numerical differentiation. Another way is simulating the dual one-way phase measurements, and then converting into the range measurements. This phase measurement simulation results are presented for verifying the range simulations.

4.2 OSCILLATOR NOISE

4.2.1 Characteristics of the GRACE Oscillator

Let us consider an oscillator signal that is presented as follows [48]

$$A(t) = A_0 \sin\left[2\pi f_0 t + \delta\phi(t)\right] \tag{4.1}$$

where A_0 and f_0 are the nominal amplitude and frequency, respectively, with corresponding phase error $\delta\phi(t)$. In this section, the radian is the unit of the phase $\phi(t)$ and phase error $\delta\phi(t)$. It is noted that the cycle is the unit of the phase $\varphi(t)$ in other sections. The oscillator's instantaneous phase is defined by

$$\phi(t) = 2\pi f_0 t + \delta\phi(t) \tag{4.2}$$

The phase error $\delta\phi(t)$ may be related to the frequency error δf as follows

$$\delta\phi(t) = 2\pi \int_{t_0}^{t} \delta f(\xi) d\xi + \delta\phi(t_0) \tag{4.3}$$

Its instantaneous frequency is defined as the time rate of the change of phase

$$f(t) = \frac{\dot{\phi}(t)}{2\pi} = f_0 + \frac{\delta\dot{\phi}(t)}{2\pi} \tag{4.4}$$

Then, the fractional frequency deviation from the nominal frequency is defined as

$$y(t) = \frac{\delta\dot{\phi}(t)}{2\pi f_0} = \frac{\delta f}{f_0} \tag{4.5}$$

In terms of this variable, the most commonly used measure of stability is the Allan variance, which is defined in the following way. The average fractional frequency error over each sampling period is represented by

$$\bar{y}_k = \frac{1}{\tau}\int_{t_k}^{t_k+\tau} y(t)dt \tag{4.6}$$

where τ is a fixed sampling period. The Allan variance is defined as

$$\sigma_y^2(\tau) = \frac{1}{2}E\left[\left(\bar{y}_{k+1} - \bar{y}_k\right)^2\right] \tag{4.7}$$

where *E* denotes the expected value. This measure uses only adjacent samples and makes the calibration and sampling periods identical. The Allan variance is a measure of frequency stability and it is dimensionless.

The GRACE satellite uses an ultra stable oscillator (USO) to generate the base frequency of the K/Ka band signals. The USO for GRACE is a quartz crystal oscillator, and is the same kind of USO as that used in for the Mars Observer and Mars Global Surveyor (MGS) mission. The Allan variance of these USOs were

measured by flight tests. Figure 4.1 shows the specified Allan variances of the GRACE USO for different averaging times [19].

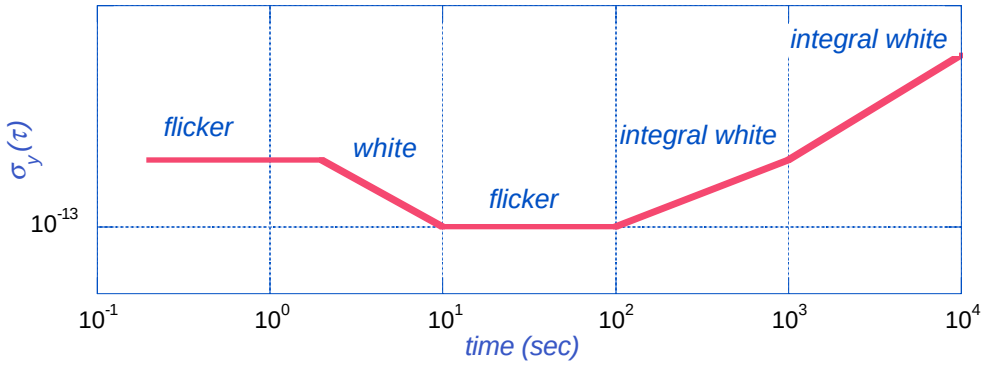

Figure 4.1 Allan variance of the GRACE oscillator

Each region may be classified into flicker noise, white noise, and integral white noise based on its slope. There exist formulations for converting this Allan variance to two-sided power spectral density (PSD) of the fractional frequency deviations [40,48]. These conversion formulations are represented in Table 4.1 for each type of noise.

Table 4.1 Allan variance and power spectral density

Error Source y(t)	***Allan Variance*** $\sigma_y^2(t)$	***Spectral Density*** $S_y(f)$
White Noise	N_0/τ	N_0
Flicker Noise	$(4ln2)N_1$	N_1/f
Integral of White Noise	$(2\pi)^2 N_2\tau/3$	N_2/f^2

Using these formulations, the PSD of the fractional frequency deviation may be represented as Figure 4.2. It is in units of cyc^2/Hz.

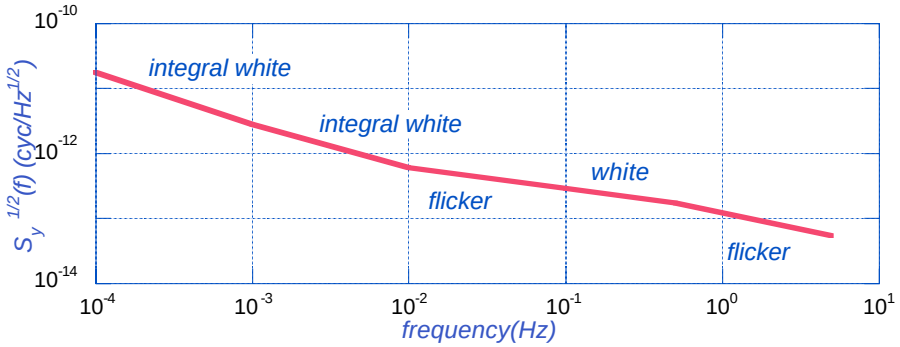

Figure 4.2 Two-sided frequency spectrum of the GRACE oscillator

Another representation of the frequency deviation is the single side-band phase noise spectrum, $L(f)$. The phase noise is the integration of the frequency noise, and can be related to the fractional frequency deviation *y* (frequency error) by combining (4.3) with (4.5):

$$\delta\phi(t) = 2\pi f_0 \int_0^t y(\xi) d\xi \tag{4.8}$$

The spectrum of the phase and frequency noise can be related as

$$F[\delta\phi(t)] = 2\pi f_0 F\left[\int_0^t y(\xi) d\xi\right] = 2\pi f_0 \left(\frac{1}{2\pi f}\right) F[y(t)] \tag{4.9}$$

where $F[\ ]$ represents the Fourier transform. By squaring these terms, one can express the single side-band phase noise spectrum $L(f)$ in terms of the two-sided frequency spectrum $S_y(f)$[44]:

$$L(f) = \frac{f_0^2}{f^2} S_y(f) \tag{4.10}$$

It is in units of rad^2/Hz and the nominal frequency f_0 should be specified. Sometimes oscillator stability is completely specified in terms of this single side-band phase noise instead of the Allan variance. The nominal output frequency f_0 of the GRACE USO is 4.832 MHz. Figure 4.3 shows its single side-band phase noise spectrum.

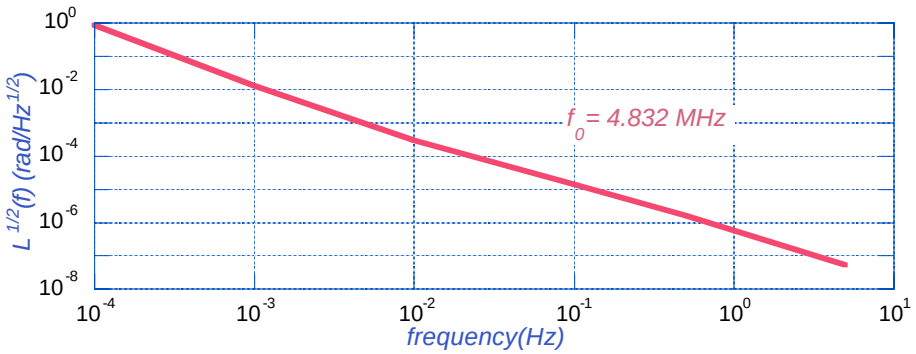

Figure 4.3 Single side-band phase noise spectrum of the GRACE oscillator

4.2.2 Transfer Function of the Oscillator Noise

The single side-band phase noise in Figure 4.3 goes through several filters before it can be realized as the range noise. The reduction of the frequency instability effect on the range measurement is described in Chapter 2. However, some oscillator noise remains after the dual one-way ranging filtering and this section describes the remaining noise characteristics by means of a spectral analysis developed by Thomas [71].

The combined phase equation (2.14) of Chapter 2 contains the three error terms related to the phase and time tag errors:

$$\delta\Theta(t) = (\delta f_1 + \delta f_2)\tau + (f_1 - f_2)(\Delta t_1 - \Delta t_2) + (\delta f_1 - \delta f_2)(\Delta t_1 - \Delta t_2) \qquad (4.11)$$

The first term is due to the phase error only, and the second term is due to the time tag error only. The third term is due to the coupling of the phase error and time tag error and is much smaller than the other terms. The unit of the phase error $\delta\varphi$ is cycle while that of $\delta\phi$ in the previous section is radian. Equation (4.11) can be rewritten with the phase error $\delta\varphi_i$ without the substitution of $\delta\dot{\varphi}_i(t) = \delta f_i(t)$:

$$\delta\Theta(t) = [\delta\varphi_1(t) - \delta\varphi_1(t-\tau)] + [\delta\varphi_2(t) - \delta\varphi_2(t-\tau)]$$
$$+(f_1 - f_2)(\Delta t_1 - \Delta t_2) \qquad (4.12)$$

The phase and time tag coupling term is ignored.

The time tags are to be corrected in ground by using the GPS measurements and the IGS network data. With these corrected time tags, the

phase measurements are to be interpolated to the value at the nominal sampling time. Different approaches may be applied to correct long and short period parts. The long period (> 6hr) error can be adjusted by the GPS clock solution. Two approaches are being considered for the short period time-tags [71]. (A) First approach (USO time-tag) is no adjustment of the short period time tags. The same time tags assigned by the GRACE USO clock signals are used after the long period correction. (B) Second approach (GPS time-tag) is the adjustment by the GPS clock solution, and the time-tag error is independent of the GRACE USO error. The selection depends on which clock data is more accurate in the short period. Current estimates suggest that GPS clock solution error might be better than the USO-induced clock error, at least lower signal band frequencies, e.g. lower than 1mHz [71]. The following derivation describes the transfer function of the dual one-way ranging for each approach.

(A) In case of the first approach, the short period time tag error is caused by the same source of the USO error. The time tag error ($\Delta t = t_{obs} - t$) can be expressed as the integration of the clock frequency error:

$$\Delta t_i(t) = -\int_{t_0}^{t} \frac{\delta f_i(\xi)}{f_0} d\xi \tag{4.13}$$

The initial time tag error is ignored. The time tag error can be related to the phase error by combining (4.3) with (4.13):

$$\Delta t_i = -\frac{\delta \varphi_i(t)}{f_i} \tag{4.14}$$

The relationship $2\pi\delta\varphi_i = \delta\phi_i$ is applied. When the oscillator runs faster than a nominal, the phase error has a positive value but the time tag error, which is the correction from the nominal time, has a negative value. Therefore, the positive phase error is related to the negative time tag error. Substitution of (4.14) into (4.12) yields the following dual one-way phase error due to the oscillator instability:

$$\delta\Theta(t) = \delta\Theta_1(t) + \delta\Theta_2(t) \tag{4.15}$$

where

$$\delta\Theta_1(t) = \left[\delta\varphi_1(t) - \delta\varphi_1(t-\tau)\right] - \left(f_1 - f_2\right)\left(\frac{\delta\varphi_1(t)}{f_1}\right)$$

$$\delta\Theta_2(t) = \left[\delta\varphi_2(t) - \delta\varphi_2(t-\tau)\right] + \left(f_1 - f_2\right)\left(\frac{\delta\varphi_2(t)}{f_2}\right) \tag{4.16}$$

$\delta\Theta_i(t)$ represents the phase error of the *i-th* satellite oscillator after the dual one-way ranging filter. The transfer function from the phase error $\delta\varphi_i(t)$ to the filtered phase error $\delta\Theta_i(t)$ may be given by

$$\sqrt{G_1(f)} = \frac{F[\delta\Theta_i(t)]}{F[\delta\varphi_i(t)]}$$

$$= \frac{F\left[\frac{f_j}{f_i}\delta\varphi_i(t) - \delta\varphi_i(t-\tau)\right]}{F[\delta\varphi_i(t)]} = \frac{\frac{f_j}{f_i}F[\delta\varphi_i(t)] - F[\delta\varphi_i(t)]e^{-i2\pi f\tau}}{F[\delta\varphi_i(t)]}$$

$$= \frac{\left[\frac{f_j}{f_i} - e^{-i2\pi f\tau}\right]F[\delta\varphi_i(t)]}{F[\delta\varphi_i(t)]} \tag{4.17}$$

For SST1's oscillator, the dual one-way ranging filter can be represented as follows [71]

$$G_1(f) = \left[\frac{f_2}{f_1} - exp(-i2\pi f \cdot \tau)\right]^2 \tag{4.18}$$

There exists an offset between the SST1 and SST2's carrier frequencies, f_1 and f_2, for either K and Ka band. τ is the time of flight of the signal between two satellites. Although τ is different for each one-way phase measurement, this difference is less than 0.005 μs and can be neglected for this oscillator noise realization. A large magnitude of the filter implies more oscillator noise in the phase measurement. Considering the first term of the above equation, one can find that a smaller frequency offset between f_1 and f_2 will increase the efficiency of the dual one-way filtering and yields lower range noise. However, due to signal interference and other design consideration, there exists a bound on its frequency offset and both frequencies should not be equal.

(B) In case of the second approach (GPS time-tag), the second terms of (4.16) are not necessary. By using the same spectral analysis, the dual one-way ranging filter becomes

$$G_1(f) = \left[1 - exp(-i2\pi f \cdot \tau)\right]^2 \tag{4.19}$$

In this approach, a separate phase error must be added to account for the GPS clock solution error.

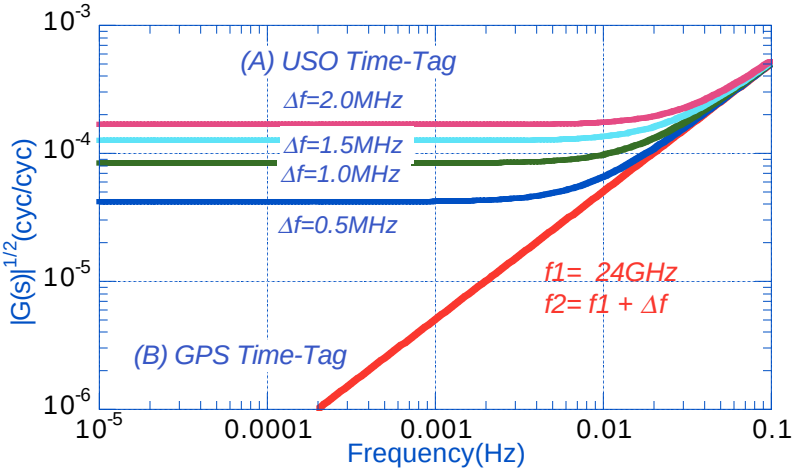

Figure 4.4 Effective filter applied to oscillator noise by dual one-way ranging for varying frequency offset

Figure 4.4 shows the magnitude of the dual one-way ranging transfer function for the first and second approaches. The second approach provides much better low frequency performance, but both approaches have similar performance at the high frequency. In order to obtain conservative results, the first approach (GRACE USO time-tag) was applied in this study.

The PSD of phase measurement noise due to oscillator drift is obtained by multiplying the phase noise $L(f)$ and the dual one-way ranging filter $G_1(f)$. Multiplying this resultant filter PSD by two to account of two oscillators, dividing by $(2\pi)^2$ to convert from rad^2 to cycle^2, and multiplying by $\left(f_{K/Ka}/f_0\right)^2$ to translate to K/Ka band.

$$S_{\Delta\Theta}(f) = 2 \cdot G_1(f) \cdot \left(\frac{1}{2\pi}\right)^2 \left(\frac{f_{K/Ka}}{f_0}\right)^2 L(f) \tag{4.20}$$

The range noise is related to the dual one-way phase noise as follows:

$$R = \frac{c}{f_1 + f_2}\Theta \qquad \text{or} \qquad R = \lambda_e \Theta \tag{4.21}$$

where λ_e is an effective wavelength for either K or Ka band. The same relationship is applied to the noise components. The PSD of the range error due to the oscillator drift becomes [71]

$$S_{\Delta\rho}(f) = 2 \cdot \left(\frac{\lambda_e}{2\pi}\right)^2 \left(\frac{f_{K/Ka}}{f_0}\right)^2 L(f) \cdot G_1(f) \tag{4.22}$$

Since the wavelength can be replaced in terms of the frequency as $\lambda_e \approx c/2f_{K/Ka}$, the carrier frequency $f_{K/Ka}$ is cancelled and the square root of the range error PSD becomes as follows

$$\sqrt{S_{\Delta\rho}(f)} = \frac{1}{4\pi}\left(\frac{c}{f_0}\right)\sqrt{2 \cdot L(f) \cdot G_1(f)} \tag{4.23}$$

The range-rate measurement is obtained by numerical differentiation of the range measurement. Since differentiation in the time domain is equivalent to frequency multiplication in frequency domain, the range-rate filter is represented by the square of the angular frequency as

$$RR(f) = (2\pi f)^2 \tag{4.24}$$

Since the filter definition used in this study corresponds to the PSD, i.e. square of the Fourier transform, the range-rate filter has the square value. It implies that the square root of the PSD of the range-rate noise grows linearly as the frequency increases. The square root of the range-rate error PSD is given by

$$\sqrt{S_{\Delta\dot{\rho}}(f)} = \sqrt{S_{\Delta\rho}(f)RR(f)} = (2\pi f)\sqrt{S_{\Delta\rho}(f)} \tag{4.25}$$

Figures 4.6 and 4.7 show the PSD of the resultant range and range-rate filters, respectively. These are not the effect of the oscillator drift itself but the effect of the residual oscillator drift after the dual one-way ranging filter. Since the range-rate noise PSD is the multiplication of the range PSD and the differentiation filter $(2\pi f)^2$, the relative magnitude of the range-rate noise increases as the frequency increases. This is why the range-rate noise start to grow in the high frequency region. It is noted that the oscillator drift effect on the range or range-rate measurement is dominant in the low frequency regions. It is opposite to other high frequency dominant noises, e.g. system or multipath noise.

In case of the real phase measurement processing, high rate phase samples (~0.1s) pass through a low pass filtering to yield low rate samples (~10s). This

process distorts the signal characteristics, and the transfer function of this low pass filtering needs to be included in the range error transfer function. However, this low pass filtering is under development and is not considered in this study.

4.2.3 Oscillator Noise Realization

Major parameters that determine the oscillator noise, which is the residual of the USO drift after the dual one-way ranging filtering, are the microwave frequency, frequency offset, and the time-of-flight. Although these values are still not determined yet, certain values were selected among many candidates for simulation purpose. To obtain a pessimistic noise level, rather than an optimistic level, several factors were taken into consideration when selecting those design parameters. For example, a larger frequency offset causes less efficient dual one-way filtering, and a higher altitude or larger separation angle implies a longer separation distance and longer time-of-flight, which causes less oscillator drift cancellation. Between K and Ka band frequencies, K band, f = 24 GHz, with frequency offset Δf = 1.5 MHz was chosen to get a feasible highest noise level.

In a real mission scenario, the separation distance will vary with time and the oscillator noise, more precisely the residual after the dual one-way ranging filtering, will change as well. Therefore, an actual oscillator noise realization needs a separation distance variation. However, in this simulation study, a fixed separation distance was used to maintain a single oscillator noise for different orbits. The operating orbit altitude will vary between from 500 km and 300 km,

and 450 km was selected because of its relatively higher altitude. The 450 km altitude with a 2° separation angle leads to a the separation distance of 238 km. Since the variation of the time-of-flight due to altitude is very small as long as a fixed separation angle is applied, the oscillator noise variation due to altitude can be ignored without loss of generality. Instead, the separation angle is much more important, and the variation due to separation angle is discussed in Chapter 6. Table 4.2 shows the simulation parameters used in this study.

Table 4.2 Simulation parameters for generating oscillator noise

Frequency(f_1)	*24 GHz*
Frequency Offset (f_2 - f_1)	*1.5 MHz*
Altitude	*450 km*
Separation Angle	*2 °*
Separation Distance	*238 km*
Time-of-Flight	*0.80 ms*

To realize the effect of oscillator drift error on the range measurement, the resultant transfer function was approximated by dual lag compensation. Instead of realizing every sub-transfer function, it is more efficient to realize the resultant transfer function only. Since the PSD of the range noise has a slope of $1/f^4$ and single lag compensation has a slope of $1/f^2$, dual lag compensation was used as follows [41]

$$G(s) = \left(\frac{\beta(s+\omega_f)}{\alpha(s+\omega_i)} \right)^2 \tag{4.26}$$

where $\alpha > 1$, $\omega_f = \alpha\omega_i$ and $\beta > 0$ are adjustable within a specified range. The details on determining these values are described in [48]. A higher order transfer function can be applied by using several numerical packages, e.g. MATLAB, but even higher order transfer functions yielded similar results and the dual lag compensation was used for its simplicity.

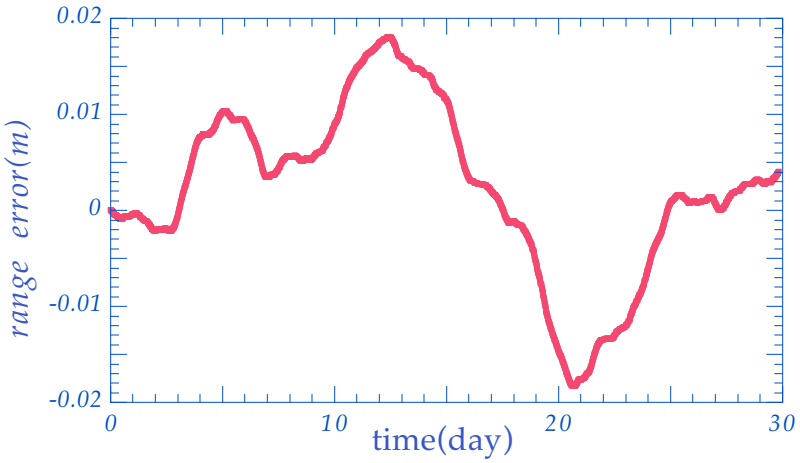

Figure 4.5 Time series of the SST range noise due to the oscillator drift

The noise time series was generated by MATLAB's continuous simulation function. The input white noise with the PSD of 1 m^2/Hz passed through the approximated transfer function to generate the noise time series. Figure 4.5 shows the time series of the range measurement noise due to the oscillator drift. Due to

its strong long wavelength characteristic, the leakage may harm the PSD of that time series. Therefore, the Hanning window function was applied to compute the PSD for leakage reduction purpose. Although this noise level is relatively large, the low frequency part of this noise can be effectively removed by applying piecewise empirical parameters.

Figure 4.6 compares the simulated noise PSD with the design range noise PSD in (4.23). The range-rate noise time series was obtained by numerical differentiation of the simulated range noise time series. Figure 4.7 compares the simulated range-rate noise PSD with the design PSD of (4.25).

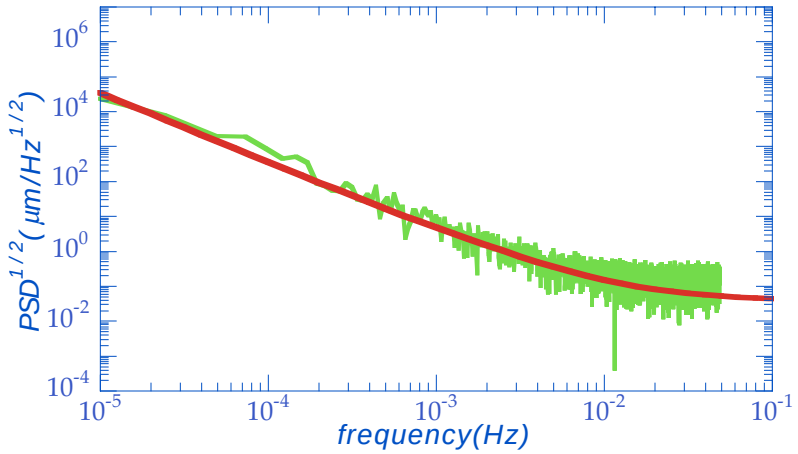

Figure 4.6 Power spectral density of the SST range noise due to the oscillator drift (Design vs. Simulated)

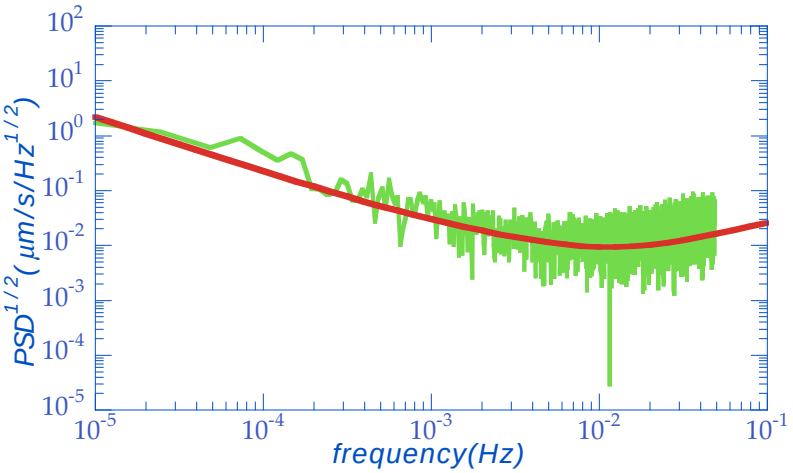

Figure 4.7 Power spectral density of the SST range-rate noise due to oscillator drift (Design vs. Simulated)

4.3 SYSTEM NOISE

Another type of SST measurement noise is the system noise, which is due to the receiver noise. It can be approximated as white noise for the range measurement. Its magnitude depends on the distance between two GRACE satellites, and the nominal value is the PSD of $(1\ \mu m/\sqrt{Hz})^2$ at 230 km separation that is the distance for 2° separation [71]. This is the value after a dual-band calibration to remove the ionosphere effect with the SNR (Signal-to-Noise Ratio) of 69 dB-Hz. The SNR decreases as the separation distance increases, and the system noise is assumed to increase linearly as the separation increase.

Since the noise variation is small for altitude change, the same system noise was used for all simulations, except the parameter study on the separation

distance, which is covered in Chapter 6. The noise variation due to temperature was not considered in this study. The range-rate noise may be obtained by numerical differentiation of the range noise. Therefore, the range-rate noise PSD is obtained by multiplying the range noise by $(2\pi f)^2$. Figure 4.8 shows the PSD of the range and range-rate noises due to the system noise. It is noted that the range-rate noise due to the system noise is dominant in the high frequency range since it grows as frequency increases.

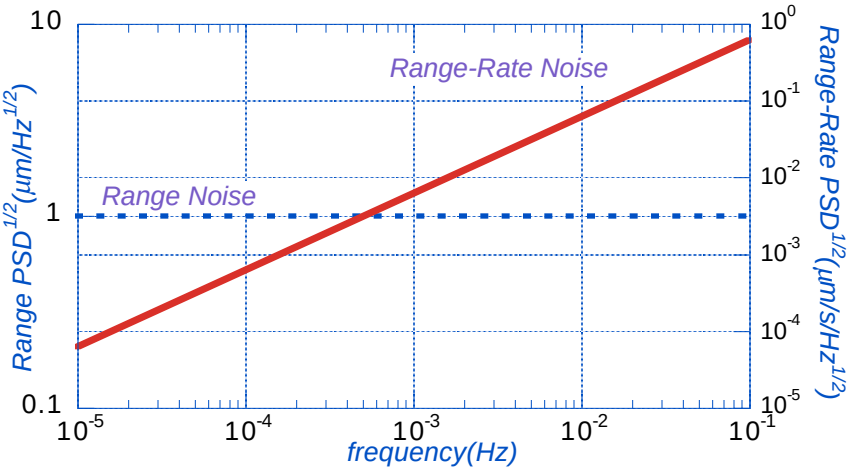

Figure 4.8 SST measurement error due to the system noise

4.4 TIME -TAG ERROR

This section quantifies the range error due to the measurement time-tag errors. In Section4.2.2, two types of the time-tags were considered: USO and GPS time-tags. In case of the USO time-tag, the range error due to the time-tag error is

correlated to the oscillator noise, so that the range error due to the oscillator noise already includes the time-tag error effect. The following description is more directed to the GPS time-tag case, where the time-tag error is treated as an independent error source (separated from the oscillator noise).

Most of the oscillator drift errors can be canceled out by combining two one-way measurements. However, if the measurement times of two satellites are different, there will be some additional error. Since initial measurement time tag difference may be relatively large, e.g. 1ms, interpolation of the SST measurement is required to make the two measurement time tags close each other as much as possible. This interpolation process may utilize the corrected time tag using the GPS measurements. There would be still time tag error even after this interpolation, and the impact of this residual on the SST range measurement is analyzed in this section.

Equation (2.14) of Chapter 2 describes the dual one-way phase measurement with the time tags of Δt_1 and Δt_2. Its third and fourth terms represent the time tag error:

$$\begin{aligned}\delta\Theta(t) &= \left[\left(f_1+\delta f_1\right)-\left(f_2+\delta f_2\right)\right]\left(\Delta t_1-\Delta t_2\right)\\ &= \left(f_1-f_2\right)\left(\Delta t_1-\Delta t_2\right)+\left(\delta f_1-\delta f_2\right)\left(\Delta t_1-\Delta t_2\right)\end{aligned} \tag{4.27}$$

where f_i represents a constant nominal frequency and δf_i does a frequency instability. The first term is due to the time tag errors and the second term is due to the coupling between the phase error and the time tag error. Since the magnitude of the frequency error is much smaller than that of the nominal

frequency, $\delta f_i / f_i \approx 2 \times 10^{-13}$, the second term is very much smaller than the first term and it can be ignored. Of interest is not the individual time tag errors, Δt_1 and Δt_2, but the time tag error difference, $\Delta t_1 - \Delta t_2$. Therefore, a new time tag error definition $\Delta t = \Delta t_1 - \Delta t_2$ is used in the following derivation. The range measurement error due to the time tag error can be obtained by multiplying the phase error (4.27) by $c/(f_1 + f_2)$:

$$\delta\rho = c\frac{f_1 - f_2}{f_1 + f_2}\Delta t \tag{4.28}$$

This error depends on the frequency offset $\Delta f = f_2 - f_1$ as well as the time tag error Δt.

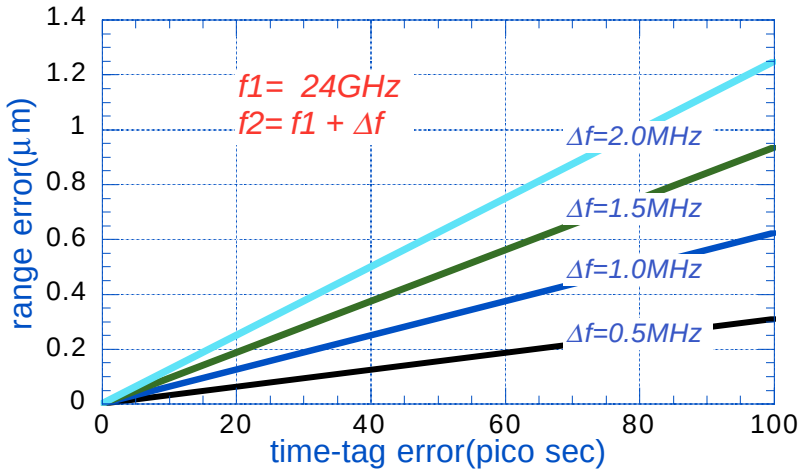

Figure 4.9 SST range error due to the time-tag error

Figure 4.9 shows the variation of the range error $\delta\rho$ for different frequency offsets $\Delta f = f_2 - f_1$. Only the K-band (24 GHz) results are shown since the K-band error is grater than the Ka-band error is for a same amount of the time-tag error. It is clear that a larger frequency offset causes a larger range error.

If the nominal requirement of the range error is set as 1 μm/s, the corresponding time-tag error for Δf = 1.5 MHz should be less than 80 pico second. However, if this time-tag error is constant over some period, it may not affect the gravity solution since the primary measurement is not the true range but the biased range. Of interest is not the absolute magnitude of the time-tag error but the stability of it. The single one-way phase measurements would be interpolated before forming a dual one-way phase measurement using the time tag correction from the GPS and the ground stations. In that case, the time tag error residuals after this correction becomes much less than the original time tag errors and replace the time tag errors in the above equations. In the IGS network, the time-tag difference is stable, and is estimated accurately to better than 70 pico second over a day after a linear term is removed [71]. Since the GRACE satellites have more GPS satellites in view, their GPS solution should be at least as good as an IGS station, if not better. Therefore, the range error can be within the specification.

Because of this low level of noise, the time-tag error was not implemented in this study. In case of actual data processing, the time-tag error can be efficiently reduced during pre-processing.

4.5 INSTANTANEOUS RANGE CORRECTION

The dual one-way ranging description in Chapter 2 assumed the same time-of-flight τ for both satellite phase signals. Since the two satellites are always moving in a similar direction, the time-of-flight for the phase signal from the leading satellite to the trailing satellite is shorter than the time-of-flight from the trailing one to the leading one. The actual range measurement derived from the dual one-way ranging phase measurements contains both of these different time-of-flights. Since the estimation equations derived in Section 2.2 utilize the instantaneous range between two satellites at specified time, it is necessary to convert the phase-derived range into the instantaneous range. However, any other errors in the phase-derived range, e.g. bias, are not affected by this conversion.

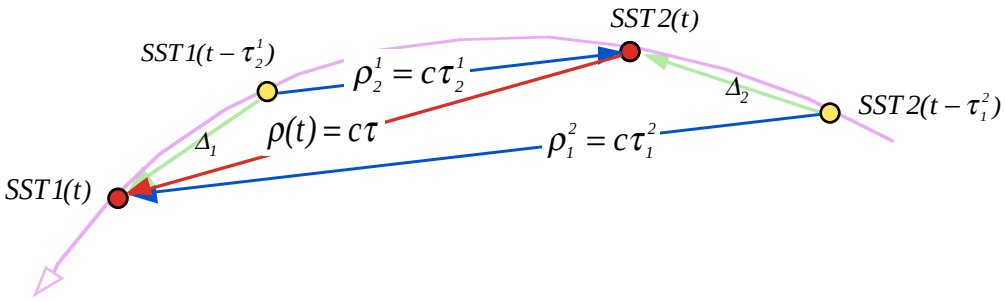

Figure 4.10 Relationship between the instantaneous range $\rho(t)$ and the phase-derived ranges ρ_1^2 and ρ_2^1.

Figure 4.10 illustrates the relationship between the instantaneous range $\rho = c\tau$ and the phase-derived ranges $\rho_2^1 = c\tau_2^1$ and $\rho_1^2 = c\tau_1^2$. The instantaneous range ρ is the distance between the two satellites at the same nominal time *t*. The phase-derived range ρ_i^j is the travel distance of the phase signal that is transmitted by *j-th* satellite at $t - \tau_i^j$ and received by the *i-th* one at t. The displacement vector $\boldsymbol{\Delta}_i$ represents the displacement of the *i-th* satellite for τ_j^i.

The relationship between the instantaneous range $\rho(t)$ and the actual dual one-way range observable can be derived in the following way. In Section 2.2.2, the dual one-way ranging observable $\Theta(t)$ is represented as follows:

$$\begin{aligned}\Theta(t) = &\left(f_1\tau_2^1 + f_2\tau_1^2\right) + \left(\delta f_1\tau_2^1 + \delta f_2\tau_1^2\right) \\ &+\left(f_1 - f_2\right)\left(\Delta t_1 - \Delta t_2\right) + \left(\delta f_1 - \delta f_2\right)\left(\Delta t_1 - \Delta t_2\right) \\ &+N + d + \varepsilon \end{aligned} \tag{4.29}$$

The first and second terms contain two time-of-flight values. The first term represents a nominal value and the second term represents the coupling effect between the time-of-flight difference and the frequency error δf_i. Since the magnitude of the frequency error is much smaller than that of the reference frequency, $\delta f_i / f_i \approx 2\times 10^{-13}$, the second term is much smaller than the first term and can be ignored without loss of generality. The other terms are time tag error and miscellaneous terms. Without the oscillator drift, cycle delay, and ambiguity terms, the observable $\Theta(t)$, the sum of two phase measurements, may be given by

$$\Theta(t) = f_1\tau_2^1 + f_2\tau_1^2 \tag{4.30}$$

It can be converted into a phase-derived range equation by multiplying the speed-of-light *c* and dividing by the sum of the carrier frequencies:

$$\frac{c}{f_1 + f_2}\Theta(t) = \frac{1}{f_1 + f_2}\left(f_1\rho_2^1 + f_2\rho_1^2\right) \tag{4.31}$$

Two ranges ρ_2^1 and ρ_1^2 can be related to the instantaneous range ρ at *t*, which is used for estimation process:

$$\rho_2^1 = F_1(\boldsymbol{\rho}, \boldsymbol{\Delta}_1) = \sqrt{(\boldsymbol{\rho} - \boldsymbol{\Delta}_1)^T(\boldsymbol{\rho} - \boldsymbol{\Delta}_1)}$$

$$\rho_1^2 = F_2(\boldsymbol{\rho}, \boldsymbol{\Delta}_2) = \sqrt{(\boldsymbol{\rho} + \boldsymbol{\Delta}_2)^T(\boldsymbol{\rho} + \boldsymbol{\Delta}_2)} \tag{4.32}$$

In this expression, $\boldsymbol{\Delta}_i$ is the vector from the position of *i-th* satellite at τ_j^i to the position at *t*. The instantaneous range vector $\boldsymbol{\rho}$ is equivalent to $\mathbf{r}_1 - \mathbf{r}_2 = \rho\hat{\mathbf{e}}_{12}$ and its magnitude is the instantaneous range ρ. The right sides can be expanded by the first order Taylor series about the instantaneous range ρ as

$$\rho_j^i \approx \left[F_i\right]_{\boldsymbol{\Delta}_i = \mathbf{0}} + \left[\frac{\partial F_i}{\partial \boldsymbol{\Delta}_i}\right]_{\boldsymbol{\Delta}_i = \mathbf{0}} \cdot \boldsymbol{\Delta}_i \qquad (\ i=1,2\ ) \tag{4.33}$$

These first order approximation becomes the sum of the instantaneous range ρ and the projection of the displacement vector $\boldsymbol{\Delta}_i$ on the line-of-sight (LOS) vector $\hat{\mathbf{e}}_{12}$:

$$\rho_2^1 \approx \rho - \boldsymbol{\Delta}_1^T\hat{\mathbf{e}}_{12}$$

$$\rho_1^2 \approx \rho + \boldsymbol{\Delta}_2^T\hat{\mathbf{e}}_{12} \tag{4.34}$$

Substitution of Eqns. (4.34) into (4.31) expresses the phase-derived range as a function of the instantaneous range and other terms:

$$\frac{c\Theta(t)}{f_1 + f_2} = \rho - \frac{f_1}{f_1 + f_2}\left(\boldsymbol{\Delta}_1 - \boldsymbol{\Delta}_2\right)^T \hat{\boldsymbol{e}}_{12} - \frac{f_1 - f_2}{f_1 + f_2}\left(\boldsymbol{\Delta}_2{}^T \hat{\boldsymbol{e}}_{12}\right) \tag{4.35}$$

The second term, which is the projection of the displacement vector difference on the LOS vector, can be related to the instantaneous range-rate $\dot{\rho}$ at time t in the following way. The displacement vector Δ_i can be approximated by the product of the velocity at time t and the time-of-flight τ_j^i:

$$\boldsymbol{\Delta}_i = \mathbf{r}_i(t) - \mathbf{r}_i\left(t - \tau_j^i\right) \approx \dot{\mathbf{r}}_i(t)\tau_j^i \tag{4.36}$$

Using this relationship, the second term of (4.35) becomes

$$\left(\boldsymbol{\Delta}_1 - \boldsymbol{\Delta}_2\right)^T \hat{\boldsymbol{e}}_{12} \approx \dot{\rho}\tau_2^1 - \Delta\tau\left(\dot{\mathbf{r}}_2(t)^T \hat{\boldsymbol{e}}_{12}\right) \tag{4.37}$$

where the time-of-flight difference $\Delta\tau = \tau_1^2 - \tau_2^1$ and the instantaneous range-rate $\dot{\rho} = \left(\dot{\mathbf{r}}_1(t) - \dot{\mathbf{r}}_2(t)\right)^T \hat{\boldsymbol{e}}_{12}$ are used. The instantaneous range ρ can be expressed as a sum of the phase measurement and the correction term after substitution of (4.37) into (4.35),

$$\rho = \rho_{obs} + \rho_{TOF} \tag{4.38}$$

where $$\rho_{obs} = \frac{c\Theta(t)}{f_1 + f_2}$$

The second term is the instantaneous correction term as follows:

$$\rho_{TOF} = \frac{f_1}{f_1 + f_2}\dot{\rho}\tau_2^1 - \frac{f_1}{f_1 + f_2}\eta_2\Delta\tau + \frac{f_1 - f_2}{f_1 + f_2}\eta_2\tau_1^2 \tag{4.39}$$

where $\eta_2 = \dot{\boldsymbol{r}}_2(t)^T \hat{\boldsymbol{e}}_{12}$ is a velocity component along the LOS vector. The first term represents the range variation during the time-of-flight and the second term does the time-of-flight difference. The last term results from the frequency offset. For the error analysis of the correction algorithm, of interest is not its magnitude but its accuracy. Therefore, it is necessary to quantify how accurately the individual parameters can be predicted. Table 4.3 lists the magnitude and accuracy assumptions of those parameters in (4.39). These accuracy levels are based on the estimation error using the GPS measurements, which are independent of the SST measurements. Therefore, these accuracy levels can be obtained during the pre-processing.

Table 4.3 Magnitude and accuracy assumptions on the instantaneous range correction related parameters

	magnitude	*accuracy*
Range ρ	*< 500km*	*< 1cm*
Range-Rate $\dot{\rho}$	*< 1m/s*	*< 0.1 mm/s*
TOF τ	*<* 2×10^{-3} *sec*	*<* 3×10^{-11} *sec*
TOF difference $\Delta\tau$	*<* 5×10^{-8} *sec*	*<* 1×10^{-13} *sec*
velocity η_1	*< 8km/s*	*< 1cm/s*

With the dynamic estimation approach, which is used in this study, the SST observation signals were generated with a truth gravity field and then compared with the nominal signals generated with a nominal gravity field. These error levels are far lower than the accuracy levels in the table. Since the estimation accuracy by the dynamic approach depends heavily on the accuracy of the nominal gravity field, a smaller error level would be possible after an improved gravity field is obtained.

Since two GRACE satellites have almost the same altitude and GPS satellite views, it is ideal to use the double-difference measurements between two GPS satellites and two GRACE satellites. This method can estimate the inter-satellite range and range-rate with much higher accuracy than the conventional approach, i.e. forming the double difference measurements between two GPS, one low satellite, and one ground station.

The time-of-flight (TOF) accuracy in the table results from the range accuracy of *1 cm*. The magnitude and accuracy of the TOF difference $\Delta\tau$ result from the following analogy. Each satellite moves about *7.5 m* for *1 ms* that is a usual time-of-flight, and maximum $\Delta\tau$ happens when both satellites moves along the same way, i.e. along the LOS. Therefore, the maximum becomes 5×10^{-8} sec for the time-of-flight of 15 m = 7.5 m + 7.5m as follows

$$|\Delta\tau| \le \frac{|\dot{\boldsymbol{x}}_1|\tau_2^1}{c} + \frac{|\dot{\boldsymbol{x}}_2|\tau_1^2}{c} \approx \frac{2|\dot{\boldsymbol{x}}|\tau}{c} \approx 5\times10^{-8}\,sec \tag{4.40}$$

Its estimate of the accuracy follows from the accuracy of the velocity and TOF estimates

$$\delta(\Delta\tau) \le \frac{2\delta(\dot{x})\tau}{c} + \frac{2|\dot{x}|\delta(\tau)}{c} \approx 10^{-13}\, sec \tag{4.41}$$

The instantaneous correction accuracy $\delta\rho_{TOF}$ can be obtained by the following variational equation

$$\begin{aligned}\delta\rho_{TOF} \approx & \frac{f_1}{f_1+f_2}\delta(\dot{\rho})\tau_2^1 + \frac{f_1}{f_1+f_2}\dot{\rho}\delta\left(\tau_2^1\right) \\ & -\frac{f_1}{f_1+f_2}\left[\delta(\eta_2)\Delta\tau + \eta_2\delta(\Delta\tau)\right] + \frac{f_1-f_2}{f_1+f_2}\left[\delta(\eta_2)\tau_1^2 + \eta_2\delta\left(\tau_1^2\right)\right]\end{aligned} \tag{4.42}$$

The products of two error terms are ignored. Two carrier frequencies are assumed as $f_1 = 26\ GHz$ and $f_2 = f_1 + 1\ MHz$, respectively. With the accuracy in the table, all the terms are much less than $1\ \mu m$, which is the expected range noise level. Therefore, this TOF correction can be ignored for most error analyses. It can be computed during the pre-processing with a sufficient accuracy. The most dominant term is the first one that has an order of $10^{-1}\ \mu m$ level. Therefore, the range correction accuracy mostly depends on the range-rate accuracy.

The correction (4.39) is a function of the carrier frequencies f_1 and f_2, and two values need to be computed for the two frequency bands, K or Ka. Since these corrections are an addition to the dual one-way ranges, the same ionosphere correction algorithm as the range combination can be used for computing the correction corresponding to the ionosphere-free instantaneous range:

$$\rho_{TOF} = \frac{\bar{f}_K^2 \left(\rho_{TOF}\right)_K - \bar{f}_{Ka}^2 \left(\rho_{TOF}\right)_{Ka}}{\bar{f}_K^2 - \bar{f}_{Ka}^2} \tag{4.43}$$

where $\bar{f}_K$ and $\bar{f}_{Ka}$ are the effective frequencies as defined in (2.19).

Figure 4.11 shows the TOF corrections for the two range signals, one with true states and the other with nominal states. Although the signal itself has a large magnitude, the difference between two corrections is very small as presented in Figure 4.12. A numerical simulation was performed with the correction error applied range-rate measurements, and the degradation of the gravity coefficients due to the correction error was negligible. The instantaneous range correction should be implemented in the pre-processing, but the correction error can be ignored for most of the simulations.

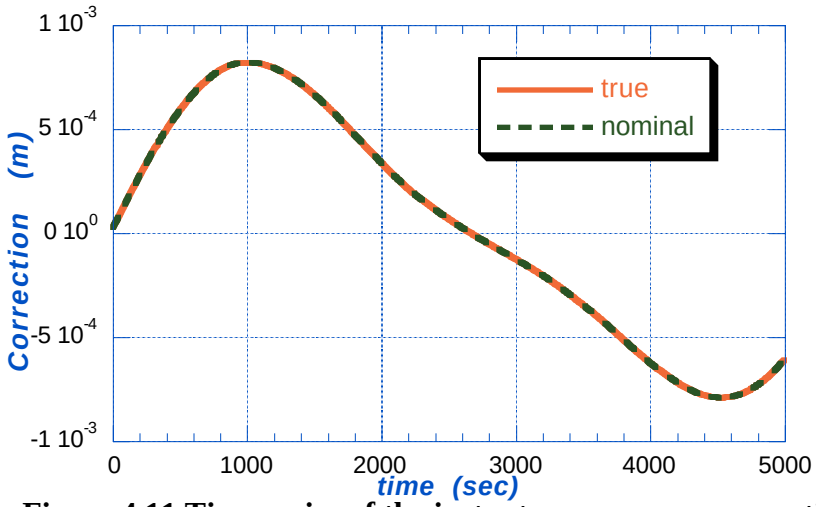

Figure 4.11 Time series of the instantaneous range corrections (by true and nominal states)

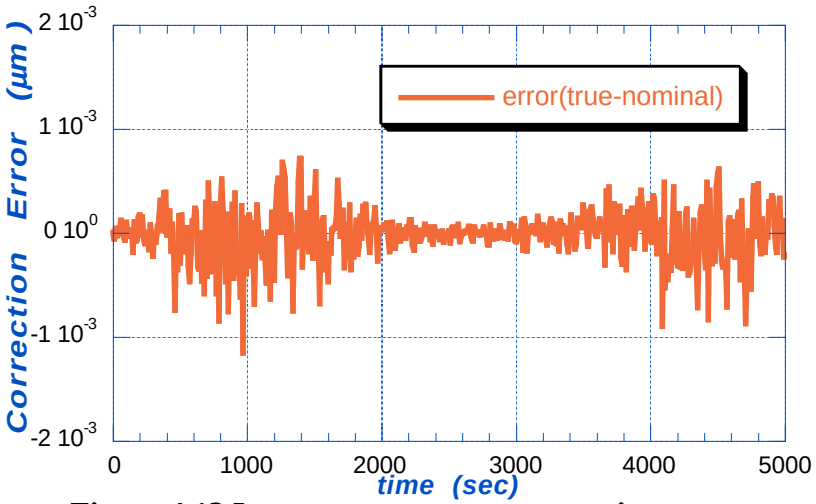

Figure 4.12 Instantaneous range correction error

4.6 MULTIPATH NOISE

The straight line between two satellites' phase center is defined as the line-of-sight (LOS). If the LOS is perfectly aligned with the K-band boresight (KBB) or the *x*-spacecraft-body-fixed-axis (SCA), the carrier phase measurement gives true distance. In the real situation, the nominal LOS that is predicted by on-board attitude controller to control the satellite attitude is not exactly same as the true LOS. Even the attitude error exists in keeping the satellite in the nominal attitude, where the KBB is parallel to the nominal LOS. When the KBB is not parallel to the true LOS, indirect signals are reflected near the phase center and the carrier phase measurements are affected. Because of the arbitrarily different geometric situation, there is no general model of multipath effect. However, with some approximation made by Thomas [18], it is possible to derive a simple relationship between the attitude variation and pessimistic multipath noise. The original purpose of this analysis was to determine the attitude deadband, and it is why the simple relationship was implemented. One of the attitude simulation results from AMA [24] was used to get attitude variation time series and to realize the multipath noise. Numerical simulations were performed to analyze the effect of multipath noise on gravity solution,.

4.6.1 Multipath Formulations

The effect of multipath on carrier phase may be estimated by the following consideration. The carrier phase observable consists of a direct signal and an indirect signal that is reflected near the antenna phase center [42]:

$$direct: \quad Ae^{i\phi} \tag{4.44}$$

$$indirect: \quad \varepsilon Ae^{i(\phi+\Delta\phi)} \tag{4.45}$$

where

ϕ = *phase*

A = *amplitude*

$\Delta\phi$ = *phase shift by multipath*

ε = *amplitude reduction factor*

The amplitude of the indirect signal is reduced by the reduction factor ε because of the reflection of a surface. The phase of the indirect signal is delayed by the phase shift $\Delta\phi$, which is a function of geometric configuration. The superposition of two signals in (4.44) and (4.45) becomes

$$Ae^{i\phi} + \varepsilon Ae^{i(\phi+\Delta\phi)} \tag{4.46}$$

It can be represented as a composite signal of the following form

$$composite: \quad \varepsilon_M Ae^{i(\phi+\Delta\phi_M)} \tag{4.47}$$

In the imaginary domain, it is easier to represent the relationship between the direct and composite signals. Figure 4.13 shows that the composite signal is the vector sum of the direct and indirect signals.

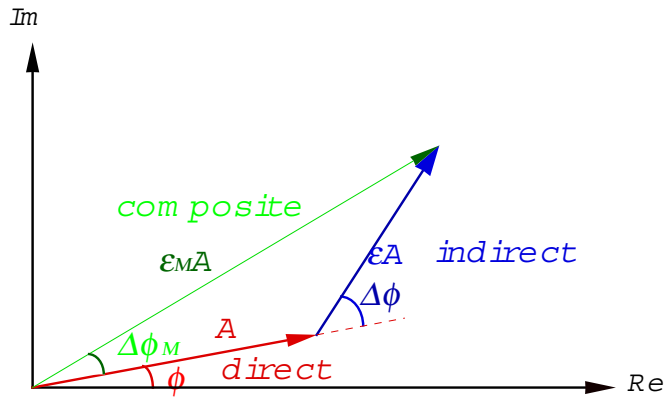

Figure 4.13 Phase diagram of direct, indirect, and composite signals

Using this graphic representation, one can find the composite phase shift and amplitude reduction factor as a function of indirect signal reduction factor and phase shift:

$$tan\,\Delta\phi_M = \frac{\varepsilon \sin\Delta\phi}{1+\varepsilon\cos\Delta\phi} \tag{4.48}$$

$$\varepsilon_M = \sqrt{1+\varepsilon^2+2\varepsilon\cos\Delta\phi} \tag{4.49}$$

The maximum phase shift occurs when the composite signal phase is perpendicular to the indirect signal phase, and the maximum value $\Delta\phi_M$ may be obtained by the following relationship

$$sin\,\Delta\phi_M = \varepsilon \tag{4.50}$$

The minimum phase shift occurs when the composite signal phase is parallel to the indirect signal phase. The minimum value becomes zero:

$$\Delta\phi_M = 0 \tag{4.51}$$

This minimum condition yields the maximum or the minimum value of the composite reduction factor as

$$\varepsilon_M = 1 \pm \varepsilon \tag{4.52}$$

The GRACE multipath error can be related to the cone angle, which is defined as the angle between the LOS and *x*-spacecraft-body-fixed-axis (SCA) or the tilt angle of the satellite front. Figure 4.14 shows the cone angle θ and the reflection distance *y*, which is the distance between the phase center and the reflection point [18].

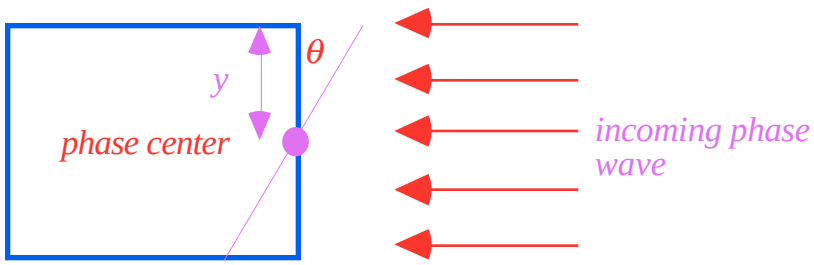

Figure 4.14 Definition of cone angle and multipath reflection point

The indirect signal phase shift may be related to the cone angle as follows

$$\Delta\phi = 2\pi\left(\frac{y}{\lambda} - \frac{y\theta}{\lambda}\right) \tag{4.53}$$

λ is the wavelength of carrier phase signal (K or Ka band)

In case of the GRACE mission, the multipath interference can not be avoided since the line-of-sight is not perfectly known during flight, where the on-board controller uses a predicted value. However, the angle between the LOS and the *x*-SCA or the K-band boresight (KBB) can be determined accurately by post processing. In addition, the SST observable is not a true range but a biased-range, so it is not an important factor. Of interest is the variability of indirect signal phase shift, which is directly related to attitude variation. The variability of composite signal phase-shift depends on the mean part of attitude variation. The worst case happens when the amplitude reduction factor has a value near its maximum or minimum. Let us assume that the distance *y* meets the following condition [18]:

$$e^{2\pi i(y/\lambda)} = \pm 1 \text{ or } 2\pi\left(\frac{y}{\lambda}\right) = N\pi \tag{4.54}$$

For small indirect signal phase-shift $\Delta\phi$, (4.48) becomes

$$\Delta\phi_M \approx \frac{\varepsilon\Delta\phi}{1+\varepsilon} \tag{4.55}$$

For small amplitude reduction factor ε, the composite phase shift may be given by

$$\Delta\phi_M \approx \varepsilon\Delta\phi \quad = \varepsilon \cdot 2\pi\left(\frac{y\theta}{\lambda}\right)$$

$$= \varepsilon\left(\frac{2\pi}{\lambda}\right)y\theta \tag{4.56}$$

Then, the range error due to multipath becomes

$$\Delta R = \frac{\lambda}{2\pi}\Delta\phi_M = \varepsilon y\theta \tag{4.57}$$

The above error is for one satellite and actual multipath interference occurs at two satellites independently. The dual one-way range error is obtained by multiplying the one way error by $\sqrt{2}$ as

$$\Delta\rho = \sqrt{2}\varepsilon y\theta \tag{4.58}$$

The range-rate error is obtained by differentiation of that range error:

$$\Delta\dot{\rho} = \sqrt{2}\varepsilon y\dot{\theta} \tag{4.59}$$

4.6.2 Multipath Noise Realization

Since the attitude variation directly affects the multipath, it is important to control the attitude variation to within a specific level to minimize this error. The GRACE team at LaRC/AMA performed some preliminary attitude simulations

and one of the simulation results is presented here. These attitude variation characteristics are expected to change, but are useful for a tool for sensitivity study. Exact condition is difficult to simulate realistically because disturbance environment is unpredictable.

The moment of inertia of the satellite was assumed as (75, 364, 421) kg/m^2. The satellite uses a magnetic torquer and thrusters to control the attitude but the magnetic torquer is in charge of most attitude maneuvers. The satellite attitude is adjusted when the cone angle is greater than specified deadband limits. The cone angle is computed from the yaw and pitch angle, and independent of the roll angle. Due to this reason, the roll angle has a larger deadband than the yaw and pitch angles.

Figure 4.15 shows the Euler angle variations. The yaw and pitch angles have some bias due to the star tracker bias. The maximum yaw angle variation is 0.5 mrad, but the pitch angle variation is 0.2 mrad and is smaller than the yaw angle. The maximum roll angle is 10 mrad. The cone angle variations are presented in Figure 4.16. Due to the yaw and pitch angle biases, the cone angle has a bias of 2mrad and this bias causes a range bias. Since the SST measurement is a biased-range, the range bias does not affect the SST measurement accuracy. Of interest is not the bias but the variation of the range error. This bias is removed for the range-rate measurement. The maximum cone angle variation is 0.5 mrad.

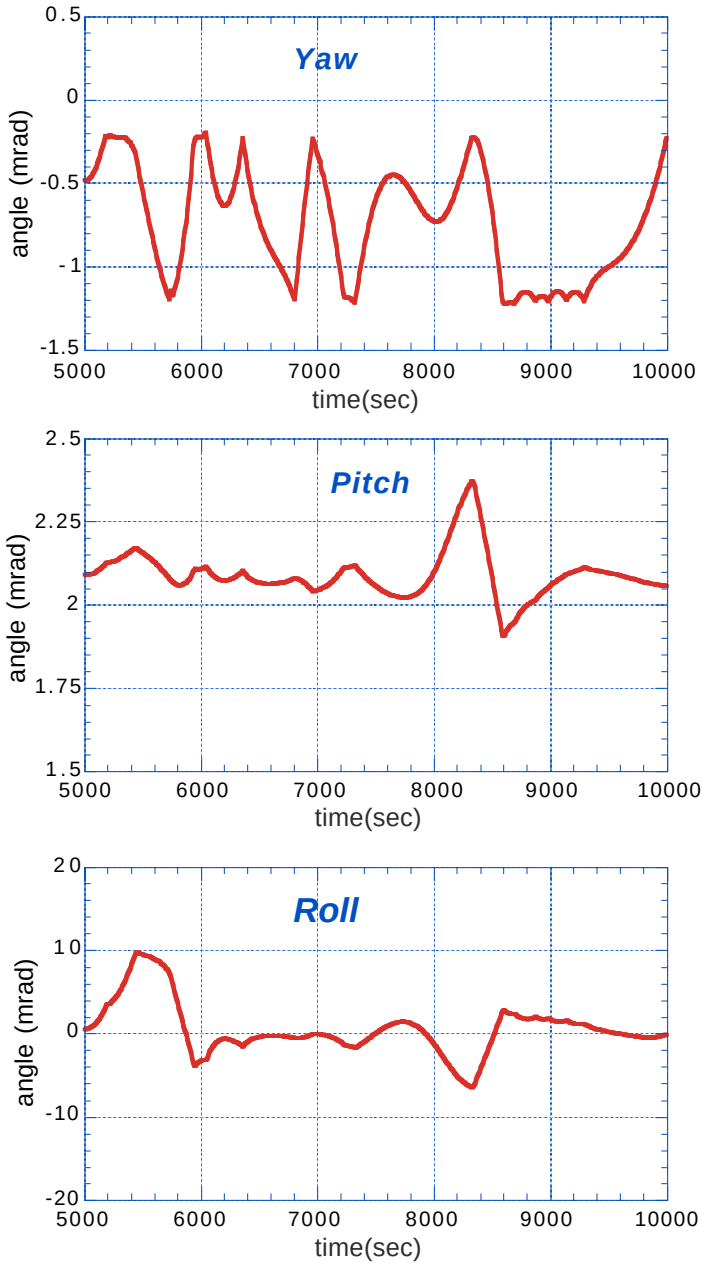

Figure 4.15 Attitude angle variation

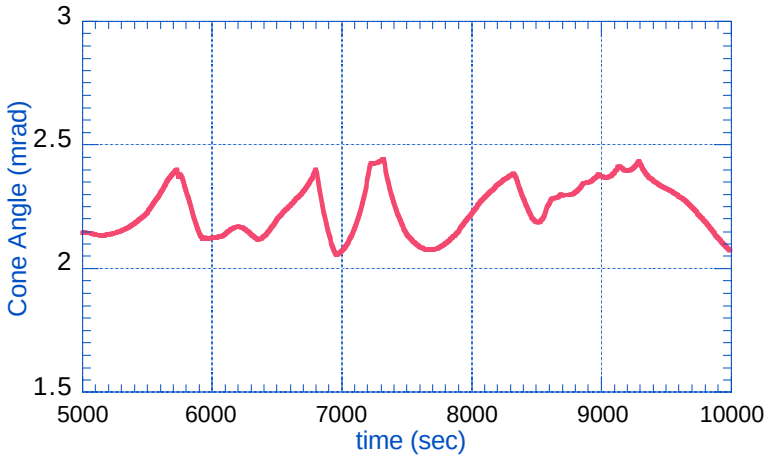

Figure 4.16 Cone angle variation

The simplified relationship between the multipath noise and the cone angle variation was derived in (4.58) and (4.59). To obtain the range/range-rate noise, one needs three quantities, the amplitude reduction factor ε, the distance between the reflection point and the phase center y, and the cone angle error θ. The cone angle variation comes from the attitude simulation results. To determine the amplitude reduction factor ε, a full-scale mockup of the front of the satellite in conjunction with one of the prototype horns was tested [66]. With the correction for the effect of non-uniform illumination of the nearest edge of the satellite front, the reduction factor was down by at least -56 dB. For the present numerical simulations, a more pessimistic value of -50 dB was used instead. The distance between the phase center and the reflection point is a random number and dependent on the shape of the front of the satellite. With the GRACE configuration B, the distance varies from 27.5 cm to 74 cm. Theoretically, circular approximation of the front area yields the average distance from the phase center

to edges of 42 cm. However, $y = 70\ cm$ was used as a pessimistic value. With these values, the sensitivity of the multipath range error for the cone angle error becomes 3 μm/mrad.

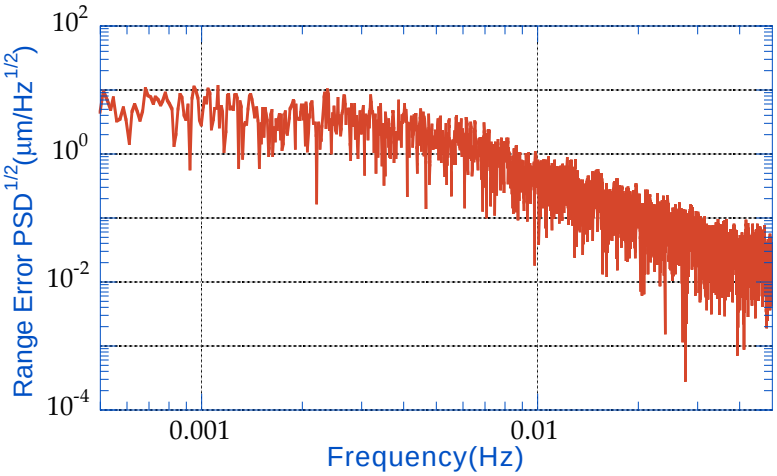

Figure 4.17 Power spectral density of the range multipath noise

The range multipath noise was computed using (4.58) with 10s cone angle data. Then, the range-rate noise was obtained by differentiation of the range noise time series so that the power spectrum is amplified in the high frequency region. Figure 4.17 shows the spectral density of the range noise. This noise spectrum has a high power at the low frequency, but has a low power at the high frequency. Comparing with the oscillator and system noise, this multipath noise is smaller than the two noises at all the frequencies, lower than the oscillator noise at the low frequency and lower than the system noise at the high frequency. Moreover, the simulation assumes some pessimistic situations, i.e. maximum phase variability

by the attitude motion, larger offset value y, and larger reduction factor ε. Therefore, one can expect that the effect of the multipath noise is not significant. This is validated by the gravity estimation simulation results, which shows no significant degradation when comparing with the other error sources.

4.7 PHASE MEASUREMENT SIMULATION

The SST range errors described in the previous sections are applied to the instantaneous range instead of the phase measurements. Their effect on the phase measurement is converted to the effect on the range measurement by using the spectral analysis of the dual one-way ranging system. In order to validate the SST error models, especially the oscillator noise, a set of the SST phase measurements were generated by using the algorithm developed by Key [36]. Using these phase measurements, the dual one-way range was obtained. The instantaneous correction algorithm was applied to convert the dual one-way range into the instantaneous range. This instantaneous range was compared with true instantaneous range that was computed by true satellite states. The difference between these two ranges represents the inter-satellite range error.

Two sets of phase measurements were generated for the K and Ka bands. For each band, two phase measurements were generated for the two satellites. Therefore, four phase measurements were generated for a nominal observation time. Each of the phase measurements contains the reference and received phases,

and the latter represents the phases before the time-of-flight of the phase signals. An iteration method was applied to compute the time-of-flights, which include the geometric range, ionosphere phase advance, and antenna offset [36]. The transmit time becomes the receive time minus the time-of-flight. On each transmit time, the received phase, sum of nominal phase and phase error, was computed. On the receive time the reference phases were generated. The phase measurements were computed by subtracting the received phase from the reference phase and by adding the system noise.

The two phase measurements of each band were added to form a dual one-way phase measurement. And then, the dual one-way range for each band was obtained. These two ranges were combined by using (2.20) to form an ionosphere-free biased-range. The instantaneous range correction of (4.39) was computed using nominal satellite states; accuracy of 50 cm position and 5 cm/s velocity. Then, this observed instantaneous range was compared with the true instantaneous range that was computed from the true states. This difference represents the inter-satellite range measurement error due to the oscillator and system noise.

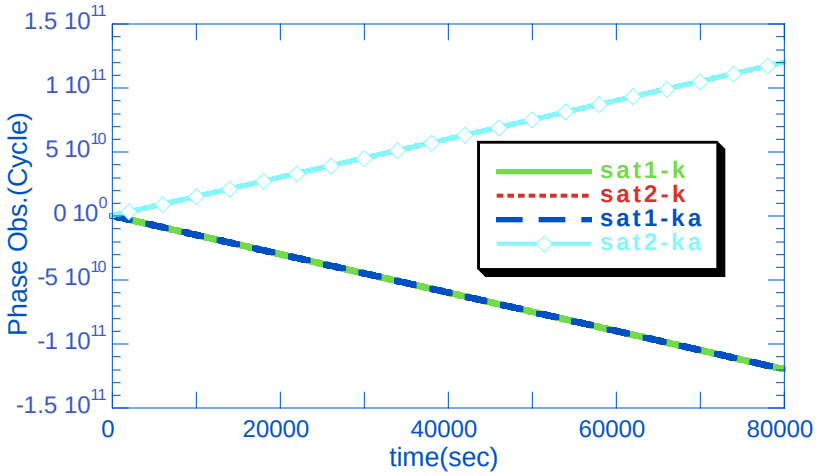

Figure 4.18 Time series of GRACE phase measurements

Figure 4.18 shows the time series of the four phase measurements for the two satellite and two frequency bands. The unit is a cycle. Due to the difference between the reference and the received frequencies, one measurement increases linearly but the other decreases linearly. In case of the actual mission, a phase locked loop will be reset periodically to avoid the overflow of the phase measurements after a long period [23].

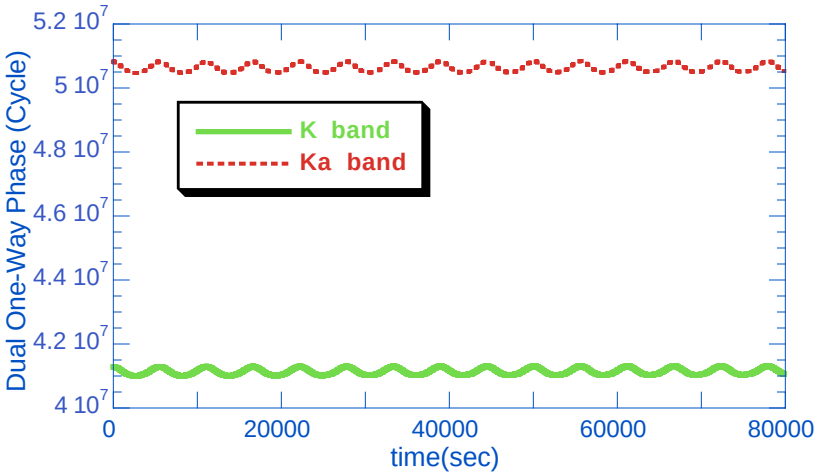

Figure 4.19 Dual one-way phase measurements for K and Ka bands

Figure 4.19 shows the dual one-way phases for the K and Ka bands. They are just the sum of the SST1 and SST2 phase measurements and show strong 1-cpr signals. The difference between the two measurements represents the different phase shifts due to the ionosphere effect. No phase ambiguities were applied to these measurements.

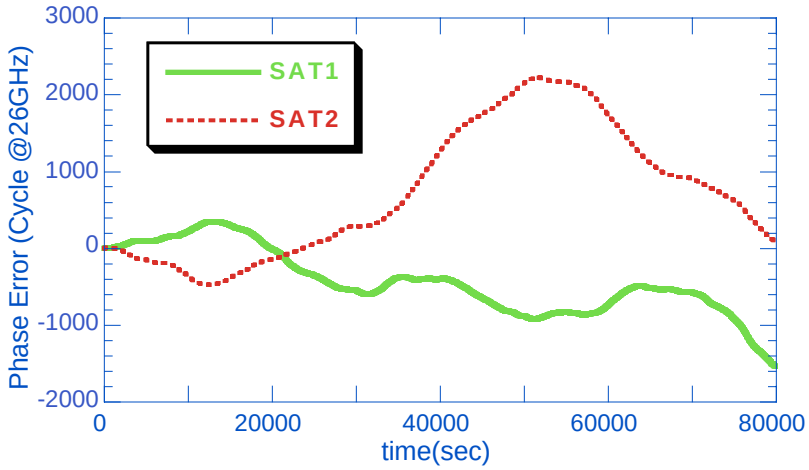

Figure 4.20 Phase error time series of two K band signals

Figure 4.20 shows the phase errors of the two USOs. Both errors are scaled to the carrier frequency (K band) phase errors. Phase errors for the Ka band have the same patterns but the scales are different. Two cases were performed, one with the oscillator noise only and the other with both the oscillator and system noises. Figure 4.20 (and following plots) are the results of the first case. The second case was also compared with the range simulation model and it shows good agreement with the range model.

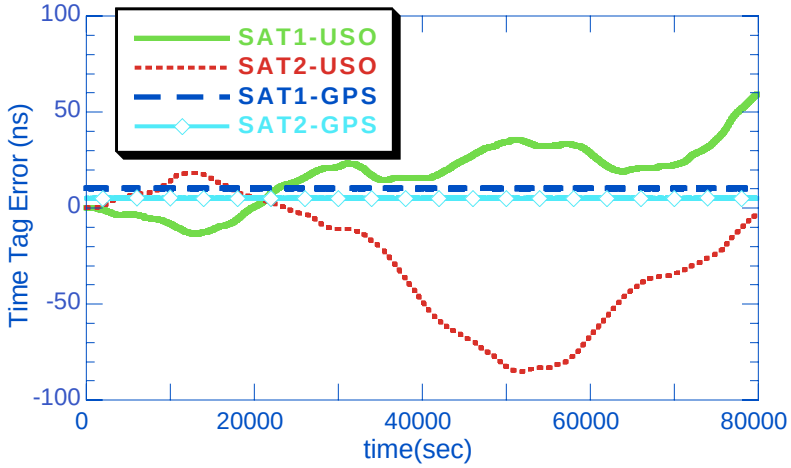

Figure 4.21 Time series of the time tag errors for two time tag cases – GRACE USO time tag and GPS clock solution

Figure 4.21 shows the time-tag errors used in this simulation. As mentioned in Section 4.2.2, the two time-tag approaches were used. The first one is the use of the time-tag assigned by the GRACE onboard USO (called USO time-tag). The second one is the use of the time tag corrections from the GPS clock solution (called GPS time-tag). For the first approach, the time-tag error is related to the phase error by the equation (4.14). For the second approach, 10ns

bias and 30ps white noise variations were applied to the time-tag errors of the SST1. For the SST2, 5ns bias with 30ps variation was applied. The USO time-tag case shows much larger errors.

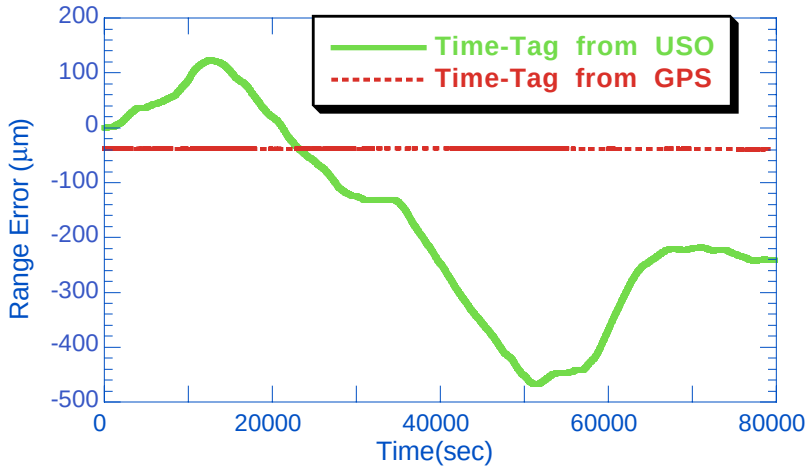

Figure 4.22 Time series of the range error due to the oscillator noise for two time-tag cases

Figure 4.22 shows the time-series of the range errors. The USO time-tag case show much larger variation. In Figure 4.23, the spectrum of these two errors are compared with the spectrum of the range error described in Section 4.2.3, which is comparable to the USO time-tag case.

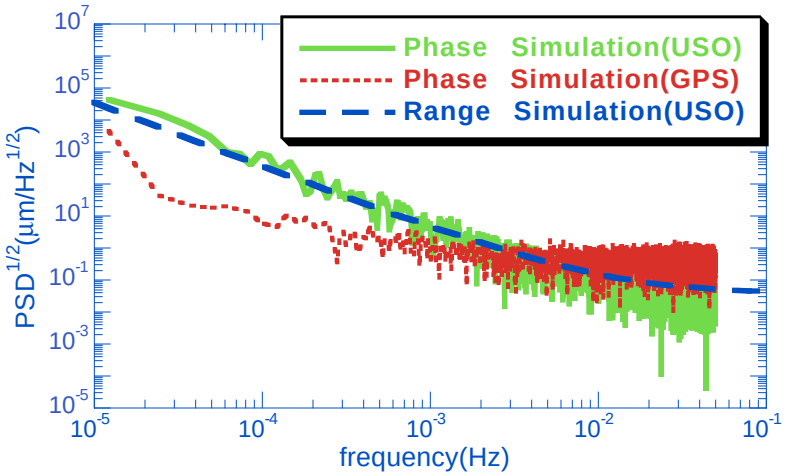

Figure 4.23 Power spectrum of the range error due to the oscillator noise

The phase simulation results very well agree to the range simulation results, and it validates the simulation models used in this study. The GPS time-tag case has a higher error level at the high frequency than the USO time-tag case. However, after the system noise is applied (1μm/√Hz), this difference becomes insignificant.

This phase simulation validates the simulation models on the range error. Therefore, the use of the range error model is sufficient to simulate the noise characteristics of the dual one-way ranging system. By using the range error model, the simulation procedure can be simplified and more effort can be directed to implement the other error sources.

4.8 COMPARISON OF THE SST ERROR SOURCES

The power spectrum of the SST observation error due to the oscillator, system, and multipath error sources are compared. The accelerometer random noise, which is the most dominant accelerometer noise, is also included for comparison. Details on the accelerometer random noise are described in the following chapter. The SST error sources are modeled as the phase or range error and then differentiated for obtaining range-rate and range-acceleration errors. However, the accelerometer noise is modeled as the satellite acceleration and is not able to map into the inter-satellite range and range-rate directly. An analytic transfer function was derived in Appendix A in order to convert a perturbed acceleration into an equivalent range or range-rate perturbation. The transfer function described in Figure A.3 was used to predict the range or range-rate error spectrum due to the accelerometer error. The range-acceleration error is comparable to the acceleration error if the out-of-plane term (second term of (2.26)) is ignored.

Figure 4.24 compares the SST measurement error sources for the range, range-rate, and range-acceleration observables. All the three SST noises are smaller than the accelerometer noise at the low frequency ($< 2\text{mHz} \approx 10$ cpr). Despite of its strong long wavelength signal, the oscillator noise is still smaller than the accelerometer noise. One can expect that the accuracy of the low degree gravity coefficients is mainly affected by the accelerometer noise. At the high frequency, the SST system noise is dominant. As the size of the estimated gravity increases, the SST noise effect becomes more significant.

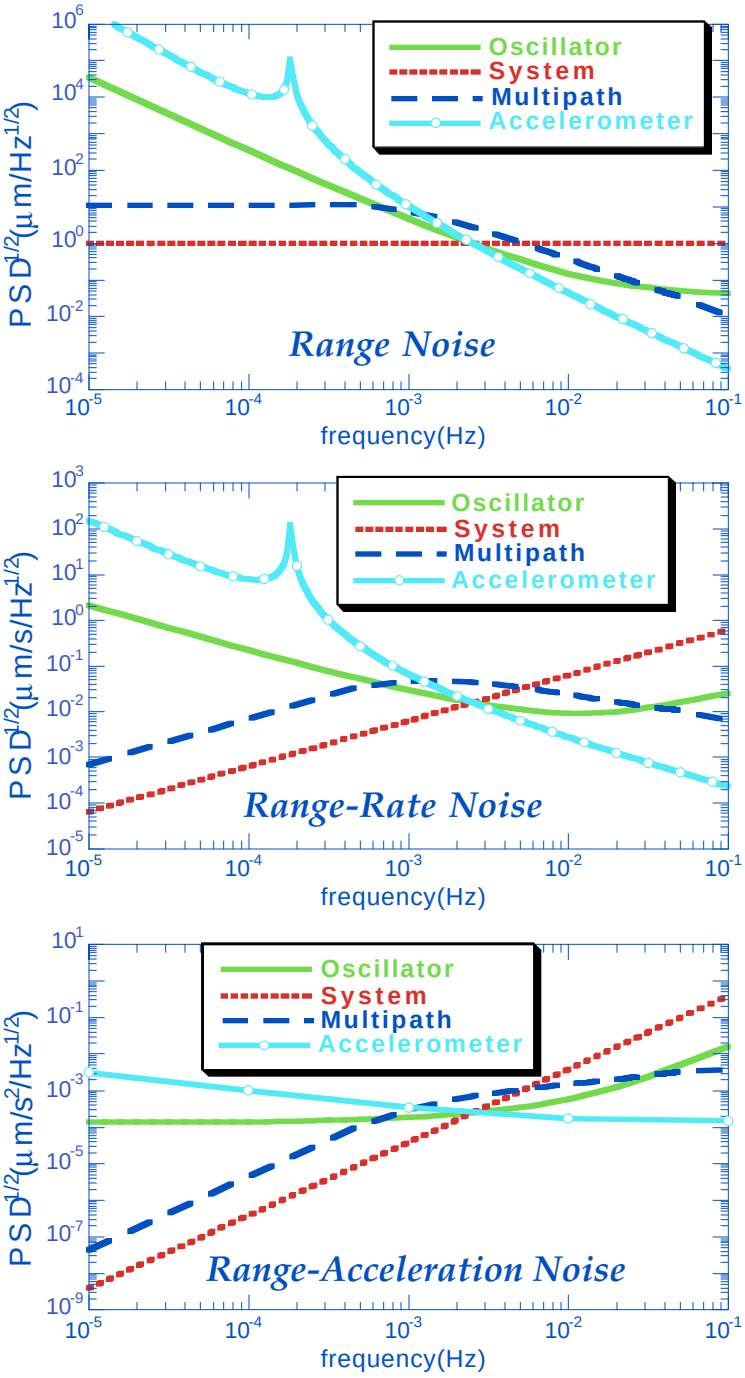

Figure 4.24 Comparison of the SST measurement error sources for the range, range-rate, and range-acceleration observables

To compare the effect of individual SST measurement noise component on the gravity recovery, each error source was applied separately without any other noises. Three error sources, oscillator drift, system, and multipath noises were applied, and a (50×50) gravity field was estimated by using 7 day measurements.

Table 4.4 Comparison of range-rate error sources

Noise Type	Pre-fit RMS	Post-fit RMS	Cumulative Geoid Error
Oscillator	*0.031 μm/s*	*0.018 μm/s*	*0.011 cm*
System	*0.045 μm/s*	*0.045 μm/s*	*0.010 cm*
Multipath	*0.009 μm/s*	*0.008 μm/s*	*0.015 cm*

Table 4.4 shows the range-rate residual RMS and the cumulative geoid error due to each error source. The pre-fit RMS values are the original noise levels. The post-fit RMS values are computed by removing low-low biases from the residual, Since the low-low bias and bias-rate remove very low frequency signal, i.e. below 1 cpr, the RMS value represents the power of the high frequency signal. The details on the low-low bias parameterizations are described in Chapter 3. The oscillator drift noise shows a significant difference between the pre-fit and post-fit RMS values since its strong low frequency signal is effectively removed by the low-low biases. The system noise has a higher value than the oscillator

noise because of its dominant high frequency characteristics, i.e. the system noise increases linearly as frequency increases. Since the low-low bias adjustments were applied for the low frequency only, the high frequency noise level was not reduced and it yields the higher RMS.

The cumulative geoid errors, which are the sum of degree difference variances multiplied by the Earth radius, were computed up to degree 50. The multipath noise has the highest error. It is mainly because of its higher range-rate error level around the 20-cpr (3×10^{-3}Hz) frequency as shown in Figure 4.24. Therefore, the effect of the multipath noise would be significant only for a small size of gravity estimation and can be negligible for larger gravity estimation. The oscillator and system noises yielded the same level of errors. These results are not consistent with the post-fit RMS levels, where the system noise has the higher value. This is due to the fact that the high frequency part of the system noise, which did not affect the (50×50) gravity solution significantly, was counted in computing the RMS value. The system noise would be dominant as the degree and order of the estimated gravity field increases.

5 ACCELEROMETER MEASUREMENT ERRORS

5.1 INTRODUCTION

The GRACE satellites will use three-axis accelerometers, located at the mass center of each satellite, to eliminate the effects of the non-gravitational forces. Each instrument is a servo controlled electrostatic accelerometer, which measures the electrostatic force necessary to maintain the accelerometer proof-mass motionless with respect to the sensor cage. The proof-mass motion comes from the fact that the gravitational forces affect both the cage and the proof-mass, but the non-gravitational forces, e.g. drag, affect the cage only. The GRACE satellites will use the SuperSTAR accelerometer developed by the French space agency CNES [19]. It is a modified version of the previously flown ASTRE high precision accelerometer and shown in Figure 5.1 [17].

The accelerometer measurements will not contain just the surface force effects since they contain various other error sources, e.g. scale factor, bias, misalignment, attitude and so on. Therefore, it is necessary to analyze how these error sources will degrade the accelerometer measurements and the estimation of the orbit and gravity solutions. The following sections depict the generation and processing of the simulated accelerometer measurements. The numerical simulation results with independent error sources are compared as well.

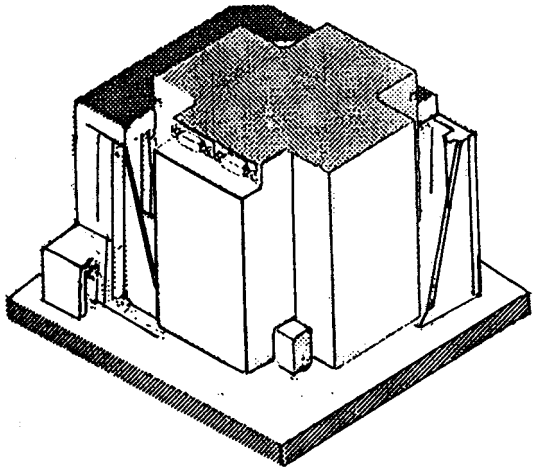

Figure 5.1 Illustration of the SuperSTAR accelerometer [17]

5.2 SIMULATION PROCEDURE

5.2.1 Measurement Models

The accelerometer measurement is the sum of the non-gravitational accelerations, including atmospheric drag, solar radiation pressure, earth radiation pressure, and so on. However, it is corrupted by unknown scale factors, biases, random noise, and so on. The measurement model may be given by

$$\boldsymbol{f}^{obs} = M\boldsymbol{f}^{acc} + \boldsymbol{b} + \boldsymbol{S} \tag{5.1}$$

where

$\boldsymbol{f}^{obs}$ = *accelerometer output*

$\boldsymbol{f}^{acc}$ = *true non-gravitational acceleration expressed in*

the accelerometer coordinates

M = *scale factor matrix*

$$= \begin{bmatrix} M_{11} & M_{12} & M_{13} \\ M_{21} & M_{22} & M_{23} \\ M_{31} & M_{32} & M_{33} \end{bmatrix}$$

$\boldsymbol{b}$ = *bias vector*

$$= \begin{bmatrix} b_1 & b_2 & b_3 \end{bmatrix}^T$$

$\boldsymbol{S}$ = *random noise vector*

The scale factor matrix M multiplies the true acceleration $\boldsymbol{f}^{obs}$. Ideally, M should be an identity matrix, but it has non-unit diagonal elements with non-zero off-diagonal terms due to the influence of acceleration along any one axis on the output for other axis. The diagonal elements change the magnitude of the true acceleration components, and the off-diagonal elements reflect cross-talk among three axis, which come from non-orthogonality of the alignment of the three axes. In this study, the cross-talk terms were ignored, so that the scale factor matrix could be assumed to have diagonal elements only. The bias term $\boldsymbol{b}$ has constant values and it is distinguished from the random noise, which has a frequency dependent characteristic. Also there may be higher order terms of $\boldsymbol{f}$, but those terms were ignored in this study since the simulation results with the quadratic term did not show significant degradation of the gravity solution [58]. It should be noted that the important thing is not the size of these scale factors and biases, but the accuracy of their estimates.

The accelerations $\boldsymbol{f}^{obs}$ and $\boldsymbol{f}^{acc}$ are expressed in the accelerometer coordinates, not in the inertial coordinates which are used for orbit processing. Therefore, some coordinate transforms are necessary to process the accelerometer outputs, and it causes another type of error. For this error aspect, it is essential to define the coordinate system properly. The following coordinate systems, illustrated in Figure 5.2, are defined for the GRACE satellite system [19].

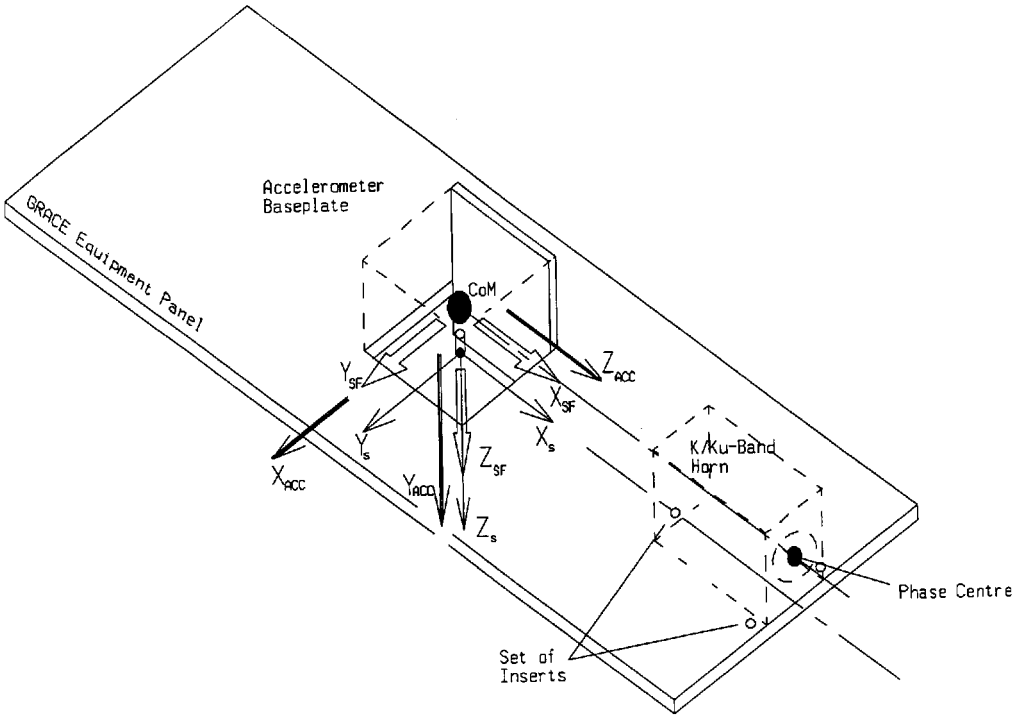

Figure 5.2 GRACE satellite coordinate systems [19]

(x_S, y_S, z_S) are the satellite coordinates defining location and coordinates of satellite hardware, and $(x_{acc}, y_{acc}, z_{acc})$ are the accelerometer coordinates centered at the target center-of-mass (CM). (x_{SF}, y_{SF}, z_{SF}) are the ideal satellite frame

centered at the accelerometer proof-mass and used for the primary satellite frame in this study. Depending on whether the GRACE satellite is the leading one (SST1) or the trailing one (SST2), the direction of the orbital reference coordinates is changed. The transverse direction becomes $-x_{SF}$ for the leading satellite and $+x_{SF}$ for the trailing satellite. Another important thing is the definition of the accelerometer axes. Due to ground test limitations, one of the accelerometer axes has less accuracy than two other axes. That axis is referred to as the less sensitive axis and labeled x_{acc}. After some numerical simulations, y_{SF} or the out-of-plane (or normal) direction was chosen for the less sensitive axis. The details on those simulations are described in Section 5.4.1.

Due to the misalignment in installing the accelerometer in the spacecraft, the accelerometer coordinates $(x_{acc}, y_{acc}, z_{acc})$ do not coincide with the spacecraft coordinates (x_{SF}, y_{SF}, z_{SF}) perfectly. The accelerometer error due to this misalignment is called misalignment error.

Another type of measurement error, called attitude measurement error, results from the uncertainty between the satellite coordinates and the inertial coordinates. It is noted that this is related not to the attitude control error but to the accuracy of attitude determination. Two star cameras determine the rotation matrix between these two coordinates, but those measurements contain some errors. These errors corrupt the transformation matrix between the spacecraft coordinates (x_{SF}, y_{SF}, z_{SF}) and the inertial coordinates (e.g. J2000).

5.2.2 Accelerometer Measurement Generation

Two kinds of measurements were generated with the truth models, one was the accelerometer measurement and the other was the rotation matrix from the inertial coordinates to the satellite coordinates. This section describes how the measurement errors are applied to those simulated measurements.

The satellites' trajectories were integrated using the truth models for the gravitational and non-gravitational forces. The non-gravitational accelerations were computed along the true trajectory, which are expressed in the inertial coordinates (*J2000* frame). Then those inertial accelerations were transformed into the accelerations expressed in the satellite coordinates, also called the SF accelerations:

$$\boldsymbol{f}^{SF} = R_{I\to S}^{true}\boldsymbol{f}^{I} \tag{5.2}$$

where $\boldsymbol{f}^{I}$ and $\boldsymbol{f}^{SF}$ are the accelerations expressed in the inertial and satellite coordinates, respectively. The subscript *I* represents the inertial coordinate system and *S* does the satellite coordinate system. The true transformation matrix (without attitude measurement errors) was used for this transformation.

Transforming these SF accelerations into the ACC accelerations that are expressed in the accelerometer coordinates was affected by the misalignment error. Since the rotation angles were assumed small, the transformation was realized by multiplying the SF accelerations by a small angle rotation matrix $R_{S\to A}^{err}$ [25]:

$$\boldsymbol{f}^{acc} = R_{S\to A}^{err}\boldsymbol{f}^{SF} = \begin{bmatrix} 1 & \varepsilon_3 & -\varepsilon_2 \\ -\varepsilon_3 & 1 & \varepsilon_1 \\ \varepsilon_2 & -\varepsilon_1 & 1 \end{bmatrix}\boldsymbol{f}^{SF} \tag{5.3}$$

where $(\varepsilon_1, \varepsilon_2.\varepsilon_3)$ represent the small angular rotation vector components. This transform is independent of the order of rotation. The misalignment error is caused by this rotation matrix error. The uncertainty of this misalignment may be as much as *0.3 mrad*. Since the accelerometer error from this transformation error is the multiplication of the accelerometer input and the rotation matrix, its magnitude is proportional to that of the accelerometer input, i.e. non-gravitational acceleration.

After being transformed from the SF accelerations, the ACC accelerations were multiplied by the scale factor matrix and then the biases and the random noise were added:

Accelerometer Obs.: $$\boldsymbol{f}^{obs} = M\left(R_{S\to A}^{err}R_{I\to S}^{true}\boldsymbol{f}^{I}\right) + \boldsymbol{b} + \boldsymbol{S} \tag{5.4}$$

This quantity was used as the accelerometer output and was assumed to be comparable to the measurements made during the actual mission.

The attitude measurement error is associated with the rotation matrices from the inertial coordinates to the satellite coordinates, which are measured by the star cameras. The requirements for the star camera are the 1σ value of 30 μrad for the single axis accuracy at orbital rate, relative to the star camera line-of-sight (LOS) and 240 μrad for the LOS axis [19]. The maximum update rate is 2 Hz. These errors may be assumed as the white noise. Since the star camera axes are

tilted 45° from the satellite $-z_{SF}$ axis in the $y_{SF} - z_{SF}$ plane, a transformation is required to convert the uncertainty level of the attitude measurements in the star camera coordinates into the uncertainty in the satellite coordinates [21]. The satellite axes $\boldsymbol{r}_{SF} = \left(x_{SF}, y_{SF}, z_{SF}\right)$ may be converted into the *i-th* star camera axes $\boldsymbol{r}_{SCF_i} = \left(x_{SCF_i}, y_{SCF_i}, z_{SCF_i}\right)$ using the transformation matrix $R_{S\to C}$:

$$\boldsymbol{r}_{SCF_i} = R_{S\to C}\boldsymbol{r}_{SF} \tag{5.5}$$

where

$$R_{S\to C} = \begin{bmatrix} 1 & 0 & 0 \\ 0 & \cos\theta & \sin\theta \\ 0 & -\sin\theta & \cos\theta \end{bmatrix} \qquad \theta = \begin{Bmatrix} 180^o + 45^o \ for\ i = 1 \\ 180^o - 45^o \ for\ i = 2 \end{Bmatrix}$$

The y_{SCF_i} represents the star camera LOS axis component. The covariance along the star camera axes, P_{SCF_i}, can be transformed into the covariance along the satellite axes, P_{SF}, as follows

$$P_{SF} = R_{S\to C}^{T} P_{SCF_i} R_{S\to C} \tag{5.6}$$

The actual variance is the sum of two variances from the 1st and 2nd star cameras. The standard deviations of these errors are 0.2 mrad, 0.04 mrad, and 0.2 mrad along the radial, transverse, and normal axes, respectively. Because of its high sampling rate of 2Hz (0.5s), the standard deviations for the 0.1Hz (10s) sampling rate have the lower values of 0.05 mrad, 0.009 mrad, and 0.05 mrad. As for the

misalignment error, the small angle rotation matrix was used to apply this transformation error to the rotation matrix $R_{I\to S}$:

$$\text{Attitude Obs.:} \qquad R_{I\to S}^{obs} = R_{I\to S}^{err} R_{I\to S}^{true} = \begin{bmatrix} 1 & \varepsilon_3 & -\varepsilon_2 \\ -\varepsilon_3 & 1 & \varepsilon_1 \\ \varepsilon_2 & -\varepsilon_1 & 1 \end{bmatrix} R_{I\to S}^{true} \tag{5.7}$$

The flow chart of the generation procedure is presented in Figure 5.3. This procedure describes how the two simulated measurements of (5.4) and (5.7) are generated.

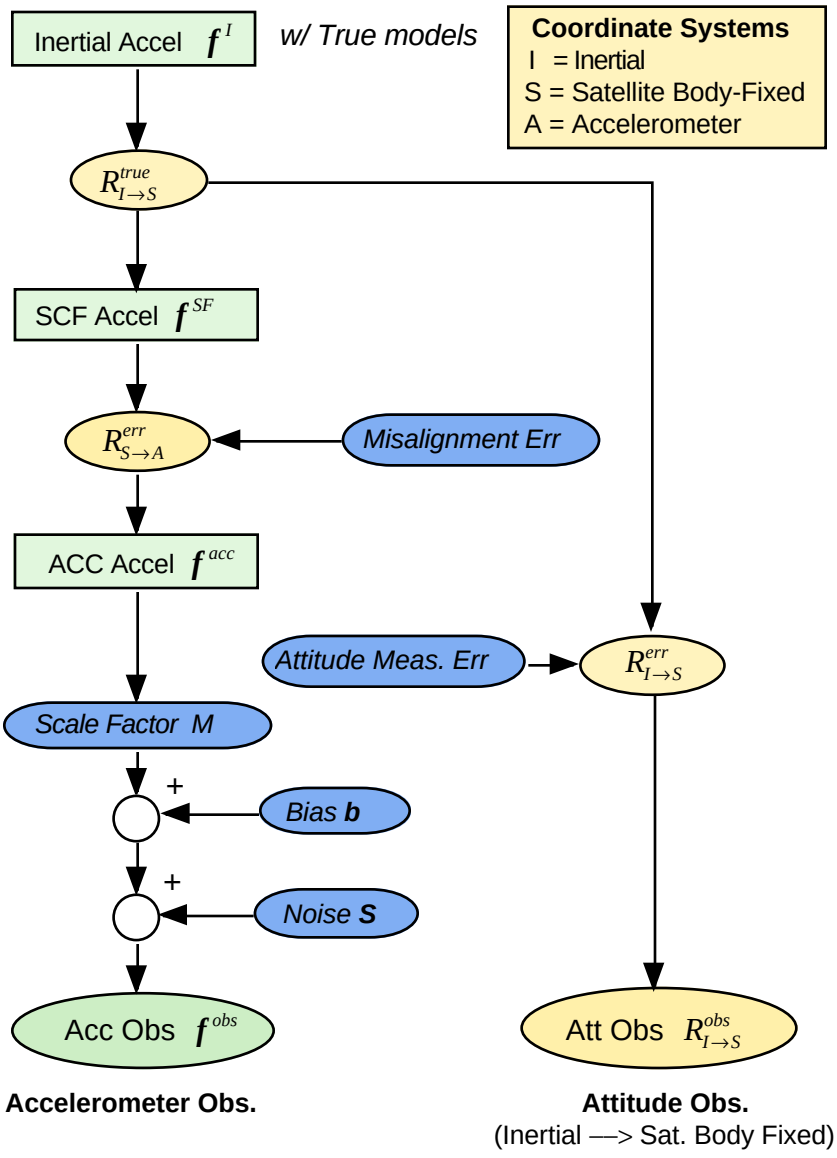

Figure 5.3 Generation procedure of the simulated accelerometer observations

5.2.3 Accelerometer Measurement Processing

When computing the nominal trajectory, the accelerometer measurements are used for the non-gravitational acceleration information in place of the nominal non-gravitational models, which include the atmospheric drag model, radiation pressure models, and so on. However, these measurements contain the errors as described in the previous section. Among those error sources, the scale factors and biases vary slowly enough to be estimated during the data processing activity.

The nominal accelerometer observation $\boldsymbol{f}^{acc}$ is obtained from the noisy observation $\boldsymbol{f}^{obs}$, which is the simulated or real accelerometer measurement, by using the nominal scale factors and biases:

$$\boldsymbol{f}^{acc} = M_c^{-1}\boldsymbol{f}^{obs} - M_c^{-1}\boldsymbol{b}_c \tag{5.8}$$

where M_c and $\boldsymbol{b}_c$ are the nominal scale factors and biases, respectively, and should be distinguished from the true scale factors and biases in (5.1). This nominal accelerometer observation $\boldsymbol{f}^{acc}$ is the acceleration expressed in the accelerometer coordinates, and it must be transformed to the inertial acceleration $\boldsymbol{f}^{I}$ for numerical integration:

$$\boldsymbol{f}^{I} = R_{S\to I}^{obs}\boldsymbol{f}^{acc} \tag{5.9}$$

Since the misalignment between the accelerometer and satellite coordinates is unknown, the accelerometer coordinates are assumed to be coincident with the satellite coordinates. The inverse of the star camera observation $R_{I\to S}^{obs}$ of (5.7) is used for the transformation. Substitution of (5.8) into (5.9) relates the noisy

observation $\boldsymbol{f}^{obs}$ to the nominal inertial acceleration $\boldsymbol{f}^{I}$ that is used to compute the nominal trajectory as follows

$$\boldsymbol{f}^{I} = R_{S\to I}^{obs}\left(\tilde{M}\boldsymbol{f}^{obs} + \tilde{\boldsymbol{b}}\right) \tag{5.10}$$

where

$\boldsymbol{f}^{I}$ = *nominal non-gravitational acceleration expressed in the inertial coordinates*

$\boldsymbol{f}^{obs}$ = *accelerometer measurement vector*

$\tilde{M}$ = *inverse scale factor matrix*

$$= \begin{bmatrix} \tilde{M}_{11} & 0 & 0 \\ 0 & \tilde{M}_{22} & 0 \\ 0 & 0 & \tilde{M}_{33} \end{bmatrix} = \begin{bmatrix} 1/M_{c11} & 0 & 0 \\ 0 & 1/M_{c22} & 0 \\ 0 & 0 & 1/M_{c33} \end{bmatrix}$$

$\tilde{\boldsymbol{b}}$ = *inverse bias vector*

$$= \begin{bmatrix} \tilde{b}_1 \\ \tilde{b}_2 \\ \tilde{b}_3 \end{bmatrix} = -\tilde{M}\begin{bmatrix} b_{c1} \\ b_{c2} \\ b_{c3} \end{bmatrix} = \begin{bmatrix} -b_{c1}/M_{c11} \\ -b_{c2}/M_{c22} \\ -b_{c3}/M_{c33} \end{bmatrix}$$

$R_{S\to I}^{obs}$ = *rotation matrix from the satellite body-fixed coordinates to the inertial coordinates*

$$= \begin{bmatrix} R_{11} & R_{12} & R_{13} \\ R_{21} & R_{22} & R_{23} \\ R_{31} & R_{32} & R_{33} \end{bmatrix}_{S\to I}^{obs}$$

The actual estimated parameters were the inverse scale factors $\tilde{M}$ and the inverse biases $\tilde{\boldsymbol{b}}$ instead of the scale factors M and biases $\boldsymbol{b}$ in (5.1). It makes the estimates, e.g. inverse scale factors and biases, be linear with respect to the observation $\boldsymbol{f}^{obs}$. These inverse scale factors and biases are updated through the numerical iterations to be close to the true values. The flow chart of this estimation procedure is presented in Figure 5.4.

The accelerometer measurements were related to the inverse scale factors and the inverse biases by the partial derivatives of the accelerations with respect to the dynamic parameters as

$$\frac{\partial \boldsymbol{f}^{I}}{\partial \tilde{M}_{ii}} = \begin{bmatrix} R_{1i} \\ R_{2i} \\ R_{3i} \end{bmatrix}_{S\to I}^{obs} f_i^{obs} \tag{5.11}$$

$$\frac{\partial \boldsymbol{f}^{I}}{\partial \tilde{b}_{ii}} = \begin{bmatrix} R_{1i} \\ R_{2i} \\ R_{3i} \end{bmatrix}_{S\to I}^{obs} \qquad i = 1,2,3 \tag{5.12}$$

where

$\begin{bmatrix} R_{1i} \\ R_{2i} \\ R_{3i} \end{bmatrix}_{S\to I}^{obs}$ = *i-th* column vector of the rotation matrix $R_{S\to I}^{obs}$

f_i^{obs} = *i-th* element of the accelerometer output vector $\boldsymbol{f}^{obs}$

Since neither the GPS measurement equations nor the SST range/range-rate measurement equations contain the acceleration terms explicitly, the

accelerometer parameters are treated as the dynamic parameters, rather than the kinematic parameters [8,58]. The difference between the two parameter types is described in Chapter 2. The $\tilde{H}$ matrix elements, which correspond to the accelerometer estimation parameters, have zero values:

$$\frac{\partial Obs}{\partial \tilde{M}_{ii}} = \frac{\partial Obs}{\partial \tilde{b}_i} = 0 \qquad Obs = \begin{cases} GPS\ DD \\ SST\ range / range\text{-}rate \end{cases} \tag{5.13}$$

However, the corresponding H matrix elements have non-zero values since those estimation parameters are mapped by the non-zero state-transition matrix as is the characteristics of the dynamic parameters.

At initiation of the orbit adjustment process, the nominal values for the inverse scale factors and biases were set to *1* and *0*, respectively. Through iterations, the nominal values were updated and converged to the truth values.

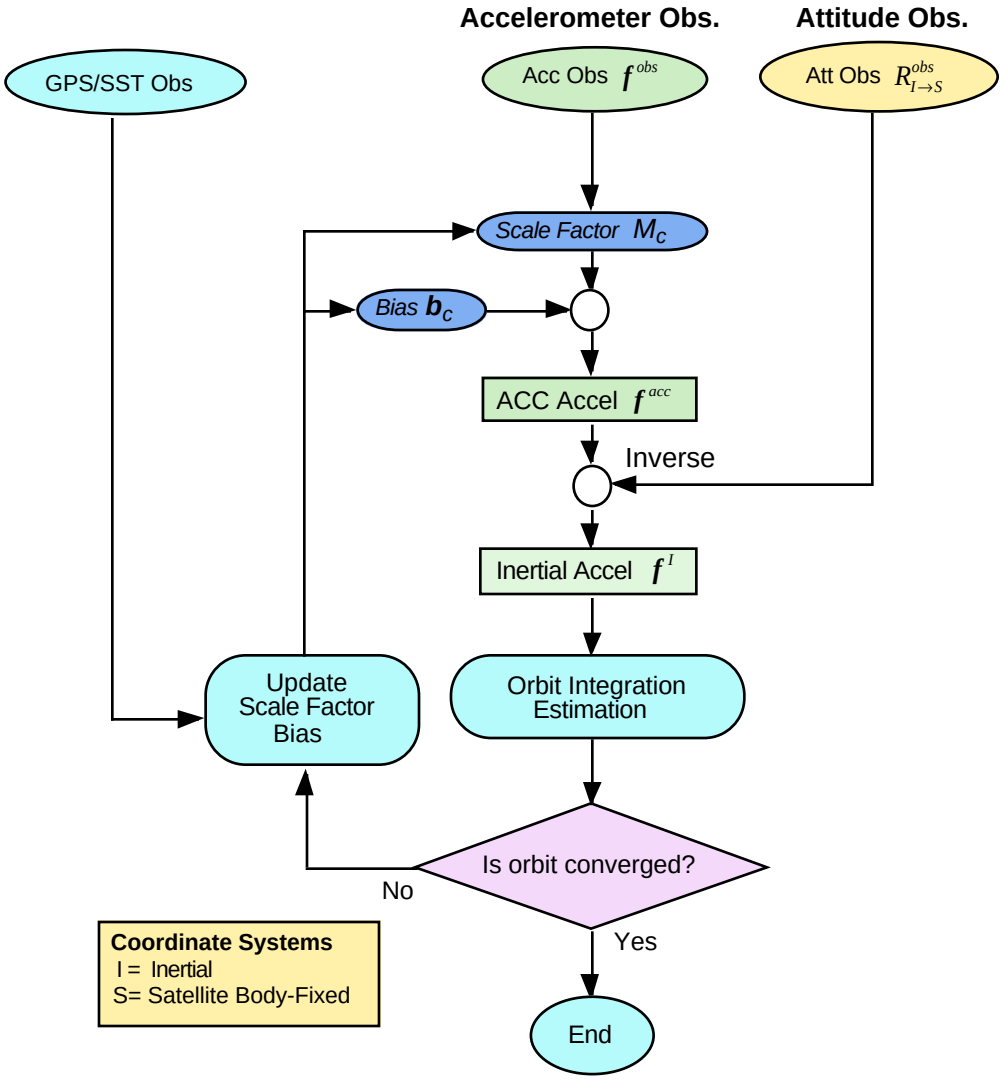

Figure 5.4 Estimation procedure of the accelerometer scale factors and biases

5.3 SIMULATION RESULTS

To determine how each accelerometer error source affects the estimate of the gravity field parameters as well as the scale factors and biases, each error source was applied separately. Those included random noise, attitude measurement error, and misalignment error.

Table 5.1 Simulation parameters of the accelerometer errors

Random Noise (PSD$^{1/2}$)	*$(1+0.005/f)^{1/2}\times10^{-10}$ m/s^2/Hz$^{1/2}$ (R,T)* *$(1+0.1/f)^{1/2}\times10^{-9}$ m/s^2/Hz$^{1/2}$ (N)*
Attitude Meas. Error	*White Noise σ = 0.009 mrad(Roll)* *σ = 0.05 mrad (Yaw, Pitch)*
Misalignment Error	*Constant 0.3 mrad*

Table 5.1 describes the accelerometer error sources used in this study. Among the three accelerometer axes, the normal axis was selected for the less sensitive axis, which has a higher noise level than other axes. Details are depicted in Section 5.4.1. The attitude measurement error results from the uncertainty of the spacecraft body-fixed coordinate estimation with respect to the inertial coordinates. These errors are mainly determined by the star camera with the standard deviation of σ = *0.05 mrad* for yaw and pitch motion and σ = *0.009 mrad* for roll motion. Equation (5.7) represents this error, and the white noise variation was assumed for each infinitesimal angle error $(\varepsilon_1, \varepsilon_2. \varepsilon_3)$. The

alignment error represents the uncertainty in the alignment of the spacecraft axes and the accelerometer axes. The values of *0.3 mrad* were applied for $(\varepsilon_1, \varepsilon_2. \varepsilon_3)$ in (5.3), and remained as constants through all data spans. The expected time variability, which may be less than *0.1 mrad*, was not applied in this study.

Both the attitude and misalignment errors affect the accelerometer measurement through interference from the other axis components. Therefore, their magnitudes are dependent on the magnitude of the accelerometer measurements, e.g. the non-gravitational accelerations. These errors grow as the non-gravitational accelerations are increased. In other words, these errors are more significant for lower altitude orbits where larger atmospheric drag is present. Figures 5.5 and 5.6 represent the magnitude of the individual accelerometer errors at the altitude of 300km and 450km, respectively. The misalignment error is significant at the 300km, but is negligible at the 450km.

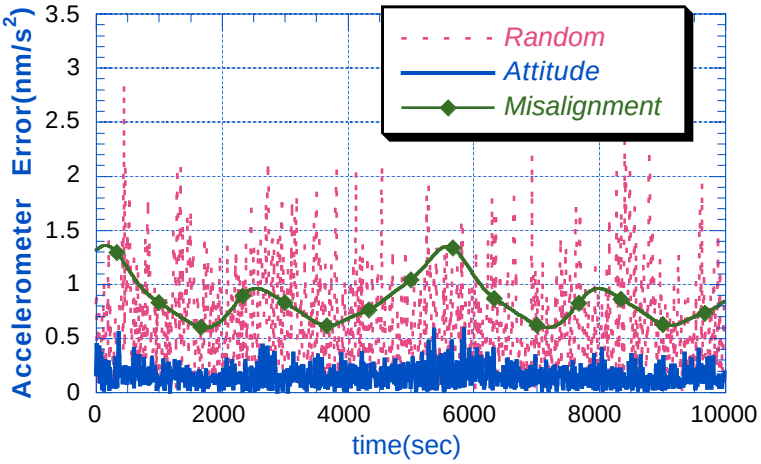

Figure 5.5 Magnitude of individual accelerometer errors at 300km altitude

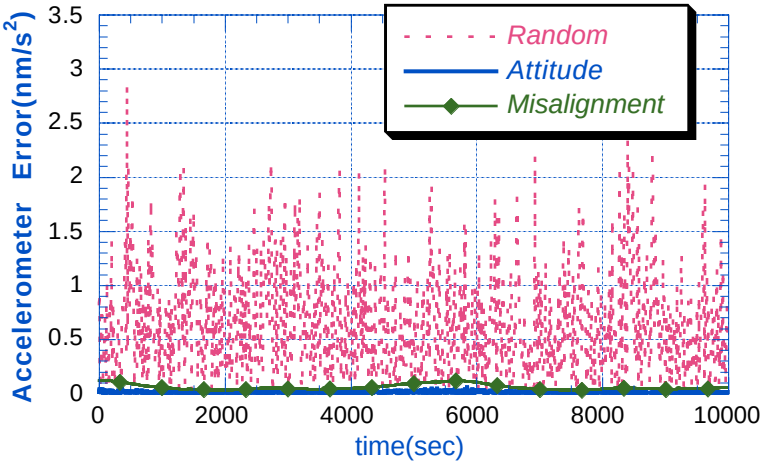

Figure 5.6 Magnitude of individual accelerometer errors at 450km altitude

In addition to the magnitude, these errors have the same frequency characteristics as the drag acceleration, i.e. large 1 and 2 cpr (cycle-per-revolution) signals. Figures 5.7 and 5.8 represent the power spectral density of the individual accelerometer errors at the altitude of 300km and 450km, respectively. In the case of the attitude measurement error, the angle errors were assumed to be white noise rather than constants, and those strong tone signals were alleviated by multiplication of the white noise. However, the misalignment error, which was made by multiplication of the acceleration by constant values, retains a large 1 and 2 cpr signals. Its tone signals are greater than the random noise at the 300km altitude. Unlike the 1-cpr noise, which can be effectively removed by applying empirical parameters, the 2-cpr noise may degrade the estimation of the J_2 coefficient significantly.

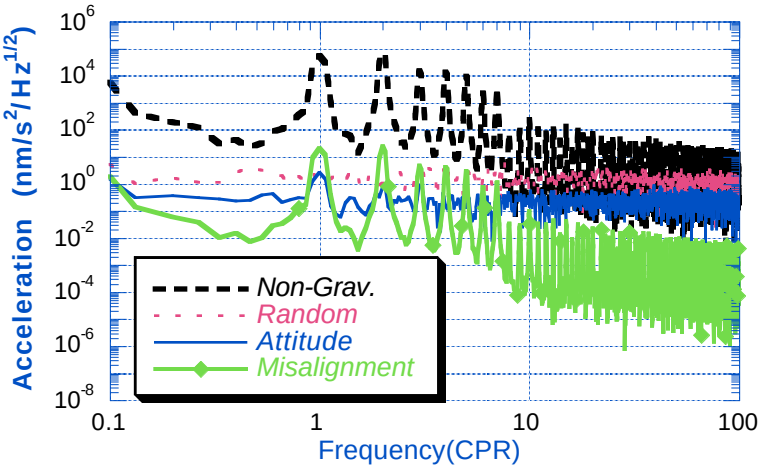

Figure 5.7 Power spectral density of individual accelerometer errors at 300km altitude

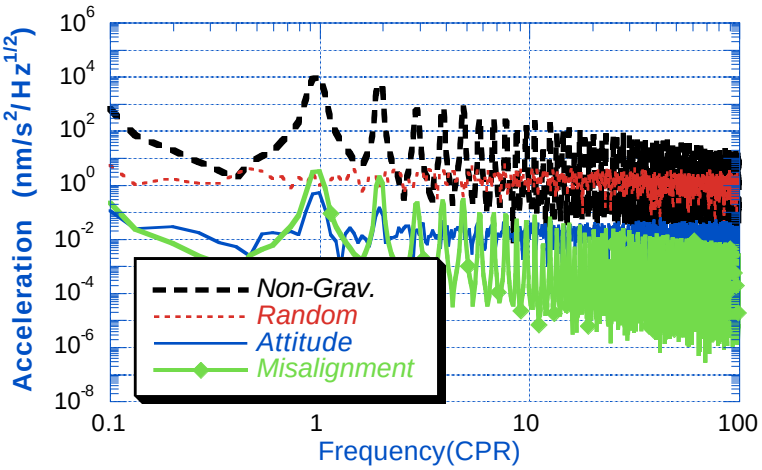

Figure 5.8 Power spectral density of individual accelerometer errors at 450km altitude

To maximize the accelerometer errors, a lower altitude of 300 km, was used for the simulations in this section. The separation angle was 2° and a (50×50) gravity field was estimated using a 7 day measurement interval. No other errors except the accelerometer errors were applied. Initial scale factor and bias were 1.0 and 0, respectively.

Another consideration is the effect of solar radiation pressure. With atmospheric drag only, the non-gravitational acceleration is acting along the transverse direction, and it causes a singularity problem in estimating the radial and normal scale factors and biases. More important is the radial component since the radial motion is coupled with the transverse motion that is a major part of the SST signals. In addition, the normal acceleration can be enhanced by horizontal wind. One of the ways to enhance the radial acceleration is to include the radiation pressure models. It is significant to note that the solar radiation pressure varies as a function of β', which is the angle between the orbit plane and the geocentric direction to the Sun [15]. To maximize the radial acceleration, the initial orbit condition with $\beta' = 0°$ was used. The smaller radial acceleration case with $\beta' = 63°$ was also tried, but the gravity solution was two times worse for this case than for the $\beta' = 0°$ case. In case of the actual mission, β' is changing as the orbit plane is moving, and it can not be fixed or selected. Some data span periods will have a lower β' angle to yield an accurate scale factor and bias estimate. However, some periods will have a higher β' angle to yield less accurate estimates. The scale factors and biases estimated during the lower β' angle periods can be used as the nominal values during the high β' angle periods.

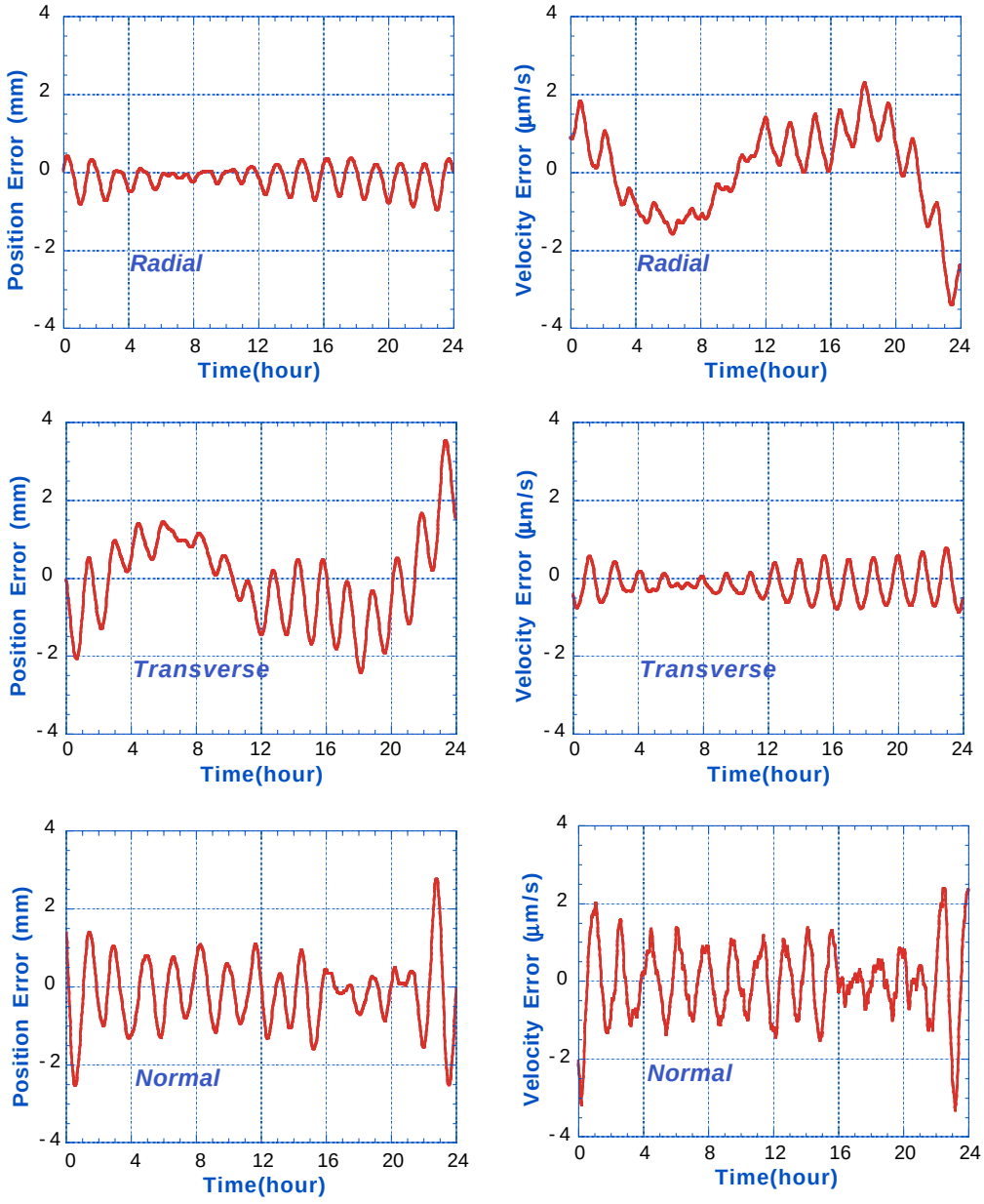

Figure 5.9 Time series of position and velocity errors due to the accelerometer noise

To analyze the effect of the accelerometer error on orbit estimation, the satellite orbit error due to individual accelerometer error sources are analyzed. Only the time series and amplitude spectrum plots of the all accelerometer noise case, e.g., random, attitude, and misalignment errors with initial scale factor and bias offsets are presented. Figure 5.9 shows the time series of position and velocity errors due to all the accelerometer error sources. The gravity error is not included with the same truth gravity field as the nominal one. Dominant signals are 1-cpr signals in all the cases. The RMS of the position errors are 0.3 mm, 1.1 mm, and 0.9 mm for the radial, transverse, and normal directions, respectively. The transverse direction has the largest position error. In the case of the velocity errors, the radial, transverse, and normal components are 1.1 μm/s, 0.4 μm/s, and 1.0 μm/s, respectively. Unlike the position error, the transverse velocity error is relatively lower than the others are. There exists a similarity between the radial position and the transverse velocity errors, or the transverse position and the radial velocity errors. This similarity corresponds to the relationship between the radial velocity and the transverse position in the second term of (A.1), which describes Hill's equation. The normal direction behavior can be predicted by the third equation. The phase of the normal position is shifted from the velocity components by 90°. The position and velocity error time series due to the individual error components are also plotted and compared with a reference, e.g. no errors and the all error results. However, it is hard to distinguish the difference among those errors due to their strong 1-cpr components.

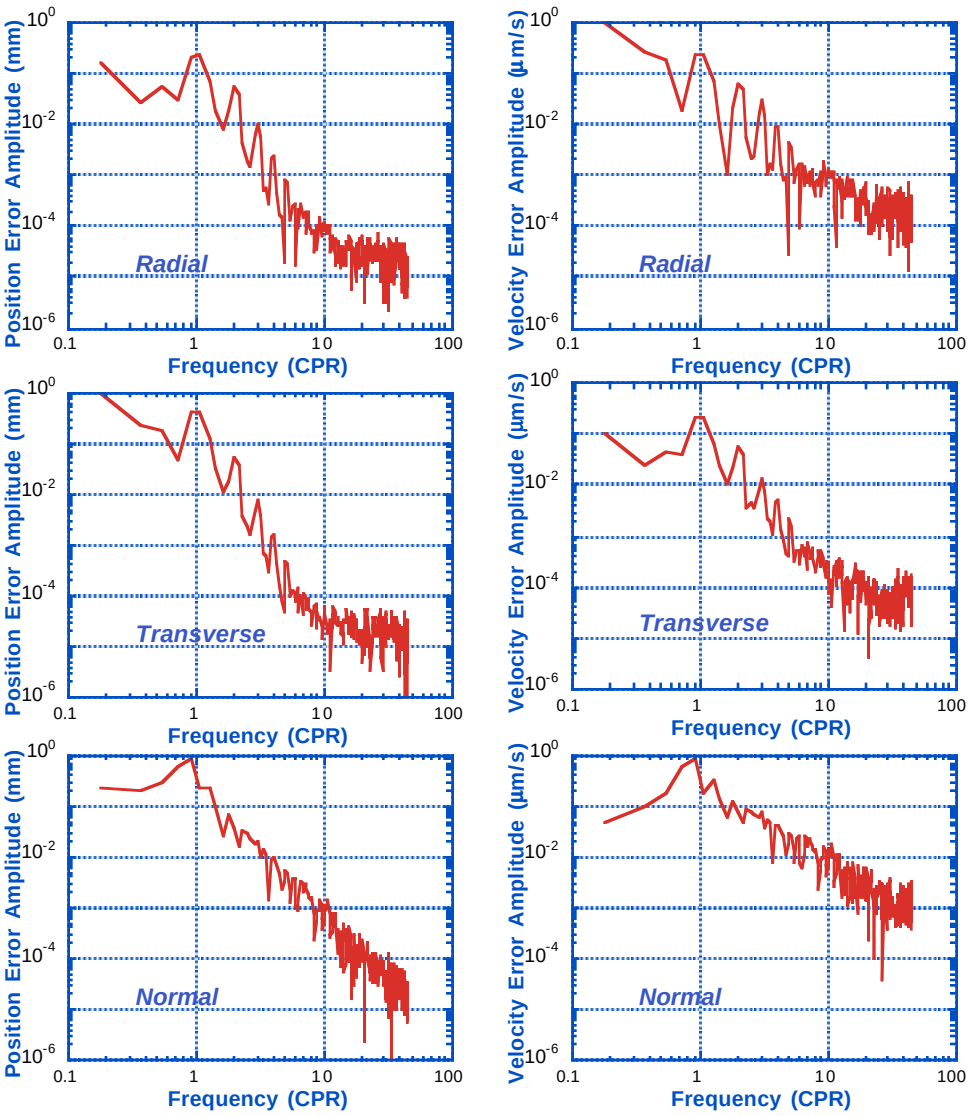

Figure 5.10 Amplitude spectrum of position and velocity errors due to the accelerometer noise

The amplitude power spectrum of the orbit error due to each accelerometer error component is plotted and compared with each other. The position and velocity error amplitudes for the all error case are shown in Figure 5.10. The radial and transverse components, both position and velocity, have strong tone signals, i.e. *N*-cpr signals. These tone signals mainly result from the misalignment error that has a similar frequency as the atmospheric drag. The normal direction errors are higher than the others in high frequency region and this corresponds to the fact that the accelerometer less-sensitive axis is aligned with the normal direction.

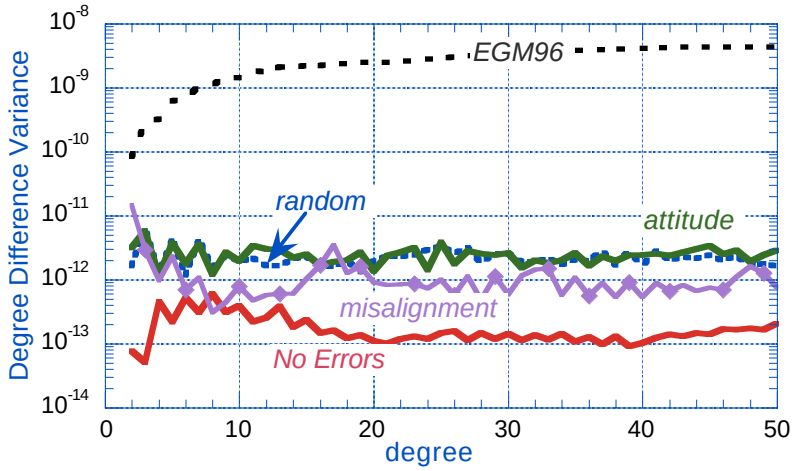

Figure 5.11 Degree difference variances due to various accelerometer error sources

Figure 5.11 shows the degree difference variance for each accelerometer error case. The reference solution was obtained without any noise. The attitude

measurement error and the random noise cause a similar level of degradation. Both errors have nearly uniform degradation over all frequency range. The degradation due to the misalignment error is lower than for the other two error sources except for degree 2. This is caused by the poor estimate of the J_2 coefficient, which is related to the 2-cpr signal of the satellite motion. The degradations related to the resonance coefficients are significant since the misalignment error signal spectrum is similar to that of the resonance signals. Details are discussed in Section 6.4.

Table 5.2 Scale factor estimation error

	Radial	*Transverse*	*Normal*
No errors	*0.00005*	*< 0.00001*	*0.00001*
Random noise	*0.00012*	*< 0.00001*	*< 0.00001*
Attitude error	*0.00055*	*< 0.00001*	*0.00004*
Misalignment error	*0.00640*	*< 0.00001*	*0.00007*

Table 5.3 Bias estimation error ($\times 10^{-6}$)

	Radial	*Transverse*	*Normal*
No errors	*0.00018*	*< 0.00001*	*0.00008*
Random noise	*0.00112*	*0.00001*	*0.00016*
Attitude error	*0.00212*	*0.00001*	*0.00005*
Misalignment error	*0.02504*	*0.00002*	*0.00042*

Tables 5.2 and 5.3 represent the estimation error of the scale factors and biases due to each of that error source. In all the cases, the transverse component estimation is better than the radial and normal ones. The reason is that the dominant non-gravitational acceleration is due to the drag that is acted along the transverse direction. In other words, the transverse direction has more information for estimating the scale factor and bias. For both scale factor and bias estimations,

the misalignment error caused the largest degradation, followed by the attitude measurement error.

As mentioned before, the magnitude of the misalignment error, which is the effect of the off-diagonal components, is proportional to the magnitude of the non-gravitational acceleration, particularly the atmospheric drag. To examine the effect of the non-gravitational accelerations on the misalignment error, another set of the simulations with higher altitude, h = 450 km, were also performed, but no significant J_2 degradation was shown for the misalignment error. This is due to the lower atmospheric drag at the higher altitude, which results in a lower misalignment error. Since the attitude measurement error is also related to the coordinate transform and is proportional to the non-gravitational acceleration, a higher altitude reduces the attitude measurement error as well. Therefore, estimating the scale factors and biases accurately at the higher altitude during initial period may reduce the effect of the misalignment and attitude measurement errors at the lower altitude. The estimates at the higher altitude may be useful as a priori values at the lower altitude unless those values are changed significantly during the mission.

5.4 OTHER ACCELEROMETER ERROR SOURCES

5.4.1 Alignment of the Less Sensitive Axis

The accelerometer requires some pre-launch calibrations to measure its scale factors and biases. It involves a free-fall experiment of the accelerometer

under 1-g inside a drop-tower. Due to the 1-g acceleration, which is significantly higher than space environment acceleration, one of three axes needs a higher electrostatic force to keep the proof-mass motionless inside the cage. The measurement accuracy of this accelerometer axis, which corresponds to the thin dimension of the proof mass, is substantially lower than that of the other two axes. The noise power spectral density (PSD) of the sensitive and the less sensitive axes are presented with mathematical equations in Figure 5.12.

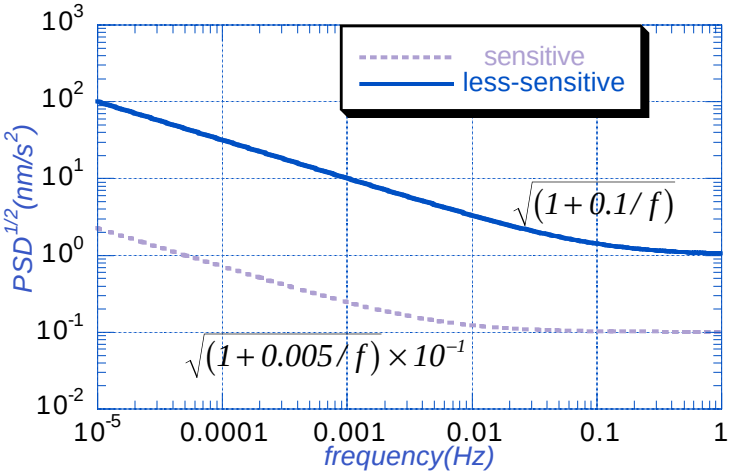

Figure 5.12 Power spectral density of the accelerometer random noises

This raised a question for the satellite design of which satellite body-fixed direction would be aligned with the less sensitive axis. Among the three directions, i.e. radial, transverse, and normal, the transverse direction needs the highest accuracy since it is almost parallel to the line-of-sight (LOS) for the SST measurements of the range and range-rate. Therefore, only two choices, radial and

normal direction, are available for the less sensitive axis. In view of the satellite design, configuring the less sensitive axis along the radial direction is preferred to maintain the symmetry of satellite. However, radial and transverse motions are coupled, so that radial acceleration error propagates to transverse position and velocity errors and this would degrade the SST measurement accuracy. On the other hand, the normal motion is uncoupled with radial and transverse motions in the linear region. Therefore, it is better to align the less sensitive axis along the normal direction. However, this decision breaks the symmetry of the satellite in the cross-track direction and makes it hard to maintain the proof-mass at the center of gravity of the satellite.

To quantify the effect of the less sensitive axis orientation on gravity recovery, some numerical simulations were performed. Two alignment options, the less sensitive axis along the normal or radial directions, were considered. In addition to the ordinary tandem formation, the echelon formation, which is described in Chapter 6, was considered. In the case of the tandem formation, the SST observations come from the in-plane motions, so that the dependency on radial orbit accuracy is high. In the case of the echelon formation, the SST observations also depend on the out-of-plane (normal) motion, so that the dependency on radial orbit accuracy is alleviated. In addition, the case of the no reduced sensitivity axis was performed for the reference case.

For the simulations, 10-day measurement data were processed. The initial altitude was 451km and the along-track separation angle was 2 degree. The right ascension separation of the echelon formation was 0.13 degree, which is equivalent to the cross-track distance of 15km on the equator. To the GPS double

difference measurements, 5mm white noise was applied. The SST oscillator and system noises were applied to the range-rate measurements. The MSIS90 atmospheric drag model with HWM93 horizontal wind model was used for generating simulated accelerometer measurements. The transverse and normal 1-cpr empirical parameters and the constant tangential empirical parameter were adjusted.

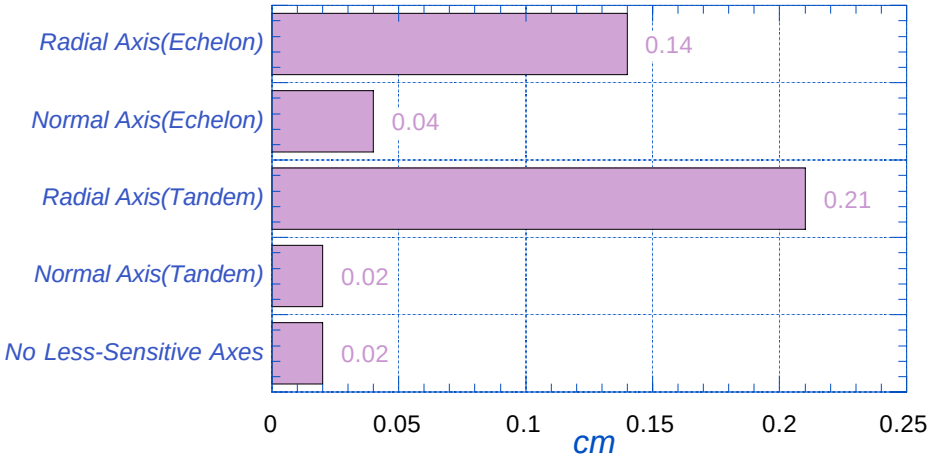

Figure 5.13 Cumulative geoid error for different configurations of the accelerometer less sensitive axis

The cumulative geoid errors up to degree 50 were computed from the estimated gravity fields, which are shown in Figure 5.13. The less sensitive axis along normal direction with the tandem formation gives the best accuracy. The less sensitive radial axis with the tandem formation is an order of magnitude worse than the less sensitive normal case. The reference case with no reduced sensitivity axis shows the same accuracy as the less sensitive normal case. This

proves that the out-of-plane motion (normal) is decoupled from in-plane motion (radial and transverse) and the effect of the normal motion on the SST measurements can be ignored.

The less sensitive normal case of the echelon formation is worse than that of the tandem formation. It is because of SST observation's dependency on the normal motions. The echelon less sensitive radial case shows an improvement upon the tandem less sensitive radial case, but it is still substantially worse than the tandem less sensitive normal case. Based on these simulation results, the normal direction was selected as the less sensitive axis.

5.4.2 Center of Mass Offset-Induced Error

Since satellite orbit is described by the motion of its center of mass (CM), the accelerometer should be close enough to the center of mass to provide non-gravitational acceleration to orbit integrator. Due to satellite fabrication and assembly limitations and variation of satellite mass distribution, the accelerometer may not be exactly at the center of mass of the satellite. The offset between the center of mass of the satellite and the accelerometer makes the accelerometer measurements different from the actual non-gravitational acceleration acting on the center of mass. This accelerometer error depends on the CM offset size and the attitude control method, but both of them have not been fully determined yet. Due to this limitation, the error level from the following analysis might be

premature. It is why this CM offset-induced error is separated from the other error sources.

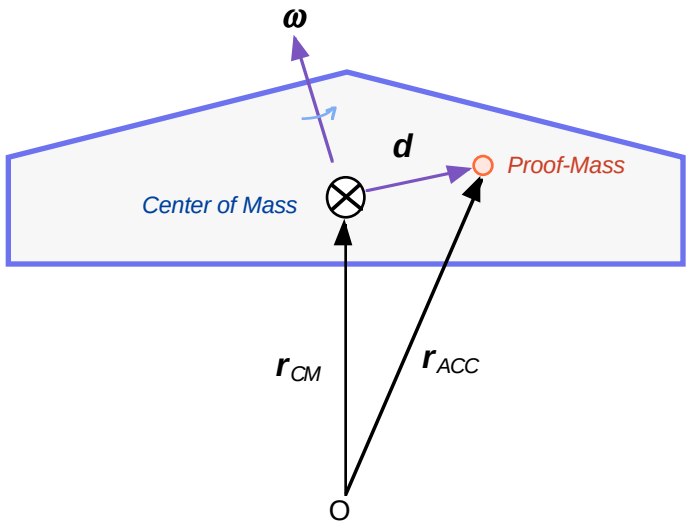

Figure 5.14 Accelerometer proof-mass offset from the center of mass

The vector $\boldsymbol{d}$ in Figure 5.14 represents the offset of the accelerometer proof-mass from the center of mass. The vectors $\boldsymbol{r}_{CM}$ and $\boldsymbol{r}_{ACC}$ represent the positions of the center of mass and the proof-mass, respectively. The equations of motion of those two points are given by [8,51,54]

$$\ddot{\boldsymbol{r}}_{CM} = \nabla U(\boldsymbol{r}_{CM}) + \boldsymbol{f}_{NG} \tag{5.14}$$

$$\ddot{\boldsymbol{r}}_{ACC} = \nabla U(\boldsymbol{r}_{ACC}) + \boldsymbol{f}_{ACC} \tag{5.15}$$

where $\boldsymbol{f}_{NG}$ is the non-gravitational acceleration acting on the center of mass and $\boldsymbol{f}_{ACC}$ is the electrostatic force acting on the proof-mass, which is equivalent to the

accelerometer measurement. With the offset $\boldsymbol{d}$, the accelerometer measurement is not same as the true non-gravitational acceleration, and it is required to derive the relationship between the two quantities. This measurement error comes from two sources, one is from different motions of two points, and the other one is from different gravity accelerations acting on two points. The motion of the proof-mass may be related to that of the center of mass as follows

$$\ddot{\boldsymbol{r}}_{ACC} = \ddot{\boldsymbol{r}}_{CM} + (\ddot{\boldsymbol{d}})_r + \boldsymbol{\omega}\times(\boldsymbol{\omega}\times\boldsymbol{d}) + 2\boldsymbol{\omega}\times(\dot{\boldsymbol{d}})_r + \dot{\boldsymbol{\omega}}\times\boldsymbol{d} \tag{5.16}$$

where $(\dot{\boldsymbol{d}})_r$ and $(\ddot{\boldsymbol{d}})_r$ are the time derivatives expressed in the satellite body fixed coordinates, and $\boldsymbol{\omega}$ is the angular velocity of the satellite. The gravity acceleration on the proof-mass can be approximated by a Taylor series expansion as

$$\nabla U(\boldsymbol{r}_{ACC}) \approx \nabla U(\boldsymbol{r}_{CM}) + \nabla\left[\nabla U(\boldsymbol{r}_{CM})\right]\cdot\boldsymbol{d} \tag{5.17}$$

Substitution of (5.14) and (5.15) into (5.16) yields the equation of the accelerometer measurement $\boldsymbol{f}_{ACC}$ as a function of the true non-gravitational acceleration , center of mass offset, and angular velocity:

$$\boldsymbol{f}_{ACC} = \boldsymbol{f}_{NG} + (\ddot{\boldsymbol{d}})_r + \boldsymbol{\omega}\times(\boldsymbol{\omega}\times\boldsymbol{d}) + 2\boldsymbol{\omega}\times(\dot{\boldsymbol{d}})_r + \dot{\boldsymbol{\omega}}\times\boldsymbol{d} - G\cdot\boldsymbol{d} \tag{5.18}$$

The gravity gradient matrix G is given by

$$G = \begin{bmatrix} \frac{\partial^2 U}{\partial x^2} & \frac{\partial^2 U}{\partial x \partial y} & \frac{\partial^2 U}{\partial x \partial z} \\ \frac{\partial^2 U}{\partial y \partial y} & \frac{\partial^2 U}{\partial y^2} & \frac{\partial^2 U}{\partial y \partial z} \\ \frac{\partial^2 U}{\partial z \partial x} & \frac{\partial^2 U}{\partial z \partial y} & \frac{\partial^2 U}{\partial z^2} \end{bmatrix} \tag{5.19}$$

where (x, y, z) denote the satellite-body-fixed coordinates. The difference $\boldsymbol{f}_{ACC} - \boldsymbol{f}_{NG}$ represents the measurement error due to the center of mass offset.

To analyze the effect of this CM offset-induced error on the gravity estimation, several numerical simulations were performed by adding the error $\boldsymbol{f}_{ACC} - \boldsymbol{f}_{NG}$ of (5.18) to the simulated accelerometer measurements. The same attitude data [24], which was used for the multipath error analysis in Chapter 4, was used. As like the multipath simulation results, the following simulation results are subject to change due to the preliminary status of the attitude simulation data. Figure 5.15 represents the time series of angular rate and accelerations in the three directions. The orbit altitude was 300km. The acceleration plots have some spikes, which result from rapid attitude changes.

Two sets of three random numbers, all approximately near *0.1 mm*, were used for the three-dimensional offsets $\boldsymbol{d}$ of two satellites. It assumed the use of the CM trim mechanism, which adjusts the CM position by means of a moving mass, and the offset is relatively small. The time variation $\dot{\boldsymbol{d}}$ was not considered in this simulation.

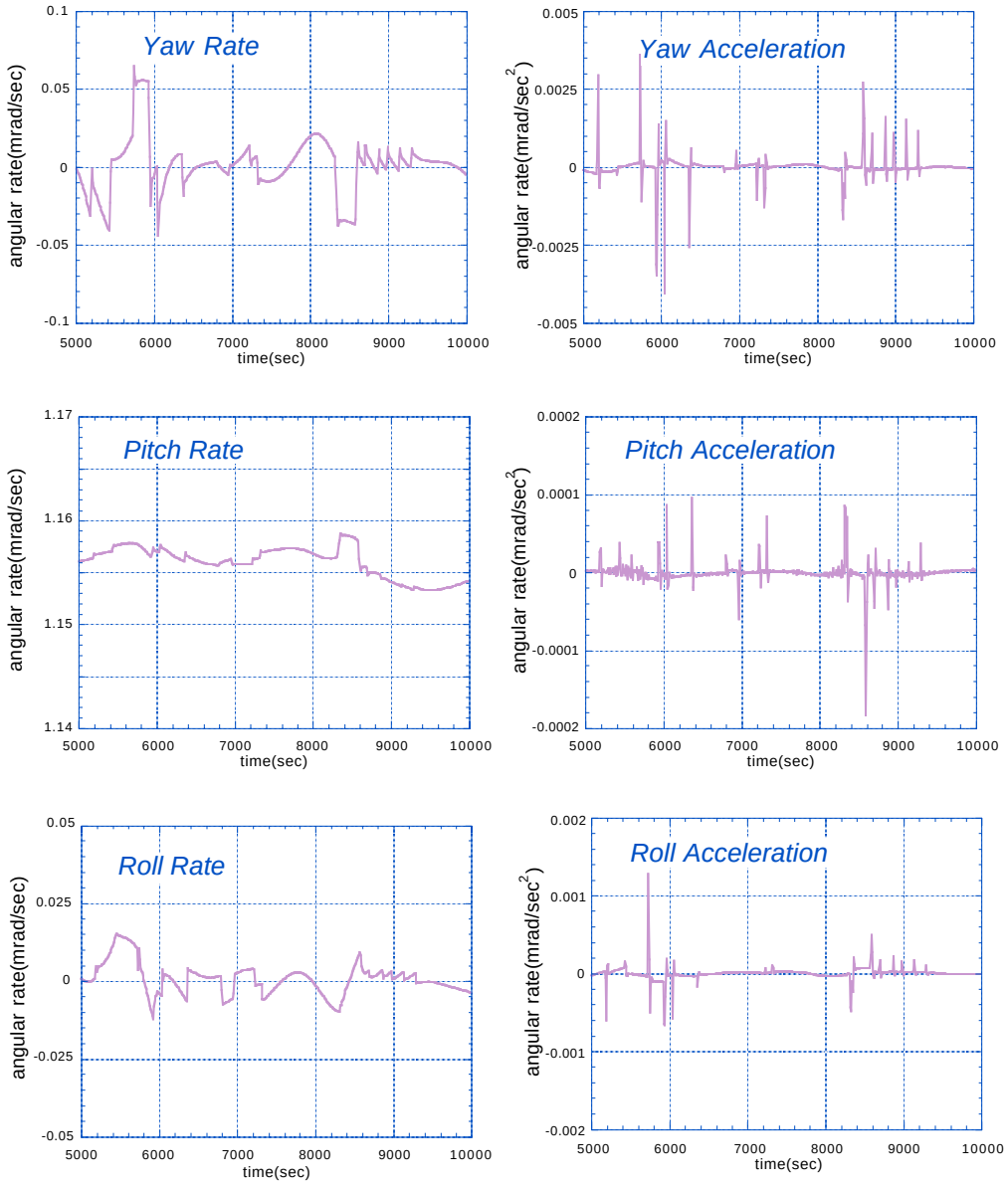

Figure 5.15 Angular rate and acceleration time series

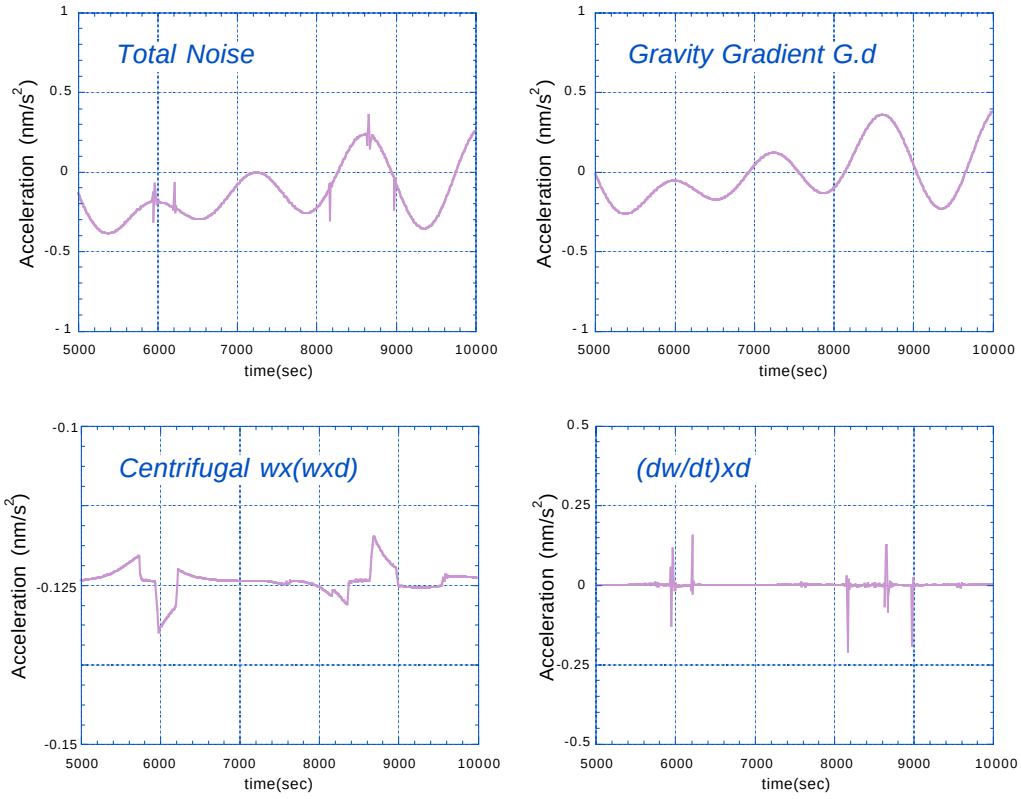

Figure 5.16 Transverse components of the accelerometer noise due to the CM offset ($\sigma(d) = 0.1$ mm)

Figure 5.16 shows the total accelerometer noise due to the CM offset with three independent components described in (5.18). All of them are transverse direction components. The total acceleration error is mainly driven by the gravity gradient term, which has a strong long wavelength signal. The $\dot{\boldsymbol{\omega}}\times\boldsymbol{d}$ term has some large magnitude of spikes, which caused the spikes in the total error. While the gravity gradient term is less dependent on the attitude motion (angular rate and acceleration), the other two terms ($\boldsymbol{\omega}\times(\boldsymbol{\omega}\times\boldsymbol{d})$ and $\dot{\boldsymbol{\omega}}\times\boldsymbol{d}$) are heavily

dependent of it. One of the purposes of this analysis is to understand how the individual components affect the gravity estimation. Therefore, two types of simulations were performed; one with the gravity gradient term only and the other with the attitude terms only. The combined case was simulated as well.

(50×50) gravity fields was estimated from 7 day measurements. Most other noise effects were applied, which include inter-satellite system, oscillator, and multipath noises, accelerometer random, attitude, and misalignment errors. Initial scale factor and bias offsets were 2% and 10^{-6}, respectively, which would be the uncertainties after ground testing of the accelerometer.

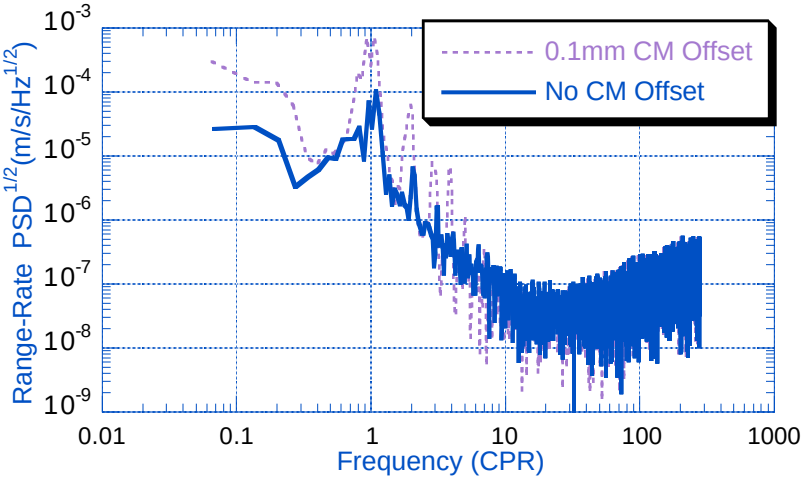

Figure 5.17 Spectrum of the range-rate residual due to the CM offset error

Figure 5.17 compares the range-rate residual due to the CM offset error with a reference residual. The reference case has the same error sources except the CM offset error. These residuals are pre-fit quantities, i.e. before applying the

low-low empirical parameterizations. Only the gravity gradient case is presented. The attitude case was analyzed as well, but it is hard to distinguish the difference from the reference case. The combined case is almost identical to the gravity gradient case. The tone signal (*N*-cpr) increase is significant. This kind of tone signal is similar to the gravity signal, so that it may affect the gravity estimation.

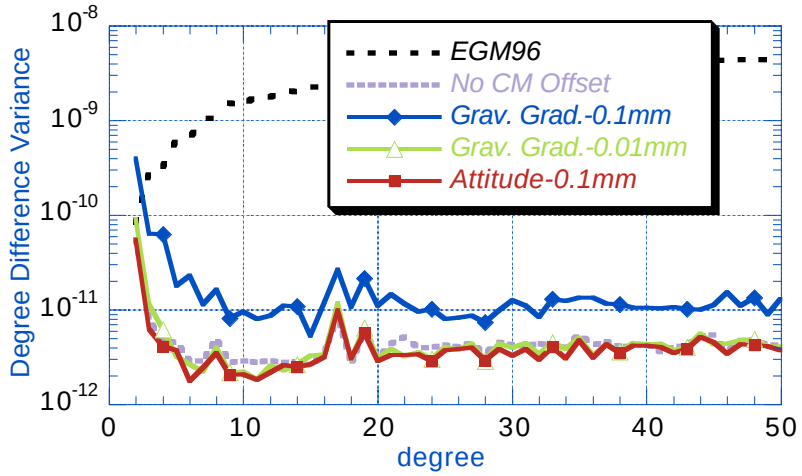

Figure 5.18 Degree difference variances due to the CM offset error

Figure 5.18 shows the degradation of the estimated gravity field due to the CM offset error. The results of the gravity gradient and attitude cases are presented. The combined case is not presented due to its similarity to the gravity gradient case. For a sensitivity study, a smaller offset of 0.01mm was also applied for the gravity gradient case. The result of the 0.1mm gravity gradient case is substantially worse than that of the reference case. However, the attitude case is almost identical to the reference case. The small difference from the reference case is due to the slightly different measurement weightings. The rapid attitude

motion (spikes) hardly affects the gravity solution. The degradation of the 0.01mm gravity gradient case is negligible as well.

The degradation is mainly caused by the gravity gradient error and the degradation is proportional to the CM offset size. Therefore, it is necessary to reduce the offset size or to improve its estimation accuracy. If the CM offset is known with certain accuracy, its effect can be reduced during the post processing on ground. The current estimate of the CM offset estimation accuracy is as much as 0.03mm [81]. Since the gravity degradation is proportional to the CM offset size, the gravity degradation can be negligible with the 0.03mm offset.

6 SENSITIVITY STUDIES

6.1 INTRODUCTION

The accuracy of gravity estimation is affected by various parameters. To understand this, it is necessary to identify and to quantify the effect of each parameter, which may include orbit selection, instrument noise level, and so on. Most of the major design parameters, instrument noise levels and orbit selections, should be determined with consideration of the performance that is the accuracy of the gravity estimation in case of the GRACE mission. Since major instrument noises, the SST and accelerometer measurement noises were covered in the previous chapters, this chapter focuses on the orbit selection.

The orbit selection issues include inclination, altitude, and separation. The effect of the orbit parameters was analyzed by numerical simulations and the semi-analytic method. The difference from the previous studies [29,45,65] is the consideration of the instrument noise level change due to the orbit parameters, e.g. altitude and separation. This kind of comprehensive error modeling enables more realistic sensitivity studies.

The comparison between the range and range-rate measurement is also described. The issues in the optimal combination of the GPS and SST information matrices is studied further. The orbit resonant characteristics are examined for better understanding of its effect on the SST measurements.

The expected gravity recovery accuracy is presented with typical simulation results. To the extent that the error sources assumed in these

simulations represent the actual errors, the GRACE mission can achieve this accuracy.

6.2 ORBIT SELECTION

6.2.1 Separation

Two GRACE satellites will be orbiting in the same plane within a nominal separation distance. The separation distance affects the gravity solution as well as other orbit maintenance activities, so that it is interesting to analyze the effect of the separation distance on the gravity solution. In general, the gravity signal strength increases as the separation increases since the SST measurements is the difference between the two perturbations acting on the satellites. This increase in signal was shown in [65]. However, the larger separation may cause several other problems, including measurement noise increase and observability problem.

The SST measurement noise level grows as the separation increases. The separation distance affects two types of the SST measurement noises as described in Chapter 4, the system and oscillator noises. The range system noise that has the power spectral density of $(1\ \mu m/\sqrt{Hz})^2$ at 230 km increases linearly as the separation increases. That value becomes $(0.5\ \mu m/\sqrt{Hz})^2$ for 1° separation and $(2\ \mu m/\sqrt{Hz})^2$ for 5° separation. The oscillator noise, which represents the oscillator drift residual after the dual one-way ranging filtering, grows as the cancellation effect of the oscillator noise decreases due to the increase of the microwave time-of-flight.

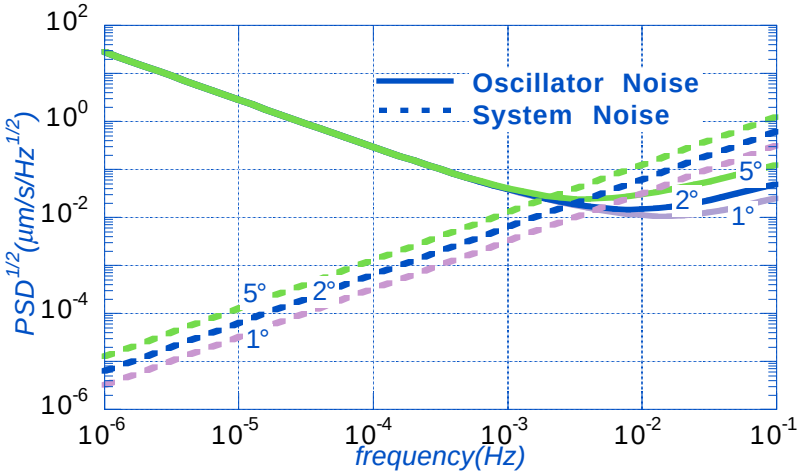

Figure 6.1 Variation of the range-rate oscillator and system noises along the separation angles

Figure 6.1 shows the increase of the oscillator and system noise on the range-rate measurement due to the increase of the separation angle. Because of its linear variation, the system noise increases over the entire frequency range. On the other hand, the oscillator noise is affected only in the high frequency region since the low frequency signals are still effectively removed after dual one-way ranging filtering. The system noise level is much lower than the oscillator noise level at the low frequency, so that the system noise increase for the longer separation may not affect the low frequency SST noise. Considering these two major SST noise behaviors, one can expect that the separation change may not affect the low frequency noise but the high frequency noise.

Another aspect is the change of the gravity perturbation signal on the SST measurement. The high frequency part of the gravity spectrum tends to be

attenuated as the separation increases [45]. This attenuation can be predicted by the semi-analytic method described in Chapter 3. The equation relating the range-rate error variance to the gravity error variance is given by

$$\sigma_n^2(\delta T) = \frac{1}{1-P_n(\cos\theta)} \frac{R_e}{GM} \left(\frac{r}{R_e} \right)^{2n+1} \sigma_n^2(\delta\dot{\rho}) \tag{6.1}$$

The inverse of $1-P_n(\cos\theta)$ reflects the effect of the separation angle θ on the gravity recovery. This is a weighting function, which determines how much the SST noise is transformed into the gravity error. With same noise levels, the degree variance is entirely dependent on this term theoretically.

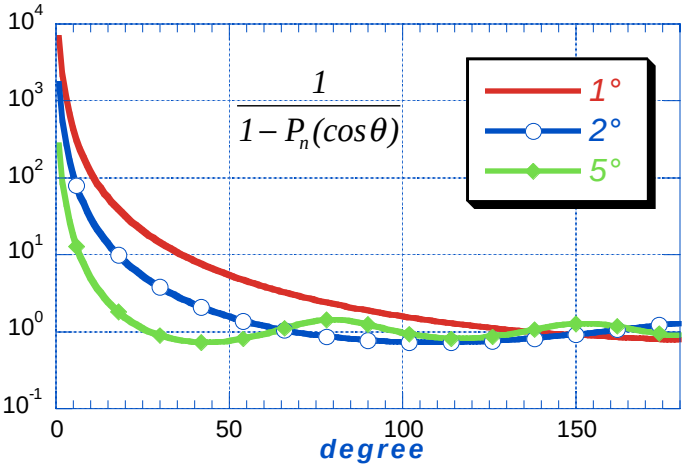

Figure 6.2 Inverse separation functions vs. degree

Figure 6.2 shows the variation of the inverse separation function for three separations. Higher value means higher error in gravity solution for the same level of noise. In the low degrees, the 5° function has a lower value than the others, so

that the 5° provides a better gravity solution if the same level of measurement noise is present. In the high degrees, the 5° function has the same level of magnitude as the others. In other words, the advantage of large separation is reduced for the higher degrees and the high degree accuracy might be dependent of the noise level.

Another issue is the observability problem for certain gravity coefficients. When the separation distance is identical to the wavelength of a certain gravitational signal, each satellite experiences the same phase of the gravity perturbation due to this signal. Therefore, the SST measurement, which is the differenced quantity, does not contain this gravity signal. In other words, the gravity coefficients producing this signal are hard to observe. For θ° separation with a polar orbit, integer multiple of $360/\theta$ zonal terms are not observable. The geopotential degrees corresponding to some separation angles are presented in Wagner's study [79]. The correlation between the unobservable coefficients and other terms degrades the other terms as well; on the other hand, this correlation mitigates the singularity of the unobservable coefficients.

The question is whether the increase of gravity signal with larger separation surpasses the increase of the measurement noise. To analyze the effect of the separation distance on the gravity recovery, three numerical simulations were performed with different separations and noise models. Three separation angles of 1°, 2°, and 5° with 450 km altitude correspond to the distance of 119 km, 238 km, and 596 km, respectively. Most of the other errors, accelerometer noises and multipath noise, were the same for all three cases, but the inter-satellite system and oscillator noise levels were different.

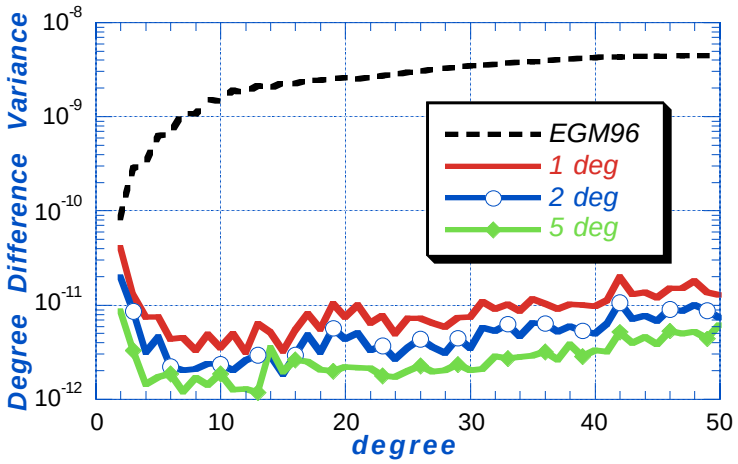

Figure 6.3 Variation of degree difference variances due to separation angle changes

Figure 6.3 shows the degree difference variance for different separation angles. As predicted by the separation function, the error level grows as the separation is decreased. This means that the decrease in the SST measurement noise level for smaller separation does not significantly affect the results.

To analyze the effect of the separation on high degree coefficients, the semi-analytic method was applied to predict gravity recovery error. The same types of noise as used in the numerical simulations were applied to realize the range-rate noise residual. To obtain enough sampling, 30-day measurements were used.

The degree error variances, which were predicted by the semi-analytic method, are presented in Figure 6.4. Unlike the low degree accuracy, the high degree accuracy increases as the separation decreases. This is contrary to the inverse separation function behavior in Figure 6.2, where all the three weighting

functions have the same levels in the high degrees. It implies that this accuracy difference is due to the increase of the SST noise for the longer separation.

In summary, a longer separation is better for the low degree gravity recovery, but a shorter separation is better for the high degree gravity recovery. For balancing the low and high degree performance, the 2° can be a good choice, and this value was selected as the nominal separation angle.

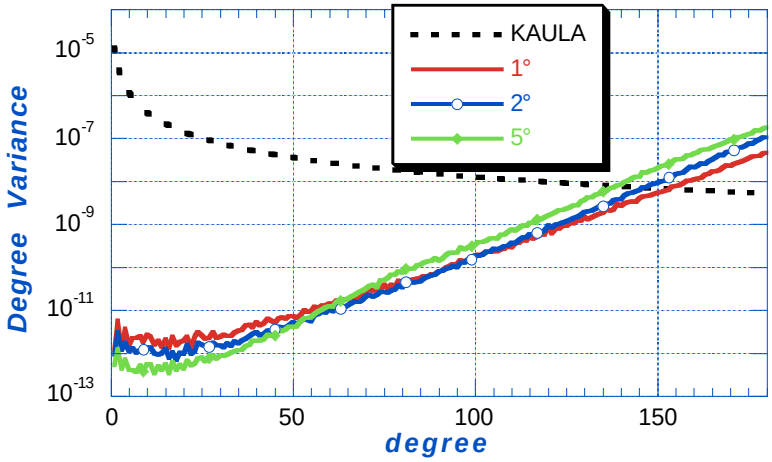

Figure 6.4 Error predictions by the semi-analytic method for different separation angles

6.2.2 Altitude

Due to the attenuation effect of the gravitational field with increasing altitude, a lower altitude is preferred for gravity estimation in general. The GRACE satellites' altitude range may be from 500 km to 300 km, which is substantially lower than other geodetic satellites. However, low altitude causes other problems. The atmospheric drag grows with decreasing altitude, and it accelerates the decay of the satellite altitude and reduces the lifetime. Another problem is the increase of the accelerometer noise. Some types of accelerometer errors depend on the magnitude of the accelerometer input, i.e. non-gravitational acceleration, so that they are increased as the altitude is decreased. In addition to the noise, the high atmospheric density environment of low altitude requires more frequent attitude maneuver and may degrade the SST measurement performance. Therefore, it is necessary to quantify the effect of altitude on gravity estimation.

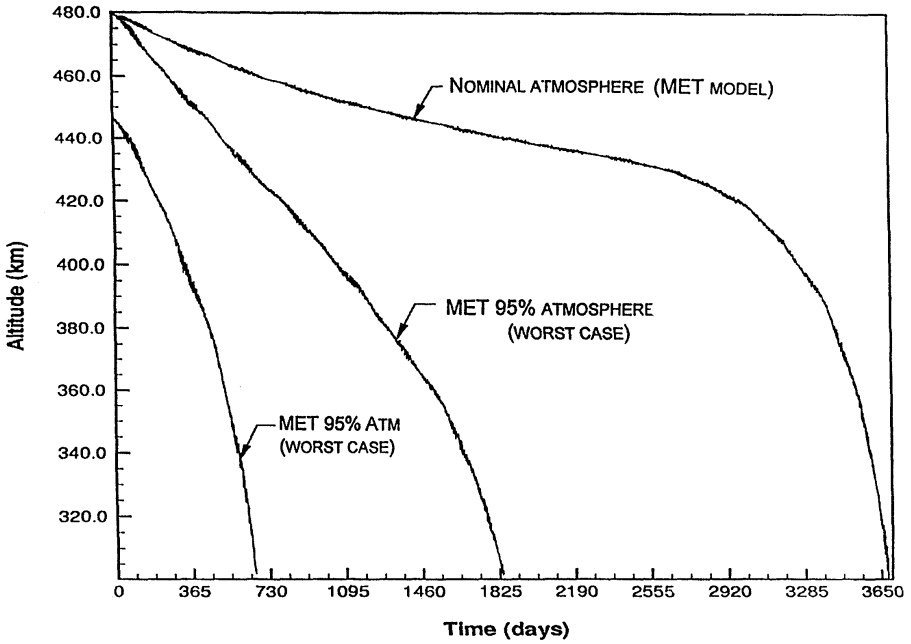

Figure 6.5 Predicted GRACE satellite altitude variation [20,24]

The predicted GRACE satellite altitude variation is shown in Figure 6.5. This prediction was made with the MET atmospheric model [20,24]. The initial altitude is 480km or 450km. In the nominal case, the satellite may stay above the 400 km during most of its mission lifetime, five years, but the worst case scenarios predict a fast decrease of the altitude. Therefore, the altitude prediction heavily depends on the atmospheric density modeling. Since the satellite design is still changing and the prediction of the atmospheric density is becoming close to the actual density, the altitude variation will be more accurately predicted later.

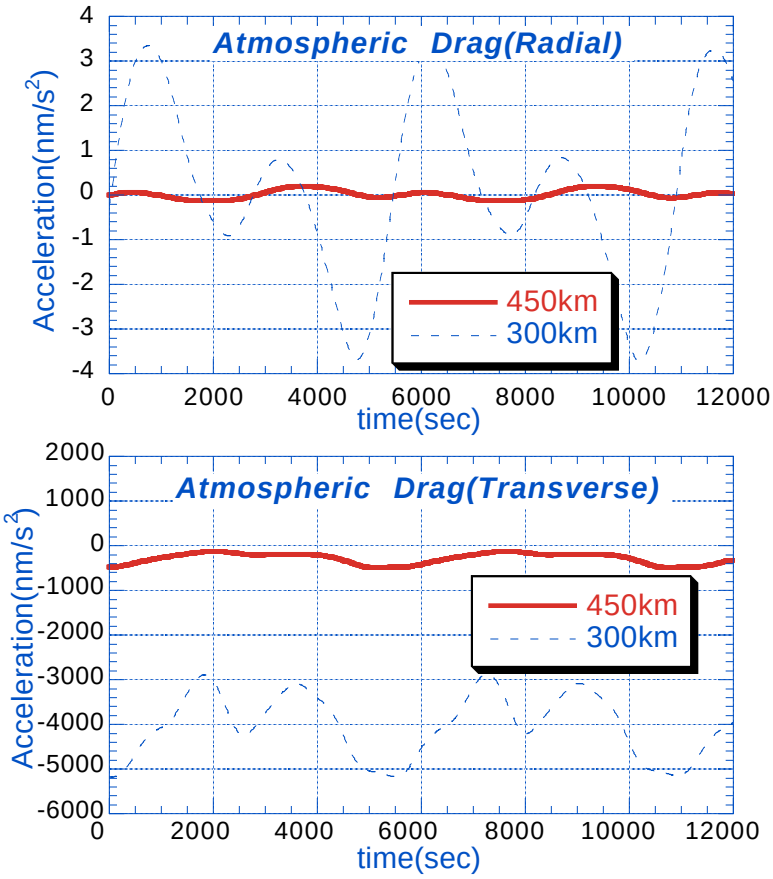

Figure 6.6 Atmospheric drag accelerations at 300km and 450km altitudes

The predicted atmospheric drag accelerations at 450km and 300km are shown in Figure 6.6. The magnitude of the acceleration at the low altitude is increased nearly ten times. These increased drag acceleration affects some accelerometer noises and causes more frequent attitude maneuvers. Among the accelerometer noise models described in Chapter 5, the noise due to the scale factor and misalignment errors increases for a lower altitude. The former is

proportional to the scale factor uncertainty and the non-gravitational acceleration, and the latter is proportional to the accelerometer alignment offset and the non-gravitational acceleration. At the lower altitude, the accelerometer scale factor offset or uncertainty does not increase, but the scale factor error increases due to higher non-gravitational (drag) acceleration. The misalignment error increases as well for the lower altitude. At the lower altitude, more attitude maneuver is necessary to maintain the satellite nominal attitude, and this yields higher satellite angular rate and acceleration. The accelerometer CM offset-induced error, coupling between the CM offset and the angular rate and acceleration, increases for the lower altitude.

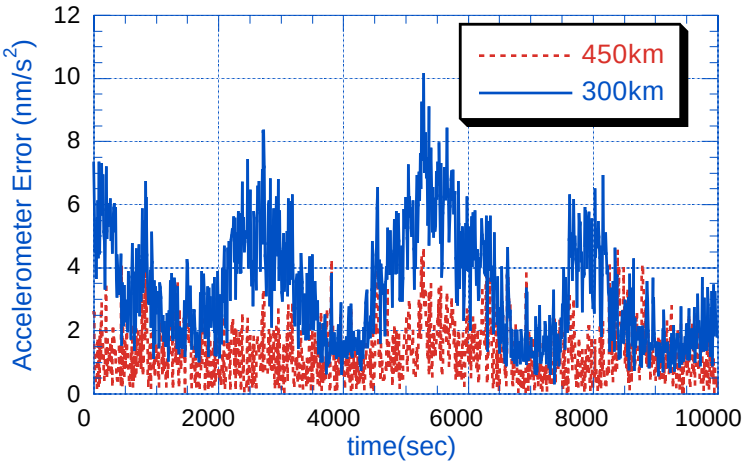

Figure 6.7 Accelerometer noise increase for a lower altitude

The accelerometer noise levels for 300 km and 450 km are compared in Figure 6.7. The accelerometer scale factor, bias, misalignment, random, and attitude noises are included. As shown in the previous figure, the drag acceleration at the 300 km is ten times larger than at the 450 km. However, due to

the presence of other altitude independent errors, the noise at the 300km is three times larger. This three times increase may be very significant for the gravity estimation at the lower altitude.

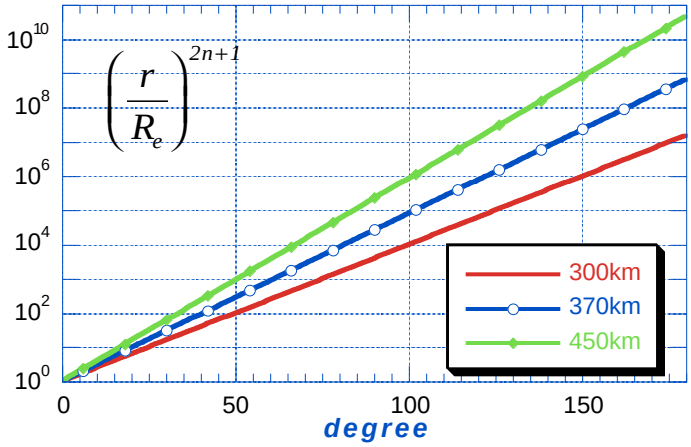

Figure 6.8 Inverse attenuation factors for different altitudes

The degree variance equation in Chapter 3, which is also mentioned in the previous section as equation (6.1), is also useful to predict the attenuation effect. The inverse attenuation factor, $\left(r/R_e\right)^{2n+1}$, reflects the variation of the gravity error due to altitude change. Figure 6.8 shows the inverse attenuation factor of different altitudes as a function of degree. Under same level of noise, higher value represents more degradation of gravity solution. The differences between altitudes grow as degree increases, which reflect the advantage of lower altitude in estimating high degree gravity fields.

Since the attenuation factor difference is smaller in low degree regions, the semi-analytic method was necessary to predict high degree errors. Up to degree 180 were predicted for the three altitudes, 300km, 360km, and 450km. Smaller size (50×50) of numerical simulations were also performed to verify the prediction results at the low degrees. The predictions and simulations had both the accelerometer and SST noises. The former included random noise, scale factor and bias offsets, attitude error, and misalignment error. The later included oscillator, system, and multipath noises. All the three cases have the same 2° separation angle, and the separation distances are slightly different. However, the change of the SST noises due to the separation distance variation was ignored.

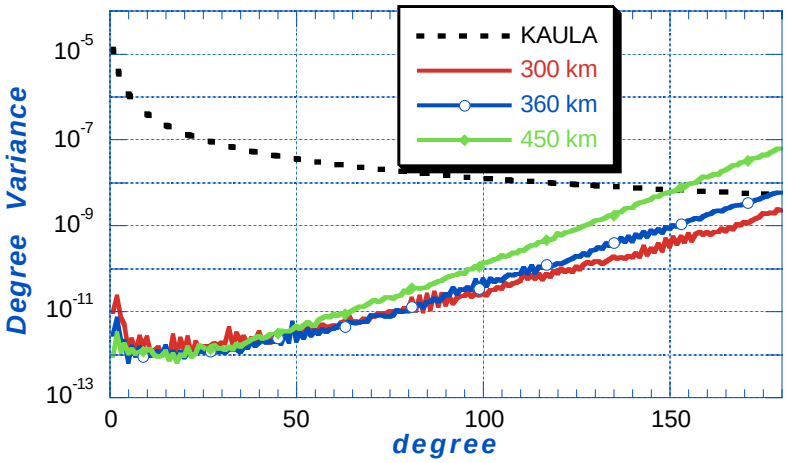

Figure 6.9 Error predictions by the semi-analytic method for different altitudes

Figure 6.9 shows the degree variance of the three different altitudes, which were predicted by the semi-analytic method. In high degree region, the lower

altitude improves the gravity estimation, but the improvement is not as much as the prediction by the attenuation factor. It is because of the higher accelerometer noise at the low altitude. In the low degree region, below degree 50, the 300km case shows a worse accuracy than others do. To clarify the cause of this worse accuracy of the 300 km case, another set of (50×50) numerical simulations were performed without applying any accelerometer or SST noises. In this case, the accuracy of all the altitude cases has the same accuracy below degree 50. In other words, the GRACE SST measurement is less sensitive to the altitude change. It shows that the worse accuracy of the 300km case at the low degree is due to its higher accelerometer noise.

6.2.3 Ground Track

Another effect of the orbit altitude is the variation of the ground track pattern, which is a function of various orbit parameters but is mainly a function of the altitude. Uniform ground tracks are ideal for the gravity estimation since they provide the best condition for detecting the gravity coefficients. Due to the thruster fuel limitation, the GRACE orbit may not be maintained to keep the uniform ground tracks all the time and the non-uniform ground tracks may be unavoidable for certain mission period. To analyze the impact of the non-uniform ground tracks on the gravity solution, numerical simulations were performed with four different ground track patterns.

Figures 6.10 through 6.13 show the ground tracks for different periods and altitudes. An orbit trajectory was integrated for one-year period and then four time spans were selected. The separation angle was 2° and those ground tracks represent the trajectory of the midpoint between the two satellites, which is nearly identical to the trajectory of the individual satellites. Each span has a 15-day period and a (70x70) gravity model with DTM atmospheric model was used to integrate the trajectories. All spans have 229 orbit revolutions.

The initial orbit period, Span1, has a 15-day repeat period as shown in Figure 6.10. This period has even ground track spacing of 1.5°. Its altitude was 452 km. As the altitude changes, the orbit repeat period deviates from the initial 15-day period. Figure 6.11 shows the ground track of Span2, which has an initial altitude of 446 km. The ground track spacing is not even, and it has a 3-day (47 revolutions) main repeat period with a 5-day sub-repeat period. The maximum spacing (longitude gap size) is about 4°. Span3 in Figure 6.12 has an initial altitude of 434km and shows a 3-day repeat period. The ground tracks are overlapped every three days and the gap size is about 8°. Span4 in Figure 6.13 has an initial altitude of 421km and shows an intermediate uniformity of the ground track spacing between Span1 and Span2. The gap size is about 2°. Since the minimum wavelength of the degree 70 sectorial coefficient is 5.14°, and one can expect that Span3, whose gap size is larger than the minimum wavelength, may degrade the gravity solution.

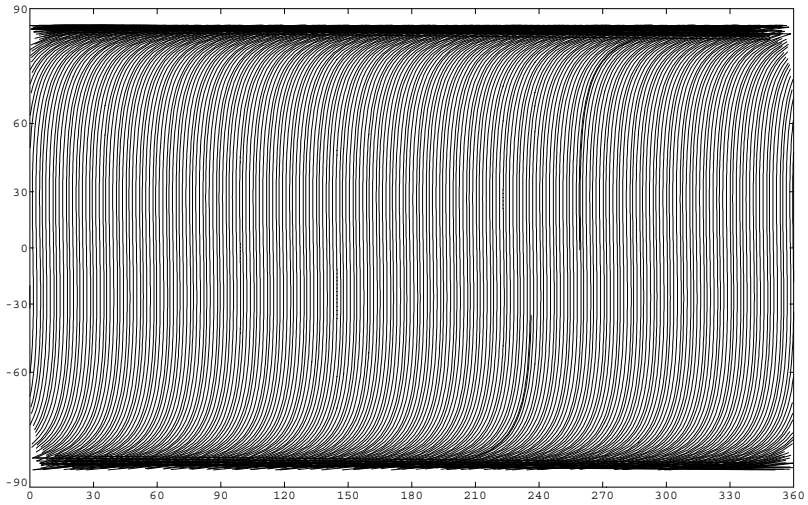

Figure 6.10 Ground track of Span1 (452km)

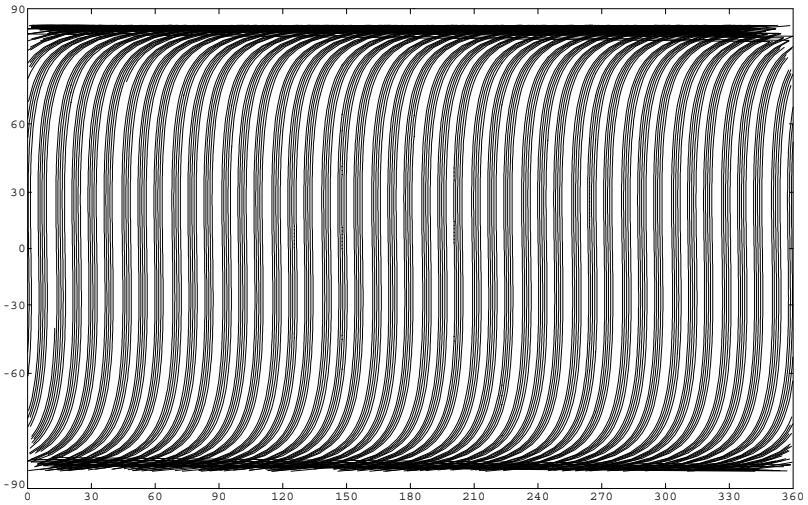

Figure 6.11 Ground track of Span2 (446km)

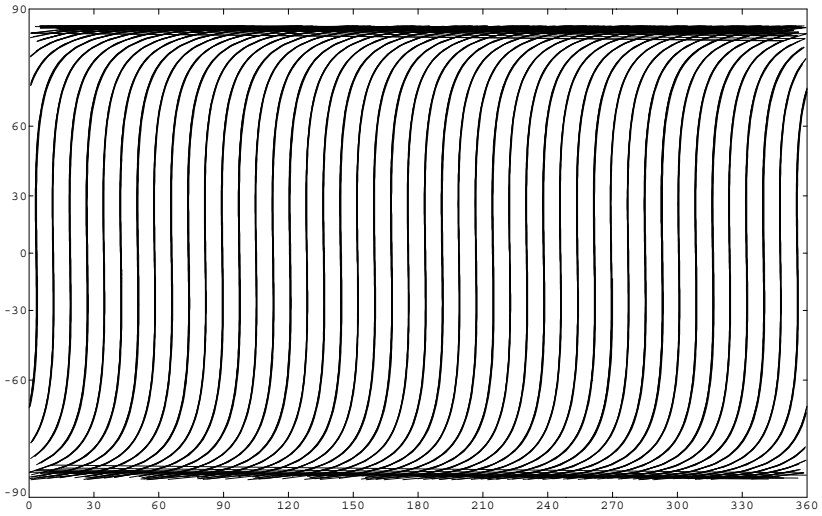

Figure 6.12 Ground track of Span3 (434km)

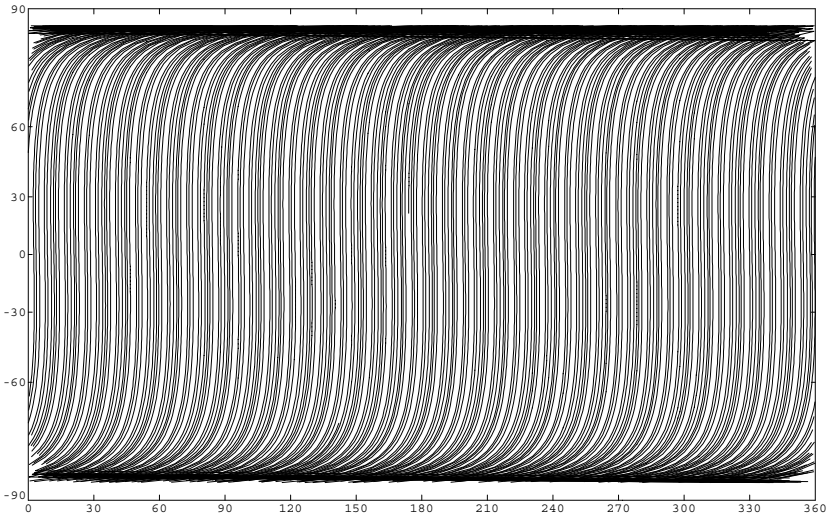

Figure 6.13 Ground track of Span4 (421km)

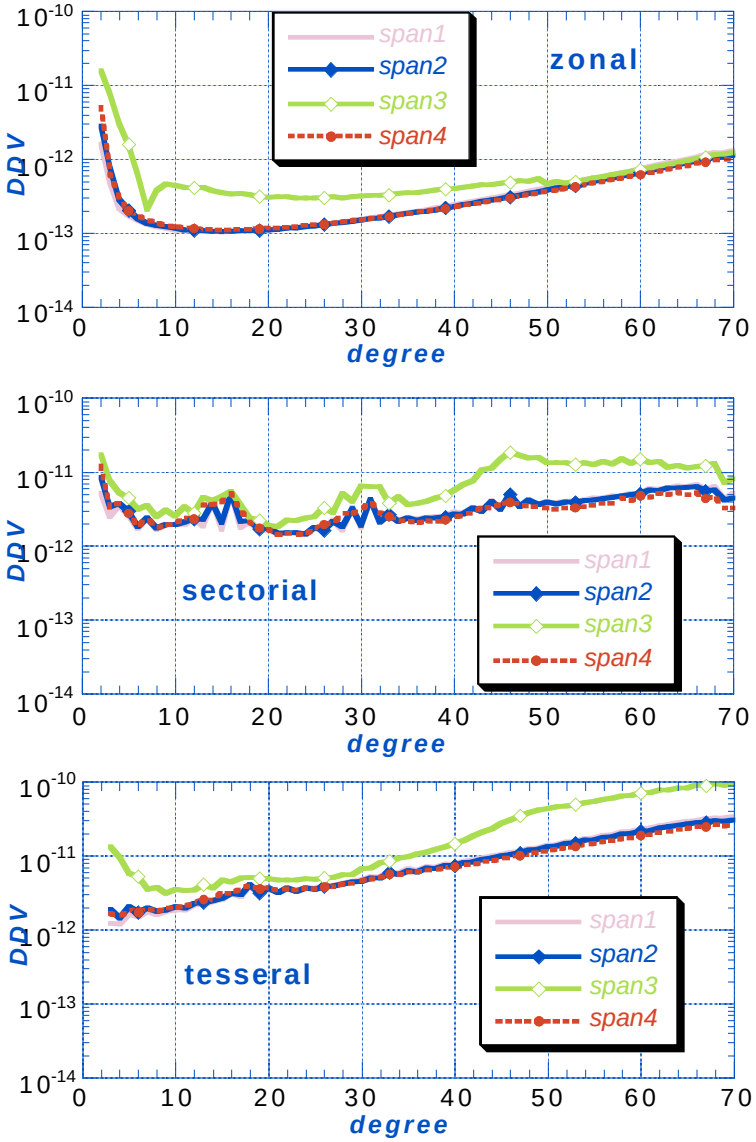

Figure 6.14 Degree difference variance of zonal, sectorial, and tesseral components for different time spans

Figure 6.14 shows the degree error variances of zonal, sectorial, and tesseral terms for the four spans. The results from Spans 1, 2, and 4 have nearly the same level of accuracy but Span3 has large degradation in all terms. In the sectorial terms, Span3 shows a large degradation in the high degrees. A peak around the degree 46 represents the fact that the minimum wavelength of the degree 46 sectorial coefficient is the same as Span3's gap size of 8°. However, the zonal terms of Span3 has a large degradation in the low and mid degrees and this may be due to the interaction between the high degree sectorial and low degree zonal terms. The tesseral terms have the similar behavior as the sectorial terms since the near sectorial terms, which are close to the sectorial ones, are included in the tesseral terms.

As shown in the figures, a uniform ground track is preferred for the gravity estimation. Otherwise, it is safe to minimize the longitude gap size as far as the thruster fuel is allowed. If a large longitude gap is unavoidable, the use of a priori information at the previous estimation period can be utilized to prevent the degradation. Alternatively, we might extend the solution span beyond 30 days until a satisfactory coverage is obtained.

6.2.4 Inclination

Due to some restrictions on the launcher system, the GRACE orbit inclination may not be a perfect polar orbit. The non-polar orbit does not provide complete coverage of the sphere with data. The polar gaps, which are not covered

by ground tracks of the satellite orbit, have the size of $2 \times (i - 90)°$, where i is the inclination. These gaps may degrade the accuracy of global gravity estimation. To quantify this effect, numerical simulations were performed for different inclinations ranging from 83° to 90°.

The impact of the polar gaps depends not only on the gap size but also on the estimated gravity size. If the polar gap size is relatively small with respect to the maximum gravity size or the minimum wavelength, it may not degrade the gravity solution significantly. The minimum wavelength of the gravity harmonics is given by $(360/N_{max})$, where N_{max} is the maximum degree. To analyze this relationship, three sets of simulations were performed with different gravity sizes, (60×60), (99×99), and (120×120). For each set, three or four inclination cases were analyzed by using the gravity coefficient difference and predicted geoid error.

Table 6.1 Altitudes for each inclination and gravity field size

Inclination	(60×60)	(99×99)	(120×120)
***i* = 83°**	445 km	428 km	N/A
***i* = 87°**	451 km	435 km	448 km
***i* = 88.5°**	N/A	437 km	450 km
***i* = 90°**	456 km	440 km	453 km

Slightly different initial altitudes were used for each inclination to fulfill a repeat orbit condition and Table 6.1 lists the altitude of each case. The maximum

altitude differences range from 7km to 11km. In Section 6.2.2, the change of gravity estimation accuracy along the altitude is discussed with the wide altitude range, from 300km to 450km. Considering the size of its gravity accuracy difference, one can assume that these small altitude differences do not impact the comparison study significantly.

Table 6.2 Simulation conditions for each gravity field size

	(60×60)	**(99×99)**	**(120×120)**
Data Span	30 days	14 days	16 days
No. of orbit revolutions	459	215	245
Min. gravity wavelength	6°	3.6°	3°

Table 6.2 lists the observation data spans, the number of revolutions during those spans, and the minimum gravity wavelength of each gravity field size. The minimum data span should be long enough for the number of revolutions to be greater than $2\times N_{max}$. This is in order to provide enough sampling for the sectorial terms, which depend on the longitudinal gravity variation. The data spans were selected to be close to the minimum spans. In the case of the (60×60) cases, a longer 30 day data span was used to minimize other effects, e.g. resonance at a certain altitude. The separation angle was 2°, and the accelerometer and SST noises were applied. The 1-cpr, tangential, and the low-low empirical parameters were adjusted.

Figure 6.15 represents the gravity recovery accuracy of the (60×60) cases with degree difference variance, zonal and tesseral degree difference variances, and the geoid height error predicted from the solution covariance. Sectorial degree difference variances were analyzed as well, but they are not presented since the accuracy level differences are not significant.

The 83° case shows a better accuracy than the others do mainly due to its better tesseral coefficients accuracy. This better accuracy can be explained by the increase of the measurement data density. A lower inclination orbit has a higher data density than a higher inclination has due to a less coverage area with the same period. A simple equation can be used to quantify the data density increase. The 83˚ case has 14 % higher data density than the 90˚ case, and the 87˚ case has 5 % higher data density. This type of improvement by non-polar orbit is identified by other investigators who analyzed gradiometer measurements [39,61,76]. Another reason can be a better measurement geometry of the low inclination orbit. The angle between the two line-of-sight vectors, one from the ascending orbit and the other from the descending orbit, is dependent of the inclination. This measurement crossover angle of the low inclination orbit is larger than that of the high inclination orbit. The larger crossover angle may provide a better observability for the gravity estimation.

The zonal accuracy of the 83˚ case is much worse than that of the others. This can be explained by the fact that the zonal terms solely depend on the latitudinal gravity variation. The lack of data at certain latitude region, i.e. the polar gaps, degrades the zonal coefficient accuracy. The minimum wavelength of the (60×60) gravity field is 6˚, and it is much smaller than the gap size of the 83˚

inclination, 14˚. The 87° case does not show a significant degradation since the minimum wavelength is not smaller than the polar gap size, 6°.

Mackenzie [45] explained this zonal coefficient degradation by using the inclination function $F_{nmp}(i)$ of Kaula's equation [33]. The high frequency part of the zonal inclination function is generally greater as the orbital inclination is close to 90°. The high frequency range-rate signal due to the zonal coefficients increases as the inclination increases. Under the same noise level, a high amplitude signal provides a better observability and a better gravity solution. In other words, the accuracy of the high frequency zonal coefficients will be degraded for a low inclination orbit.

To identify the geographically correlated errors, the error level of the geoid height was computed from the solution covariance. The fourth of Figure 6.15 shows the RMS of the geoid height error along the latitude. The 83° case has a lower error level in the mid-latitude region but has a significant degradation in the polar regions. As like the degree difference variances, the 87° and 88.5° do not show significant degradation due to their relatively small gap sizes.

Figure 6.16 shows the gravity accuracy of the (99×99) solutions. In the case of the 83°, the zonal coefficient degradation is more significant than the (60×60) 83° case. Since this large degradation exceeds its tesseral coefficient improvement, the overall degree difference variance of the 83° case is much higher than that of the others. Unlike the (60×60) 87° case, the geoid error of the 87° case becomes significant in the polar region. It is because its minimum wavelength 3.6° is smaller than the gap size 6°. Two changes from the (60×60) results, the more degradation of the 83° case and the increased geoid error of the

87° case, prove that the impact of the polar gap depends on the minimum wavelength of the estimated gravity. The fact that the 88.5° case does not show high geoid error in the polar region can be explained by its relatively small gap size 3°.

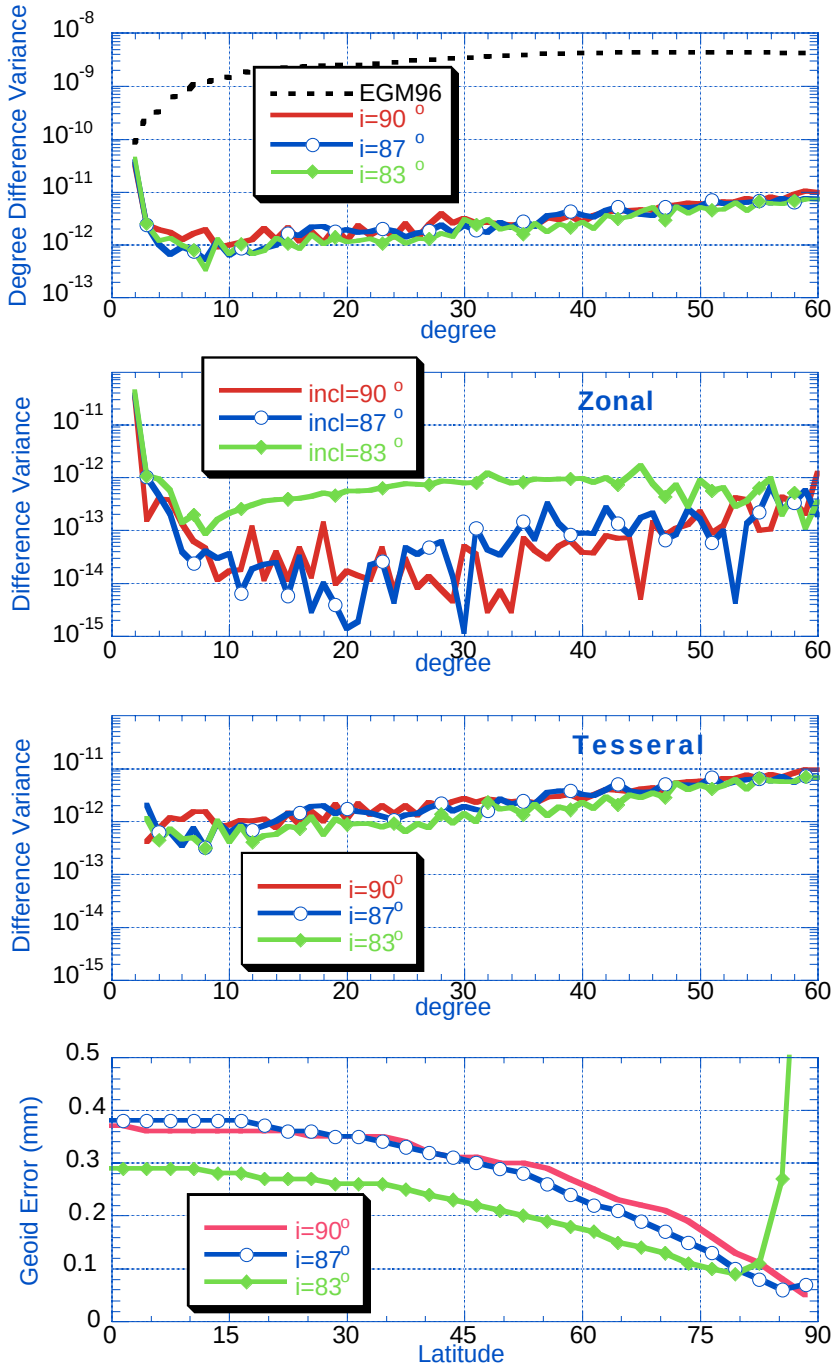

Figure 6.15 (60×60) gravity solutions for different inclinations

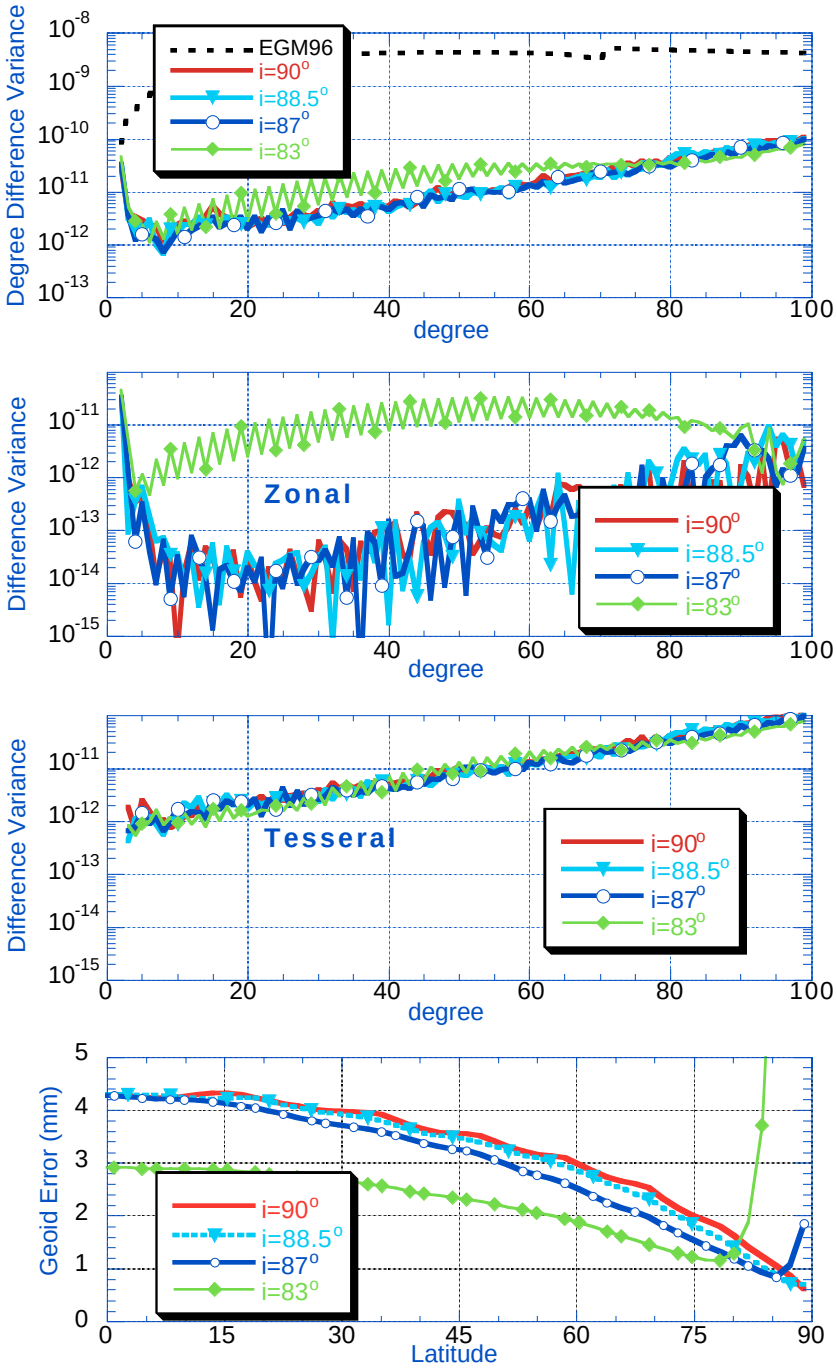

Figure 6.16 (99×99) gravity solutions for different inclinations

For more analysis on the 88.5° case, a set of (120×120) simulations were performed, and the results are presented in Figure 6.17. Since the (120×120) 88.5° case has the same size of minimum wavelength as the polar gap size 3°, it still does not show significant degradation. However, its geoid error begins growing in the polar region. Considering the 87° result change from the (60×60) to (99×99) cases, one can expect that even the 88.5° case would show some degradation if a much higher gravity field is estimated. Figure 6.18 shows the geoid error mapped into the Earth surface. The geoid RMS plot of Figure 6.17 is an average of these geoid errors along the longitude direction. The same latitude variation appears as the RMS plot. The longitude variation is not significant except some vertical patterns, but they can be reduced by using longer data spans or different empirical parameterizations.

With the consideration of the impact of the polar gaps on the zonal coefficients, the 90° inclination may be safe. Otherwise, the inclination should be selected for the minimum wavelength of the estimated gravity field to be greater than the polar gap size.

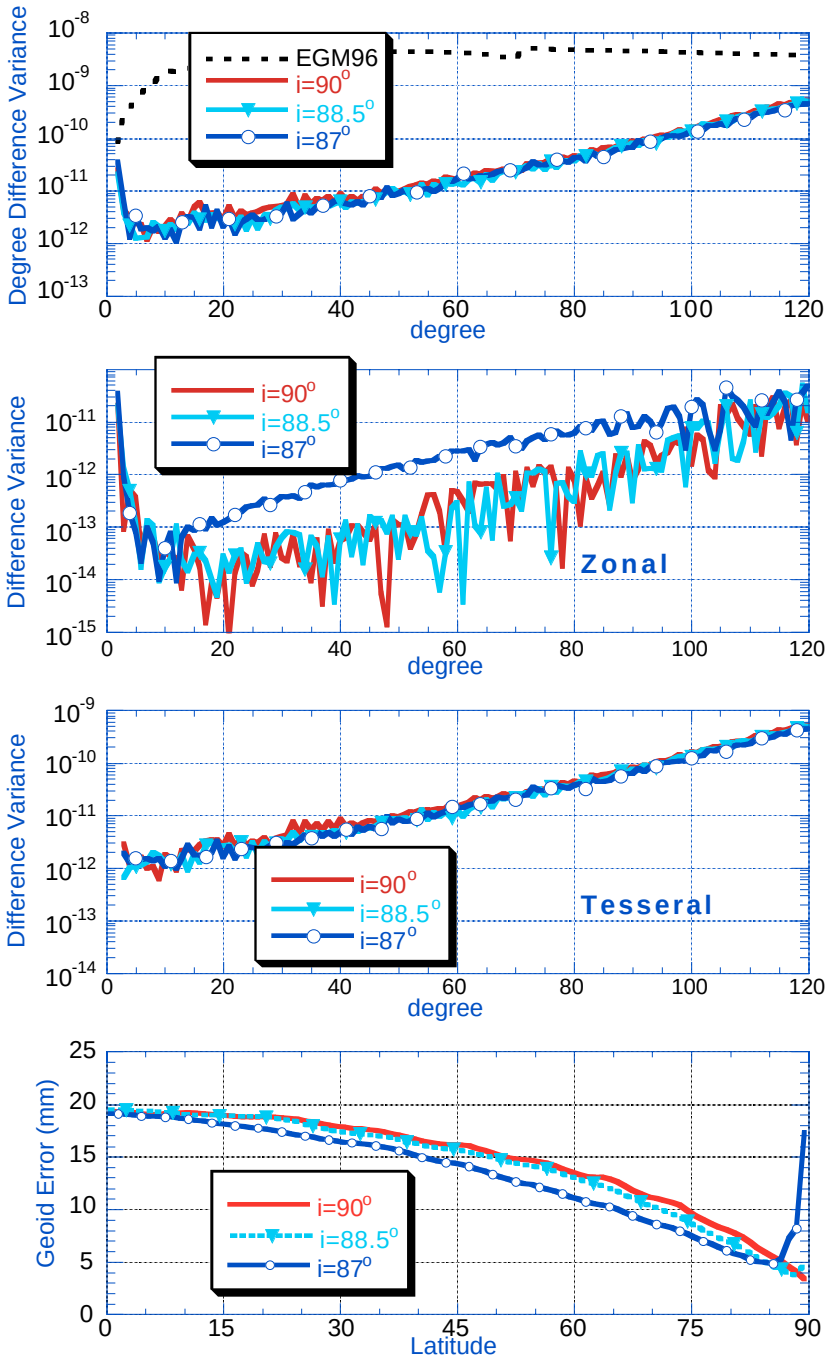

Figure 6.17 (120×120) gravity solutions for different inclinations

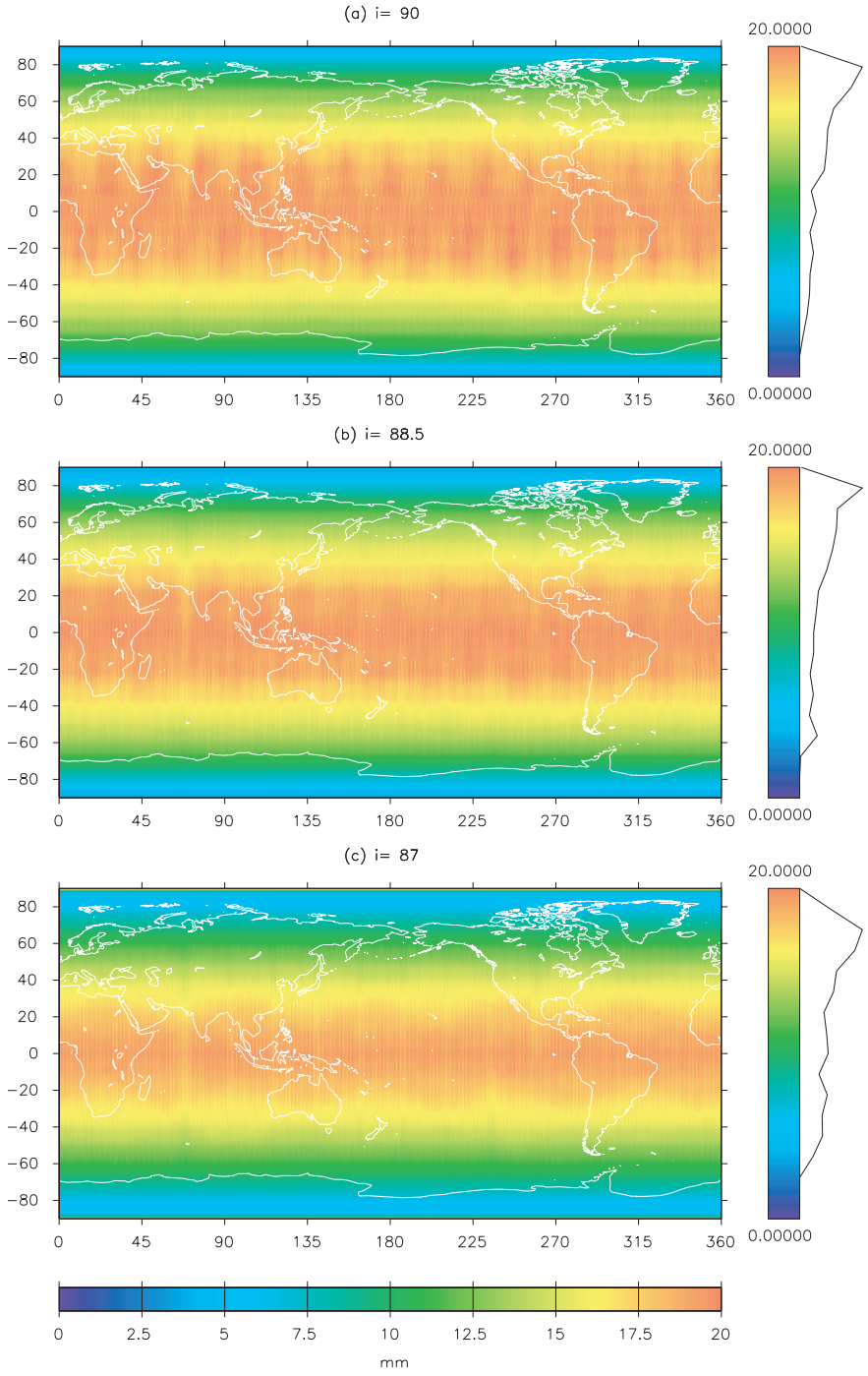

Figure 6.18 Geoid errors predicted from (120x120) solution covariance

6.3 MEASUREMENT TYPES

6.3.1 Low-Low SST Measurement Type

The primary observable of the GRACE mission is the biased-range, which is derived from the phase measurements of the two low satellites. The range-rate and range-acceleration measurements are then obtained by the numerical differentiation of the biased-range. Most of the numerical simulations in this study used the range-rate measurements for the gravity estimation. However, to prepare the use of range measurements in the actual mission, all the simulated SST noises were generated as the range noise and then differentiated to get the range-rate noises. With this approach, the correlation between the range and range-rate measurement noises makes it possible to compare the two measurements quantitatively. This type of the consistency is different from the previous studies [65], where the two noise types are not correlated. This section compares the characteristics of the range and range-rate measurements by numerical simulations and signal analyses.

One of the crucial factors determining the range-rate measurement characteristics is the way of differentiation. In the actual GRACE mission, a sophisticated differentiation filter may be used [71] to reduce the distortion during the conversion from the range to the range-rate. However, it is under development at this moment and further study is necessary for its optimal use. In this study, the no-error range-rate measurements were computed by using the range-rate equation of (2.25). This range-rate measurement does not include any numerical

errors due to the differentiation, and its quality may be better than the actual range-rate measurement. However, the simulated range-rate noise is obtained from the range by the numerical differentiation. The total range-rate signal is a sum of the no-error signal and the differentiated range noise signal. The comparison results can be changed if a different type of filtering is applied. In addition, the numerical differentiation introduces extra noise, and this makes the simulation results be pessimistic.

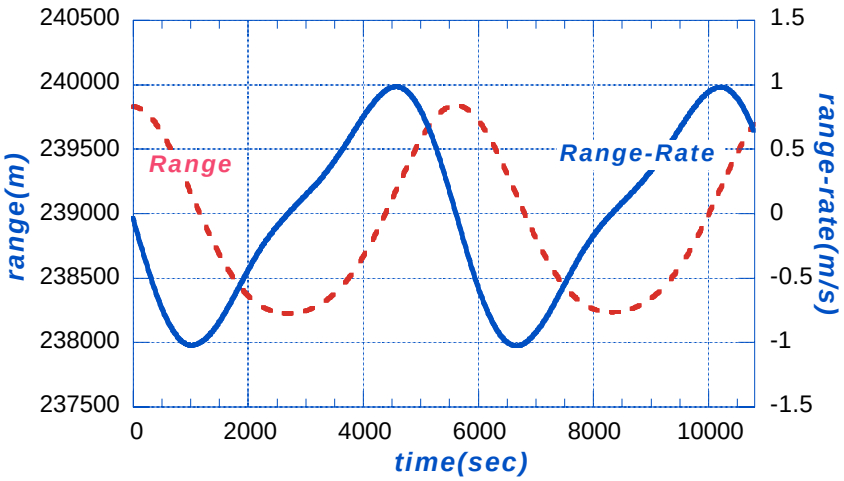

Figure 6.19 Time series of range and range-rate observations

Figure 6.19 shows the time series of the typical range and range-rate signals. The orbit altitude is 450 km with the orbit period of 5500 seconds. The inclination is 87° and the separation angle is 2°. The orbit eccentricity is 0.001. The range signal has the amplitude of 1 km with the mean value of 239 km. Its

dominant signal is 1-cpr (cycle-per-revolution) component mainly due to the orbit eccentricity. Since the time scale is short, a secular effect, which is dominant in the long term, is not shown in the graph. The range-rate signal has the amplitude of less than 1m/s, and 1-cpr signal is dominant. Two-cpr signal, which is due to the Earth oblateness, appears as well. The range-acceleration, which is not shown in the figure, has the amplitude of 1mm/s^2.

These measurement types can be better compared by analyzing their spectral components. In spectral domain, the differentiated signal amplitude becomes a multiplication of original signal amplitude and an angular frequency $(2\pi f)$, where f is a linear frequency. Upon this rule, the differentiation process amplifies the high frequency signals $(2\pi f > 1)$ but reduces the low frequency signal $(2\pi f < 1)$. Comparing the ratio of the high and low frequency signals, one can expect that the range-rate have more high frequency signal than the range but less low frequency signal.

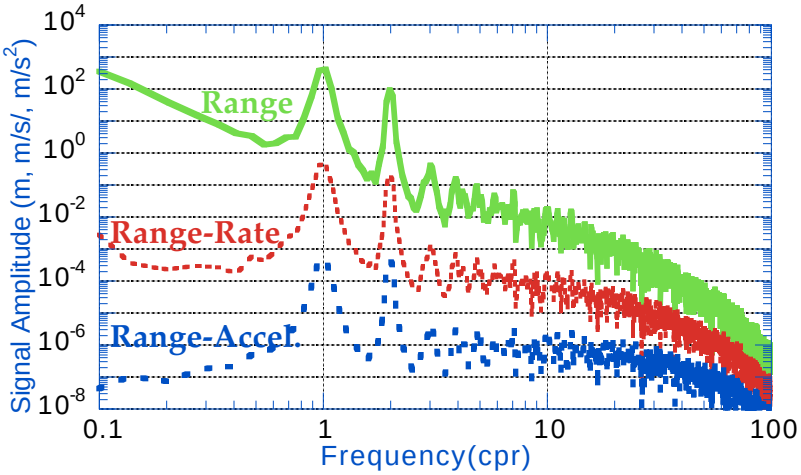

Figure 6.20 Amplitude spectrum of range, range-rate, and range-acceleration signals

Figure 6.20 compares the amplitude spectrum of the range, range-rate, and range-acceleration signals. As predicted by the analytic theory, the range-rate amplitude is close to the multiplication of the range by $(2\pi f)$ and the range-acceleration is the multiplication by $(2\pi f)^2$. With the 5500 seconds orbit period, 1-cpr frequency is about 0.001 rad/sec. The 1-cpr magnitude of the range-rate is about 1m/s and close to the multiplication of the range 1-cpr magnitude by the 1-cpr frequency, i.e. 10^3m $\times$ 0.001 rad/sec. The same relation is applied to the range-acceleration over the range-rate. Since the amplitude slope is affected by this amplification, the high frequency signal reduction is most significant in the range spectrum. The range has a strong signal at the low frequency but the range-acceleration has a relatively strong signal at the high frequency.

A strong signal at a certain frequency range does not imply a better gravity recovery at that frequency range. Instead, the gravity recovery accuracy is affected by the signal to noise ratio (SNR) between the gravity signal and the noise. The noise consists of the measurement noise and dynamic noise, and the latter is due to the orbit error and unknown force models. Of interest is the change of the noise amplitude as well as the signal amplitude along the frequency.

In the case of the range measurement processing, different measurement error characteristics should be considered. In Chapter 3, the choice of range-rate low-low empirical parameters is explained by using Hill's equations. Unlike the range-rate perturbation, the range perturbation includes a quadratic term (t^2) and it should be included in the empirical parameterizations as

$$\rho_{obs} - \rho_{nom} = A + Bt + Ct^2 + (E + Ft)\cos u + (G + Ht)\sin u \qquad (6.2)$$

where C is the quadratic empirical parameter. Inclusion of this parameter improves the gravity solution of the range measurement case, but it does not improve the range-rate solution. A cubic empirical parameter (t^3) was also experimented for the range measurement, but it does not improve the gravity solution. These facts prove that the selection of the empirical polynomial orders, linear for the range-rate and quadratic for the range, is appropriate to handle the SST errors.

To fully incorporate the dynamic noise, e.g. orbit error, full numerical simulations are necessary instead of the analytic or semi-analytic method, where the orbit error is neglected. Several sets of numerical simulations were performed for the estimation of (50×50) gravity fields by using 7 day range and range-rate measurements. The range-acceleration was also examined, but its high dependency on the nominal orbit accuracy restricts its application. If the nominal orbit is very close to the truth orbit, e.g. the truth gravity field as the nominal under no accelerometer errors, the range-acceleration solution is better or equivalent to either the range or the range-rate solution. However, in conventional cases, e.g. an inaccurate nominal gravity field and the presence of the accelerometer errors, its solution is much worse than the others are. This fact can be explained by the lack of the low frequency signal in the range-acceleration. Proper use of the range-acceleration requires a further study, and it is not covered in this study.

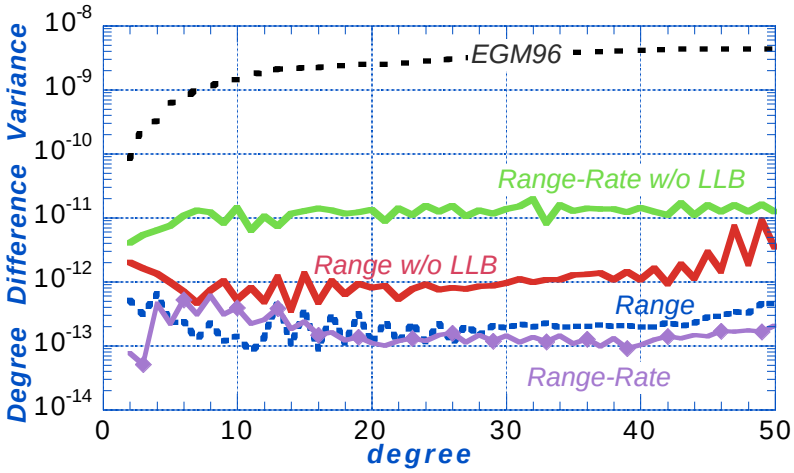

Figure 6.21 Comparison of range and range-rate gravity solutions (with and without low-low empiricals)

Figure 6.21 compares two sets of (50×50) gravity solutions and each set includes the range and range-rate solutions. One set is obtained by adjusting the dynamic empirical parameters only, constant and 1-cpr parameters. The other set is obtained by adjusting both the dynamic and low-low empirical (LLB) parameters. None of the SST and accelerometer errors was applied.

Without the low-low empiricals, the range solution is far better than the range-rate solution, especially in the low degree (frequency) region. After adjusting the low-low empiricals, the improvement of the range-rate solution is greater than that of the range solution, so that the two solutions now have the same level of accuracy. It implies that the low-low empirical parameterization is more effective on the range-rate solution. This different effectiveness can be explained by analyzing the signal residuals before and after applying the low-low empiricals. The signal residual (O-C) is the difference between the simulated

(Observation) and nominal (Computed) signals, where the latter is generated from the updated gravity and orbit parameters.

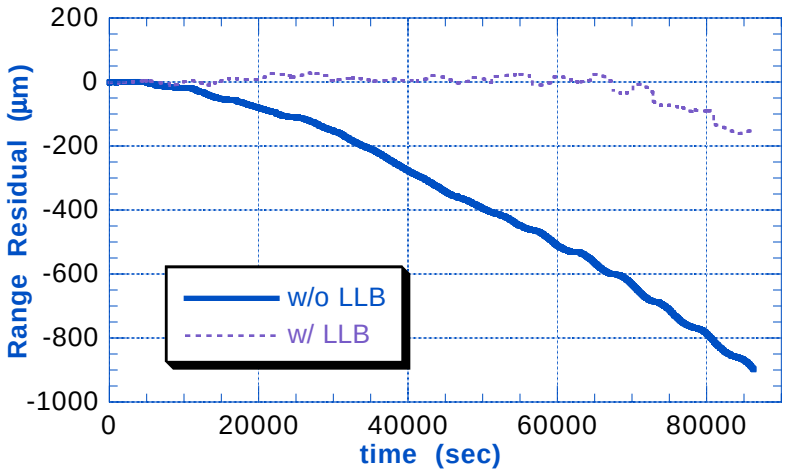

Figure 6.22 Range residual time series (with and without low-low empiricals (LLB))

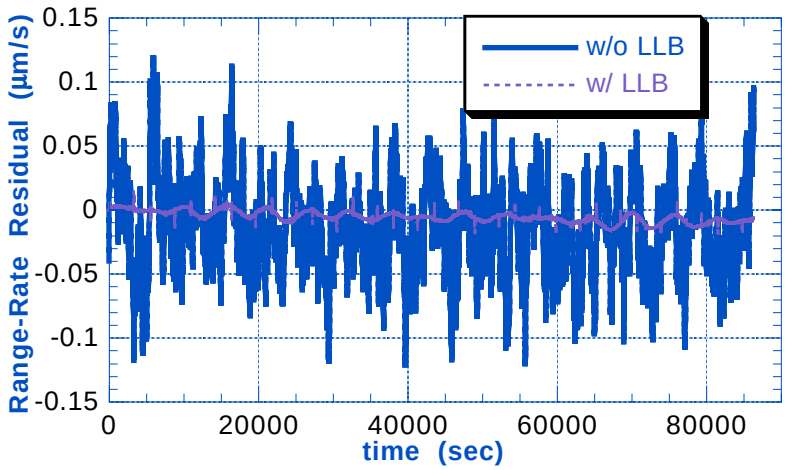

Figure 6.23 Range-rate residual time series (with and without low-low empiricals (LLB))

Figure 6.22 shows the range residuals before and after the low-low empirical parameterizations. Figure 6.23 shows the range-rate residuals. As predicted from Hill's equations, the range residual shows a strong secular behavior or drift without the low-low empiricals, but the range-rate does not show significant drift. The strong secular behavior of the range residual makes it difficult to remove by adjusting the low-low empirical parameters. Even after adjusting the low-low empiricals, the range residual still has some drift. The arc lengths of the low-low empiricals were 45 minutes (coefficients *A*, *B*, *C*) and 90 minutes (*E*, *F*, *G*, *H*). In general, a dense parameterization is necessary to adjust this type of strong drifts, but this causes more discontinuities at the arc points. For example, 45 minute arc length yields 31 (=32-1) discontinuities for one day. Since the gravity signal is a continuous quantity, this kind of discontinuity degrades the gravity solution and it should be minimized. Series of simulations were performed with different arc lengths, but no improvement was achieved. Another type of parameterization, e.g. smooth filtering or no discontinuities, may be helpful for this problem.

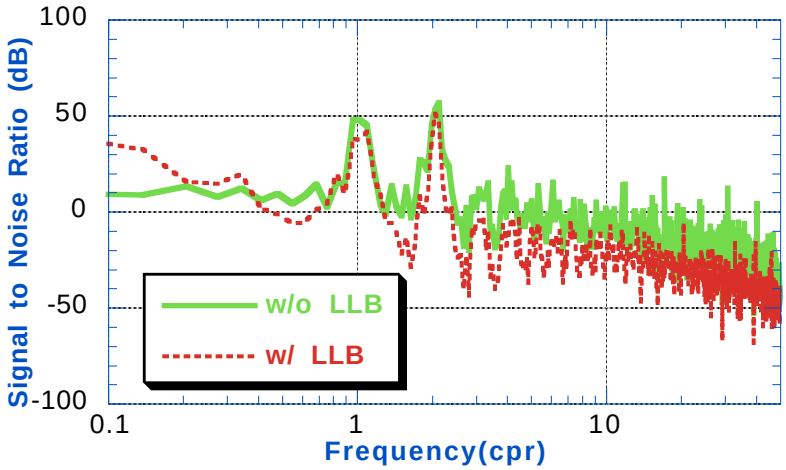

Figure 6.24 Effect of the low-low empirical (LLB) parameterizations on the range SNR

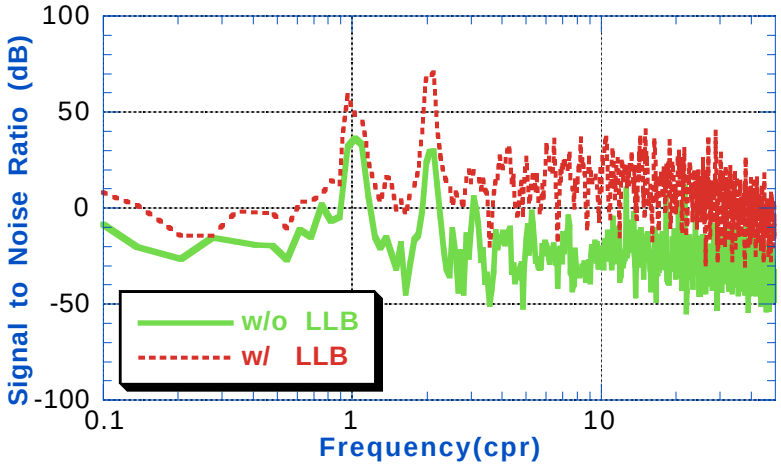

Figure 6.25 Effect of the low-low empirical (LLB) parameterizations on the range-rate SNR

This parameterization effectiveness can be explained by the signal-to-noise ratio (SNR) between the gravity signal and the residual. Figures 6.24 and 6.25 show the range and range-rate SNR before and after the low-low empirical

parameterizations. Before the low-low empirical parameterizations, the range shows a higher SNR than the range-rate over all frequency range. After the parameterizations, very low frequency part (< 0.5 cpr) of the range SNR is increased but the other frequency part is same or even lower than before. The decrease of the high frequency SNR is due to the inaccurate low-low parameterization. Unlike the range SNR, the range-rate SNR is increased over all frequency range after the parameterization.

Even without the low-low empiricals the range has positive SNR (dB) values over almost all frequency range and has a higher SNR than the range-rate especially at the low frequency. Since the low-low empirical parameterization is applied to only the very low frequency noise (≤ 1 cpr), one can expect that the contribution of the low-low empiricals on the range is not as much as the contribution on the range-rate.

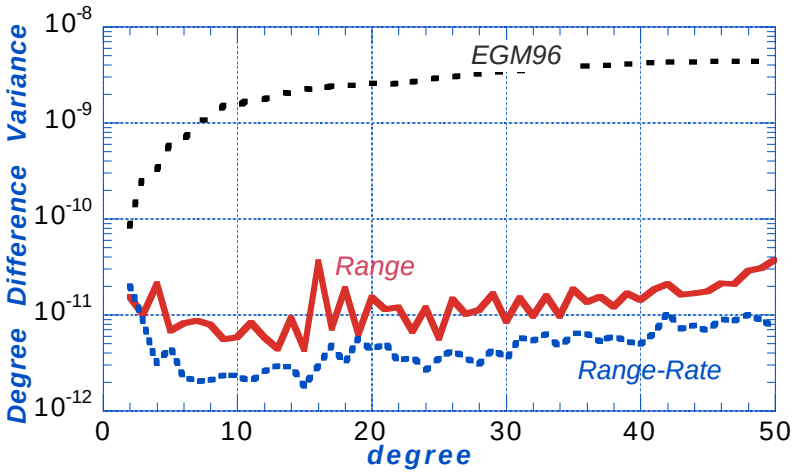

Figure 6.26 Range and range-rate solutions when the SST and accelerometer errors are applied

When the actual errors are applied, the range solution is more affected by the errors than the range-rate solution is. Figure 6.26 compares the range and range-rate solutions when all the SST and accelerometer errors are applied. The range solution is slightly worse than the range-rate solution over all the degrees.

Considering the incomplete low-low empirical parameterization on the range measurements, one can expect that a better way of the empirical parameterization may improve the range solution. It is noted that these comparison results are subject to the differentiation filtering method and the empirical parameterizations. Instead, this study can be used to develop or select the differential filter and empirical parameterization.

All the gravity estimation procedures have been developed for using either the range or range-rate. At this moment, it is not necessary to decide which measurement type should be used in the actual mission. At the initial mission period, both measurements would be processed and their gravity solutions would be compared to decide which measurement type is better for the gravity recovery.

6.3.2 Combination of GPS and SST Information

Since the SST measurement is the relative distance between two satellites, it does not provide enough information to estimate the absolute states of both satellites. This singularity makes it necessary to use the GPS measurements as supplements during the estimation process. The GPS and SST measurements are used to make a GPS information matrix and a SST information matrix,

respectively. Due to lower accuracy of the GPS measurements, the GPS matrix contains a less accurate orbit and gravity information than the SST matrix does and it is mainly used to mitigate the singularity of the SST information. Since most singularity of the SST information is contained in the estimates of orbit initial conditions, the gravity coefficients can be estimated solely from the SST matrix without the GPS information as long as the orbits are not estimated. However, the gravity solution is closely related to the orbit error, and the SST only gravity solution is less accurate than the combined solution. It is necessary to determine the orbit and gravity simultaneously for the best gravity recovery.

All the simulations in this study combine the same size of the GPS and the SST information matrices. However, it seems possible that a smaller size GPS information matrix could be used to save computing time since the GPS information does not contain the same high frequency gravity information as the SST. Series of numerical simulations were performed by combining a (70×70) SST information matrix with a (60×60) GPS matrix by changing various simulation parameters.

As for the usual numerical simulations, this case used the 100% EGM96 clone gravity field as a nominal gravity field. The clone gravity fields were generated by using the covariance matrix of the truth field (EGM96) as described in Section 3.2. The deviation from the truth gravity coefficients can be controlled by scaling the covariance matrix but no scaling is applied for the usual clone. The percentage numbers (100%, 10%, and 0%) represent the coefficient difference ratio between the truth and clone gravity fields. The 100% means that the coefficient difference level is the same as the uncertainly level (1σ) of the truth

one. The 10% means the covariance level is reduced to one-tenth of its original value and its clone gravity field is much closer to the truth one than the 100% clone.

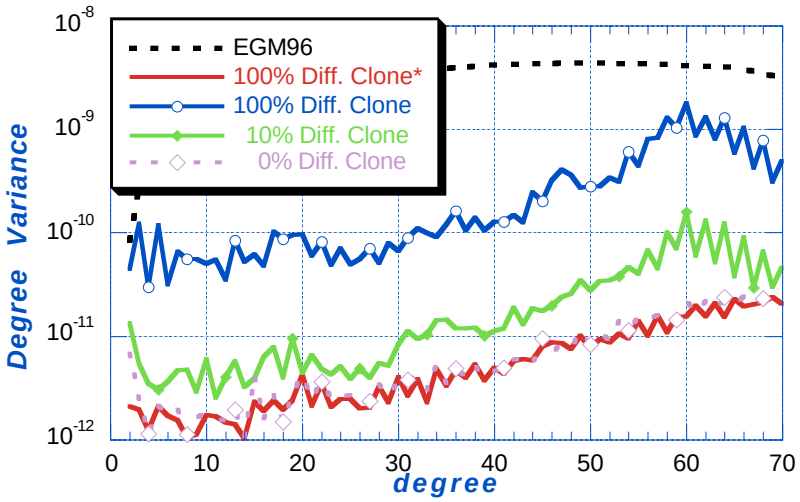

Figure 6.27 Gravity estimates by combining (60×60) GPS and (70×70) SST information matrices (* uses (70×70) GPS) with different nominal gravity fields

Figure 6.27 shows the four simulation results with the different nominal gravity fields. The first case (100% difference. clone*) is the standard one by combing the same sizes of the GPS and SST matrices. The second through forth ones (100%, 10%, 0% difference. clones) use the GPS information matrix of the (60×60) gravity field, and the second case shows more than an order of magnitude degradation. The third case (10% difference clone) uses a more accurate nominal gravity field and shows the more accurate solution than the second one. The

fourth one (0% difference clone) uses the same truth gravity field as the nominal field and produces nearly the same accuracy as the standard results.

These results imply that the estimation accuracy depends on how close the nominal dynamic model is to the truth model. A more accurate dynamic model yields a more accurate gravity solution. However, the standard simulations, which combine the same size of the GPS and SST information matrices, hardly depend on the accuracy of the nominal gravity field. In other words, a more accurate nominal gravity does not produce a better gravity solution in the standard simulations. It is related to the robustness of the estimation process. The standard case, i.e. the same size of the GPS and SST matrices, is a more robust estimation than the mixed-size cases. The 10% and 0% cases show a large degradation in degree 2 since lack of the gravity signals between degree 61 and 70 mainly affects the J_2 signal.

In real world, the 0% difference clone or the true gravity field is not available, and an alternative gravity field, which is close to the true gravity field, e.g. 10% difference clone, should be used instead. After first several months from the GRACE mission, a gravity estimate from the GRACE mission will be available and this may be the closest one to the true gravity field at that time. The level of this GRACE tuned gravity field would be equivalent to the results from the (70×70) GPS and the (70×70) SST matrices. The question is whether this gravity field is close to the true field for utilizing the smaller size of GPS matrix or not. Another simulation was performed with the GRACE tuned gravity as the nominal gravity field instead of the clones. With this improved gravity, the combined solution with the (60×60) GPS and the (70×70) SST matrices was

nearly identical to the standard one. Therefore, it is possible to use a smaller size of the GPS information matrix after an improved gravity field is obtained.

With these results, the following estimation procedure may be planed for the gravity estimation. The gravity field will be estimated every one month during the GRACE mission, but the estimation procedure may be different for three periods. During the first several months, full-size GPS information matrix, i.e. same size as the SST matrix, needs to be produced. This process will provide a substantially improved gravity field, which is close to the true Earth gravity field. With this accurate nominal gravity field, several types of processing may be performed with the different sizes of the GPS information matrices. This experiment determines the minimum size of the GPS gravity field to obtain the equivalent level of the gravity solution as the standard one. The third processing period would use that minimum size GPS matrix and it would save substantial amount of computing time.

6.4 SPECTRUM OF THE SST SIGNAL

This section describes the spectral analysis of the inter-satellite signals in order to analyze the effect of some non-gravitational force related errors on the gravity recovery. In order to analyze the relationship between the non-gravitational force related errors and specific gravity coefficients, e.g. resonant terms, it is necessary to identify resonant terms in the GRACE orbit. As for other near Earth satellites, the GRACE satellites would experience large perturbations

caused by the resonance of the Earth gravity force. This effect will occur when the secular rates of the arguments, which are in some terms of Kaula's disturbing function, become so close to zero that their periodic variation could be more significant [33]. The frequency function may be given by

$$\dot{\psi}_{nmpq} = (n-2p)\dot{\omega} + (n-2p+q)\dot{M} + m\left(\dot{\Omega} - \dot{\theta}\right) \tag{6.3}$$

where

ω = argument of perigee

M = mean anomaly

Ω = right ascension of node

θ = right ascension of Greenwich

n, m = degree and order

p = inclination function variable ($0 \le p \le n$)

q = eccentricity function variable ($-\infty \le q \le \infty$)

A deep resonance occurs if this frequency is equal to zero and a shallow resonance occurs if it is close to zero. The periodic perturbation with an ($nmpq$) index combination contributes to the total perturbation as follows [56]

$$T_{nmpq} = \frac{2\pi}{\left|\dot{\psi}_{nmpq}\right|} \tag{6.4}$$

Since the orbit elements vary along the altitude, the shallow resonance period varies along the altitude.

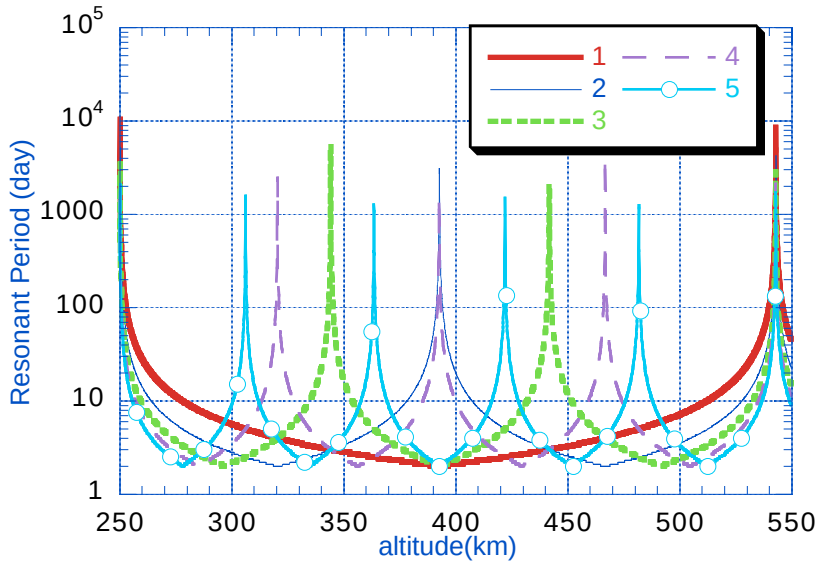

Figure 6.28 Resonance periods for different resonant orders and altitudes

Figure 6.28 shows the variation of the resonance period along the altitude. The deep resonance occurs at the two altitudes, 250 km and 540 km. Since both of the altitudes are out of the GRACE altitude range, between 300 km and 500 km, the GRACE satellites would avoid such a big perturbation. The numbers, one through five, represent the resonance order. The primary order is between 15 and 16, and the other orders are the integer multiples of the primary order. For example, at 450 km, the order three resonance, which is due to the order 46 gravity coefficients, has a period of ten days, while the others have less than five day period. This implies that a ten-day arc length is necessary to estimate the order 46 coefficients at 450 km. However, a shorter arc length is preferred since it provides better orbit fit and enables more efficient concurrent processing. Therefore, the degradation of the order 46 coefficients may not be avoided with a

short arc-length. Instead, the order 46 coefficients estimated at the higher altitude could be used as a priori value at the 450 km. These curves enables one to predict which gravity coefficients would have low observability at a specific altitude.

Most of the numerical simulations in this study used one-day or shorter arc-lengths; one day for initial conditions and several hours for empirical parameters. Extensive numerical simulations were performed by changing the arc-length up to five days. The longer arc-lengths were applied for not only the initial conditions but also the empirical parameters. However, these long arc-lengths degraded the orbit accuracy, and the gravity improvement by the longer arc-lengths was not significant in most cases. With the consideration of actual computing time, the short arc-length is preferred since it enables one to process multiple days of observations simultaneously.

To examine the effect of a specific set of gravity coefficients on the SST signals, two SST observation time series were generated, and then differentiated. One was generated with a two-body term only and the other was generated with the two-body term plus a specific term, e.g. J_2 or resonant terms. One-day orbit with 451-km altitude was analyzed.

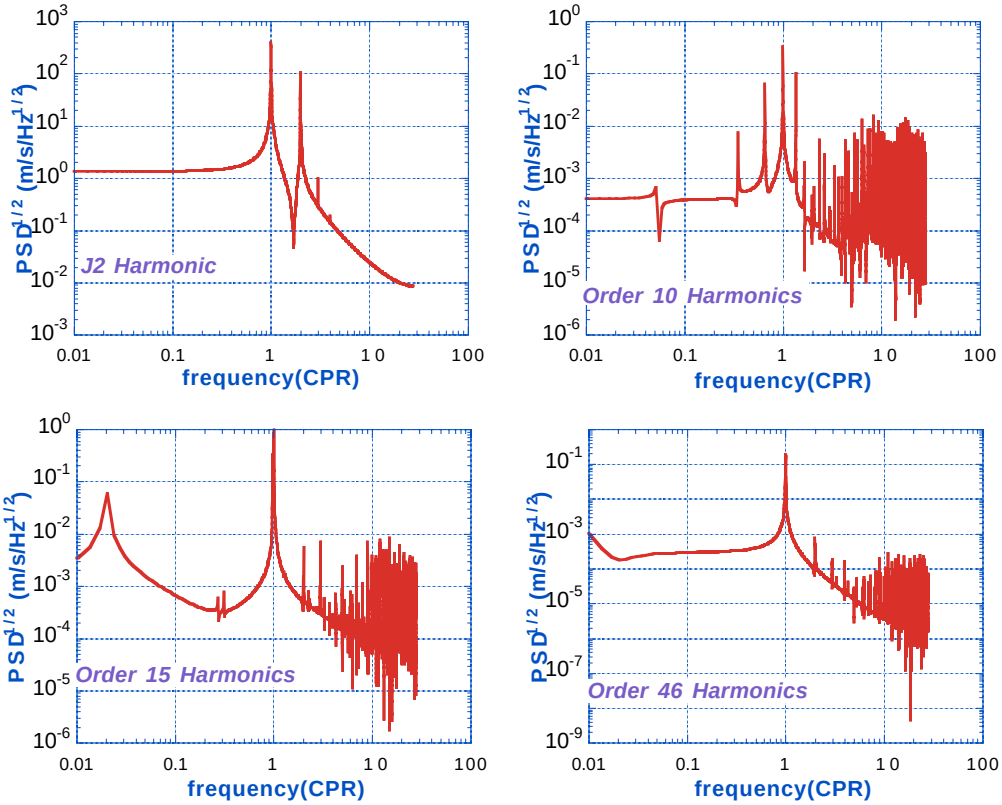

Figure 6.29 SST range-rate signal spectrum due to several sets of gravity coefficients

Figure 6.29 compares the range-rate signal spectrums due to J_2, order 10, order 16, and order 46. The GRACE orbit has the first order resonance near order 15. Most of the 1-cpr (cycle-per-revolution) signals are caused by the orbit difference. Beside the 1-cpr signal, the 2-cpr signal of the J_2 case shows a high magnitude. The order 15 case shows a tone signal, which has the peaks at *N*-cpr frequencies, e.g. 2-cpr, 3-cpr, etc. Its very low frequency peak (3 days period) corresponding to the resonance period will be discussed later. The order 46, which

is the third resonance order, has similar tone signals as the order 15 case. On the other hand, the order 10 case, which is a non-resonant term, has peaks, which have the offsets from the *N*-cpr frequencies, and do not have exact or close tone frequencies. The presence of this offset is a major difference between the resonant and the non-resonant signals. The numerical simulation in Chapter 5 with the accelerometer misalignment error shows the large degradation in the resonant terms. This degradation is due to the similarity between the misalignment error and non-gravitational signals. As shown in Chapter 3, the non-gravitational accelerations, i.e. atmospheric drag and radiation pressure, have the tone signals at *N*-cpr frequencies. Therefore, the misalignment error has the similar characteristics as the resonant term induced signals, and this similarity degrades the accuracy of those coefficient estimates.

The existence of the *N*-cpr signals in the resonant terms can be explained by analyzing the frequency function $\dot{\psi}_{nmpq}$ in (6.3). Roughly speaking, a satellite rotates the Earth m_o times per day, where m_o is a primary or lowest resonant order, e.g. 15. The mean anomaly frequency $\dot{M}$ may be approximated as an integer multiple of the Earth rotation rate $\dot{\theta}$ and m_o:

$$\dot{M} \approx m_o \dot{\theta} \tag{6.5}$$

Considering the slow variations of the argument of perigee and right ascension, $\dot{\omega}$ and $\dot{\Omega}$ can be ignored in the frequency function and $\dot{\theta}$ may be replaced with $\dot{M}$ as follows:

$$\dot{\psi}_{nmpq} \approx k\dot{M} - m\dot{\theta}$$

$$= \left(k - \frac{m}{m_o} \right) \dot{M} \tag{6.6}$$

where $k = (n - 2p + q)$ represents an integer number. The ratio m / m_o becomes an integer for the resonant term whose order m is the integer multiple of the primary resonant order m_o. In this case, the frequency $\dot{\psi}_{nmpq}$ becomes an integer multiple of $\dot{M}$, in other word, $N = (k - m / m_o)$ cpr. This frequency causes the N-cpr peaks in the SST signal spectrum. On the contrary, $(k - m / m_o)$ becomes a non-integer value for the non-resonant terms, so that $\dot{\psi}_{nmpq}$ has an offset from the N-cpr frequency.

Figure 6.30 shows the amplitude spectrum of the range-rate signal sampled at each order and frequency. An analytic method developed by Sharma [65] was used to reduce the computation time, instead of the numerical method used for the Figure 6.29. Each horizontal bin represents 0.5-cpr frequency region, and the horizontal intervals are [0, 0.25], [0.25, 0.75], [0.75, 1.25], … cpr. The difference between the resonant signal (around order 15 and 30) and the non-resonant signal (around order 10 and 23) clearly shows that the resonant signals have strong N-cpr signals. Very low order terms (< order 4) have similar tone signals, and their estimation accuracy also depends on the accelerometer/SST tone errors.

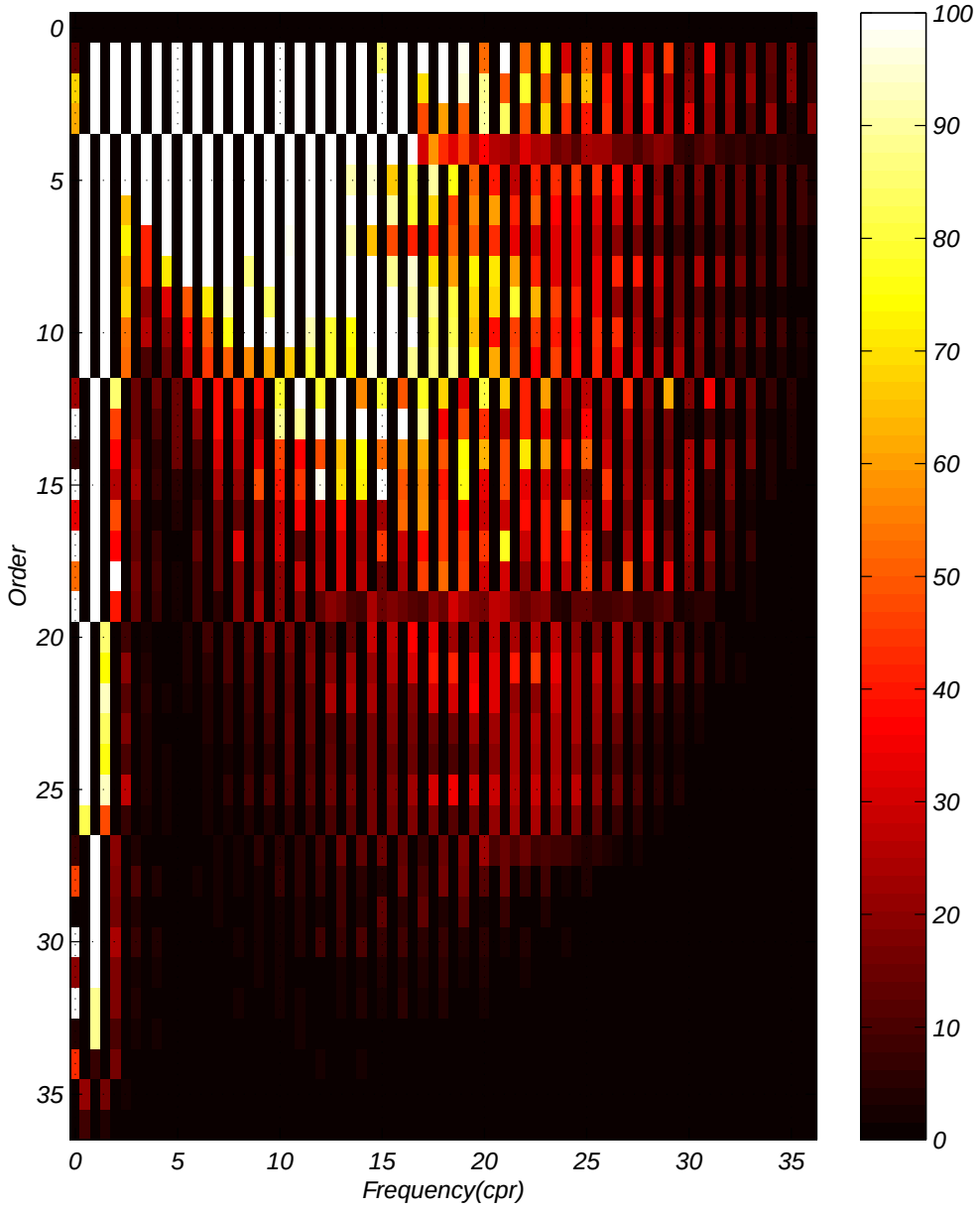

Figure 6.30 Amplitude spectrum of the range-rate signal for each order and frequency (unit = μm/s)

6.5 EXPECTED GRAVITY RECOVERY ACCURACY

This section describes the expected gravity accuracy from the GRACE mission. As described in the previous sections, the gravity recovery accuracy depends on various parameters and it is not easy to select one gravity estimation results for discussing the expected accuracy. Among various results, one typical simulation result is selected to discuss the expected accuracy. A (120×120) gravity field was estimated by using 32 day measurements. The orbit conditions include 88.5° inclination, 2° separation angle, and 448km initial altitude. The inter-satellite oscillator, system, and multipath noise were applied. The accelerometer random, attitude, and misalignment errors were applied. The empirical parameters were adjusted. With the assumption that all the significant error sources were applied in the simulations and an optimal estimation method was used, one can predict the estimated gravity accuracy from the simulation results.

The expected geoid height errors predicted by these numerical simulations are presented in Figure 6.31. The geoid height error is obtained by multiplying the degree difference variances with the Earth radius R_e. It shows up to 1000 times improvement over the EGM96 that represents the current knowledge level of the Earth gravity field.

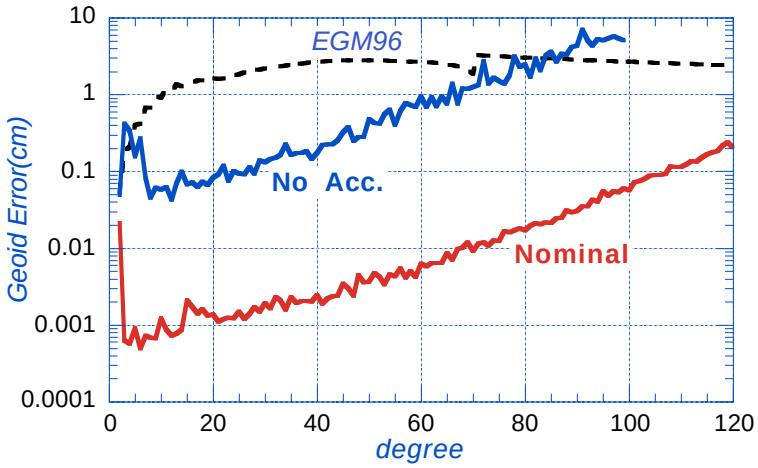

Figure 6.31 Expected geoid height error predicted by numerical simulations

A worst case is performed without any accelerometer measurements of the two satellites. However, the low-low SST measurement is still available and the accelerometer measurement is replaced by a nominal non-gravitational model. DTM atmospheric model was used for the truth model and MSIS was used for the nominal model. The solar and earth radiation forces are applied with 5% errors of reflectivity, Earth albedo and emissivity parameters. The low-low SST error model is the same as the nominal. This less accurate non-gravitational information degrades the gravity solution by two order of magnitude. This degradation can be reduced using more accurate non-gravitational model. Another consideration is the loss of the low-low SST measurement but this result is not plotted. This is the same as the usual high-low SST mission with two satellites and accelerometers. In this case, the gravity improvement is confined to very low degrees (<30).

Table 6.3 Geoid height error predicted by the numerical simulation - the nominal case (unit = cm)

Harmonic Degree	**Cumulative** (from n=3)	**Per Degree**	**Cumulative (EGM96)** (from n=3)	**Per Degree (EGM96)**
n = 2	-	0.02	-	0.05
3 ≤ n ≤ 10	0.002	< 0.001	1.76	< 0.97
11 ≤ n ≤ 40	0.009	< 0.002	10.93	< 2.66
41 ≤ n ≤ 70	0.033	< 0.012	18.07	< 2.78
71 ≤ n ≤ 100	0.183	< 0.060	24.21	< 3.25
101 ≤ n ≤ 120	0.657	< 0.239	26.71	< 3.25

The geoid error of the nominal case is cumulated up to degree 10, 40, 70, 100, and 120. These values are listed in Table 6.3. The degree 2 value is excluded from those cumulative values since its error level is usually much higher than the other degree terms and subject to change. The maximum per-degree errors are also presented and compared with the EGM96 error levels, which represent the current knowledge level of the Earth gravity field. About three order of magnitude improvement can be obtained over the EGM96 accuracy in the low degrees and one order of magnitude can be obtained in the high degrees. To the extent that the error sources assumed in these simulations represent the actual errors, the GRACE mission will provide a significant improvement in the Earth gravity field knowledge.

7 CONCLUSIONS

7.1 SUMMARY AND CONCLUSIONS

This study analyzed the effect of the error sources on the performance of the GRACE mission. Most of the significant error sources were described and implemented in the simulations. With these error models, extensive numerical simulations were performed to quantify the effect of the error sources on the gravity and orbit estimation.

Formulations for processing the GPS and SST measurements were derived. With the dual one-way ranging system, the oscillator noise, which is the most significant error source on the microwave ranging measurement, can be effectively reduced. This enables the measurement of the biased-range between the two GRACE satellites with an unprecedented accuracy. Processing the GPS double difference measurements was described as well. The measurement partial equations were derived, which were implemented in the MSODP orbit determination program and used for the numerical simulations. Several empirical parameters were applied to reduce the dynamic and measurement model errors.

The dynamic force models, the gravitational and the non-gravitational models, were described and their signal characteristics were analyzed. Computing the optimal weighting of the information equations was described. To overcome the available computational limit, a semi-analytic method was used for predicting the geoid error spectrum in the high degree field above degree 100.

The error models of the inter-satellite measurements were described. All the error models were developed as a range error time series so that either the range-rate or range-acceleration error time series can be easily obtained by numerical differentiation. This range error approach makes it possible to compare the range and range-rate measurement characteristics more accurately. The other SST errors, which were related to the actual data processing, but not included in the simulations, were also described. These errors included the time tag error and the instantaneous range correction. Both of the errors are closely related to the pre-processing so that their implementation should be done simultaneously with the pre-processor development. The accelerometer error models included the scale factor error, bias error, random noise, attitude error, misalignment error, and CM-offset error. The estimation parameters used for adjusting these errors were the scale factors and biases. The simulation results prove that these parameters can be estimated with a sufficient accuracy.

Series of the extensive simulations were performed to analyze the impact of the various simulation parameters, which included the orbit selections, measurement types, and so on. The orbit selection issues include inclination, altitude, and separation. The effect of the orbit parameters was analyzed by numerical simulations and the semi-analytic method. The difference from the previous studies is the consideration of the instrument noise level change due to the orbit parameters, e.g. altitude and separation. This kind of comprehensive error modeling enables more realistic sensitivity studies. The simulation results on the inclination quantified the effect of the polar gap on the gravity estimation. The

polar gap size should be smaller than the minimum wavelength of the estimated gravity field. Therefore, the inclination selection depends on the maximum gravity field to estimate. In case of the separation distance analysis, the SST noise level increase for a larger separation should be considered. This type of measurement noise increase also affects the altitude analysis, where the accelerometer noise increase becomes significant at the lower altitude.

The comparison between the range and range-rate measurement is also described. With current empirical parameterizations, the range-rate solution is better than the range solution. The refinement of the empirical parameterization and differential filtering may affect the analysis. The combination of the GPS and SST information matrices is studied by applying a smaller size of the GPS matrix. The orbit resonant characteristics are examined for better understanding of its effect on the SST measurements.

To the extent that the error sources assumed in these simulations represent the actual errors, the GRACE mission will provide a significant improvement in the Earth gravity field. The presented simulation results are useful for design and trade studies and can be a guide for developing data processing methodologies.

7.2 RECOMMENDATIONS

The actual size of the gravity estimate by the GRACE mission will be greater than that of the current simulations. A parallel linear system solver is being developed at the UT/CSR, and it will make it possible to solve a larger

gravity field with less computing time. The high frequency feature of the gravity signal and measurement noise can be well analyzed with this capability.

Estimating the time varying gravity field with a high precision would be a challenge since the satellite altitudes and ground tracks are changing during the estimation interval. The measurement noise characteristics and the other dynamic forces are changing as well. The impact of those variations on the gravity estimate needs to be examined to extract the gravity variation signal accurately. Combination of the GRACE gravity data with the terrestrial data can be another topic. The combination of the GPS and SST measurements needs further study, e.g. optimal weightings and GPS gravity sizes.

The measurement noise model can be appropriately implemented with the development of the pre-processor for handling the actual measurements. More realistic noise models are helpful to develop a more proper empirical parameterization. The accelerometer measurement processing is a critical part of the mission, and the current dynamic approach might be improved by applying another approach. Comprehensive models on the GPS measurements are necessary to process real GPS measurements. More simulations on the instrument failure, e.g. accelerometer failure, are helpful to analyze their effect on the mission.

APPENDIX A SKETCH OF HILL'S EQUATIONS

A.1 HILL'S EQUATIONS

The GRACE satellite's nominal orbit is near circular and an analytic form of perturbation equation is available for the near-circular orbits. For circular reference orbit with the mean motion of $n = \sqrt{\mu / r_o^3}$, the perturbation equation may be given by

$$\begin{aligned} \ddot{u} - 2n\dot{v} - 3n^2 u &= f_u \\ \ddot{v} + 2n\dot{u} &= f_v \\ \ddot{w} + n^2 w &= f_w \end{aligned} \tag{A.1}$$

Where (u, v, w) are the perturbed components in the satellite radial, transverse, and nominal directions. The right side terms f_u, f_v, and f_w denote the disturbing force in three directions. These are sometimes called Hill's equations [32]. Small perturbed motion in radial and normal directions are assumed, but there are no assumptions on transverse motion.

Hill's equations are not solvable in general. However, some analytic solutions are available for some special cases. The homogeneous solution represents the orbit perturbation caused by the initial condition errors. For the initial position error (u_0, v_0, w_0) and the initial velocity error $(\dot{u}_0, \dot{v}_0, \dot{w}_0)$ without perturbing forces, the solution is given by the following expressions

$$u(t) = \left(-3u_o - \frac{2}{n}\dot{v}_o\right)\cos nt + \frac{\dot{u}_o}{n}\sin nt + \left(4u_o + \frac{2}{n}\dot{v}_o\right)$$

$$v(t) = \frac{2}{n}\dot{u}_o\cos nt + \left(6u_o + \frac{4}{n}\dot{v}_o\right)\sin nt - (6nu_o + 3\dot{v}_o)t + \left(v_o - \frac{2}{n}\dot{u}_o\right)$$

$$w(t) = w_o\cos nt + \frac{\dot{w}_o}{n}\sin nt \qquad \text{(A.2)}$$

For the perturbing force function expressed in a Fourier series, an analytic solution exits. If the force function is given by

$$f_i = P_i\cos\omega t + Q_i\sin\omega t \qquad (i = u\ ,\ v\ ,\ w) \qquad \text{(A.3)}$$

where P_i and Q_i are constants and ω is an angular frequency. The solution becomes [62]

$$u(t) = -\frac{1}{n\omega\left(n^2-\omega^2\right)}\times\Big\{\ -2\left(n^2-\omega^2\right)Q_v$$

$$+\left[n\omega P_u - 2\omega^2 Q_v\right]\cos nt + \left[2n\omega P_v + \omega^2 Q_u\right]\sin nt$$

$$+\left[2n^2 Q_v - n\omega P_u\right]\cos\omega t - \left[2n^2 P_v + n\omega Q_u\right]\sin\omega t\Big\}$$

$$v(t) = \frac{1}{n\omega^2\left(n^2-\omega^2\right)}\times\Big\{\ \left(n^2-\omega^2\right)\left(-2\omega Q_u - 3nP_v - 3n\omega Q_v t\right)$$

$$+\left[-4n\omega^2 P_v - 2Q_u\omega^3\right]\cos nt + \left[2n\omega^2 P_u - 4\omega^3 Q_v\right]\sin nt$$

$$+\left[n\left(3n^2+\omega^2\right)P_v+2n^2\omega Q_u\right]\cos\omega t-\left[2n^2\omega P_u-n\left(3n^2+\omega^2\right)Q_v\right]\sin\omega t\Big\}$$

$$w(t)=\frac{1}{n\left(n^2-\omega^2\right)}\left[-nP_w\cos n\,t-\omega Q_w\sin n\,t+nP_w\cos\omega\,t+nQ_w\sin\omega\,t\right. \qquad \text{(A.4)}$$

This is called non-resonant solution and the initial condition errors are not considered. In addition to the applied frequency ω signals, the solutions have the 1-cpr (cycle-per-revolution) signals. This implies that any frequency of the perturbation causes the 1-cpr signals in the satellite motion as well as its own frequency. It is why the 1-cpr empirical parameters are used to adjust the mismodeled dynamic models, which have frequencies other than 1 cpr.

When the perturbing force has constant or 1-cpr components ($\omega \approx 0$ or $\pm n$), these solutions are no longer valid and another solution called resonant solution exists for the perturbing force of

$$f_i = R_i + P_{ni}\cos n\,t + Q_{ni}\sin n\,t \qquad (i = u\,,\,v\,,\,w) \qquad \text{(A.5)}$$

The solution of each term is given by

$$u(t)=\left[-\frac{1}{n^2}\left(2Q_{nv}+R_u\right)-\frac{1}{2n}\left(2P_{nv}+Q_{nu}\right)t\right]\cos n\,t$$

$$+\left[\frac{1}{2n^2}\left(2P_{nv}+Q_{nu}-4R_v\right)+\frac{1}{2n}\left(P_{nu}-2Q_{nv}\right)t\right]\sin n\,t$$

$$+\left[\frac{1}{n^2}\left(2Q_{nv}+R_u\right)+\frac{2}{n}R_v\,t\right]$$

$$v(t)=\left[\frac{1}{n^2}\left(3P_{nv}+2Q_{nu}-4R_v\right)+\frac{1}{n}\left(P_{nu}-2Q_{nv}\right)t\right]\cos n\,t \qquad \text{(A.6)}$$

$$+\left[-\frac{1}{n^2}\left(P_{nu}-5Q_{nv}-2R_u\right)+\frac{1}{n}\left(2P_{nv}+Q_{nu}\right)t\right]\sin n\,t$$

$$-\frac{1}{n^2}\left(3P_{nv}+2Q_{nu}-4R_v\right)-\frac{1}{n}\left(3Q_{nv}+2R_u\right)t-\frac{3}{2}R_v t^2$$

$$w(t)=\left[-\frac{1}{n^2}R_w-\frac{1}{2n}Q_{nw}\,t\right]\cos n\,t+\left[\frac{1}{2n^2}Q_{nw}+\frac{1}{2n}P_{nw}\,t\right]\sin n\,t+\frac{1}{n^2}R_w$$

A.2 RANGE AND RANGE-RATE EQUATIONS

The partial derivative of inter-satellite range or range-rate signal with respect to a certain parameter, e.g. initial condition, disturbing force, or gravity coefficient can be derived in the following way [9,45].

The nominal range ρ_o may be given by

$$\rho_0=\left(\boldsymbol{r}_{10}-\boldsymbol{r}_{20}\right)\cdot\hat{\boldsymbol{e}}_0 \tag{A.7}$$

where $\boldsymbol{r}_{i0}$ represents nominal position vector of the *i-th* satellite and $\hat{\boldsymbol{e}}_0$ does the nominal line-of-sight (LOS) vector. The perturbed range ρ can be expressed in the same way:

$$\rho=\left(\boldsymbol{r}_1-\boldsymbol{r}_2\right)\cdot\hat{\boldsymbol{e}} \tag{A.8}$$

The perturbed position and LOS vectors, $\boldsymbol{r}_i$ and $\hat{\boldsymbol{e}}$, are sum of the nominal values and the perturbed values, $\delta\boldsymbol{r}_i$ and $\delta\hat{\boldsymbol{e}}$:

$$\boldsymbol{r}_i = \boldsymbol{r}_{i0} + \delta\boldsymbol{r}_i$$

$$\hat{\boldsymbol{e}} = \hat{\boldsymbol{e}}_0 + \delta\hat{\boldsymbol{e}} \tag{A.9}$$

After substitution of (A.9) into (A.8), comparison with (A.7) yields the range variation equation as

$$\delta\rho = \left(\delta\boldsymbol{r}_1 - \delta\boldsymbol{r}_2\right)\cdot\hat{\boldsymbol{e}}_0 \tag{A.10}$$

The range variation is the projection of relative position variation on the LOS vector. With similar procedures, the range-rate variational equation may be given by

$$\begin{aligned}\delta\dot{\rho} = {} & \left(\delta\dot{\boldsymbol{r}}_1 - \delta\dot{\boldsymbol{r}}_2\right)\cdot\hat{\boldsymbol{e}}_0 \\ & + \frac{1}{\rho_0}\left(\dot{\boldsymbol{r}}_{10} - \dot{\boldsymbol{r}}_{20}\right)\cdot\hat{\boldsymbol{f}}_0\left(\delta\boldsymbol{r}_{10} - \delta\boldsymbol{r}_{20}\right)\cdot\hat{\boldsymbol{f}}_0 \\ & + \frac{1}{\rho_0}\left(\dot{\boldsymbol{r}}_{10} - \dot{\boldsymbol{r}}_{20}\right)\cdot\hat{\boldsymbol{g}}_0\left(\delta\boldsymbol{r}_{10} - \delta\boldsymbol{r}_{20}\right)\cdot\hat{\boldsymbol{g}}_0\end{aligned} \tag{A.11}$$

where $\hat{\boldsymbol{e}}_0$, $\hat{\boldsymbol{f}}_0$, and $\hat{\boldsymbol{g}}_0$ are defined as an orthonormal triad. The first term represents the relative velocity variation along the LOS, and the second and third terms represent the variation along the directions perpendicular to the LOS. If the directions of $\hat{\boldsymbol{f}}_0$ and $\hat{\boldsymbol{g}}_0$ are chosen as cross-track and complete of the LOS and the cross-track, then the second term becomes zero with the assumption of the tandem formation. The third term contains a relatively large denominator ρ_0 so that it can

be neglected. With these assumptions, the range-rate perturbation due to perturbed motion can be simplified as follows

$$\delta\dot{\rho} = \left(\delta\dot{\boldsymbol{r}}_1 - \delta\dot{\boldsymbol{r}}_2\right) \cdot \hat{\boldsymbol{e}}_0 \tag{A.12}$$

Substitution of the analytic solutions, which are derived in the previous section, yields the sensitivity of the range-rate with respect to a certain parameter, e.g. initial condition error or disturbing force.

The range equation can be expressed in the local frames, which correspond to the radial, transverse, and normal directions of each satellite [46]. Figure A.1 describes those local coordinates $\hat{\boldsymbol{h}}_{ij}$, where the subscript i represents (u,v,w) component and j represents the j-*th* satellite.

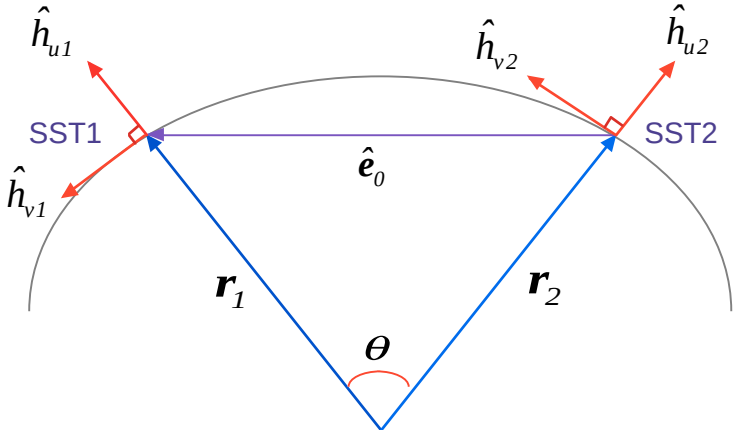

Figure A.1 Local coordinate frame of each low satellite

The solution of the range equation can be written in the following form

$$\delta\rho = \left(\sum_{i=u,v,w} (\delta x_i)_1 \hat{\boldsymbol{h}}_{i1} - \sum_{i=u,v,w} (\delta x_i)_2 \hat{\boldsymbol{h}}_{i2} \right) \cdot \hat{\boldsymbol{e}}_0 \tag{A.13}$$

With the assumptions of circular tandem orbits, this equation can be simplified by

$$\delta\rho = (u_1 + u_2) sin\frac{\theta}{2} + (v_1 - v_2) cos\frac{\theta}{2} \tag{A.14}$$

where θ represents the separation angle. The terms related to the normal direction are cancelled since the LOS plane is perpendicular to the normal direction. The range-rate has a similar form of equation as

$$\delta\dot{\rho} = (\dot{u}_1 + \dot{u}_2) sin\frac{\theta}{2} + (\dot{v}_1 - \dot{v}_2) cos\frac{\theta}{2} \tag{A.15}$$

It is noted that $(u_i, v_i, \dot{u}_i, \dot{v}_i)$ represent the perturbed quantities from the nominal circular orbit.

Several numerical simulations were performed by the MSODP to validate these equations. A circular reference orbit was used with two-body gravity term. The initial position error of 1 m along the radial direction was applied. The reference range-rate, which was computed along the reference (circular) orbit, has zero value all the time. The perturbed range-rate time series from the analytic solution and the numerical integration were compared. Figure A.2 shows the range-rate difference. Time span was one day and the discrepancy grows along time, but it has the maximum of 0.2 μm/s that is smaller than the instrument noise level. These analytic equations are useful for predicting the range or range-rate

perturbation due to initial condition error or measurement error as long as the prediction time span is short.

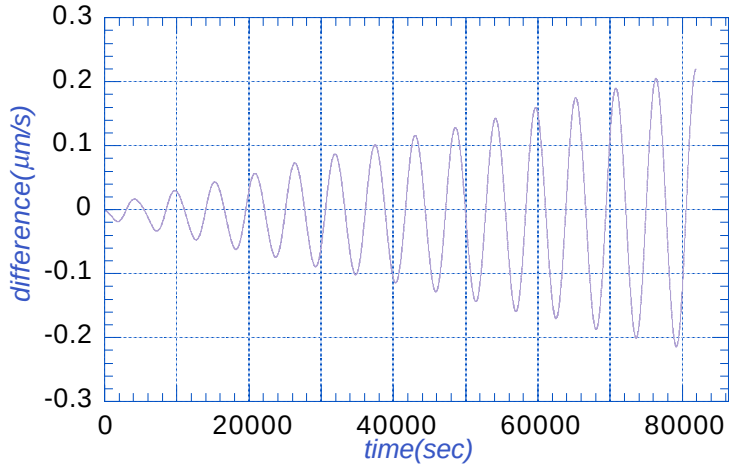

Figure A.2 Difference between the analytic and numerical range-rate signals

A.3 APPLICATIONS OF HILL'S EQUATIONS

One of the applications using the range and range-rate equations is the transfer function between the perturbing force and the range-rate perturbation. It maps the PSD of the perturbing force into the PSD of the range-rate perturbation, and it is useful to predict the effect of accelerometer noise on the range-rate measurements. The relationship between the perturbed state and the perturbed range-rate can be expressed in the following state-space form:

$$\dot{\boldsymbol{x}} = A\boldsymbol{x} + B\boldsymbol{f}$$

$$\boldsymbol{y} = D\boldsymbol{x} \tag{A.16}$$

where

$$\boldsymbol{x} = \left[u_1\ v_1\ w_1\ \ \dot{u}_1\ \dot{v}_1\ \dot{w}_1 \vdots u_2\ v_2\ w_2\ \ \dot{u}_2\ \dot{v}_2\ \dot{w}_2\right]^T$$

= perturbed state vector of two low satellites

$$\boldsymbol{f} = \left[\, f_{u_1}\ f_{v_1}\ f_{w_1} \vdots f_{u_2}\ f_{v_2}\ f_{w_2}\,\right]^T$$

= perturbing forces acting on each satellite

$$\boldsymbol{y} = \left[\delta\dot{\rho}_{u_1}\ \ \delta\dot{\rho}_{v_1}\ \delta\dot{\rho}_{w_1} \vdots \delta\dot{\rho}_{u_2}\ \ \delta\dot{\rho}_{v_2}\ \delta\dot{\rho}_{w_2}\right]^T$$

= range-rate perturbations due to each satellite's perturbation

An analytic form of transfer function with zero initial conditions can be computed by using the following equation [41]

$$G(s) = D(sI - A)^{-1}B \tag{A.17}$$

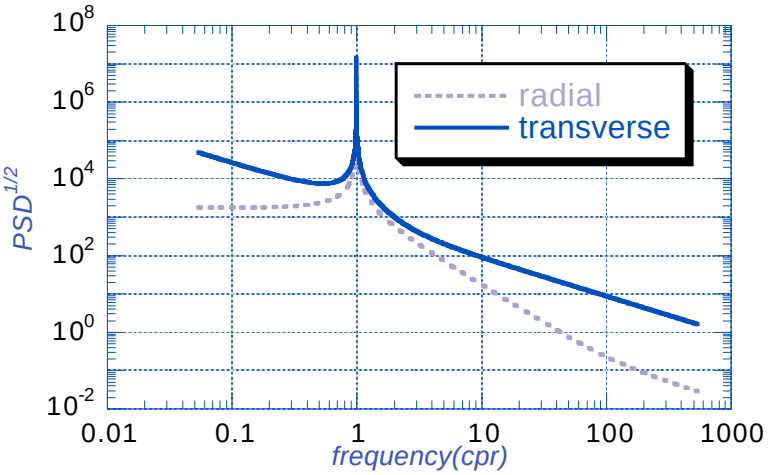

Figure A.3 Transfer functions between range-rate perturbation and disturbing forces

Figure A.3 shows the transfer function from radial and transverse perturbing force noises to the range-rate perturbations. The perturbation due to radial perturbation is lower than transverse noise' but still has significant amplitude. It means the radial motion is highly coupled with the transverse motion. The perturbation due to normal perturbation is zero theoretically, and it explains the previous numerical simulation results in Chapter 5 regarding the choice of accelerometer less-sensitive axis, where the normal (cross-track) accelerometer noise does not affect the orbit and gravity solutions significantly. The spikes in the 1 cpr are due to the resonance, but they can be removed effectively by applying the empirical parameters. Theoretically, the spikes have infinite amplitude but they are bounded within some level since the orbit acts as a filter to smooth the spikes.

To verify this equation, a numerical simulation was performed with the accelerometer random noise. The accelerometer with less-sensitive normal axis was simulated so that the accelerometer random noise has same PSD in the transverse and radial directions. Since the normal motion is decoupled from the in-plane motion and does not appear in the range-rate equation of (A.15), the random noise in the normal axis, which is higher than those in the other axes, does not need to be considered. The details on these noise spectrums are described in Chapter 5. The range-rate perturbation obtained by the numerical simulation is compared to the one by the analytic solution in Figure A.4. Both results are matched each other very well.

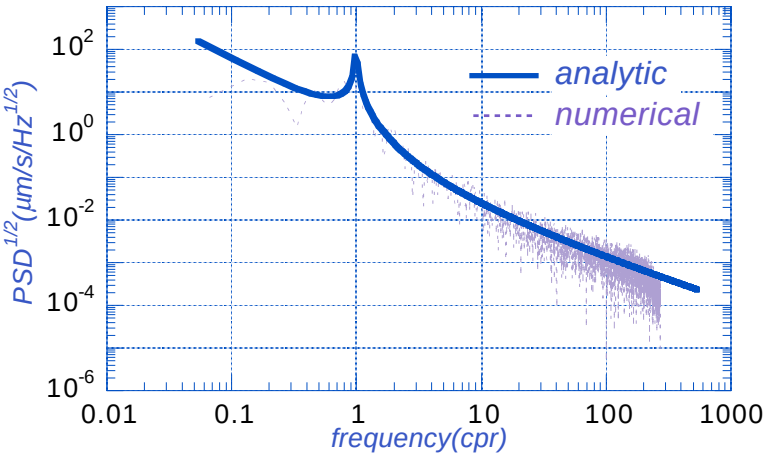

Figure A.4 Comparison of the range-rate perturbations by numerical simulation and the analytic solution

Another applications of the perturbation equation may be a variation equation of the inter-satellite range due to initial condition errors or different accelerations on two satellites. Because of limited fuel capacity, the thrust firings for orbit maintenance, e.g. maintain the range within a nominal level, should be minimized. The analytic form of the range prediction is necessary to understand the behavior and to design control algorithm.

The transfer function of Figure A.3 does not include the correlation between frequencies. As shown (A.6), a perturbation with a frequency ω causes the orbit perturbation at the frequency n as well as ω. This form of general solution is obtained by submitting the general solutions in (A.4) or (A.6) into the range/range-rate equation of (A.14). The range variation is expressed in terms of the range perturbation partials with respect to each perturbation amplitude, $\partial\rho / \partial x$, and perturbation variation, δx:

$$\delta\rho = \sum_{i=u,v}\left[\frac{\partial\rho}{\partial R_i}\delta R_i + \frac{\partial\rho}{\partial P_{ni}}\delta P_{ni} + \frac{\partial\rho}{\partial Q_{ni}}\delta Q_{ni} + \sum_{j=1}^{N}\left(\frac{\partial\rho}{\partial P_i}\delta P_i + \frac{\partial\rho}{\partial Q_i}\delta Q_i\right)_j\right] \quad \text{(A.18)}$$

where N is the number of distinctive frequencies of the perturbing forces. The partials $\partial\delta\rho / \partial x$ are written as $\partial\rho / \partial x$ for convenience. The perturbation amplitudes are defined in (A.3) and (A.5). The partial derivatives with respect to the perturbation acting on the leading satellite (SST1) are given by

$$\frac{\partial \rho}{\partial R_u} = \frac{1}{n^2}\left[-2nt\cos\frac{\theta}{2} + \sin\frac{\theta}{2} - \sin\frac{\theta}{2}\cos(nt) + 2\cos\frac{\theta}{2}\sin(nt)\right]$$

$$\frac{\partial \rho}{\partial P_{nu}} = \frac{1}{2n^2}\left[2nt\cos\frac{\theta}{2}\cos(nt) - \left(2\cos\frac{\theta}{2} - nt\sin\frac{\theta}{2}\right)\sin(nt)\right]$$

$$\frac{\partial \rho}{\partial Q_{nu}} = \frac{1}{2n^2}\left[-4\cos\frac{\theta}{2} + \left(4\cos\frac{\theta}{2} - nt\sin\frac{\theta}{2}\right)\cos(nt) + \left(2nt\cos\frac{\theta}{2} + \sin\frac{\theta}{2}\right)\sin(nt)\right]$$

$$\frac{\partial \rho}{\partial R_v} = \frac{1}{2n^2}\left[\left(8 - 3n^2t^2\right)\cos\frac{\theta}{2} + 4nt\sin\frac{\theta}{2} - 8\cos\frac{\theta}{2}\cos(nt) - 4\sin\frac{\theta}{2}\sin(nt)\right]$$

$$\frac{\partial \rho}{\partial P_{nv}} = \frac{1}{n^2}\left[-3\cos\frac{\theta}{2} + \left(3\cos\frac{\theta}{2} - nt\sin\frac{\theta}{2}\right)\cos(nt) + \left(2nt\cos\frac{\theta}{2} + \sin\frac{\theta}{2}\right)\sin(nt)\right]$$

$$\frac{\partial \rho}{\partial Q_{nv}} = \frac{1}{n^2}\left[-3nt\cos\frac{\theta}{2} + 2\sin\frac{\theta}{2}\right.$$

$$\left. -\left(2nt\cos\frac{\theta}{2} + 2\sin\frac{\theta}{2}\right)\cos(nt) + \left(5\cos\frac{\theta}{2} - nt\sin\frac{\theta}{2}\right)\sin(nt)\right]$$

$$\frac{\partial \rho}{\partial P_u} = \frac{1}{\omega\left(n^2 - \omega^2\right)}\left[-\omega\sin\frac{\theta}{2}\cos(nt) + 2\omega\cos\frac{\theta}{2}\sin(nt)\right.$$

$$\left. +\omega\sin\frac{\theta}{2}\cos(\omega t) - 2n\cos\frac{\theta}{2}\sin(\omega t)\right]$$

$$\frac{\partial \rho}{\partial Q_u} = \frac{1}{n\omega\left(n^2 - \omega^2\right)}\left[-2\left(n^2 - \omega^2\right)\cos\frac{\theta}{2} - 2\omega^2\cos\frac{\theta}{2}\cos(nt) - \omega^2\sin\frac{\theta}{2}\sin(nt)\right.$$

$$\left. +2n^2\cos\frac{\theta}{2}\cos(\omega t) + n\omega\sin\frac{\theta}{2}\sin(\omega t)\right]$$

$$\frac{\partial \rho}{\partial P_v} = \frac{1}{n^2\omega^2\left(n^2 - \omega^2\right)}\left[-3n^2\left(n^2 - \omega^2\right)\cos\frac{\theta}{2}\right.$$

$$
\begin{aligned}
&-4n^2\omega^2\cos\frac{\theta}{2}\cos(nt) - 2n^2\omega^2\sin\frac{\theta}{2}\sin(nt) \\
&+n^2\left(3n^2+\omega^2\right)\cos\frac{\theta}{2}\cos(\omega t) + 2n^3\omega\sin\frac{\theta}{2}\sin(\omega t)\Big] \\
\frac{\partial\rho}{\partial Q_v} = \frac{1}{n\omega^2\left(n^2-\omega^2\right)}\Big[&-3n\omega t\left(n^2-\omega^2\right)\cos\frac{\theta}{2} + 2\omega\left(n^2-\omega^2\right)\sin\frac{\theta}{2} \\
&+2\omega^3\sin\frac{\theta}{2}\cos(nt) - 4\omega^3\cos\frac{\theta}{2}\sin(nt) \\
&-2n^2\omega\sin\frac{\theta}{2}\cos(\omega t) + n\left(3n^2+\omega^2\right)\cos\frac{\theta}{2}\sin(\omega t)\Big] \qquad \text{(A.19)}
\end{aligned}
$$

It is noted that, for small separation angle θ, $sin(\theta/2)$ is very smaller than $cos(\theta/2)$ and the range perturbation behavior is mainly dominated by the $cos(\theta/2)$ containing terms. The range-rate partial equations can be easily obtained by differentiating these equations.

These analytic equations provide a quick solution for a certain perturbation and an insight on the characteristics of the inter-satellite range/range-rate observations. It even helps numerical simulations in design and verifications. The range perturbation equation can be rearranged as follows:

$$
\begin{aligned}
\delta\rho = A + Bt + Ct^2 + (E+Ft)\cos nt + (G+Ht)\sin nt \\
+\sum_{j=1}^{N}\left[\left(E_j+F_jt\right)\cos\omega_j t + \left(G_j+H_jt\right)\sin\omega_j t\right] \qquad \text{(A.20)}
\end{aligned}
$$

Any force components at a certain frequency ω_j are grouped into one *j-th* force. This equation implies that the range error is the sum of quadratic and harmonic terms. The purpose of the low-low empirical parameters is to remove the error contribution from the observation, and then this expression (A.20) provides a guide to an optimal set of the low-low empiricals. In this study, the coefficients of the quadratic and 1-cpr terms, *A*, *B*, *C*, *E*, *F*, *G*, and *H* were estimated. It is not realistic to estimate all the ω_i frequency terms, E_j, F_j, G_j, and H_j for a large number *N*. In case of the range-rate observations, the perturbation equation does not include the quadratic term, and the coefficient *C* is not necessary to estimate. This set of the empirical parameters is very effective to remove the range/range-rate error, and it proves the usefulness of this analytic approach.

APPENDIX B SIMULATION PROCEDURE

This section describes the procedures for the numerical simulation and the optimal scale factor determination. The **Bold** capital represents the output files from each step and the ***Bold-Italic*** capital does the input files for each step.

B.1 NUMERICAL SIMULATION PROCEDURE

B.1.1 Generation of the Truth Measurements

- To generate the truth measurement time series using the truth dynamic models.
- In actual mission, real measurements replace the output from this part.

Dynamic Models: Truth gravity (***TRUEGEO***)
Truth initial conditions (***TRUEIC***)
Truth accelerometer scale factors and biases (***TRUESCA***)
Atmospheric drag, radiation pressure

Measurement Models: Inter-satellite system, oscillator, and multipath noise

Output Files: **SST**: Noisy SST measurements (range & range rate)
ACC: Accelerometer measurements
GPSDD: GPS double difference measurements

B.1.2 Orbit Adjustment

- To adjust the orbit initial conditions using the GPS measurements.

Input Files: ***ACC***, ***GPS DD***

Dynamic Models: Nominal gravity (***NOMGEO***)

Accelerometer measurements (***ACC***)

Output Files: **IC2**: Adjusted initial conditions

SCA: Adjusted scale factors and biases

B.1.3 Gravity Estimation by the GPS Measurements

- To make an information matrix using the GPS measurements.

Input Files: ***ACC, GPSDD, IC2, SCA***

Dynamic Models: Nominal gravity (***NOMGEO***)

Accelerometer measurements (***ACC***)

Output Files: **IGPS**: Information Matrix (DUZ or REGRES file)

= Gravity coefficients

+ Initial conditions

+ Scale factors and biases

B.1.4 Gravity Estimation by the SST Measurements

- To make an information matrix using the SST measurements.

Input Files: ***ACC, SST, IC2, SCA***

Dynamic Models: Nominal gravity (***NOMGEO***)

Accelerometer measurements (***ACC***)

Output Files: **ISST**: Information Matrix (DUZ or REGRES file)

= Gravity coefficients

+ Initial conditions

+ Scale factors and biases

+ Low-low empirical parameters

B.1.5 Combination of the GPS and SST Daily Information Matrices

- To combine *N*-daily GPS and SST information matrices and estimate a gravity coefficients. An optimal weighting determined by the following section is used for the relative weighting of the GPS and SST information matrices.

Input Files: ***IGPS, ISST***

Output Files: **NEWGEO** : Gravity Estimate

NEWIC : Initial Condition

NEWSCA : Scale Factor & Bias Estimate

B.1.6 Comparison

- To compare the estimates with the truth.

Input Files: ***TTRUEGEO, NEWGEO***

TRUEIC, NEWIC

TRUESCA, NEWSCA

Output Files: **DDV** : Degree Difference Variance

DIC : Initial condition or state error

DSCA: Accelerometer scale factor and bias error

B.2 OPTIMAL WEIGHTING DETERMINATION PROCEDURE

B.2.1 Generation of the Truth Measurements

- To generate the truth measurement time series using the truth dynamic models.

- Identical to the generation part of the numerical simulation procedure.

Dynamic Models: Truth gravity (***TRUEGEO***)

Truth initial conditions (***TRUEIC***)

Truth accelerometer scale factors and biases (***TRUESCA***)

Atmospheric drag, radiation pressure

Measurement Models: SST system, oscillator, and multipath noise

Output Files: **SST**: Noisy SST measurements (range & range rate)

ACC: Accelerometer measurements

GPSDD: GPS double difference measurements

B.2.2 Orbit Adjustment

- To adjust the orbit initial conditions using the GPS measurements.

Input Files: ***ACC***, ***GPS DD***

Dynamic Models: Truth gravity (***TRUEGEO***)

Accelerometer measurements (***ACC***)

Output Files: **IC2**: Adjusted initial conditions

SCA: Adjusted scale factors and biases

SST2: New SST measurements without noise

B.2.3 Residual Computation

- To compute the SST measurement residual due to the SST and other error sources.

Input Files: ***SST, SST2***

Output Files: **DSST**: SST measurement residual time series
after removing the low-low empirical bias and bias-rate
= (SST-SST2) – low-low bias & bias-rate

LPRMS: Predicted SST Residual RMS

APPENDIX C DEFINITIONS

C.1 POWER SPECTRAL DENSITY

There exist many variations of the definition of the Fourier transforms and the power spectral density, and the definitions of this study follows Powers' [53]. For a given function of time, $x(t)$, the continuous Fourier transform (CFT) $X(f)$ may be defined by the expression

$$X(f) = \int_{-\infty}^{\infty} x(t) e^{-i2\pi f t} dt \tag{C.1}$$

and the inverse transform by

$$x(t) = \int_{-\infty}^{\infty} X(f) e^{i2\pi f t} df \tag{C.2}$$

The quantities *t* and *f* represent time and frequency, respectively. For a function of discrete time $x[n]$, the discrete Fourier transform (DFT), $X[l]$, may be defined by

$$X[l] = \frac{1}{N} \sum_{n=0}^{N-1} x[n] e^{-i2\pi l n/N} \qquad l = 0,1,2,\ldots,N-1 \tag{C.3}$$

and the inverse DFT by

$$x[n] = \sum_{l=0}^{N-1} X[l] e^{i2\pi l n/N} \qquad n = 0,1,2,\ldots,N-1 \tag{C.4}$$

Both $x[n]$ and $X[l]$ have a period of *N*, which is the number of samples. The CFT $X_T(f)$, where *T* is finite time duration, is related to the DFT $X[l]$ by

$$X_T(f) = X_T(l\Delta f) = \frac{1}{\Delta f} X[l] \tag{C.5}$$

where

$$\Delta f = \frac{1}{T} = \frac{1}{N\, t_s} \tag{C.6}$$

t_s is the sampling interval.

The two-sided discrete sample power spectrum $S[l]$ may be defined by

$$S[l] = |X[l]|^2 \tag{C.7}$$

The continuous power spectrum $S(f)$ becomes

$$S(f) = S(l\Delta f) = \frac{1}{\Delta f} S[l] \tag{C.8}$$

The amplitude at the *l-th* frequency $A[l]$ is defined by

$$A[l] = 2|X[l]| = 2\sqrt{S(f)\Delta f} \tag{C.9}$$

In order to reduce leakage, the Hanning data window function [53] was used in this study:

$$w(t) = \frac{1}{2}\left(1 - \cos\frac{2\pi t}{T}\right) \qquad 0 \le t \le T \qquad \text{(C.10)}$$

This window function is applied to the discrete sample $x[n]$ as

$$x_w[n] = x[n]w[n] \qquad \text{(C.11)}$$

Since the application of such windows results in a reduction of the total power present in the power spectral density, the following window correction factor was applied to the power spectrum:

$$W = \left[\frac{1}{N}\sum_{n=0}^{N-1} w^2[n]\right]^{-1}$$

$$S[l] \cong W\, S_w[l] \qquad \text{(C.12)}$$

$S[l]$ is the actual sample power spectrum at discrete frequency *l*. $S_w[l]$ is the sample power spectrum estimated from the windowed data $x_w[n]$.

C.2 DEGREE VARIANCES

In order to compare gravity recovery results, several quantities were utilized to characterize the errors and uncertainties in the estimation of the gravity coefficients. The degree difference variance (DDV) of *n-th* degree is defined by the difference of the reference and the estimated coefficients [59]:

$$\Delta_n = \sqrt{\sum_{m=0}^{n} \left(\Delta \bar{C}_{nm}^2 + \Delta \bar{S}_{nm}^2 \right)} \tag{C.13}$$

where

$$\Delta \bar{C}_{nm} = \left(\bar{C}_{nm} \right)_{estimate} - \left(\bar{C}_{nm} \right)_{reference}$$

$$\Delta \bar{S}_{nm} = \left(\bar{S}_{nm} \right)_{estimate} - \left(\bar{S}_{nm} \right)_{reference}$$

The subscripts *n* and *m* represent degree and order, respectively. The degree error variance (DEV) or degree variance is defined by the elements of the covariance matrix associated with the estimates of the geopotential coefficients:

$$\delta_n = \sqrt{\sum_{m=0}^{n} \left(\delta \bar{C}_{nm}^2 + \delta \bar{S}_{nm}^2 \right)} \tag{C.14}$$

where

$\delta\overline{C}_{nm}$, $\delta\overline{S}_{nm}$ = *Standard deviation of the error in the estimates of the normalized geopotential coefficients*

The degree error variance heavily depends on the measurement noise level, which is specified for solving the information equations. It is very sensitive to the weighting factors and does not give correct uncertainty level unless the weighting factors are correct. It also neglects the correlations between the estimates of the parameters and, as such, usually yields a pessimistic estimate of the overall error. In the case of simulations, the reference values are known and the degree difference variances are available. In actual situations, the reference values are not available, and only the degree error variance is available for comparison. Of two quantities, the degree difference variance represents an actual error level and it is less sensitive to the weighting factors. Therefore, it is better to use the degree difference variance as long as the reference values are available. The degree difference variance was used in most of comparisons.

Since both the degree difference and error variances are defined for each degree, sometimes it is useful to use a scalar quantity matched to a gravity coefficient set. The cumulative geoid error up to degree N is defined by [60,76]

$$\Delta_N = R_e \sqrt{\sum_{n=2}^{N}\sum_{m=0}^{n}\left(\Delta\overline{C}_{nm}^2 + \Delta\overline{S}_{nm}^2\right)} \qquad \text{(C.15)}$$

where R_e is the Earth radius. Although it is not an absolute measure of a geopotential coefficient error, it is one of the ways to judge gravity result easily.

REFERENCES

[1] Antreasian, P.G., Lundberg, J.B., and Schutz, B.E., "Simulation of the GRM Drag Compensation System", The Journal of the Astronautical Sciences, Vol.39, No.4, pp487-518, October-December, 1991

[2] Barlier, F.C. et al, "A Thermospheric Model Based on Satellite Drag Data", Ann. Geophys., Vol.34, No.1, pp9-24, 1978

[3] Bettadpur, S.V., Schutz, B.E., and Lundberg, J.B., "Spherical Harmonic Synthesis and Least Squares Computations in Satellite Gravity Gradiometry", Bulletin Géodésique, Vol. 66, pp261-271, 1992

[4] Bettadpur, S.V., "A Simulation Study of High Degree and Order Geopotential Determination using Satellite Gravity Gradiometry", Ph.D. Dissertation, Department of Aerospace Engineering and Engineering Mechanics, The University of Texas at Austin, May 1993

[5] Bettadpur, S.V. and Tapley, B.D., "Assessments of Future Dedicated Geopotential Mapping Missions", Spring American Geophysical Union Meeting, U22A-03, Baltimore, Maryland, May 20-24, 1996

[6] Bettadpur, S.V., Kim, J.R., and Tapley, B.D., "Results from Simulation Studies of Satellite-to-Satellite Tracking GRACE Mission", Spring American Geophysical Union Meeting, G31A-08, Boston, Massachusetts, May 27, 1998

[7] Bettadpur, S.V., Kim, J.R., and Tapley, B.D., "Results from GRACE SST Simulation Studies", Second Joint Meeting of the IGC and IGeC, Trieste, Italy, September 7-12, 1998

[8] Bettadpur, S.V., Private Communication

[9] Colombo, O.L., “The Global Mapping of Gravity with Two Satellites”, Netherlands Geodetic Commission, Publications on Geodesy, New Series, Vol.7, No.3, 1984

[10] Davis, G.W., "GPS-Based Precision Orbit Determination for Low Altitude Geodetic Satellites", Ph.D. Dissertation, Department of Aerospace Engineering and Engineering Mechanics, The University of Texas at Austin, August, 1996

[11] Dickey, J.O. et al," Satellite Gravity: Insights into the Solid Earth and Its Fluid Envelope", EOS, Transactions, American Geophysical Union, Vol.79, No.20, May 19, 1998

[12] DGFI, “Study of a Satellite-to-Satellite Tracking Gravity Mission”, European Space Agency Contract Report, Munich, March 1987

[13] Douglas, B.C, Goad, C.C., and Morrison, F.F., "Determination of the Geopotential From Satellite-to-Satellite Tracking Data", Journal of Geophysical Research, Vol.85, No.B10, pp5471-5480, October 10, 1980

[14] Eanes, R.J., Schutz, B.E., and Tapley, B.D., “Earth and Ocean Tide Effects on Lageos and Starlette”, Proceedings of the 9th International Symposium on Earth Tides, Ed. J.T. Kuo, pp239-249, 1983

[15] Frauenholz, R.B., Bhat, R.S., and Shapiro, B.E., “An Analysis of the TOPEX/POSEIDON Operational Orbit: Observed Variations and Why”, Proceedings of the AAS/AIAA Astrodynamics Conference, Halifax, Nova Scotia, Canada, AAS 95-366, pp1127-1144, February 14-17, 1995

[16] Gelb, A. et al, *Applied Optimal Estimation*, The Analytic Sciences Corporation, M.I.T. Press, 1994

[17] GRACE Meeting Presentation, "GRACE Project Requirement Review (PRR)", April 1998

[18] GRACE Meeting Presentation, "GRACE Mission and Science Engineering Team (MSET) Kick-Off Meeting", October 1997

[19] GRACE Team, "GRACE Science and Mission Requirements Document (SMRD)”, GRACE 327-200, JPL D-15928, July 1998

[20] GRACE Meeting Presentation, “GRACE Preliminary Design Review”, August 1998

[21] GRACE Team, “GRACE Product Specification Document”, GRACE 327-720, September 1999

[22] GRACE Team, “Attitude and Orbit Control System (AOCS) Specification and Description”, GRACE 327-440, Draft v.4.0, July 1999

[23] GRACE Team, "Instrument Processing Unit (IPU) Specification", GRACE 327-540, February 2000

[24] GRACE Team at LaRC/AMA Inc.

[25] Greenwood, D.T., *Principles of Dynamics*, 2nd edition, Prentice-Hall, 1988

[26] Heiskanen, W.A. and Moritz, H., *Physical Geodesy*, W.H. Freeman and Company, 1967

[27] Hofmann-Wellenhof, B., Lichtenegger, H., and Collins, J., *GPS Theory and Practice, 3rd Revised Edition*, Springer-Verlag, 1994

[28] Huang, C. and He, M.F., “Atmospheric Tidal Perturbation of Artificial Satellite Orbits”, Chin. Astron. Astrophys., Vol.12, pp34-37, 1988

[29] Jekeli, C. and Rapp, R.H., "Accuracy of the Determination of Mean Anomalies and Mean Geoid Undulations from a Satellite Gravity Field Mapping Mission", Department of Geodetic Science, Report No. 307, The Ohio State University, August 1980

[30] Jekeli, C., "Alternative Methods to Smooth the Earth's Gravity Field", Department of Geodetic Science and Surveying, Report No. 327, The Ohio State University, December 1981

[31] Kahn, W.D. and von Bun, F.O., "Error Analyses for a Gravity Gradiometer Mission", IEEE Transactions on Geoscience and Remote Sensing, Vol.GE-23, No.4, pp527-530, July 1985

[32] Kaplan, M.H., *Modern Spacecraft Dynamics & Control*, John Wiley & Sons, 1976

[33] Kaula, W.M., *Theory of Satellite Geodesy*, Blaisdell Publishing Company, Waltham, Massachusetts, 1966

[34] Kaula, W.M., "Interference of Variations in the Gravity Field from Satellite-to-Satellite Range Rate", Journal of Geophysical Research, Vol.88, No.B10, pp8345-8349, October 10, 1983

[35] Keating, T.P. et al, "Geopotential Research Mission, Science, Engineering, and Program Summary", NASA TM-86240, 1986

[36] Key, K., Private Communication

[37] Kim, J.R., et al, “Simulations of the Gravity Recovery and Climate Experiment (GRACE) Mission”, Proceedings of the AAS/AIAA Space Flight Mechanics Meeting, AAS 99-144, Breckenridge, Colorado, February 7-10, 1999

[38] Knocke, P. and Ries, J., “Earth Radiation Pressure Effects on Satellites”, Center for Space Research, The University of Texas at Austin, Technical Memorandum, CSR-TM-87-01, 1987

[39] Koop, R., “Global Gravity Field Modeling using Satellite Gravity Gradiometry”, Netherlands Geodetic Commission, Publications on Geodesy, New Series, No.38, 1993

[40] Kosaka, M., “Evaluation Method of Polynomial Models’ Prediction Performance for Random Clock Error”, Journal of Guidance, Vol.10, No.6, pp523-527, November-December, 1987

[41] Kuo, B.C., *Automatic Control Systems, 6th Edition*, Prentice-Hall, 1991

[42] Leick, A., *GPS Satellite Surveying, 2nd Edition*, John Wiley & Sons, 1995

[43] Lemoine, F.G., *EGM96 description*, Text File, NASA Goddard Space Flight Center, October, 1996

[44] MacArthur, J.L. and Posner, A.S., “Satellite-to-Satellite Range-Rate Measurement”, IEEE Transactions on Geoscience and Remote Sensing, Vol.GE-23, No.4, pp517-523, July 1985

[45] Mackenzie, R.A., "Gravity Field Recovery using Two Low Satellites in Different Orbital Planes", Ph.D. Thesis, The University of Aston in Birmingham, October 1995

[46] Mackenzie, R.A. and Moore, P., “A Geopotential Error Analysis for a Non Planar Satellite to Satellite Tracking Mission”, Journal of Geodesy, Vol.71, pp262-272, 1997

[47] Marcos, F.A. et al, "Satellite Drag Models: Current Status and Prospects", Proceedings of the AAS/AIAA Astrodynamics Conference, AAS 93-621, Victoria, British Columbia, Canada, August 16-19, 1993

[48] Meditch, J.S., "Clock Error Models for Simulation and Estimation", Aerospace Report TOR-0076(6474-D1)-2, The Aerospace Corporation, El Segundo, California, July 1975

[49] National Research Council, "Satellite Gravity and the Geosphere: Contributions to the Study of the Solid Earth and Its Fluid Envelope", National Academy Press, Washington, D.C., 1997

[50] Paik, H.J., "Geodesy and Gravity Experiment in Earth Orbit Using a Superconducting Gravity Gradiometer", IEEE Transactions on Geoscience and Remote Sensing, Vol. GE-23, No. 4, pp524-526, July 1985

[51] Perosanz, F. and Biancale, R., “Strategy of the In-Flight Dynamic Calibration of the STAR Accelerometer in the Frame of the CHAMP Geodetic Mission”, Fall American Geophysical Union Meeting, G22A-5, San Francisco, California, December 8-12, 1997

[52] Piscane, V.L. et al, "Description of the Dedicated Gravitational Satellite Mission (GRAVSAT)", IEEE Transactions on Geoscience and Remote Sensing, Vol. GE-20, No. 3, pp315-321, July 1982

[53] Powers, E.J., *Digital Time Series Analysis and Applications - Class Note*, Spring, 1997

[54] Ravary, F., “CHAMP Satellite – Disturbing Accelerations due to Gravity Gradients and Attitude Errors”, Center for Space Research, The University of Texas at Austin, Technical Memorandum, August 1997

[55] Reigber, C., "Representation of Orbital Element Variations and Force Function with respect to Various Reference Systems", Bulletin Géodésique, Vol.55, pp111-131, 1981

[56] Reigber, C., "Gravity Field Recovery from Satellite Tracking Data”, Theory of Satellite Geodesy and Gravity Field Determination, Lecture Notes in Earth Sciences, No. 25, Eds. F. Sanso and R. Rummel, Springer-Verlag, 1989

[57] Rim, H.J., "TOPEX Orbit Determination using GPS Tracking System", Ph.D. Dissertation, Department of Aerospace Engineering and Engineering Mechanics, The University of Texas at Austin, December 1992

[58] Roesset, P.J., Private Communication

[59] Rosborough, G.W., "Satellite Orbit Perturbations due to the Geopotential", Ph.D. Dissertation, Department of Aerospace Engineering and Engineering Mechanics, The University of Texas at Austin, January 1986

[60] Rosborough, G.W. et al, “Gravity Field Covariance Analysis for the TOPEX/POSEIDON Mission”, Proceedings of the AAS/AIAA Astrodynamics Conference, AAS 91-353, Durango, Colorado, August 19-22, 1991

[61] Rummel, R. et al, “Spherical Harmonic Analysis of Satellite Gradiometry”, Netherlands Geodetic Commission, Publications on Geodesy, New Series, No.39, 1993

[62] Schrama, E.J.O., “The Role of Orbit Errors in Processing of Satellite Altimeter data”, Netherlands Geodetic Commission, Publications on Geodesy, New Series, No.33, 1989

[63] Schutz, B.E. et al, "Simulation of a Geopotential Research Mission for Gravity Studies", Manuscripta Geodaetica, Vol.12, pp51-63, 1987

[64] Schutz, B.E. et al, " Developments in the Simulation of a Geopotential Research Mission", Proceedings of the AIAA/AAS Astrodynamics Conference, 88-4258-CP, Minneapolis, Minnesota, August 15-17, 1988

[65] Sharma, J., "Precise Determination of the Geopotential with a Low-Low Satellite-to-Satellite Tracking Mission", Ph.D. Dissertation, Department of Aerospace Engineering and Engineering Mechanics, The University of Texas at Austin, December 1995

[66] Stanton, P. et al, "GRACE Project – Multipath Test Report", Technical Note, November 14, 1997

[67] Tapley, B.D., "Statistical Orbit Determination Theory", Advances in Dynamical Astronomy, D. Reidel Publishing Co., Holland, pp396-425, 1973

[68] Tapley, B.D. et al, "Precision Orbit Determination for TOPEX", Advances in Space Research, Vol.10, No.3-4, pp(3)239-247, 1990

[69] Tapley, B.D. et al, "GRACE Mission Proposal to the ESSP Program", 1997

[70] Tapley, B.D., Bettadpur, S.V., and Kim, J.R., "Simulation Studies of the GRACE Gravity Mission, Western Pacific Geophysics Meeting, G31A-02, Taipei, Taiwan, July 21-24, 1998

[71] Thomas, J.B., "An Analysis of Gravity-Field Estimation Based on Intersatellite Dual-1-Way Biased Ranging", JPL Publication 98-15, Jet Propulsion Laboratory, Pasadena, California, May 1999.

[72] Torge, W., *Geodesy*, 2nd Edition, Walter de Gruyter, Berlin, 1991

[73] Touboul, P. et al, "Air Drag Effect on Gradiometer Measurements", Manuscripta Geodaetica, Vol.16, pp73-91, 1991

[74] van Gelderen, M. and Koop, R., "The Use of Degree Variances in Satellite Gradiometry", Journal of Geodesy, Vol.71, pp337-343, 1997

[75] van Geemert, R., Koop, R., and Visser, P., "Development of a Parallellized Data Processing Facility for Gravity Field Recovery from GOCE data", Fall American Geophysical Union Meeting, G12C-15, San Francisco, California, December 13-17, 1999

[76] Vermeer, M., "Some Simulated Noise Inversion Studies of Satellite Geopotential Missions Involving "Criterion Functions" in the Frequency Domain", Journal of Geodesy, Vol.70, pp397-409, 1996

[77] Vetter, J.R. et al, "A Historical Survey of Earth Gravitational Models Used in Astrodynamics from Sputnik and TRANSIT to GPS and TOPEX", Proceedings of the AAS/AIAA Astrodynamics Conference, AAS 93-620, Victoria, British Columbia, Canada, August 16-19, 1993

[78] Visser, P.N.A.M., “The Use of Satellites in Gravity Field Determination and Model Adjustment”, Ph.D. Thesis, Delft University Press, Delft, Netherlands, 1992

[79] Wagner, C.A., “Improved Gravitational Recovery from a Geopotential Research Mission Satellite Pair Flying en Echelon”, Journal of Geophysical Research, Vol. 92, No.B8, pp8147-8155, July 10, 1987

[80] Wakker, K.F., Ambrosius, B.A.C., and Leenman, H., "Satellite Orbit Determination and Gravity Field Recovery from Satellite-to-Satellite Tracking", Delft University of Technology, Report LR-605, The Netherlands, July 1989

[81] Wang, F., "Grace CG Offset Determination by Magnetic Torquers During the In-Flight Phase", The University of Texas at Austin / Center for Space Research, Technical Memorandum, CSR-TM-00-01,January 2000

[82] Wolff, M., "Direct Measurements of the Earth's Gravitational Potential Using a Satellite Pair", Journal of Geophysical Research, Vol. 74, No.22, pp5295-5300, October 15, 1969

[83] Wu, S.C., Yunck, T.P., and Thornton, C.L., "Reduced-Dynamic Technique for Precise Orbit Determination of Low Earth Satellites", Journal of Guidance, Vol.14, No.1, pp24-30, January-February 1991

[84] Yionoulis, S.M. and Pisacane, V.L., "Geopotential Research Mission: Status Report", IEEE Transactions on Geoscience and Remote Sensing, Vol.GE-23, No.4, pp511-516, July 1985

[85] Yuan, D.N., "The Determination and Error Assessment of the Earth's Gravity Field Model", Ph.D. Dissertation, Department of Aerospace Engineering and Engineering Mechanics, The University of Texas at Austin, May 1991

[86] Yuan, D.N., "LLISS User's Manual", Center for Space Research, The University of Texas at Austin, May 1991